Catalytic Conversion of Ethane to Ethylene and Aromatic Hydrocarbons

February 2020

Hikaru SAITO

Catalytic Conversion of Ethane to Ethylene and Aromatic Hydrocarbons

February 2020

Waseda University
Graduate School of Advanced Science and Engineering
Department of Advanced Science and Engineering
Research on Applied Chemistry B

Hikaru SAITO

Table of contents

Chapter 1 General introduction

1.1. Progress in chemical utilization of ethane

Chemical utilization of ethane has great impact on modern petroleum industry. Inexpensive ethane derived from shale gas and associated petroleum gas is vastly available in North America and the Middle East, respectively.[1] Ethane is converted to ethylene by a steam cracking process, ethane cracker. Ethylene is one of the fundamental chemicals in petrochemical industry. Annually 142.3 million tons of ethylene was produced in 2016 all over the world[2] to synthesize polyethylene, ethylene oxide, styrene and other ethylene derivatives.

Ethylene production from ethane is much superior in terms of cost to that from naphtha,[1] which is a conventional feedstock for ethylene production by the steam cracking process. However, ethane cracker is an energy-intensive process because of its high reaction temperatures (>1073 K).Therefore, the ethylene production is need to be conducted at relatively low temperatures. Furthermore, development of ethylene production from ethane instead of naphtha has induced another problem. In addition to ethylene, fundamental chemicals including propylene, 1, 3-butadiene, and aromatic hydrocarbons are produced by the steam cracking of naphtha. In contrast, these important building blocks are not obtained by the ethane cracker.[1] Therefore, other methods to produce the fundamental chemicals except for ethylene are required. For instance, propylene is produced through dehydrogenation of propane,[3] methanol to propylene[4,5] and olefin metathesis of ethylene and 2-butenes.[6]

Catalytic conversion of ethane to ethylene and aromatic hydrocarbons would be key technologies to solve the problems. Catalytic ethane dehydrogenation (EDH) over oxide or supported-metal catalysts has been widely investigated to realize environmental friendly ethylene production. For production of aromatics including benzene, toluene and xylenes (BTX), catalytic ethane dehydroaromatization (EDA) is an alternative to steam cracking of naphtha. EDA has been much attractive since valuable aromatics is produced from inexpensive ethane.

Catalytic EDH and EDA under non-oxidative conditions are described in this chapter. Excellent reviews on oxidative EDH were published elsewhere.[7,8] At the beginning, steam cracking of ethane is briefly introduced on the basis of its reaction mechanism. Next, EDH over Cr-based and Ga-based catalysts is described in detail. Influence of co-existence of CO_2 is also discussed. After that, EDA over zeolite-supported metal catalysts is described. Finally, aims of thesis are presented briefly.

1.2. Steam cracking of ethane

1.2.1. Reaction mechanism

Steam cracking of ethane is a non-catalytic process for ethane conversion to ethylene through

pyrolysis. Prior to pyrolysis, ethane is mixed with effluent steam to remove carbonaceous deposits on cracking coils, where the reaction proceeds at *ca.* 1073 K. Pyrolysis of ethane proceeds through a radical chain mechanism firstly proposed by Rice and Herzfeld.[9] This mechanism is composed of various elementary reactions such as homolysis, hydrogen abstraction, β-scission, and combination.[10] The reaction is initiated by homolytic cleavage of the C–C bond in an ethane molecule because enthalpy for the C–C bond dissociation (376 kJ mol^{-1})[11] is lower than that of the C–H bond dissociation (420 kJ mol^{-1}).[12] The activation energy of the C–C bond (*ca*. 367 kJ mol^{-1}) is also lower than that of the C–H bond (411 kJ mol^{-1}).[13,14] The C–C bond cleavage in an ethane molecule results in the formation of two methyl radicals as follows.

$$C_2H_6 \rightarrow 2CH_3\cdot \quad (1.1)$$

The methyl radical induce subsequent propagation steps.

$$CH_3\cdot + C_2H_6 \rightarrow CH_4 + C_2H_5\cdot \quad (1.2)$$

$$C_2H_5\cdot \rightarrow C_2H_4 + H\cdot \quad (1.3)$$

$$CH_3\cdot + C_2H_6 \rightarrow C_3H_9\cdot \quad (1.4)$$

$$CH_3\cdot + C_2H_4 \rightarrow C_3H_7\cdot \quad (1.5)$$

$$C_3H_9\cdot \rightarrow C_3H_8 + H\cdot \quad (1.6)$$

$$C_3H_7\cdot \rightarrow C_3H_6 + H\cdot \quad (1.7)$$

A hydrogen atom in an ethane molecule is firstly abstracted by the methyl radical, resulting in the formation of methane and an ethyl radical (reaction (1.2)). Subsequent β-scission in the ethyl radical leads to the formation of ethylene and a hydrogen radical (reaction (1.3)). The methyl radical also attacks ethane and ethylene (reactions (1.4) and (1.5)), resulting in the formation of propane and propylene (reactions (1.6) and (1.7)). Heavy hydrocarbons can be obtained through analogous reactions. Furthermore, termination steps proceeds through reactions between two radicals.

$$2H\cdot \rightarrow H_2 \quad (1.8)$$

$$CH_3\cdot + H\cdot \rightarrow CH_4 \quad (1.9)$$

$$CH_3\cdot + C_2H_5\cdot \rightarrow CH_4 + C_2H_4 \quad (1.10)$$

On the basis of temperature programmed reaction, pyrolysis of ethane to ethylene initiates at more than 873 K.[15]

Under practical situation, a lot of reactions proceed in addition to the reactions (1.1)–(1.10). Sundaram and Froment considered 49 reactions to simulate product distribution and concentration of radicals.[13] Because the cracking coils are one of the tubular reactors, temperature gradient along the radial direction is an important factor to calculate the product distribution and concentration of the radicals. Marin and co-workers reported that concentration of the methyl radical is higher near the wall of the cracking coil than its center because of high temperature near the wall.[14] This results in much methane formation if the simulation is based on a two-dimensional model.

Intrinsically, formation of by-products such as methane, C_3 and heavier hydrocarbons is inevitable in case of ethylene production through the radical chain mechanism because the reaction initiates from the C–C bond cleavage. In particular, the formation of methane and coke, which are

thermodynamically stable, is remarkable at high conversion (temperature) level.[16,17] This results in the decrease of energy efficiency for ethylene production.

1.2.2. Coke formation

Coke formation on the internal wall of the cracking coils induces severe problems such as a pressure drop and a decrease in a heat flux to the reactor.[18] In particular, the latter decreases ethylene yield because of a decrease in the reaction temperature. In order to maintain ethylene yield, temperature of the outlet gas is generally operated to be constant. This indicates that the cracking coil is heated much more than usual to supply the sufficient heat flux, resulting in the higher temperature of the internal wall than the reaction temperature. Therefore, taking the thermal resistance of the cracking coil and the tolerable pressure drop into consideration, periodic removal of the carbonaceous deposit (decoking) is conducted every 20–60 days depending on operational conditions.[17,19]

In general, three types of coke formation mechanism have been proposed: the heterogeneous catalytic mechanism, the heterogeneous radical mechanism and the homogeneous condensation mechanism.[20] The heterogeneous catalytic mechanism is based on the coke formation on the surface of the cracking coils. Fe and Ni included in Fe–Cr–Ni alloys, which are used as cracking coil materials, catalytically promote coke formation. This phenomenon is observed at the initial stage of the reaction until the surface of the cracking coil is covered with the carbonaceous deposits, indicating that the coke formation rate gradually decreases and reaches an asymptotic value.[17,21] The heterogeneous radical mechanism is growth of the carbonaceous deposits through reactions with the radical species. Wauters and Marin proposed that this mechanism is composed of five steps: hydrogen abstraction, substitution, addition by the radicals, addition to olefins and cyclization.[22] Once the coke formation occurs on the wall, growth of the coke proceeds throughout the reaction. The carbonaceous deposits also can be formed through the homogeneous condensation mechanism as the result of the chain reaction. Therefore, the coke formation *via* this route is concomitant with pyrolysis of ethane.

From a metallurgic point of view, coating the surface with inert oxides is an effective way to mitigate the coke formation. In principle, Al or Mn is included in the Fe–Cr–Ni alloys. After oxidation of the alloy at high temperatures (1323 K for Al; 1023 K for Mn), Al_2O_3 or $MnCr_2O_4$, which has high coking resistance, is deposited on the surface.[20,23] Furthermore, coating a catalyst for the water gas reaction have been developed to achieve the operation without the coke formation.

$$C(s, \text{graphite}) + H_2O(g) \rightarrow CO(g) + H_2(g) \quad \Delta_r H^{\circ}(298\ K) = 131\ kJ\ mol^{-1} \qquad (1.11)$$

For instance, BASF developed CAMOL to mitigate the coke formation. In this case, tungsten-contained oxides are used for the gasification catalysts.[24] General Electric also developed gasification catalysts for which perovskite oxides containing Ce and alkaline-earth metals are used.[25] However, introduction of the catalysts to the cracking coil is still immature technology. Further research and development are required in this field.

1.3. Dehydrogenation of ethane under non-oxidative conditions

Catalytic ethane dehydrogenation denoted as EDH enables ethylene production at relatively low temperatures in comparison with pyrolysis of ethane.

$$C_2H_6(g) \rightarrow C_2H_4(g) + H_2(g) \qquad \Delta_r H^{\ominus}(298\ K) = 137\ kJ\ mol^{-1} \qquad (1.12)$$

However, the reaction is endothermic, and therefore high reaction temperatures are required to achieve higher equilibrium conversion as shown in Figure 1.1. In addition, low pressure of ethane results in high equilibrium conversion on the basis of Le Chaterlier's principle.

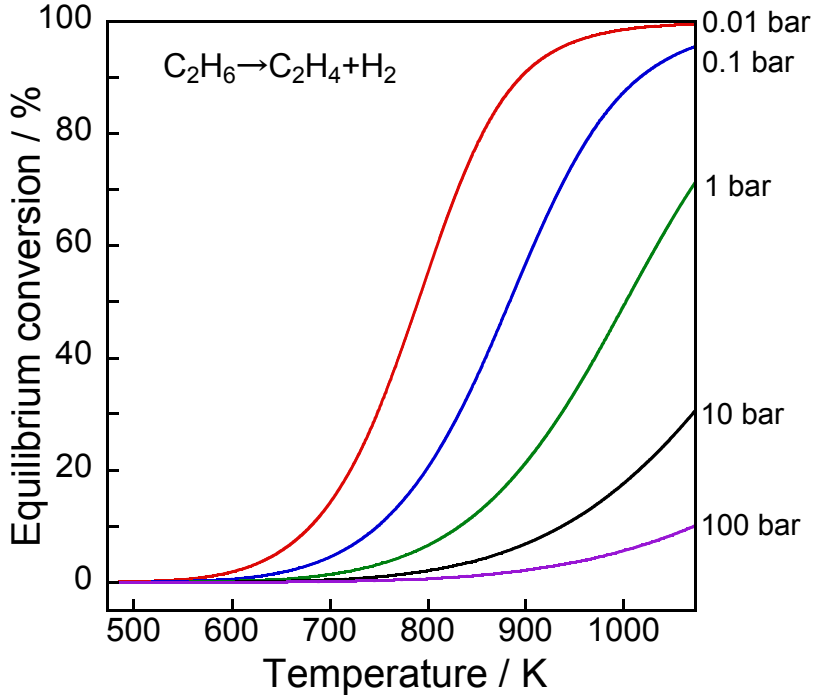

Figure 1.1. Temperature dependence of equilibrium conversion of ethane dehydrogenation at various pressure of ethane.

The reaction mechanism of EDH is intrinsically different from pyrolysis of ethane: catalysts should have an ability in selective C–H bonds dissociation. Side reactions such as hydrogenolysis of ethane, decomposition of ethane and ethylene to coke must be prohibited to achieve high selectivity to ethylene and stability. In this section, representative catalysts for EDH are described in terms of their active sites and reaction mechanism.

1.3.1. Cr oxide catalysts

Cr oxide catalysts have been one of the catalysts for dehydrogenation of light alkanes represented by the Catofin process (CB&I Lummus).[26] In terms of cost, the Cr oxide catalysts is superior to noble metal catalysts. Thorough investigations on the active sites, effects of support and influence of co-feeding CO_2 have been conducted.

1.3.1.1. Active sites

The nature of Cr species is an important factor for C–H bond activation. Basically, EDH proceeds on Cr–O sites.[27] Their structure and electronic state have been investigated by various characterizations such as temperature-programmed reduction (TPR), Raman spectroscopy, UV-Vis spectroscopy, X-ray diffraction (XRD), X-ray absorption fine structure (XAFS) spectroscopy, and X-ray photoelectron spectroscopy (XPS).[28–35]

The Cr species can be various structure. Generally, the Cr species are classified into 4 types: monochromate (isolated mononuclear Cr), polychromate (multinuclear Cr oxide cluster), amorphous Cr_2O_3 and crystalline α-Cr_2O_3.[29–31,34] The structure of the Cr species is mainly dependent on the amount of Cr loading. At the high loading amount (> 5wt%), the amorphous Cr_2O_3 and crystalline α-Cr_2O_3 are easy to be formed. These Cr species are considered to be inactive for dehydrogenation.[29,36] In contrast, mono-chromate and polychromate species are dominant at the low loading amount. The formation of Cr_2O_3 can be distinguished from the color of the catalysts. The color is varied from yellowish to greenish due to the Cr_2O_3 formation.[34,37,38]

Investigations on the nature of monochromate and polychromate have been widely conducted since these Cr species are the active sites for EDH.[27,39,40] The images of them are drawn in Figure 1.2. To identify the existence of the Cr species, UV-Vis and Raman spectroscopy are useful techniques. However, the Cr species are reduced under the reaction conditions from Cr^{6+} and/or Cr^{5+} to Cr^{3+} and/or Cr^{2+}. Therefore, evaluation of the active sites under *in-situ* conditions is important. For fresh Cr oxide catalysts, Cr^{6+} is dominant. Many reports focus on Cr^{6+} because the existence of Cr^{5+} was identified by only electron spin resonance (ESR) and infarared (IR) spectroscopy.[30,37] Also, the reduced Cr species are mainly Cr^{3+}. Although Cr^{2+} was identified by XPS and XAFS,[35,39] the proportion of Cr^{2+} in the spent catalysts was small.[39] Therefore, it is considered that Cr^{6+} is reduced to Cr^{3+} during the dehydrogenation reaction. The nature of Cr^{5+} and Cr^{2+} is still under discussion.

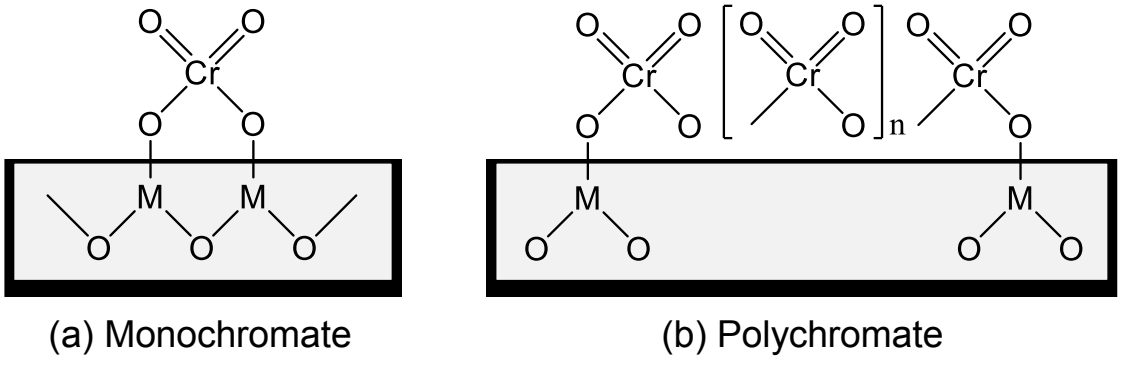

Figure 1.2. Structure of (a) monochromate and (b) polychromate supported on a metal (M) oxide.

EDH over Cr oxide catalysts proceeds on the reduced monochromate and polychromate. As shown in Figure 1.3(a), Olsbey *et al.* reported that end-on and dissociative adsorption of ethane occurs on the active sites on the basis of the isotopic study.[27] On the other hand, Shee and Sayari

observed adsorbed acetaldehyde by diffuse reflectance infrared Fourier transform (DRIFT) spectroscopy.[41] They proposed that the formation of ethoxide species is the first step for the dehydrogenation reaction (Figure 1.3(b)). Determination of the adsorbed species on the respective Cr species is challenging. Therefore, further investigations based on, for instance, density functional theory (DFT) are expected to elucidate the reaction mechanism.

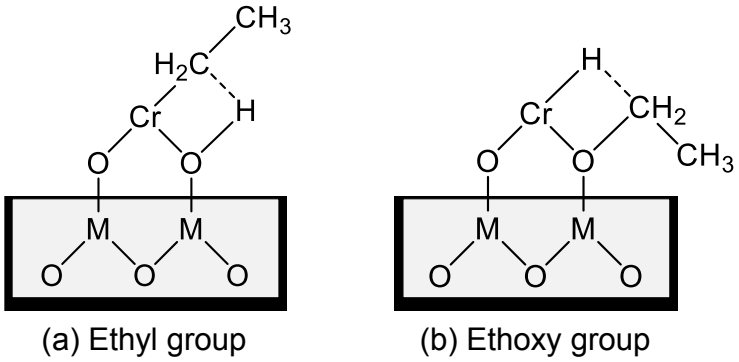

Figure 1.3. Schematic adsorption of ethane on reduced monochromate supported on a metal (M) oxide: Formation of (a) ethyl group and (b) ethoxy group.

1.3.1.2. Effects of support on the catalyst state

As described in the previous section, the ideal Cr oxide catalyst has as the large amount of monochromate or polychromate species as possible. However, the large Cr loading amount results in the formation of the inactive Cr_2O_3 species through agglomeration.[34] Therefore, selection of an appropriate support have a great influence on the catalytic activity and ethylene selectivity.

Alumina is a typical support.[27–31,34,41] Recently, Fridman *et al*. thoroughly examined the Cr species on the alumina support.[34] They reported that a part of the mono- and polychromate were unstable and reduced during dehydrogenation of isobutane. After the reduction, small Cr_2O_3 clusters were agglomerated and large Cr_2O_3 clusters were formed. Furthermore, regeneration of the catalyst under oxidative conditions induced formation of aluminum-chromium-chromate species around the periphery of the Cr_2O_3 clusters as shown in Figure 1.4. The agglomeration of the mono- and polychromate results in the irreversible deactivation of the catalysts.

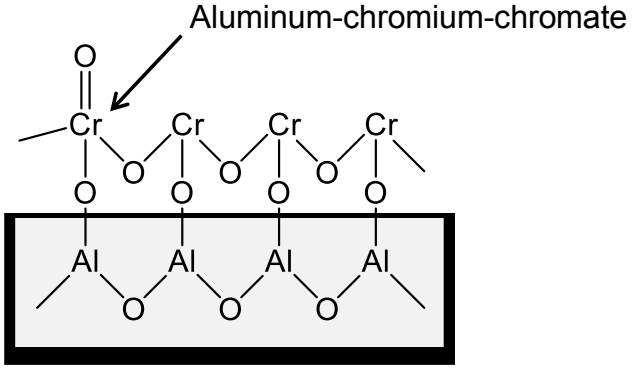

Figure 1.4. Structure of aluminum-chromium-chromate.

Silica is an alternative support to alumina. Various kinds of silica support including zeolites and mesoporous silica were examined.[33–39,42–45] These silica supports have a large surface area, resulting in the highly dispersed Cr species on the supports. The amount of SiOH groups would play an important role in stabilizing the dispersed Cr species (mono- or polychromate). Cheng *et al*. reported that the initial activity of Cr/SBA-15 was proportional to the amount of the SiOH groups contributing to the abundantly dispersed Cr species.[44] Botavina *et al*. proposed the detailed structure of monochromate on the basis of XAFS measurements.[35] The reduced monochromate was bound with two short Si–O–Cr bonds and a long Si–O–Cr bond. Its electronic state would rather Cr^{2+} than Cr^{3+}. These studies would indicate that the density of the SiOH groups have an influence on the nature of the Cr active sites.

1.3.1.3. Co-feed of CO_2

EDH in the presence of CO_2 has been investigated to enhance the catalytic performance of the Cr catalysts. In many cases, EDH in the presence of CO_2 is regarded as oxidative dehydrogenation. However, the overall reaction is still endothermic as follows.

$$C_2H_6(g) + CO_2(g) \rightarrow C_2H_4(g) + CO(g) + H_2O(g) \qquad \Delta_r\boldsymbol{H}^{\circ}(298\ K) = 178\ kJ\ mol^{-1} \quad (1.13)$$

This chemical formula is interpreted as EDH (reaction (1.12)) in combination with the reverse water gas shift (RWGS) reaction.

$$CO_2(g) + H_2(g) \rightarrow CO(g) + H_2O(g) \qquad \Delta_r\boldsymbol{H}^{\circ}(298\ K) = 41.2\ kJ\ mol^{-1} \quad (1.14)$$

Therefore, the nature of the reaction (1.13) is completely different from oxidative EDH using O_2 as an oxidizing agent, which is an exothermic reaction. The effects of the CO_2 introduction to the dehydrogenation system are generally explained on the basis of following three reasons;[46–48] decrease in the partial pressure of ethane (see also Figure 1.1); removal of H_2 from the reaction system through RWGS, resulting in the promotion of the reaction (1.12); improvement in the catalytic stability thanks to removal of carbonaceous deposit through the reverse Boudart reaction.

$$C(s, graphite) + CO_2(g) \rightarrow 2CO(g) \qquad \Delta_r\boldsymbol{H}^{\circ}(298\ K) = 172\ kJ\ mol^{-1} \quad (1.15)$$

The promotion of ethane conversion and the suppression of coke formation were practically reported.[38,47]

However, the promotive effect on EDH over Cr-based catalysts is attributed to not only the contribution of RWGS but differences in the nature of active sites and reaction mechanism. Without CO_2, the active sites are supposed to be Cr^{3+} reduced from mono- or polychromate (Cr^{6+}). At the initial stage of the reaction, where the reduction of Cr^{6+} proceeds, ethane conversion tends to decrease,[39,40] indicating that Cr^{6+} is more active for EDH than Cr^{3+}. Indeed, Mimura *et al*. reported that apparent activation energy of EDH decreased from 119.3 (without CO_2) to 91.3 (with CO_2) kJ mol^{-1} using a Cr/ZSM-5 catalyst.[37] Therefore, it is proposed that EDH proceeds through the redox mechanism as shown in Scheme 1.1. In this scheme, ethane is oxidatively activated at Cr^{6+}=O sites, resulting in formation of ethylene and water. Then, the catalytic cycle is completed through the oxidation of the reduced Cr^{3+} species with CO_2.

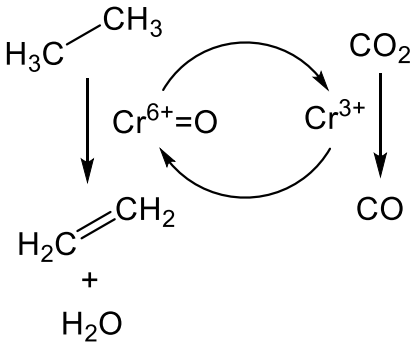

Scheme 1.1. Redox mechanism for EDH in the presence of CO_2 over Cr oxide catalysts.

The redox behavior of the Cr species was verified by various techniques such as TPR, XPS and IR spectroscopy. On the basis of TPR and XPS, the reduced Cr^{3+} can be oxidized to Cr^{6+} under CO_2 atmosphere.[38,43,47,48] In addition, Mimura *et al.* evaluated Cr=O bonds by IR spectroscopy,[37] demonstrating that intensity of the absorption band attributed to Cr=O decreased and increased by ethane and CO_2 treatments, respectively. However, the reducible Cr^{6+} species is not completely re-oxidized with CO_2 probably because of agglomeration of mono- and polychromate and low oxidizing ability of CO_2.[49] Therefore, it is required for the catalyst to stabilize the reducible Cr^{6+} species and promote the oxidation of the reduced Cr^{3+}. The silica supports would be useful to stabilize the Cr active sites as mentioned above. To promote the oxidation of the reduced Cr species, the use of additives with oxygen storage capacity is one of the options.[50,51] In addition, CO_2 activation would be a key factor because of its low reactivity. Bugrova *et al*. reported that a ZrO_2-supported Cr catalyst exhibited a high activity for EDH in the presence of CO_2 because of the basicity of ZrO_2[48] which would contribute to CO_2 activation.

Some problems are still unsolved in case of EDH in the presence of CO_2. For instance, the contribution of CO_2 to the oxidation of the reduced Cr species and RWGS, is not discussed in detail. It is required to elucidate the role of respective Cr species in dehydrogenation through the redox mechanism and RWGS. In addition, *operando* analyses in combination with isotopic CO_2 should be performed to establish the redox mechanism.

1.3.2. Ga oxide catalysts

Ga oxide catalysts are known to have a catalytic activity for EDH.[52] The Ga catalysts are classified into two types: zeolite-supported Ga oxide catalysts and other metal oxide-supported Ga oxide catalysts. Comparing zeolite supports with other metal oxides such as Al_2O_3 and TiO_2, the nature of the active sites is different because of the unique cation-exchange ability of the zeolite. In this part, differences in the nature of the active sites, which is derived from the properties of the supports, are described.

1.3.2.1. Zeolite-supported Ga oxide catalysts

Zeolite-supported Ga oxide catalysts are originally used for conversion of propane or butane into aromatic hydrocarbons.[53] Cyclar process developed by BP/UOP is one of the representative examples.[54] Among the zeolites, **MFI** type zeolite in proton form (H-ZSM-5) is used as a support. The unique nature of the Ga species, which can be formed thanks to the ion-exchange ability of the zeolite, has been investigated on the basis of practical experiments and DFT calculations.

From the practical point of view, Ga/H-ZSM-5 catalysts prepared by various methods such as physical mixing, impregnation and chemical vapor deposition (CVD) are used to elucidate the nature of the Ga species.[55–57] The pristine Ga/H-ZSM-5 usually contains highly dispersed Ga oxide species in the micropore system. At this stage, the Ga species are not sufficiently exchanged with the protons. To promote the ion-exchange, the Ga/H-ZSM-5 catalyst is need to be reduced under H_2 atmosphere. This phenomenon was verified by *in-situ* IR spectroscopy. Intensity of the absorption band at *ca.* 3610 cm^{-1} derived from acidic OH groups (Si–OH–Al) decrease under H_2 atmosphere.[55,58] Simultaneously, a new absorption band attributed to GaO–H appeared at *ca.* 3660 cm^{-1}, clearly indicating the ion-exchange of the reduced Ga species with the acidic protons. Furthermore, formation of Ga–H bonds, which is unstable at high temperatures such as 573 K, was observed at room temperature.[58] In turn, a part of these exchanged and reduced Ga species can be oxidized with N_2O and H_2O, resulting in the regeneration of the acidic OH groups concomitantly with formation of N_2 and H_2, respectively.[59]

Based on IR spectroscopy, Ga^+, GaO^+ and GaH_2^+ are the candidates for the active sites of the reduced Ga/H-ZSM-5. In addition, Rane *et al.* evaluated the electronic state of Ga by *in-situ* Ga *K*-edge X-ray absorption near-edge structure (XANES) spectroscopy.[57] At high temperatures (> 673 K) under H_2 atmosphere, a new feature was observed in a lower energy region (10371 eV), indicating the formation of Ga^+. Subsequent cooling to 373 K induce the increase of a feature at 10377 eV with the disappearance of the low energy feature, indicating the formation of GaH_2^+. However, Getsoian *et al.* reported that the absorption edge energy was dependent on not only the electronic state of Ga but the types of ligands.[60] For instance, the absorption energy can be shifted to the lower position through the formation of low-coordinated Ga^{3+} alkyl or hydride species. On the other hand, Schreiber *et al*. performed quantitative analyses to elucidate the Ga species.[61] They conducted H_2 pulses at 873 K and measured the amount of the consumed H_2 and formed H_2O. As a result, they concluded that Ga^+ was formed after the reduction at 873 K.

The activity of respective Ga species were experimentally evaluated. Rane *et al*. performed dehydrogenation of propane after reduction and/or oxidation treatments.[57] After the reduction treatment to form GaH_2^+, the activity gradually increased with time on stream. In contrast, the activity of the oxidized Ga/H-ZSM-5 containing GaO^+ rapidly decreased in 1 h. These activities was close to that of Ga^+ species. They concluded that GaH_2^+ and GaO^+ are unstable active sites in dehydrogenation of propane. Furthermore, the intrinsic activities of the Ga species are in the order of $GaO^+ > Ga^+ > GaH_2^+$ on the basis of the initial activities. On the other hand, Ausavasukhi and

Sooknoi conducted EDH in a pulse reactor.[55] They demonstrated that the activity was enhanced by introduction of the small amount of H_2, indicating the higher activity of GaH_2^+ for EDH than Ga^+ or GaO^+. The activity of GaH_2^+ decreased with subsequent C_2H_6 pulses under He. In contrast, the high activity was maintained under H_2, indicating the unstable nature of the GaH_2^+. Therefore, the Ga^+ species would be stable during the dehydrogenation reactions although the activities of the Ga species for dehydrogenation of light alkanes would be dependent on the reactants. Nascimento and co-workers proposed that the reaction mechanism was varied due to the size and type (liner or blanched) of alkanes on the basis of DFT studies.[62,63]

The reaction mechanism of EDH on the Ga species was mainly investigated by DFT calculations. As shown in Scheme 1.2, three reaction mechanisms are proposed by some research groups:[62–67] the alkyl mechanism, the carbenium mechanism and the concerted mechanism. The differences are based on the ethane activation manners.

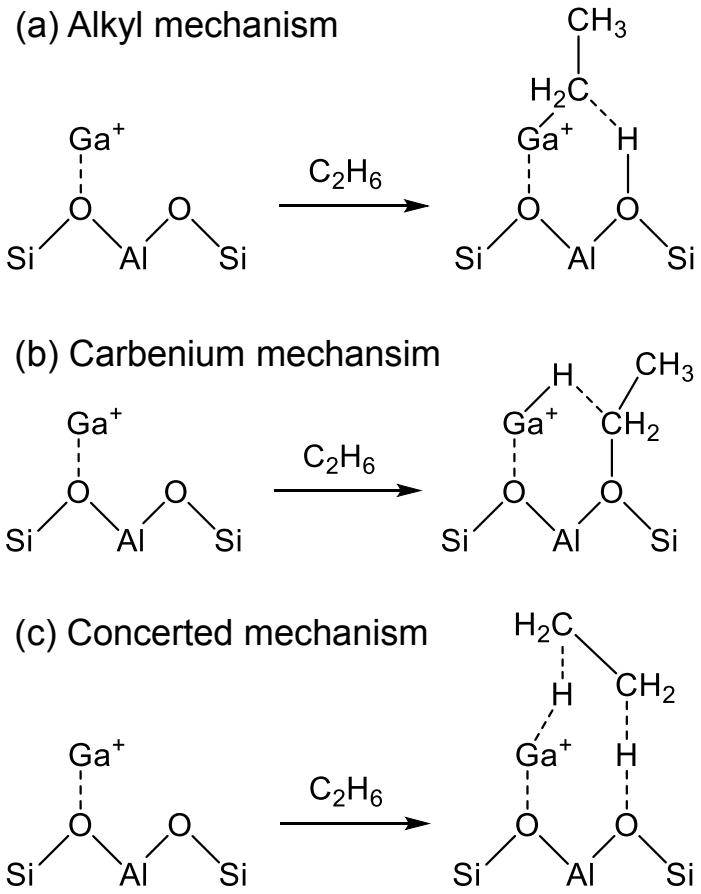

Scheme 1.2. Mechanism of ethane activation *via* (a) the alkyl mechanism, (b) the carbenium mechanism and (c) the concerted mechanism. Ga^+ is a representative active site of Ga/H-ZSM-5.

The alkyl mechanism begins from formation of $Ga–C_2H_5$ by hydrogen abstraction. In contrast, the carbenium mechanism proceeds through formation of an ethoxy group concomitantly with that of Ga–H. In the concerted mechanism, two hydrogen atoms are simultaneously abstracted from an ethane molecule, leading to the formation of ethylene and hydrogen in a step. The activation of ethane at Ga^+, GaH^{2+} and GaH_2^+ sites is investigated by DFT calculations using cluster models.

The alkyl mechanism is facile at any site.[62–66] However, Mansoor *et al.* recently reported that the carbenium mechanism is preferable at the GaH^{2+} site.[67] In addition, Schreiber *et al*. proposed that the proximity between the Ga and Brønsted acid sites promote the dehydrogenation of propane.[61] Experimentally, Kazansky *et al*. observed the adsorbed ethane on the Ga^+ sites by DRIFT spectroscopy.[59,68] They demonstrated the formation of $Ga–C_2H_5$ concomitantly with that of Ga–H. After heating, the absorption band of Ga–H at 2057 cm^{-1} was shifted to 2040 cm^{-1}, which is attributed to H–Ga–H, with the appearance of olefinic C–H. Therefore, EDH at the Ga^+ sites would proceed as following Scheme 1.3.

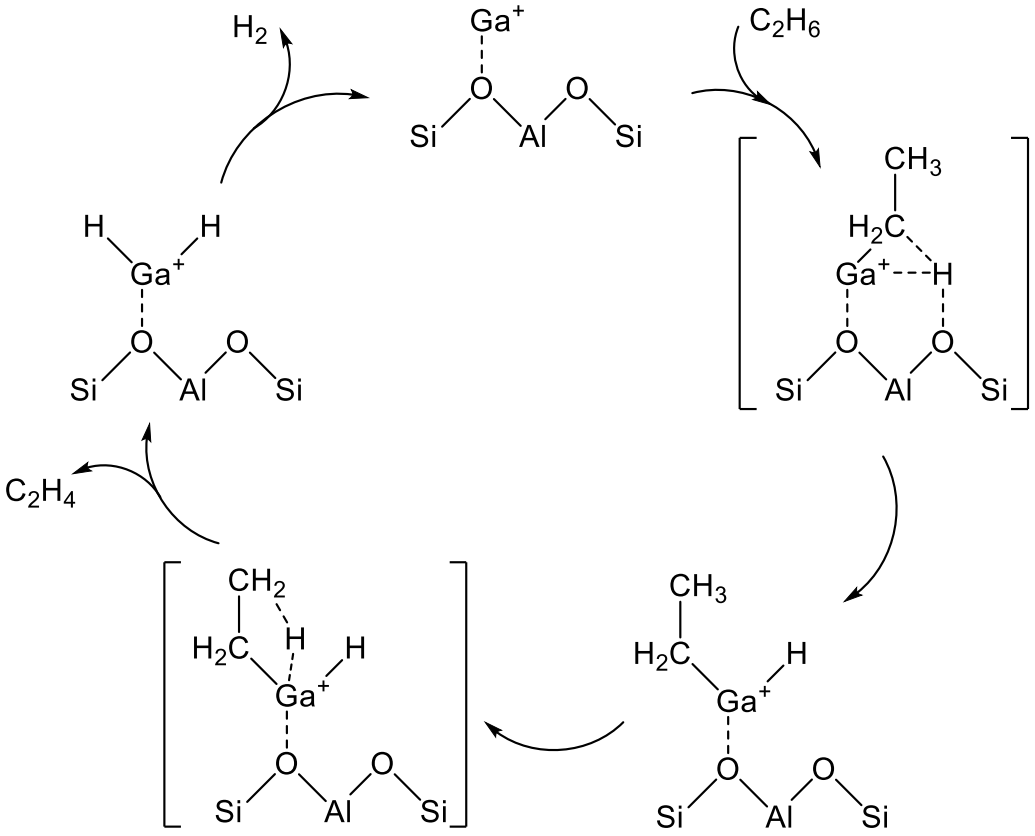

Scheme 1.3. Reaction mechanism of EDH at the Ga^+ site.

The dehydrogenation activity of the GaO^+ species was evaluated in the presence of steam because the GaO^+ species are reduced under the reaction conditions.[57] Hensen *et al.* performed dehydrogenation of propane over Ga/H-ZSM-5 in the presence of steam.[69] As a result, the stable activity was achieved. At the mononuclear GaO^+ site, the high activation barrier for hydrogen recombination was calculated among the elementary steps, resulting in the formation of a water molecule and the Ga^+ site.[65] Therefore, they proposed that multinuclear GaO clusters are the active sites for the dehydrogenation reaction.[69–72] The Ga cations included in the clusters are favorable to be tetrahedral coordination.[69] Proposed EDH at Ga_2O_2 clusters, for instance, is shown in Scheme 1.4.[71] The dehydrogenation reaction proceeds at a Ga–O Lewis acid–base pair. Hydrogen recombination is facile at the Ga oxide clusters although the formation of water is still favorable. Strong Lewis basicity of the bridged oxygen stabilizes the adsorbed hydrogen, resulting in the

inhibition of the hydrogen recombination.[72]

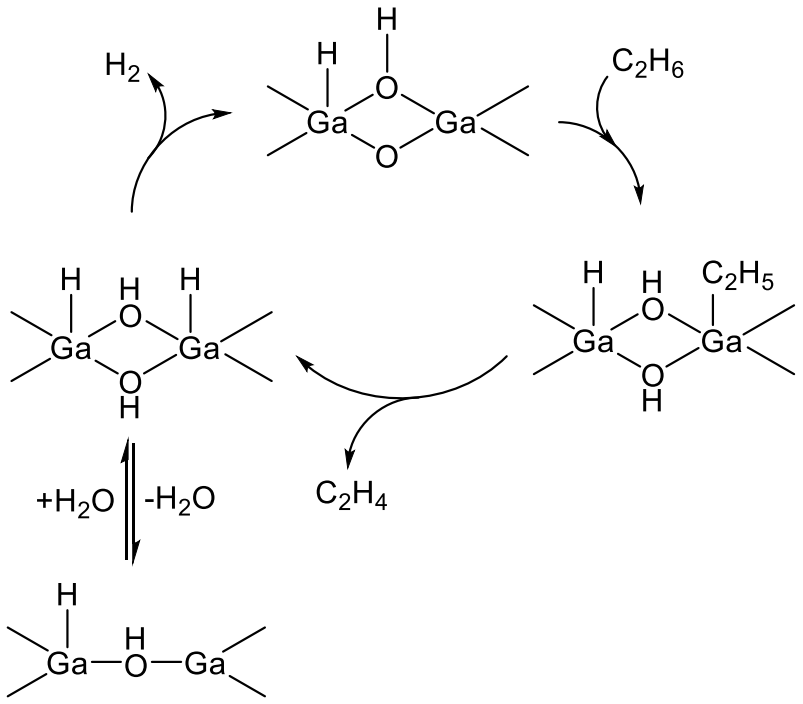

Scheme 1.4. Reaction mechanism of EDH in the presence of steam on a Ga oxide cluster.

1.3.2.2. Other metal oxide-supported Ga oxide catalysts

Supported Ga oxide catalysts such as Ga/TiO_2 are used for EDH, particularly, in the presence of CO_2.[73] On the supports, Ga oxide is basically Ga_2O_3, which has five polymorphs (α-, β-, γ-, κ-, ε-Ga_2O_3).[74] Characterizations of the Ga properties such as the structure of the active sites are indispensable since the surface Ga species play an important role in the reaction. Zheng *et al.* performed dehydrogenation of propane over Ga_2O_3 polymorphs except for ε-Ga_2O_3.[75] As a result, β-Ga_2O_3, which is the most stable polymorph, exhibited the highest activity among them. They concluded that the tetrahedrally coordinated Ga^{3+} cations facilitate the dehydrogenation reaction. The coordination environment of Ga can be evaluated by Ga *K*-edge XANES. Nishi *et al.* performed a quantitative analysis of tetrahedrally- and octahedrally coordinated Ga by XANES spectroscopy.[76] Hereafter, these Ga species are denoted as Ga(T) and Ga(O), respectively. The analysis is based on deconvolution of the XANES spectra and it is applicable to the Ga polymorphs and supported Ga oxide catalysts.[76,77]

In addition, the coordination environment of Ga_2O_3 can be evaluated by IR spectroscopy using H_2 as a molecular probe. Collins *et al.* reported that the absorption bands attributed to Ga–H bonds are observed around 2000 cm^{-1}.[78] They further measured the hydrogen adsorbed on α-, β-, γ-Ga_2O_3.[79] The spectra were consisted of the absorption bands at 2003 and 1980 cm^{-1}. The contribution of the band at 1980 cm^{-1} was in the order of α-Ga_2O_3 > γ-Ga_2O_3 > β-Ga_2O_3. This order is in agreement with that of the fraction of Ga(T) and Ga(O) in their structures. Therefore, they concluded that the Ga(T)–H and Ga(O)–H bonds are observed at 2003 and 1980 cm^{-1},

respectively. The proportion of the surface Ga(T) to Ga(O) can be calculated from the area of the absorption bands. However, the intensity of the bands is dependent on the temperatures.[80,81] At high temperatures such as 573 K, the intensity increased due to the formation of oxygen defects, resulting in the formation of new Ga–H bonds. Therefore, the coordination environment of surface Ga would be appropriately evaluated over 573 K because the dehydrogenation reaction is usually conducted over 573 K under reductive conditions.

The reaction mechanism of EDH over Ga_2O_3 is similar to the alkyl mechanism over Ga/H-ZSM-5 (Scheme 1.3). Kazansky *et al.* measured ethane adsorbed on Ga_2O_3 by DRIFT spectroscopy.[82] In this case, the polymorph of Ga_2O_3 is not clearly mentioned. They observed the formation of Ga–C_2H_5 in addition to C–H corresponded to CH_2 groups derived from ethylene, and Ga–H. The formation of Ga–C_2H_5 was also verified by ^{13}C cross-polarization (CP) magic angle spinning (MAS) nuclear magnetic resonance (NMR) spectroscopy.[83] In some cases, it is assumed the formation of Ga–H and alkoxy groups *via* the activation of light alkanes.[84,85] However, clear evidences of the formation of the alkoxy groups have not been reported yet.

The dehydrogenation of ethane over Ga oxide catalysts are mainly performed in the presence of CO_2.[52] Nakagawa *et al*. reported that Ga/TiO_2 exhibited a high activity in comparison with other supports including Al_2O_3, SiO_2, ZrO_2 and ZnO.[73] In case of Ga/Al_2O_3, a negative effect on the catalytic activity was verified in the presence of CO_2. The promotive effects of CO_2 on EDH are attributed to the hydrogen and coke removal through the RWGS and the reverse Boudart reaction, respectively (reactions (1.14) and (1.15)).[86,87] In contrast, selectivity to ethylene tends to decrease with the increase in the activity.[73,88] Methane formation is promoted instead of the decrease in ethylene selectivity, indicating the subsequent conversion of ethylene to methane. Therefore, appropriate conditions such as space velocity, partial pressure of CO_2 are required to achieve high ethylene yield.

In comparison with Cr oxides, Ga_2O_3 is a non-reducible oxide and, therefore, no report on the redox mechanism over Ga oxide catalysts in the presence of CO_2. To improve the catalytic performance, design of Ga active sites is indispensable. For instance, Ga/H-ZSM-5 catalysts exhibited a higher selectivity to ethylene than β-Ga_2O_3.[89] Ga/H-ZSM-5 exhibits the activity for RWGS, indicating that water is co-existing during EDH with CO_2. Therefore, the Ga oxide clusters, which exhibit the high dehydrogenation activity *via* Scheme 1.4, would be maintained during the reaction.

1.4. Dehydroaromatization of ethane

Ethane dehydroaromatization denoted as EDA enables the formation of BTX in one step.

$$C_2H_6(g) \rightarrow C_6H_6(g) + 6H_2(g) \qquad \Delta_r\boldsymbol{H}^{\circ}(298\ K) = 337\ kJ\ mol^{-1} \qquad (1.16)$$

This reaction is an endothermic reaction similarly to EDH. Therefore, high reaction temperatures at around 873 K are favorable to achieve high equilibrium conversion. From the practical point of view, the products are readily handled in terms of separation, storage and transportation because

the gaseous reactant is converted to the liquid products, leading to a potentially feasible process. However, commercial processes have not been developed yet using the natural gas resources (methane and ethane) in contrast with aromatization of C_3 and C_4 hydrocarbons.[54] This is because of the high reaction temperatures, resulting in the rapid deactivation of catalysts through coke formation.

This section consists of three parts: catalysts for EDA, reaction mechanism and catalyst deactivation. Some reviews on EDA are also available.[90–93]

1.4.1. Zeolite-supported metal catalysts

1.4.1.1. Zeolite supports

For EDA, the H-ZSM-5 zeolite modified with active metals is known to be an effective catalyst because the **MFI**-type zeolite has three-dimensional micropore channel systems, which consist of a straight and a sinusoidal channels.[94,95] They are composed of 10-memberd rings with a diameter of *ca.* 0.55 nm, which is close to the kinetic diameters of BTX. Thanks to the micropore channels, the **MFI**-type zeolite exhibits shape selectivity to BTX formation. In addition, H-ZSM-5 has strong Brønsted acid sites (BAS), which catalyze various reactions such as isomerization, cracking, alkylation and hydrogen transfer based on the carbenium and carbonium ions chemistry. Details of the reactions over zeolite catalysts are described in the literature.[96]

The **MEL**-type zeolite (ZSM-11) is another candidate for the support.[97,98] ZSM-11 has similar micropore channel systems to ZSM-5, which consist of two straight channels.[94,95] However, superiority of ZSM-11 to ZSM-5 is not clearly demonstrated. The **MWW**-type zeolite represented by MCM-22 has not been used in contrast with methane dehydroaromatization.[99] MCM-22 has two independent micropore channel systems.[94,95] One is composed of 12-membered ring cages connected to 10-memberd ring windows. The other is a two-dimensional micropore channel system. Difference between methane and ethane dehydroaromatization would be attributed to the kinds of active metals. Zn or Ga catalysts are mainly used for EDA in contrast with Mo catalysts for methane dehydroaromatization. Use of Mo would be a key factor for the formation of BTX in case of the MCM-22 support.

1.4.1.2. Active metals

The H-ZSM-5 zeolite is usually modified with active metals to facilitate ethane activation. It is difficult to activate ethane at BAS because the formation of primary carbenium ions is unfavorable, resulting in the low ethane conversion over H-ZSM-5 without the metal modification. In section 1.4.2, roles of the active metals are discussed in detail. As already reported, active metals including Pt, Ga and Zn are effective for the ethane activation.[100–104] However, Pt is expensive and induces hydrogenolysis of ethane to methane under H_2 atmospheres.[105]

$$C_2H_6(g) + 2H_2(g) \rightarrow 2CH_4(g) \qquad \Delta_r\boldsymbol{H}^{\ominus}(298\ \mathrm{K}) = 64.9\ \mathrm{kJ\ mol^{-1}} \qquad (1.17)$$

H-ZSM-5-supported Mo and Re catalysts also exhibit high performance for EDA[106–108] in addition to dehydroaromatization of methane.[109,110] However, these two metals are not suitable for their practical use because of sublimation of MoO_3 and Re_2O_7,[111,112] which probably exist in the pristine and regenerated catalysts, resulting in irreversible deactivation of the catalysts.

1.4.1.3. State of Zn species on H-ZSM-5

Based on the above reasons, Ga or Zn modified H-ZSM-5 is mainly used for EDA. The detailed nature of the Ga species are described in section 1.3.2.1. Here, the nature of Zn species on H-ZSM-5 is presented in detail. The nature of Zn species on H-ZSM-5 is investigated by many research groups because of its wide applications to various chemical reactions such as methane conversion and alkylation of benzene.[113]

Zn/H-ZSM-5 is prepared by various methods such as impregnation, ion-exchange, physical mixing and CVD.[114–117] The active Zn species on H-ZSM-5 are classified into two types: ZnO species and ion-exchanged Zn species. ZnO exist on the external surface and internal surface denoted as macrocrystalline ZnO and ZnO clusters, respectively. These ZnO species are conveniently analyzed by UV-Vis spectroscopy.[114,118] The macrocrystalline ZnO shows an absorption band at *ca.* 370 nm attributed to its band gap width. On the other hand, the ZnO clusters exhibit an absorption band at around 270 nm. Chen *et al*. reported that the ZnO clusters were identified by laser-induced luminescence spectroscopy.[118] Excited by a 244 nm laser, Zn/H-ZSM-5 containing the ZnO clusters showed a purple luminescence band at *ca.* 440 nm. However, the ZnO species are reduced under reductive conditions at elevated temperatures. Some are exchanged with BAS (solid state ion-exchange), resulting in the formation of ion-exchanged Zn species and H_2O.[119]

$$ZnO + 2H^+–O_z \rightarrow O_z–Zn^{2+}–O_z + H_2O \quad (1.18)$$

Here, O_z means the oxygen in the zeolite framework. This phenomena was also observed in the case where Zn metal was used instead of ZnO. Others are reduced to Zn metal vapor, resulting in the loss of Zn.

The existence of the ion-exchanged Zn species is apparently verified by temperature-programmed desorption with NH_3 (NH_3-TPD). In the TPD profile, two ammonia desorption peaks are observed in low and high temperature regions denoted as *l*-peak and *h*-peak, respectively.[120] The *l*-peak is attributed to desorption of ammonia bonded to the ammonia adsorbed on acid sites. The *h*-peak is ascribed to desorption of ammonia adsorbed on the acid sites. Although the *h*-peak contains ammonia desorbed from BAS and Lewis acid sites,[121] the intensity of *h*-peak decreases after the ion-exchange,[114] indicating the exchange of BAS with Zn cations. The decrease in BAS is also verified by ^{1}H MAS NMR spectroscopy.[117] The electronic state of the ion-exchanged Zn species is different from that of ZnO.[115] XPS studies revealed that the ion-exchanged Zn species show a peak at *ca.* 1024 eV in the $Zn2p_{3/2}$ XP spectrum.[115] In contrast, a peak corresponded to ZnO is observed at *ca*. 1021 eV. Berndt *et al*. proposed the structure of the ion-exchanged Zn.[116] They

performed temperature programmed surface reaction (TPSR) with CO and observed formation of CO_2 and H_2, indicating the existence of $[Zn(OH)]^+$ as shown in Scheme 1.5. During TPSR with CO, RWGS proceeds at $[Zn(OH)]^+$ and the nearest BAS, resulting in the formation of the isolated Zn^{2+} species.

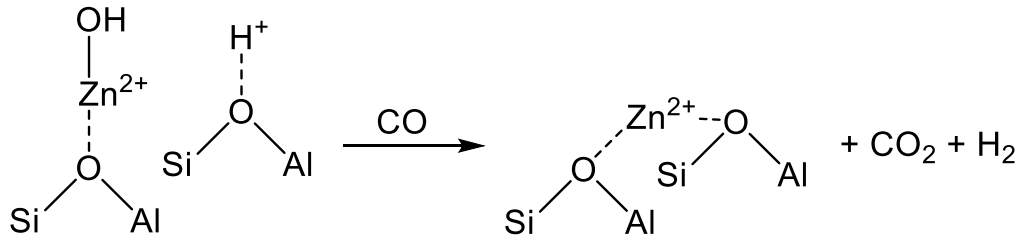

Scheme 1.5. Structural change from $[Zn(OH)]^+$ to isolated Zn^{2+} after RWGS.

However, Tamiyakul *et al.* reported that the ion-exchanged Zn species existed in pristine Zn/H-ZSM-5 were reduced under H_2 atmospheres on the basis of XPS.[115] They proposed formation of ZnH^+. Indeed, Zn hydrides were observed at room temperature by DRIFT spectroscopy.[122] In addition, Biscardi *et al*. analyzed Zn/H-ZSM-5 by *in-situ* Zn *K*-edge XANES spectroscopy.[123] The measurements were conducted in the presence of He, H_2 or C_3H_6 at up to 773 K. They concluded that $[Zn(OH)]^+$ in pristine Zn/H-ZSM-5 was dehydrated with the nearest BAS, resulting in the isolated Zn^{2+} interacting with two ion-exchange sites under the propane dehydrogenation atmosphere. Furthermore, Aleksandrov and Vayssilov investigated EDH at the isolated Zn^{2+}, $[Zn(OH)]^+$ and ZnH^+ sites on the basis of DFT.[124] As a result, EDH was facile at the isolated Zn^{2+} site thanks to the two ion-exchange sites. Therefore, the isolated Zn^{2+} would be an active center under the EDA atmosphere.

1.4.2. Reaction pathway

Reaction pathways of BTX formation were investigated using Pt, Zn, Ga and Re/H-ZSM-5.[100, 125–127] EDA is a complex reaction, and therefore elucidation of each elementary step is challenging. Irrespective of the kinds of the active metals, the proposed reaction pathway is almost the same. As shown in Scheme 1.6, ethane is first dehydrogenated at the metal sites on the external or internal surface. Subsequently, ethylene is oligomerized, cyclized and dehydrogenated to BTX in the micropore channel systems. Under low conversion levels (low residence time), ethylene is the main product. On the other hand, selectivity to BTX and methane increase with a decrease in selectivity to ethylene under high conversion levels (high residence time). C_3 and C_4 hydrocarbons, which are mainly composed of olefins, also form during the reaction.

Hagen *et al.* demonstrated the formation of linear C_4 olefins using a recirculation reactor.[128] They proposed that the linear C_4 olefins are intermediates for BTX. It was reported that oligomerization of ethylene proceeds even at room temperature.[129,130] In addition, ethylene is converted to propylene through oligomerization and cracking catalyzed by BAS.[131,132] Therefore,

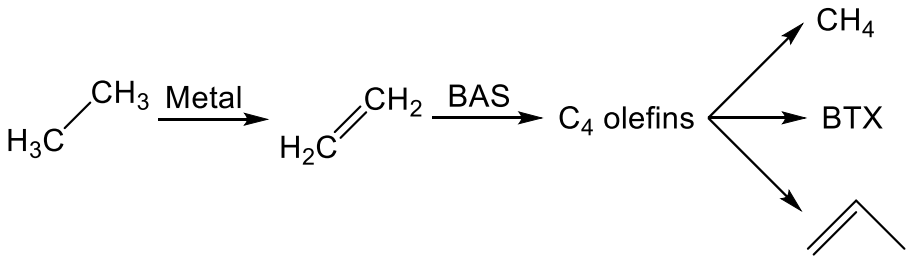

Scheme 1.6. Reaction pathway of EDA.

ethylene would be first oligomerized to C_4 olefins and subsequently cracked to propylene. Propylene could be also converted to BTX through the similar pathway of ethylene aromatization.[133,134]

Distribution of BTX depends on the reaction temperatures.[100] At lower temperatures (< 723 K), proportion of them is in the order of xylenes > toluene > benzene. In a middle temperature range (773–823 K), the proportion of toluene increases. Furthermore, benzene formation increases at higher temperatures. This tendency is the case in aromatization of ethylene and propylene.[133,135] Recently, Liang *et al.* reported that BTX formed from different olefin intermediates on the basis of transient kinetic studies of ethane and ethylene aromatization.[136] They proposed that the distribution of BTX might depend on the partial pressure of the olefin intermediates. In addition, Choudhary *et al*. reported that the proportion of BTX in aromatization of olefins is dependent on the space velocity.[134,137] Dependence of the proportion of BTX on space velocity (conversion) is similar to that on temperature. The partial pressure of the intermediates is varied with conversion of reactants, which can be controlled by the space velocity and reaction temperature, since the aromatization reactions are subsequent reactions, resulting in the different distribution of BTX.

The nature of active metals is a crucial factor in aromatization of light alkanes. Generally, the first dehydrogenation step (C–H bond activation) is a rate-determining step over H-ZSM-5. The active metals promote dehydrogenation of the alkanes. In contrast, Biscardi and Iglesia proposed hydrogen desorption step is rate-determining in dehydrogenation of propane over Zn/H-ZSM-5.[138] Indeed, Zn/H-ZSM-5 and ZnO exhibit hydrogen spillover and back-spillover effects,[139,140] indicating that hydrogen desorption is promoted by virtue of Zn. In addition, the active metals have an influence on BTX formation. Over H-ZSM-5, dienes and cyclodienes are intermediates in aromatization of ethylene reported by Marin and co-workers.[141] As shown in Scheme 1.7, aromatization over H-ZSM-5 basically proceeds through oligomerization, cyclization and dehydrogenation *via* hydrogen transfer with formation of alkanes.[142] In contrast, modification of H-ZSM-5 with Ga, Zn and Ag enhance selectivity to BTX in aromatization of ethylene.[143–145] Bandiera and Taârit proposed that dehydrogenation of cycloalkenes to form BTX is competed with the ethane activation.[146] They demonstrated that addition of cyclohexadiene, which would be a precursor of BTX, to ethane feed inhibited EDA.[147] Therefore, the active metals contribute not only activation of light alkanes but the formation of BTX because aromatization of the intermediates would be easy to proceed in comparison with hydrogen transfer catalyzed by BAS.

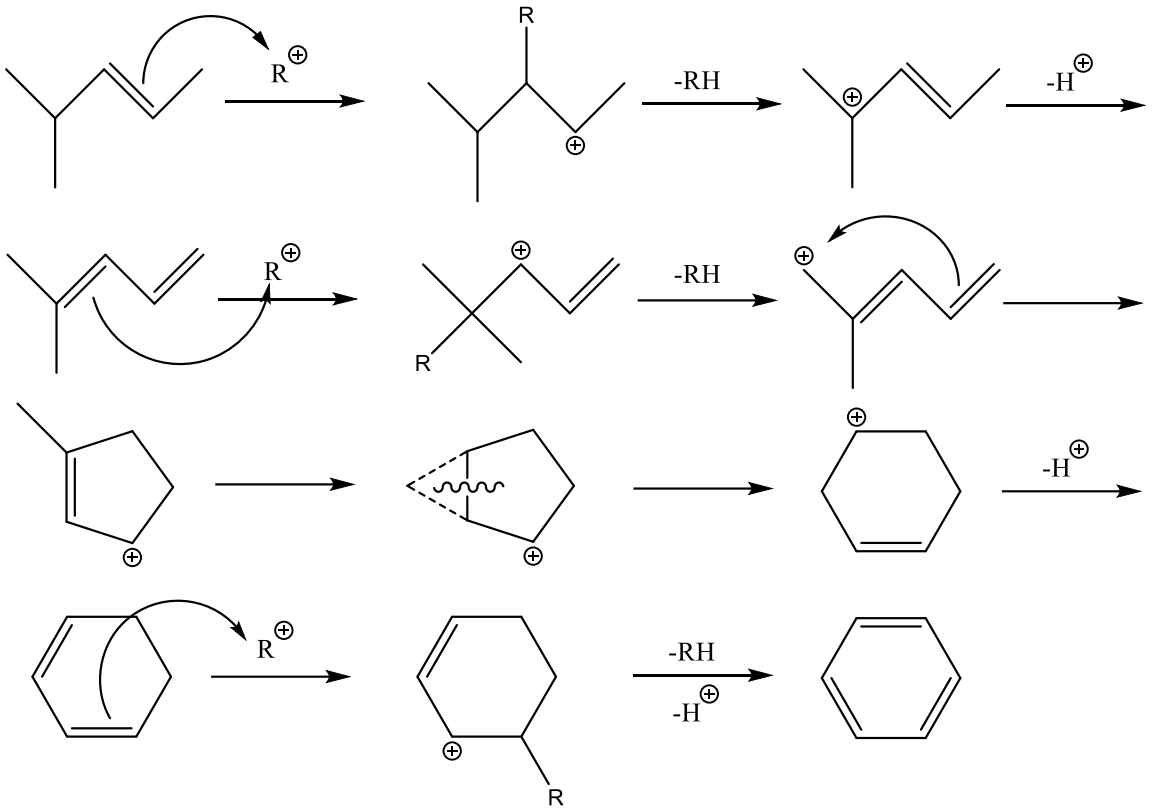

Scheme 1.7. Aromatization of oligomers over H-ZSM-5.

1.4.3. Catalyst deactivation

Deactivation of H-ZSM-5 modified with active metals is a serious problem. Coke formation over H-ZSM-5 is catalyzed by BAS. Various techniques including thermogravimetric analysis, Raman and ^{13}C MAS NMR spectroscopy are used to analyze coke species. The coke formation on zeolite catalysts is summarized in the literature.[148] The coke species are mainly polycyclic aromatic hydrocarbons under the aromatization conditions, which induce blocking of micropore channels, resulting in the deactivation of the catalysts. Therefore, the catalysts must be periodically regenerated under oxidative conditions.[149]

To suppress the coke formation, addition of a promoter to metal-modified H-ZSM-5 is one of the effective ways. Hu and co-workers performed Fe addition to Mo/ZSM-5 for EDA.[149] The Fe promoter improved the catalytic stability because carbon nanotubes formed on the external surface of H-ZSM-5. The formation of the carbon nanotubes, which have ordered structures, would maintain openings of the micropore channels. Another example is Pt addition to Ga/H-ZSM-5.[150] In addition to the stability, Ga–Pt/H-ZSM-5 exhibited higher ethane conversion and selectivity to aromatic hydrocarbons than Ga/H-ZSM-5 and Pt/H-ZSM-5. The high stability of Ga–Pt/H-ZSM-5 would be attributed to consecutive removal of the coke species through hydrogenolysis during the reaction. Indeed, Marecot *et al*. performed TPSR with H_2 using coke-deposited Pt, Re and Ir/Al_2O_3 catalysts.[151] Methane formation through hydrogenolysis of the deposited coke was verified and the temperature of methane formation increased in the order of Ir < Re < Pt.

Modification of BAS is an alternative option to inhibit the coke formation. BAS are located on the external and internal surface. BAS on external surface are not expected to exhibit shape selectivity to BTX formation since they are not located in the micropore channels. The formation of coke precursors such as polycyclic aromatic hydrocarbons rather favorable. Epelde *et al*. investigated the deactivation pathway of H-ZSM-5 during ethylene conversion to propylene.[152] They concluded that the coke species composed of condensed aromatics and long aliphatic chains are deposited on the external surface. This indicates that removal of BAS located at the external surface is effective. Inagaki *et al*. reported that HNO_3 treatment of H-ZSM-5 synthesized without organic structure-directing agent removes Al (BAS) selectively from its external surface.[153] In addition, control of distribution of framework Al would be also an effective means. Generally, the **MFI** topology has 12 T-sites, which are candidates for Al sites, as shown in Figure 1.5. Among them, T1, T4 and T6 does not face the intersections. T4 is located at the sinusoidal channels. T1 and T6 are located at the straight channels. The distribution of the Al sites can be controlled by the synthesis conditions.[154,155] Liu *et al*. synthesized H-ZSM-5 with different Al distribution and performed ethane and ethylene aromatization over Pt/H-ZSM-5.[156] They concluded that BAS located at the intersections tend to contribute to the formation of aromatic hydrocarbons. H-ZSM-5 with much Al located at the intersections exhibited high and stable conversion and BTX yield. The remaining Al sites located at straight and sinusoidal channels would induce the coke formation, resulting in blocking of the micropore channels and inhibition of diffusion of the products.

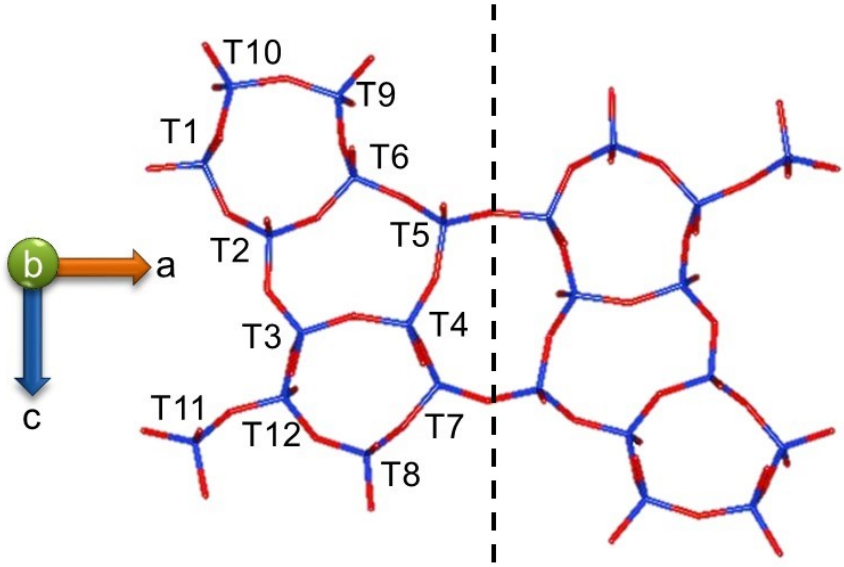

Figure 1.5. Twelve T-sites in the **MFI** topology.

1.5. Aims of the thesis

As described above, ethylene production through the thermal cracking of ethane consume much energy due to the high reaction temperatures and periodic removal of coke. In addition, an alternative process of BTX production from ethane is attractive because of the high feasibility.

Therefore, the aims of the thesis are as follows:

1. Dehydrogenation of ethane over metal oxide catalysts in the presence of steam at lower temperature (973 K) than the steam cracking process;
2. Dehydroaromatization of ethane over ZSM-5-supported metal catalysts with high catalytic performance, particularly the stability.

In chapters 2 and 3, metal oxide catalysts for EDH in the presence of steam are described. It was found that steam in the reaction system promotes EDH over reducible perovskite oxides. In chapters 4 and 5, EDA over H-ZSM-5 modified with active metals is described. It was found that the amount of active metals and BAS could be controlled by steam treatment in combination with an ion-exchange method. Various spectroscopic measurements including IR, XANES, UV-Vis and NMR in combination with DFT calculations revealed the nature and structure of active sites. Finally, catalytic science for ethane conversion is summarized in chapter 6.

References

1. A. Boulamanti, J. A. Moya, Production Costs of the Chemical Industry in the EU and Other Countries: Ammonia, Methanol and Light Olefins. *Renew. Sustain. Energy Rev.* **2017**, *68*, 1205–1212.
2. Forecast of Global Supply and Demand Trends for Petrochemical Products (for the period of 2009 to 2022), METI Japan, https://www.meti.go.jp/english/press/2018/1019_003.html, accessed on 30/7/2019.
3. J. J. H. B. Sattler, J. Ruiz-Martinez, E. Santillan-Jimenez, B. M. Weckhuysen, Catalytic Dehydrogenation of Light Alkanes on Metals and Metal Oxides. *Chem. Rev.* **2014**, *114*, 10613–10653.
4. P. Tian, Y. Wei, M. Ye, Z. Liu, Methanol to Olefins (MTO): From Fundamentals to Commercialization. *ACS Catal.* **2015**, *5*, 1922–1938.
5. U. Olsbye, S. Svelle, K. P. Lillerud, Z. H. Wei, Y. Y. Chen, J. F. Li, J. G. Wang, W. B. Fan, The Formation and Degradation of Active Species during Methanol Conversion over Protonated Zeotype Catalysts. *Chem. Soc. Rev.* **2015**, *44*, 7155–7176.
6. N. Popoff, E. Mazoyer, J. Pelletier, R. M. Gauvin, M. Taoufik, Expanding the Scope of Metathesis: A Survey of Polyfunctional, Single-Site Supported Tungsten Systems for Hydrocarbon Valorization. *Chem. Soc. Rev.* **2013**, *42*, 9035–9054.
7. R. Grabowski, Kinetics of Oxidative Dehydrogenation of C_2-C_3 Alkanes on Oxide Catalysts. *Catal. Rev. –Sci. Eng.* **2006**, *48*, 199–268.
8. C. A. Gärtner, A. C. van Veen, J. A. Lercher, Oxidative Dehydrogenation of Ethane: Common Principles and Mechanistic Aspects. *ChemCatChem* **2013**, *5*, 3196–3217.
9. F. O. Rice, K. F. Herzfeld, The Thermal Decomposition of Organic Compounds from the Standpoint of Free Radicals. VI. The Mechanism of Some Chain Reactions. *J. Am. Chem. Soc.* **1934**, *56*, 284–289.

10. M. L. Poutsma, Fundamental Reactions of Free Radicals Relevant to Pyrolysis Reactions. *J. Anal. Appl. Pyrolysis* **2000**, *54*, 5–35.
11. M. W. M. van Goethem, S. Barendregt, J. Grievink, J. A. Moulijn, P. J. T. Verheijen, Ideal Chemical Conversion Concept for the Industrial Production of Ethene from Hydrocarbons. *Ind. Eng. Chem. Res.* **2007**, *46*, 4045–4062.
12. C. Batiot, B. K. Hodnett, The Role of Reactant and Product Bond Energies in Determining Limitations to Selective Catalytic Oxidations. *Appl. Catal. A: Gen.* **1996**, *137*, 179–191.
13. K. M. Sundaram, G. F. Froment, Modeling of Thermal Cracking Kinetics. 3. Radical Mechanisms for the Pyrolysis of Simple Paraffins, Olefins, and Their Mixtures. *Ind. Eng. Chem. Fundam.*, **1978**, *17*, 174–182.
14. K. M. Van Geem, G. J. Heynderichx, G. B. Marin, Effect of Radial Temperature Profiles on Yields in Steam Cracking. *AIChE J.* **2004**, *50*, 173–183.
15. E. Heracleous, A. A. Lemonidou, Homogeneous and Heterogeneous Pathways of Ethane Oxidative and Non-Oxidative Dehydrogenation Studied by Temperature-Programmed Reaction. *Appl. Catal. A: Gen.* **2004**, *269*, 123–135.
16. G. F. Froment, B. O. van de Steene, P. S. van Damme, S. Narayanan, A. G. Goossens, Thermal Cracking of Ethane and Ethane–Propane Mixtures. *Ind. Eng. Chem. Process Des. Dev.* **1976**, *15*, 495–504.
17. K. M. Sundaram, P. S. van Damme, G. F. Froment, Coke Deposition in the Thermal Cracking of Ethane. *AIChE J.* **1981**, *27*, 946–951.
18. S. Mahamulkar, K. Yin, P. K. Agrawal, R. J. Davis, C. W. Jones, A. Malek, H. Shibata, Formation and Oxidation/Gasification of Carbonaceous Deposits: A Review. *Ind. Eng. Chem. Res.* **2016**, *55*, 9760–9818.
19. S. H. Symoens, N. Olahova, A. E. M. Gandarillas, H. Karimi, M. R. Djokic, M. Reyniers, G. B. Marin, K. M. Van Geem, State-of-the-art of Coke Formation during Steam Cracking: Anti-Coking Surface Technologies. *Ind. Eng. Chem. Res.* **2018**, *57*, 16117–16136.
20. A. E. M. Gandarillas, K. M. Van Geem, M. Reyniers, G. B. Marin, Influence of the Reactor Material Composition on Coke Formation during Ethane Steam Cracking. *Ind. Eng. Chem. Res.* **2014**, *53*, 6358–6371.
21. S. A. Sarris, N. Olahova, K. Verbeken, M. Reyniers, G. B. Marin, K. M. Van Geem, Optimization of the in Situ Pretreatment of High Temperature Ni–Cr Alloys for Ethane Steam Cracking. *Ind. Eng. Chem. Res.* **2017**, *56*, 1424–1438.
22. S. Wauters, G. B. Marin, Kinetic Modeling of Coke Formation during Steam Cracking. *Ind. Eng. Chem. Res.* **2002**, *41*, 2379–2391.
23. M. Takahashi, Y. Enjo, S. Uramaru, Cast Product Having Alumina Barrier Layer. US Patent, US 2011/0318593A1, **2011**.
24. S. S. A. Petrone, R. L. Deuis, F. Kong, Y. Chen, Catalytic Surfaces and Coatings for the Manufacture of Petrochemicals. US Patent, US 9421526B2, **2016**.
25. S. Wang, W. Peng, Q. Fu, Z. Deng, Z. Wu, C. Lin, Y. Gu, X. Zhang, L. B. Kool, Method and

Reactor for Cracking Hydrocarbon. US Patent, US 10138431B2, **2018**.
26. M. M. Bhasin, J. H. McCain, B. V. Vora, T. Imai, P. R. Pujadó, Dehydrogenation and Oxydehydrogenation of Paraffins to Olefins, *Appl. Catal. A: Gen.* **2001**, *221*, 397–419.
27. U. Olsbye, A. Virnovskaia, Ø. Prytz, S. J. Tinnemans, B. M. Weckhuysen, Mechanistic Insight in the Ethane Dehydrogenation Reaction over Cr/Al_2O_3 Catalysts. *Catal. Lett.* **2005**, *103*, 143–148.
28. F. Cavani, M. Koutyrev, F. Trifirò, A. Bartolini, D. Ghisletti, R. Iezzi, A. Santucci, G. Del Piero, Chemical and Physical Characterization of Alumina-Supported Chromia-Based Catalysts and Their Activity in Dehydrogenation of Isobutane. *J. Catal.* **1996**, *158*, 236–250.
29. B. M. Weckhuysen, R. A. Schoonheydt, Alkane Dehydrogenation over Supported Chromium Oxide Catalysts. *Catal. Today* **1999**, *51*, 223–232.
30. R. L. Puurunen, B. M. Weckhuysen, Spectroscopic Study on the Irreversible Deactivation of Chromia/Alumina Dehydrogenation Catalysts. *J. Catal.* **2002**, *210*, 418–430.
31. S. D. Yim, I.-S. Nam, Characteristics of Chromium Oxides Supported on TiO_2 and Al_2O_3 for the Decomposition of Perchloroethylene. *J. Catal.* **2004**, *221*, 601–611.
32. Y. Wang, Y. Ohishi, T. Shishido, Q. Zhang, W. Yang, Q. Guo, H. Wan, K. Takehira, Characterizations and Catalytic Properties of Cr-MCM-41 Prepared by Direct Hydrothermal Synthesis and Template-Ion Exchange. *J. Catal.* **2003**, *220*, 347–357.
33. K. Takehira, Y. Ohishi, T. Shishido, T. Kawabata, K. Takaki, Q. Zhang, Y. Wang, Behavior of Active Sites on Cr-MCM-41 Catalysts during the Dehydrogenation of Propane with CO_2. *J. Catal.* **2004**, *224*, 404–416.
34. V. Z. Fridman, R. Xing, M. Severance, Investigating the CrO_x/Al_2O_3 Dehydrogenation Catalyst Model: I. Identification and Stability Evaluation of the Cr Species on the Fresh and Equilibrated Catalysts. *Appl. Catal. A: Gen*. **2016**, *523*, 39–53.
35. M. Botavina, C. Barzan, A. Piovano, L. Braglia, G. Agostini, G. Martra, E. Groppo, Inshights into Cr/SiO_2 Catalysts during Dehydrogenation of Propane: An *Operando* XAS Investigation. *Catal. Sci. Technol*. **2017**, *7*, 1690–1700.
36. D. He, Y. Zhang, S. Yang, Y. Mei, Y. Luo, Investigation of the Isolated Cr(VI) Species in Cr/MCM-41 Catalysts and Its Effect on Catalytic Activity for Dehydrogenation of Propane. *ChemCatChem* **2018**, *10*, 5434–5440.
37. N. Mimura, M. Okamoto, H. Yamashita, S. T. Oyama, K. Murata, Oxidative Dehydrogenation of Ethane over Cr/ZSM-5 Catalysts Using CO_2 as an Oxidant. *J. Phys. Chem. B* **2006**, *110*, 21764–21770.
38. X. Shi, S. Ji, K. Wang, C. Li, Oxidative Dehydrogenation of Ethane with CO_2 over Novel $Cr/SBA\text{-}15/Al_2O_3$/FeCrAl Monolithic Catalysts. *Energy Fuels* **2008**, *22*, 3631–3638.
39. T. V. M. Rao, E. M. Zahidi, A. Sayari, Ethane Dehydrogenation over Pore-Expanded Mesoporous Silica-Supported Chromium Oxide: 2. Catalytic Properties and Nature of Active Sites. *J. Mol. Catal. A: Chem*. **2009**, *301*, 159–165.
40. H. H. Shin, S. McIntosh, Proton-Conducting Perovskites as Supports for Cr Catalysts in Short

Contact Time Ethane Dehydrogenation. *ACS Catal.* **2015**, *5*, 95–103.

41. D. Shee, A. Sayari, Light Alkane Dehydrogenation over Mesoporous Cr_2O_3/Al_2O_3 Catalysts. *Appl. Catal. A: Gen.* **2010**, *389*, 155–164.
42. S. Wang, K. Murata, T. Hayakawa, S. Hamakawa, K. Suzuki, Oxidative Dehydrogenation of Ethane by Carbon Dioxide over Sulfate-Modified Cr_2O_3/SiO_2 Catalysts. *Catal. Lett.* **1999**, *63*, 59–64.
43. L. Liu, H. Li, Y. Zhang, A Comparative Study on Catalytic Performances of Chromium Incorporated and Supported Mesoporous MSU-*x* Catalysts for the Oxidehydrogenation of Ethane to Ethylene with Carbon Dioxide. *Catal. Today* **2006**, *115*, 235–241.
44. Y. Cheng. L. Zhou, J. Xu, C. Miao, W. Hua, Y. Yue, Z. Gao, Chromium-Based Catalysts for Ethane Dehydrogenation: Effect of SBA-15 Support. *Micropor. Mesopor. Mater*. **2016**, *234*, 370–376.
45. Y. Cheng, C. Miao, W. Hua, Y. Yue, Z. Gao, Cr/ZSM-5 for Ethane Dehydrogenation: Enhanced Catalytic Activity through Surface Silanol. *Appl. Catal. A: Gen.* **2017**, *532*, 111–119.
46. S. Wang, K. Murata, T. Hayakawa, S. Hamakawa, K. Suzuki, Dehydrogenation of Ethane with Carbon Dioxide over Supported Chromium Oxide Catalysts. *Appl. Catal. A: Gen*. **2000**, *196*, 1–8.
47. N. Mimura, I. Takahara, M. Inaba, M. Okamoto, K. Murata, High-Performance Cr/H-ZSM-5 Catalysts for Oxidative Dehydrogenation of Ethane to Ethylene with CO_2 as an Oxidant. *Catal. Commun*. **2002**, *3*, 257–262.
48. T. A. Bugrova, V. V. Dutov, V. A. Svetlichnyi, V. C. Corberán, G. V. Mamontov, Oxidative Dehydrogenation of Ethane with CO_2 over CrO_x Catalysts Supported on Al_2O_3, ZrO_2, CeO_2 and $Ce_xZr_{1-x}O_2$. *Catal. Today* **2019**, *333*, 71–80.
49. T. Shishido, K. Shimamura, K. Teramura, T. Tanaka, Role of CO_2 in Dehydrogenation of Propane over Cr-Based Catalysts. *Catal. Today* **2012**, *185*, 151–156.
50. X. Shi, S. Ji, K. Wang, Oxidative Dehydrogenation of Ethane to Ethylene with Carbon Dioxide over Cr–Ce/SBA-15 Catalysts. *Catal. Lett*. **2008**, *125*, 331–339.
51. F. Rahmani, M. Haghighi, B. Mohammadkhanai, Enhanced Dispersion of Cr Nanoparticles over Nanostructured ZrO_2-Doped ZSM-5 Used in CO_2-Oxydehydrogenation of Ethane. *Micropor. Mesopor. Mater.* **2017**, *242*, 34–49.
52. K. Nakagawa, M. Okamura, N. Ikenaga, T. Suzuki, T. Kobayashi, Dehydrogenation of Ethane over Gallium Oxide in the Presence of Carbon Dioxide. *Chem. Commun*. **1998**, 1025–1026.
53. A. Bhan, W. N. Delgass, Propane Aromatization over HZSM-5 and Ga/HZSM-5 Catalysts. *Catal. Rev. –Sci. Eng.* **2008**, *50*, 19–151.
54. G. Giannetto, R. Monque, R. Galiasso, Transformation of LPG into Aromatic Hydrocarbons and Hydrogen over Zeolite Catalysts. *Catal. Rev. –Sci. Eng.* **1994**, *36*, 271–304.
55. K. M. Dooley, T. F. Guidry, G. L. Price, Control of Intrazeolitic Gallium Cation Content and Its Effects on C_2 Dehydrogenation in Ga-MFI Catalysts. *J. Catal.* **1995**, *157*, 66–75.

56. A. Ausavasukhi, T. Sooknoi, Tunable Activity of [Ga]HZSM-5 with H_2 Treatment: Ethane Dehydrogenation. *Catal. Commun.* **2014**, *45*, 63–68.
57. N. Rane, A. R. Overweg, V. B. Kasansky, R. A. van Santen, E. J. M. Hensen, Characterization and Reactivity of Ga^+ and GaO^+ Cations in Zeolite ZSM-5. *J. Catal.* **2006**, *239*, 478–485.
58. V. B. Kazansky, I. R. Subbotina, R. A. van Santen, E. J. M. Hensen, DRIFTS Study of the Chemical State of Modifying Gallium Ions in Reduced Ga/ZSM-5 Prepared by Impregnation I. Observation of Gallium Hydrides and Application of CO Adsorption as a Molecular Probe for Reduced Gallium Ions. *J. Catal.* **2004**, *227*, 263–269.
59. V. B. Kazansky, I. R. Subbotina, R. A. van Santen, E. J. M. Hensen, DRIFTS Study of the Nature and Chemical Reactivity of Gallium Ions in Ga/ZSM-5 II. Oxidation of Reduced Ga Species in ZSM-5 by Nitrous Oxide or Water. *J. Catal*. **2005**, *233*, 351–358.
60. A. B. Getsoian, U. Das, J. Camocho-Bunquin, G. Zhang, J. R. Gallagher, B. Hu, S. Cheah, J. A. Schaidle, D. A. Ruddy, J. E. Hensley, T. R. Krause, L. A. Curtiss, J. T. Miller, A. S. Hock, Organometallic Model Complexes Elucidate the Active Gallium Species in Alkane Dehydrogenation Catalysts Based on Ligand Effects in Ga K-Edge XANES. *Catal. Sci. Technol.* **2016**, *6*, 6339–6353.
61. M. W. Schreiber, C. P. Plaisance, M. Baumgärtl, K. Peuter, A. Jentys, R. Bermejo-Deval, J. A. Lercher, Lewis–Brønsted Acid Pairs in Ga/H-ZSM-5 to Catalyze Dehydrogenation of Light Alkanes. *J. Am. Chem. Soc.* **2018**, *140*, 4849–4859.
62. M. S. Pereira, M. A. C. Nascimento, Theoretical Study on the Dehydrogenation Reaction of Alkanes Catalyzed by Zeolites Containing Nonframework Gallium Species. *J. Phys. Chem. B* **2006**, *110*, 3231–3238.
63. M. S. Pereira, A. M. da Silva, M. A. C. Nascimento, Effect of the Zeolite Cavity on the Mechanism of Dehydrogenation of Light Alkanes over Gallium-Containing Zeolites. *J. Phys. Chem. C* **2011**, *115*, 10104–10113.
64. E. A. Pidko, V. B. Kazansky, E. J. M. Hensen, R. A. van Santen, A Comprehensive Density Functional Theory Study of Ethane Dehydrogenation over Reduced Extra-Framework Gallium Species in ZSM-5 Zeolite. *J. Catal*. **2006**, *240*, 73–54.
65. E. A. Pidko, E. J. M. Hensen, R. A. van Santen, Dehydrogenation of Light Alkanes over Isolated Gallyl Ions in Ga/ZSM-5 Zeolites. *J. Phys. Chem. C* **2007**, *111*, 13068–13075.
66. Y. V. Joshi, K. T. Thomson, High Ethane Dehydrogenation Activity of $[GaH]^{2+}$–Al Pair Sites in Ga/H-[Al]ZSM-5: A DFT Thermochemical Analysis of the Catalytic Sites under Reaction Conditions. *J. Catal.* **2007**, *246*, 249–265.
67. E. Mansoor, M. Head-Gordon, A. T. Bell, Computational Modeling of the Nature and Role of Ga Species for Light Alkane Dehydrogenation Catalyzed by Ga/H-MFI. *ACS Catal*. **2018**, *8*, 6146–6162.
68. V. B. Kazansky, I. R. Subbotina, N. Rane, R. A. van Santen, E. J. M. Hensen, On Two Alternative Mechanisms of Ethane Activation over ZSM-5 Zeolite Modified by Zn^{2+} and Ga^{1+} Cations. *Phys. Chem. Chem. Phys.* **2005**, *7*, 3088–3092.

69. E. J. M. Hensen, E. A. Pidko, N. Rane, R. A. van Santen, Water-Promoted Hydrocarbon Activation Catalyzed by Binuclear Gallium Sites in Zeolite. *Angew. Chem. Int. Ed*. **2007**, *46*, 7273–7276.
70. E. A. Pidko, E. J. M. Hensen, G. M. Zhidomirov, R. A. van Santen, Non-Localized Charge Compensation in Zeolites: A Periodic DFT Study of Cationic Gallium-Oxide Clusters in Mordenite. *J. Catal*. **2008**, *255*, 139–143.
71. E. A. Pidko, R. A. van Santen, E. J. M. Hensen, Multinuclear Gallium-Oxide Cations in High-Silica Zeolites. *Phys. Chem. Chem. Phys.* **2009**, *11*, 2893–2902.
72. E. A. Pidko, R. A. van Santen, Structure–Reactivity Relationship for Catalytic Activity of Gallium Oxide and Sulfide Clusters in Zeolite. *J. Phys. Chem. C* **2009**, *113*, 4246–4249.
73. K. Nakagawa, C. Kajita, Y. Ide, M. Okamura, S. Kato, H. Kasuya, N. Ikenaga, T. Kobayashi, T. Suzuki, Promoting Effect of Carbon Dioxide on the Dehydrogenation and Aromatization of Ethane over Gallium-Loaded Catalysts. *Catal. Lett.* **2000**, *64*, 215–221.
74. M. Zinkevich, F. Aldinger, Thermodynamic Assessment of the Gallium-Oxygen System. *J. Am. Ceram. Soc.* **2004**, *87*, 683–691.
75. B. Zheng, W. Hua, Y. Yue, Z. Gao, Dehydrogenation of Propane to Propene over Different Polymorphs of Gallium Oxide. *J. Catal.* **2005**, *232*, 143–151.
76. K. Nishi, K. Shimizu, M. Takamatsu, H. Yoshida, A. Satsuma, T. Tanaka, S. Yoshida, T. Hattori, Deconvolution Analysis of Ga K-Edge XANES for Quantification of Gallium Coordinations in Oxide Environments. *J. Phys. Chem. B* **1998**, *102*, 10190–10195.
77. K. Shimizu, M. Takamatsu, K. Nishi, H. Yoshida, A. Satsuma, T. Tanaka, S. Yoshida, T. Hattori, Alumina-Supported Gallium Oxide Catalysts for NO Selective Reduction: Influence of the Local Structure of Surface Gallium Oxide Species on the Catalytic Activity. *J. Phys. Chem. B* **1999**, *103*, 1542–1549.
78. S. E. Collins, M. A. Baltanás, J. L. G. Fierro, A. L. Bonivardi, Gallium–Hydrogen Bond Formation on Gallium–Palladium Silica-Supported Catalysts. *J. Catal*. **2002**, *211*, 252–264.
79. S. E. Collins, M. A. Baltanás, A. L. Bonivardi, Hydrogen Chemisorption on Gallium Oxide Polymorphs. *Langmuir* **2005**, *21*, 962–970.
80. W. Jochum, S. Penner, K. Föttinger, R. Kramer, G. Rupprechter, B. Klötzer, Hydrogen on Polycrystalline β-Ga_2O_3: Surface Chemisorption, Defect Formation, and Reactivity. *J. Catal*. **2008**, *256*, 268–277.
81. Y. Pan, D. Mei, C. Liu, Q. Ge, Hydrogen Adsorption on Ga_2O_3 Surface: A Combined Experimental and Computational Study. *J. Phys. Chem. C* **2011**, *115*, 10140–10146.
82. V. B. Kazansky, I. R. Subbotina, A. A. Pronin, R. Schlögl, F. C. Jentoft, Unusual Infrared Spectrum of Ethane Adsorbed by Gallium Oxide. *J. Phys. Chem. B* **2006**, *110*, 7975–7978.
83. A. A. Gabrienko, S. S. Arzumanov, A. V. Toktarev, A. G. Stepanov, Metal-Alkyl Species Are Formed on Interaction of Small Alkanes with Gallium Oxide: Evidence from Solid-State NMR. *Chem. Phys. Lett.* **2010**, *496*, 148–151.
84. Y. Cheng, T. Lei, C. Miao, W. Hua, Y. Yue, Z. Gao, Ga_2O_3/NaZSM-5 for C_2H_6

Dehydrogenation in the Presence of CO_2: Conjufated Effect of Silanol. *Micropor. Mesopor. Mater.* **2018**, *268*, 235–242.

85. H. Xiao, J. Zhang, P. Wang, X. Wang, F. Pang, Z. Zhang, Y. Tan, Dehydrogenation of Propane over a Hydrothermal-Synthesized Ga_2O_3–Al_2O_3 Catalyst in the Presence of Carbon Dioxide. *Catal. Sci. Technol*. **2016**, *6*, 5183–5195.
86. K. Nakagawa, C. Kajita, K. Okumura, N. Ikenaga, M. Nishitani-Gamo, T. Ando, T. Kobayashi, T. Suzuki, Role of Carbon Dioxide in the Dehydrogenation of Ethane over Gallium-Loaded Catalysts. *J. Catal.* **2001**, *203*, 87–93.
87. T. Lei, Y. Cheng, C. Miao, W. Hua, Y. Yue, Z. Gao, Silica-doped TiO_2 as Support of Gallium Oxide for Dehydrogenation of Ethane with CO_2. *Fuel Process. Technol.* **2018**, *177*, 246–254.
88. R. Koirala, R. Buechel, F. Krumeich, S. E. Pratsinis, A. Baiker, Oxidative Dehydrogenation of Ethane with CO_2 over Flame-Made Ga-Loaded TiO_2. *ACS Catal.* **2015**, *5*, 690–702.
89. Z. Shen, J. Liu, H. Xu, Y. Yue, W. Hua, W. Shen, Dehydrogenation of Ethane to Ethylene over a Highly Efficient Ga_2O_3/HZSM-5 Catalyst in the Presence of CO_2. *Appl. Catal. A: Gen*. **2009**, *356*, 148–153.
90. Y. Ono, Transformation of Lower Alkanes into Aromatic Hydrocarbons over ZSM-5 Zeolites. *Catal. Rev. –Sci. Eng.* **1992**, *34*, 179–226.
91. M. A. Bañares, Supported Metal Oxide and Other Catalysts for Ethane Conversion: A Review. *Catal. Today* **1999**, *51*, 319–348.
92. A. Hagen, F. Roessner, Ethane to Aromatic Hydrocarbons: Past, Present, Future. *Catal. Rev. –Sci. Eng.* **2000**, *42*, 403–437.
93. Y. Xiang, H. Wang, J. Cheng, J. Matsubu, Progress and Prospects in Catalytic Ethane Aromatization. *Catal. Sci. Technol.* **2018**, *8*, 1500–1516.
94. C. Baerlocher, L. B. McCusker, D.H. Olson, Atlas of Zeolite Framework Types 6th Ed. **2007**, Elsevier, Amsterdam.
95. Database of Zeolite Structure, Structure Commission of the International Zeolite Association, http://www.iza-structure.org/databases/, accessed on 26/11/2019.
96. M. Stöcker, Gas Phase Catalysis by Zeolites. *Micropor. Mesopor. Mater.* **2005**, *82*, 257–292.
97. O. A. Anunziata, G. A. Eimer, L. B. Pierella, Ethane Conversion into Aromatic Hydrocarbons over Molybdenum-Containing MEL Zeolites. *Appl. Catal. A: Gen.* **1999**, *182*, 267–274.
98. O. A. Anunziata, G. A. Eimer, L. B. Pierella, Catalytic Activity of ZSM-11 Zeolites Modified with Metal Cations for the Ethane Conversion. *Catal. Lett*. **2001**, *75*, 93–97.
99. Y. Shu, D. Ma, L. Xu, Y. Xu, X. Bao, Methane Dehydro-Aromatization over Mo/MCM-22 Catalysts: A Highly Selective Catalyst for the Formation of Benzene. *Catal. Lett*. **2000**, *70*, 67–73.
100. K.-H. Steinberg, U. Mroczek, F. Roessner, Aaromatization of Ethane on Platinum Containing ZSM-5 Zeolites. *Appl. Catal.* **1990**, *66*, 37–44.
101. A. Hagen, F. Roessner, I. Weingart, B. Spliethoff, Synthesis of Iron-Containing MFI Type Zeolites and Its Application to the Conversion of Ethane into Aromatic Compounds. *Zeolites*

1995, *15*, 270–275.

102. V. I. Yakerson, T. V. Vasina, L. I. Lafer, V. P. Sytnyk, G. L. Dykh, A. V. Mokhov, O. V. Bragin, Kh. M. Minachev, The Properties of Zinc and Gallium Containing Pentasils – The Catalysts for the Aromatization of Lower Alkanes. *Catal. Lett*. **1989**, *3*, 339–346.
103. P. Schulz, M. Baerns, Aromatization of Ethane over Gallium-Promoted H-ZSM-5 Catalysts. *Appl. Catal.* **1991**, *78*, 15–29.
104. F. Roessner, A. Hagen, U. Mroczek, H. G. Karge, K.-H. Steinberg, Conversion of Ethane into Aromatic Compounds on ZSM-5 Zeolites Modified by Zinc. *Stud. Surf. Sci. Catal.* **1993**, *75*, 1707–1710.
105. H. Song, R. M. Rioux J. D. Hoefelmeyer, R. Komor, K. Niesz, M. Grass, P. Yang, G. A. Somorjai, Hydrothermal Growth of Mesoporous SBA-15 Silica in the Presence of PVP-Stabilized Pt Nanoparticles: Synthesis, Characterization, and Catalytic Properties. *J. Am. Chem. Soc*. **2006**, *128*, 3027–3037.
106. F. Solymosi, A. Szőke, Conversion of Ethane into Benzene on Mo_2C/ZSM-5 Catalyst. *Appl. Catal. A: Gen.* **1998**, *166*, 225–235.
107. A. Krogh, A. Hagen, T. W. Hansen, C. H. Christensen, I. Schmidt, Re/HZSM-5: A New Catalyst for Ethane Aromatization with Improved Stability. *Catal. Commun*. **2003**, *4*, 627–630.
108. F. Solymosi, P. Tolmacsov, Conversion of Ethane into Benzene on Re/ZSM-5. *Catal. Lett.* **2004**, *93*, 7–11.
109. L. Wang, L. Tao, M. Xie, G. Xu, J. Huang, Y. Xu, Dehydrogenation and Aromatization of Methane under Non-Oxidative Conditions. *Catal. Lett*. **1993**, *21*, 35–41.
110. L. Wang, R. Ohnishi, M. Ichikawa, Novel Rhenium-Based Catalysts for Dehydrocondensation of Methane with CO/CO_2 towards Ethylene and Benzene. *Catal. Lett.* **1999**, *62*, 29–33.
111. R. W. Borry III, Y. H. Kim, A. Huffsmith, J. A. Reimer, E. Iglesia, Structure and Density of Mo and Acid Sites in Mo-Exchanged H-ZSM5 Catalysts for Nonoxidative Methane Conversion. *J. Phys. Chem. B* **1999**, *103*, 5787–5796.
112. C. Bolivar, H. Charcosset, R. Frety, M. Primet, L. Tournayan, C. Betizeau, G. Leclercq. R. Maurel, Platinum-Rhenium/Alumina Catalysts: I. Investigation of Reduction by Hydrogen. *J. Catal.* **1975**, *39*, 249–259.
113. G. Chen, Y. Zhao, L. Shang, G. I. N. Waterhouse, X. Kang, L.-Z. Wu, C.-H. Tung, T. Zhang, Recent Advances in the Synthesis, Characterization and Application of Zn^+-Containing Heterogeneous Catalysts. *Adv. Sci.* **2016**, *3*, 1500424.
114. X. Niu, J. Gao, Q. Miao, M. Dong, G. Wang, W. Fan, Z. Qin, J. Wang, Influence of Preparation Method on the Performance of Zn-Containing HZSM-5 Catalysts in Methanol-to-Aromatics. *Micropor. Mesopor. Mater.* **2014**, *197*, 252–261.
115. S. Tamiyakul, T. Sooknoi, L. L. Lobban, S. Jongpatiwut, Generation of Reductive Zn Species over Zn/HZSM–5 Catalysts for *n*–Pentane Aromatization. *Appl. Catal. A: Gen.* **2016**, *525*, 190–196.

116.H. Berndt, G. Lietz, J. Völter, Zinc Promoted H-ZSM-5 Catalysts for Conversion of Propane to Aromatics II. Nature of the Active Sites and Their Activation. *Appl. Catal. A: Gen.* **1996**, *146*, 365–379.

117.S. M. T. Almutairi, B. Mezari, P. C. M. M. Magusin, E. A. Pidko, E. J. M. Hensen, Structure and Reactivity of Zn-Modified ZSM-5 Zeolites: The Importance of Clustered Cationic Zn Complexes. *ACS Catal.* **2012**, *2*, 71–83.

118.J. Chen, Z. Feng, P. Ying, C. Li, ZnO Clusters Encapsulated inside Micropores of Zeolites Studied by UV Raman and Laser-Induced Luminescence Spectroscopies. *J. Phys. Chem. B* **2004**, *108*, 12669–12676.

119.A. Hagen, E. Schneider, A. Kleinert, F. Roessner, Modification of Acid Supports by Solid-State Redox Reaction Part I. Preparation and Characterization. *J. Catal.* **2004**, *222*, 227–237.

120.F. Lónyi, J. Valyon, On the Interpretation of the NH_3-TPD Patterns of H-ZSM-5 and H-Mordenite. *Micropor. Mesopor. Mater.* **2001**, *47*, 239–301.

121.N. Katada, Analysis and Interpretation of Acidic Nature of Aluminosilicate. *Mol. Catal.* **2018**, *458*, 116–126.

122.V. B. Kazansky, A. I. Serykh, Unusual Localization of Zinc Cations in MFI Zeolites Modified by Different Ways of Preparation. *Phys. Chem. Chem. Phys.* **2004**, *6*, 3760–3764.

123.J. A. Biscardi, G. D. Meitzner, E. Iglesia, Structure and Density of Active Zn Species in Zn/H-ZSM5 Propane Aromatization Catalysts. *J. Catal.* **1998**, *179*, 192–202.

124.H. A. Aleksandriv, G. N. Vayssilov, Theoretical Investigation of Ethane Dehydrogenation on Cationic Zn Species in ZSM-5 Zeolites–The Second Al Center in Vicinity of the Cation Is Essential for the Accomplishment of the Complete Catalytic Cycle. *Catal. Today* **2010**, *152*, 78–87.

125.A. Hagen, F. Roessner, W. Reschetilowski, Conversion of Ethane on Modified ZSM-5 Zeolites: A Study of Aromatization as a Function of Reaction Media. *Chem. Eng. Technol.* **1995**, *18*, 414–419.

126.O. P. Keipert, D. Wolf, P. Schulz, M. Baerns, Kinetics of Ethane Aromatization over a Gallium-Doped H-ZSM-5 Catalyst. *Appl. Catal. A: Gen.* **1995**, *131*, 347–365.

127.L. Ma, X. Zou, Cooperative Catalysis of Metal and Acid Functions in Re-HZSM-5 Catalysts for Ethane Dehydroaromatization. *Appl. Catal. B: Environ*. **2019**, *243*, 703–710.

128.A. Hagen, O. P. Keipert, F. Roessner, Activation of Ethane on Modified ZSM-5 Zeolites Studied under Transient Conditions. *Stud. Surf. Sci. Catal*. **1996**, *101*, 781–790.

129.A. G. Stepanov, M. L. Luzgin, V. N. Romannikov, V. N. Sidelnikov, E. A. Paukshtis, The Nature, Structure, and Composition of Adsorbed Hydrocarbon Products of Ambient Temperature Oligomerization of Ethylene on Acidic Zeolite H-ZSM-5. *J. Catal.* **1998**, *178*, 466–477.

130.J. N. Kondo, K. Domen, IR Observation of Adsorption and Reactions of Olefins on H-Form Zeolites. *J. Mol. Catal. A: Chem. 2003*, *199*, 27–38.

131.T. Koyama, Y. Hayashi, H. Horie, S. Kawauchi, A. Matsumoto, Y. Iwase, Y. Sakamoto, A.

Miyaji, K. Motokura, T. Baba, Key Role of the Pore Volume of Zeolite for Selective Production of Propylene from Olefins. *Phys. Chem. Chem. Phys*. **2010**, *12*, 2541–2554.

132. Y. Iwase, Y. Sakamoto, A. Shiga, A. Miyaji, K. Motokura, T. Koyama, T. Baba, Shape-Selective Catalysis Determined by the Volume of a Zeolite Cavity and the Reaction Mechanism for Propylene Production by the Conversion of Butene Using a Proton-Exchanged Zeolite. *J. Phys. Chem. C* **2012**, *116*, 5182–5196.
133. M. Shibata, H. Kitagawa, Y. Sendoda, Y. Ono, Transformation of Propene into Aromatic Hydrocarbons over ZSM-5 Zeolites. *Stud. Surf. Sci. Catal.* **1986**, *28*, 717–724.
134. V. R. Choudhary, D. Panjala, S. Banerjee, Aromatization of Propene and *n*-Butene over H-Galloaluminosilicate (ZSM-5 Type) Zeolite. *Appl. Catal. A: Gen.* **2002**, *231*, 243–251.
135. V. R. Choudhary, S. Banerjee, D. Panjala, Product Distribution in the Aromatization of Dilute Ethylene over H-GaAlMFI Zeolite: Effect of Space Velocity. *Micropor. Mesopor. Mater.* **2002**, *51*, 203–210.
136. T. Liang, H. Toghiani, Y. Xiang, Transient Kinetic Study of Ethane and Ethylene Aromatization over Zinc-Exchanged HZSM-5 Catalyst. *Ind. Eng. Chem. Res.* **2018**, *57*, 15301–15309.
137. V. R. Choudhary, P. Devadas, S. Banerjee, A. K. Kinage, Aromatization of Dilute Ethylene over Ga-Modified ZSM-5 Type Zeolite Catalysts. *Micropor. Mesopor. Mater.* **2001**, *47*, 253–267.
138. J. A. Biscardi, E. Iglesia, Reaction Pathways and Rate-Determining Steps in Reactions of Alkanes on H-ZSM5 and Zn/H-ZSM5 Catalysts. *J. Catal.* **1999**, *182*, 117–128.
139. L. A. Dufresne, R. Le Van Mao, Hydrogen Back-Spillover Effects in the Aromatization of Ethylene on Hybrid ZSM-5 Catalysts. *Catal. Lett.* **1994**, *25*, 371–383.
140. S. Triwahyono, A. A. Jalil, R. R. Mukti, M. Musthofa, N. A. M. Razali, M. A. A. Aziz, Hydrogen Spillover Behavior of Zn/HZSM-5 Showing Catalytically Active Protonic Acid Sites in the Isomerization of *n*-Pentane. *Appl. Catal. A: Gen.* **2011**, *407*, 91–99.
141. R. Batchu, V. V. Galvita, K. Alexopoulos, K. Van der Borght, H. Poelman, M.-F. Reyniers, G. B. Marin, Role of Intermediates in Reaction Pathways from Ethene to Hydrocarbons over H-ZSM-5. *Appl. Catal. A: Gen.* **2017**, *538*, 207–220.
142. M. Guisnet, N. S. Gnep, D. Aittaleb, Y. J. Doyemet, Conversion of Light Alkanes into Aromatic Hydrocarbons VI. Aromatization of C_2–C_4 Alkanes on H-ZSM-5—Reaction Mechanisms. *Appl. Catal. A: Gen.* **1992**, *87*, 255–270.
143. P. Qiu, J. H. Lunsford, M. P. Rosynek, Characterization of Ga/ZSM-5 for the Catalytic Aromatization of Dilute Ethylene Streams. *Catal. Lett*. **1998**, *52*, 37–42.
144. H. Coqueblin, A. Richard, D. Uzio, L. Pinard, Y. Pouilloux, F. Epron, Effect of the Metal Promoter on the Performance of H-ZSM5 in Ethylene Aromatization. *Catal. Today* **2017**, *289*, 62–69.
145. M.-F. Hsieh, Y. Zhou, H. Thirumalai, L. C. Grabow, J. D. Rimer, Silver-Promoted Dehydroaromatization of Ethylene over ZSM-5 Catalysts. *ChemCatChem* **2017**, *9*, 1675–

1682.
146. J. Bandiera, Y. B. Taârit, Ethane Conversion: Kinetic Evidence for the Competition of Consecutive Steps for the Same Active Centre. *Appl. Catal. A: Gen*. **1997**, *152*, 43–51.
147. J. Bandiera, Y. B. Taarit, On the Inhibition of Light Alkane Conversion by Intermediates to Aromatics The Effect of Cyclohexadiene on the Conversion of Ethane. *Appl. Catal. A: Gen*. **1997**, *161*, L43–L45.
148. M. Guisnet, L. Costa, F. R. Ribeiro, Prevention of Zeolite Deactivation by Coking. *J. Mol. Catal. A: Chem.* **2009**, *305*, 69–83.
149. B. Robinson, X. Bai, A. Samanta, V. Abdelsayed, D. Shekhawat, J. Hu, Stability of Fe- and Zn-Promoted Mo/ZSM-5 Catalysts for Ethane Dehydroaromatization in Cyclic Operation Mode. *Energy Fuels* **2018**, *32*, 7810–7819.
150. A. Samanta, X. Bai, B. Robinson, H. Chen, J. Hu, Conversion of Light Alkane to Value-Added Chemicals over ZSM-5/Metal Promoted Catalysts. *Ind. Eng. Chem. Res*. **2017**, *56*, 11006–11012.
151. P. Marecot, S. Peyrovi, D. Bahloul, J. Barbier, Regeneration by Hydrogen Treatment of Bifunctional Catalysts Deactivated by Coke Deposition I. Regeneration of Precoked Catalysts. *Appl. Catal.* **1990**, *66*, 181–190.
152. E. Epelde, M. Ibañez, A. T. Aguayo, A. G. Gayubo, J. Bilbao, P. Castaño, Differences among the Deactivation Pathway of HZSM-5 Zeolite and SAPO-34 in the Transformation of Ethylene or 1-Butene to Propylene. *Micropor. Mesopor. Mater.* **2014**, *195*, 284–293.
153. S. Inagaki, S. Shinoda, Y. Kaneko, K. Takeuchi, R. Komatsu, Y. Tsuboi, H. Yamazaki, J. N. Kondo, Y. Kubota, Facile Fabrication of ZSM-5 Zeolite Catalyst with High Durability to Coke Formation during Catalytic Cracking of Paraffins. *ACS Catal*. **2013**, *3*, 74–78.
154. J. Dědeček, Z. Sobalík, B. Wichterlová, Siting and Distribution of Framework Aluminum Atoms in Silicon-Rich Zeolites and Impact on Catalysis. *Catal. Rev. –Sci. Eng*. **2012**, *54*, 135–223.
155. T. Yokoi, H. Mochizuki, S. Namba, J. N. Kondo, T. Tatsumi, Control of the Al Distribution in the Framework of ZSM-5 Zeolite and Its Evaluation by Solid-State NMR Technique and Catalytic Properties. *J. Phys. Chem. C* **2015**, *119*, 15303–15315.
156. H. Liu, H. Wang, A.-H. Xing, J.-H. Cheng, Effect of Al Distribution in MFI Framework Channels on the Catalytic Performance of Ethane and Ethylene Aromatization. *J. Phys. Chem. C* **2019**, *123*, 15637–15647.

Chapter 2 Dehydrogenation of ethane over Ga oxide catalysts in the presence of steam

2.1. Introduction

Ethylene, an important chemical in the petrochemical industry, is converted to fundamental chemicals such as polyethylene, ethylene oxide, vinyl chloride, and vinyl acetate. Steam cracking of naphtha is mainly used for ethylene production in Europe and Japan. However, ethane is a main feedstock to produce ethylene in the United States and the Middle East because ethane is cheaply available by virtue of the development of shale gas and associated petroleum gas, respectively.[1,2] Steam cracking of ethane, a non-catalytic process, requires high reaction temperatures (1023–1148 K) to achieve high ethylene yield.[2] Additionally, it is necessary to remove carbonaceous deposits from the cracking coils frequently to prevent plugging and increased thermal resistance.[3] As a result, steam cracking of ethane is an energy-intensive process. Therefore, it is necessary to develop a cracking coils to overcome these shortcomings. AFFTALLOY (Kubota), the latest cracking coil, has excellent ability to suppress carbon deposition and carburization because its internal surface is covered with α-Al_2O_3.[4] Furthermore, the reaction temperature can be lowered and coke formation can be suppressed if a catalyst for dehydrogenation of ethane is introduced to the cracking coils.

In general, supported Cr, Ga or Pt catalyst is used for non-oxidative dehydrogenation of ethane.[5–21] Unlike non-oxidative dehydrogenation of ethane, the reaction atmosphere of steam cracking of ethane includes steam. Therefore, the catalyst introduced to the cracking coils must inhibit side reactions such as steam reforming and coke formation to achieve high ethylene selectivity. Furthermore, an inexpensive catalyst is preferred, rendering Pt and other noble metals unsuitable for these purposes. Moreover, Cr catalysts are cheaper catalysts, but they are known to be deactivated at the initial stage of non-oxidative dehydrogenation of ethane.[20,21]

The present work in this chapter, therefore, focuses on Ga catalysts. Considering the practical use of the catalyst together with a famous cracking coil AFTALLOY, the use of the α-Al_2O_3 support is desirable for application of the Ga catalyst because the inner wall of AFTALLOY

consists of α-Al_2O_3.[4] In other words, the use of α-Al_2O_3 support as a model of its inner wall is favorable to reflect the real situation. In addition, a second metal was added to Ga-α-Al_2O_3 catalyst to improve its catalytic performance. Results demonstrated that Ba-modified Ga-α-Al_2O_3 showed higher ethylene selectivity than Ga-α-Al_2O_3. Various characterizations including theoretical investigation have been conducted to elucidate the effects of Ba addition on catalytic activity, selectivity, and coke formation.

2.2. Experimental

2.2.1. Catalyst preparation

To obtain α-Al_2O_3, γ-Al_2O_3 (JRC-ALO-6; Catalysis Society of Japan) was calcined at 1573 K in static air for 3 h. Prior to the calcination, γ-Al_2O_3 was crushed into powder using a planetary ball mill (P-6; Fritsch GmbH). Ga, Ge, In, or Sn was loaded on the support by an impregnation method. The catalyst support was soaked in distilled water for 2 h *in vacuo*. Then an aqueous solution of $Ga(NO_3)_3 \cdot nH_2O$ (n = 7–9), $In(NO_3)_3 \cdot 3H_2O$, $GeCl_2$ or $Sn(CH_3COO)_2$ was added. After the slurry was stirred at room temperature for 2 h, water was evaporated with heating and stirring. Then, the obtained powder was dried in an oven at 393 K overnight in air and was calcined in a muffle furnace at 1323 for 3 h.

Second metal-modified Ga catalysts were prepared by a co-impregnation method. The metal precursors of the second metals are summarized in Table 2.1. Procedure of the co-impregnation method is basically the same as the impregnation method except for the simultaneous addition of Ga and a second metal precursors to the α-Al_2O_3 slurry. The Ga content was fixed at 5wt%. The M/Ga molar ratio was 0.20. Ba-modified catalysts with various Ba/Ga molar ratios were prepared using the same method.

2.2.2. Catalytic activity tests

Catalytic activity tests were conducted at atmospheric pressure in a fixed bed flow-type quartz tube reactor (i.d., 4 mm; o.d., 6 mm). The catalyst (100 mg) sieved to 425–850 μm was charged in the reactor with SiC (*ca.* 392 mg). The reaction gas composition was C_2H_6 : H_2O : N_2 = 1.0 : 1.4 : 5.5 at a total flow rate of 143.3 mL min^{-1} except for preliminary screening of active metals (281.6 mL min^{-1}). The catalyst bed was heated to 973 K in a N_2 flow before the reaction gas was introduced. Products including CH_4, CO, CO_2, and C_2H_4 were analyzed using GC-FID (GC-8A; Shimadzu Corp.) equipped with a Porapak Q packed column. No other product such as C_3 hydrocarbons was detected. CO and CO_2 were converted to CH_4 through methanation catalyzed by Ru/Al_2O_3 to detect them using FID. Ethane conversion and selectivity to each product were calculated as shown below.

$$\text{Ethane conversion [\%]} = \frac{r_{CO} + r_{CH_4} + r_{CO_2} + 2r_{C_2H_4}}{2f_{C_2H_6}} \cdot 100 \qquad (2.1)$$

$$\text{Selectivity [\%]} = \frac{r_{\mathrm{p}}}{r_{\mathrm{CO}} + r_{\mathrm{CH_4}} + r_{\mathrm{CO_2}} + r_{\mathrm{C_2H_4}}} \cdot 100 \quad (2.2)$$

In those equations, r denotes the formation rate of each product (CO, CH_4, CO_2, and C_2H_4) represented by the subscripts. Ethane feed rate was denoted respectively as $f_{\mathrm{C_2H_6}}$. Subscript "p" in equation (2.2) stands for one of the products (CO, CH_4, CO_2 or C_2H_4).

2.2.3. Characterizations

X-ray diffraction (XRD) patterns were measured using an X-ray diffractometer (Smart Lab-III; Rigaku Corp.) at 40 kV and 40 mA with Cu *K*α radiation.

The specific surface area was measured by nitrogen adsorption using Brunauer–Emmett–Teller (BET) method (Gemini VII 2390a; Micromeritics Instrument Corp.). The samples were heated to 473 K for 2 h under N_2 atmosphere before the measurements.

The loaded amounts of Ga and Ba were measured using an inductively coupled plasma (ICP) optical emission spectrometer (iCAP-6500; Thermo Scientific). For the ICP measurements, each sample (*ca.* 10 mg) was mixed with $Li_2B_4O_7$ (*ca.* 1.5 g) and the mixture was heated to 1273 K and hold the temperature for 15 min. After cooling to room temperature, the obtained transparent material was dissolved in HNO_3 aqueous solution (HNO_3 : H_2O = 3 : 50). To quantify Ga and Ba content, Ga and Ba standard solutions (Kanto Chemical Co., Inc.) were mixed with HNO_3 and $Li_2B_4O_7$ solutions. The concentration of HNO_3 and $Li_2B_4O_7$ in the prepared standard solution was the same as the sample solutions.

The amount of carbon deposition was measured by temperature programmed oxidation (TPO). The catalysts (*ca.* 30 mg) were used after reaction at 1073 K for 24 h. The sample was heated to 873 K for 30 min to remove adsorbed water in Ar. After the sample was cooled to 373 K, it was heated to 1173 K in 5vol% O_2/Ar at a ramping rate of 10 K min^{-1}. The amount of carbon deposition was calculated based on the weight loss measured using thermogravimetry (TGA-50; Shimadzu Corp.).

To evaluate the electronic state and coordination environment of Ga, Ga *K*-edge X-ray absorption fine structure (XAFS) measurements were conducted at the BL14B2 of SPring-8 in Japan. The catalysts were mixed with BN. Then 7 mmϕ pellets were formed. As a reference, β-Ga_2O_3 (99.99%; Fujifilm Wako Pure Chemical Corp.) mixed with BN was used to prepare a pellet. XAFS measurements were conducted in transmission mode using a Si(111) crystal monochromator. Analyses of X-ray absorption near-edge structure (XANES) were conducted using software (Demeter ver. 0.9.025; Bruce Ravel).

The electronic state of surface Ga in the fresh samples was measured by X-ray photoelectron spectroscopy (XPS) with an XPS instrument (VersaProbeII; Ulvac-Phi Inc.). XPS measurements were conducted with an Al *K*α X-ray source. The binding energy in the spectra for the Ga2p peak was referenced to the C1s peak at 284.8 eV.

Phase identification of Ga oxide was conducted using a field emission-scanning transmission electron microscope (FE-STEM) with an energy dispersive X-ray (EDX) spectrometer (JEM2100-F; JEOL Ltd.).

Hydrogen adsorption was observed using Fourier transform-infrared (FT-IR) spectroscopy with a FT-IR spectrometer (FT/IR-6100; Jasco Corp.). The catalyst (130 mg) was shaped to a 10 mmϕ self-supported disk placed into an IR cell. First, the disk was heated to 873 K in Ar to remove adsorbed water. Subsequently, the background spectrum was measured at 323 K. Next, the disk was heated to 873 K again. The IR spectrum was measured in Ar as a reference spectrum. Then, H_2 was fed to the disk. The IR spectrum was measured after the peak intensity becomes stable. The reference spectrum was subtracted from the spectrum after H_2 adsorption. The resolution was 2 cm^{-1}. The number of scans was 500 times. The ratio of surface tetrahedrally coordinated Ga to octahedrally coordinated Ga was estimated based on peak areas of Ga-H peaks (2003 cm^{-1} and 1980 cm^{-1}).[22]

2.2.4. Computational method

All density functional theory (DFT) calculations were performed using Vienna *ab initio* simulation package (VASP) ver. 5.4.1.[23–27] The projector-augmented wave (PAW) method[25,27] was used for core electrons. Plane wave basis sets with cutoff energy of 400 eV were used for valence electrons. The adopted exchange-correlation functional was re-parameterized Perdew–Burke–Ernzerhof (RPBE) out of the generalized gradient approximation (GGA). The *k*-point separation in Monkhorst–Pack reciprocal space was 0.04 $Å^{-1}$. The tetrahedron method with Blöchl correction (σ = 0.2 eV) was applied to band occupations around the Fermi level. The van der Waals corrections were calculated using zero damping DFT-D3 method of Grimme. Geometry optimizations were conducted with the conjugate-gradient algorithm. Convergence was assumed to be reached when the total energy change was smaller than 10^{-5} eV. In all calculations, the spin was polarized.

We constructed β-Ga_2O_3(111) and β-Ga_2O_3(002) slab models using four layers containing 16 gallium atoms and 24 oxygen atoms with a 15 Å vacuum layer. The top two layers were relaxed for structure optimization. These surfaces were confirmed by the experimental XRD pattern of β-Ga_2O_3. β-Ga_2O_3(111) slab models were considered to be of two patterns: one containing the tetrahedral Ga atoms (Ga(T)-(111)) and the other containing the octahedral Ga atoms (Ga(O)-(111)) in the top layer. β-Ga_2O_3(002) slab models contained the tetrahedral Ga atoms in the surface (Ga(T)-(002)) and the octahedral Ga atoms in the surface (Ga(O)-(002)). Details are shown in Figure 2.1. The adsorption energy of ethane and ethylene ($\Delta \boldsymbol{E}$) was defined as

$$\Delta \boldsymbol{E}_{ad} = \boldsymbol{E}_{molecule/slab} - \boldsymbol{E}_{slab} - \boldsymbol{E}_{molecule} \quad (2.3)$$

where $\boldsymbol{E}_{molecule/slab}$, $\boldsymbol{E}_{slab}$ and $\boldsymbol{E}_{molecule}$ respectively represent the energy of the β-Ga_2O_3 slab with an adsorbed molecule such as ethane and ethylene, the clean β-Ga_2O_3 slab, and the molecule. The

energies of ethane and ethylene molecules were calculated in the 10 × 10 × 10 Å cubic box. All calculation models were drawn using VESTA.[28]

2.3. Results and discussion

2.3.1. Preliminary screening of active metals

Four chemical elements (Ga, Ge, In, and Sn) were tested to investigate their catalytic activities for dehydrogenation of ethane in the presence of steam. The dehydrogenation reaction of ethane was conducted at 973 K. Since the internal surface of AFTALLOY is composed of α-Al_2O_3, 5wt% Ga, Ge, In or Sn was impregnated on α-Al_2O_3. Results of screening tests are presented in Table 2.2. These results indicate that Ga-Al_2O_3 has a high ethylene formation rate and high ethylene selectivity. Although In-Al_2O_3 exhibited a high ethylene formation rate, ethylene selectivity was about 70%, which was lower than those on the other catalysts. Ge-Al_2O_3 was slightly inferior to the Ga catalyst in terms of the ethylene formation rate and selectivity, but it showed high stability. Considering the price of Ge, it is not feasible for industrial use. The catalytic activity of Sn-Al_2O_3 was almost identical to that of α-Al_2O_3, indicating that Sn has no catalytic activity for dehydrogenation of ethane. From the results presented above, Ga is the most effective active metal for dehydrogenation of ethane under the reaction condition.

2.3.2. Screening of second metals

To find a better catalyst than Ga-α-Al_2O_3, the effects of second metal addition to Ga-α-Al_2O_3 on the catalytic performance were investigated. Various M-Ga-α-Al_2O_3 catalysts with M/Ga molar ratio = 0.20 (M = Ba, Bi, Ce, Co, Cu, Fe, La, Mn, Mo, Ni, Sn, Sr, W or Zr) were prepared. Dehydrogenation of ethane in the presence of steam was conducted at 973 K. Catalytic activity tests are conducted in a kinetic region (*i.e.* low conversion condition). The ethylene formation rate vs. ethylene selectivity over these catalysts is presented in Figure 2.2. Specific values are presented in Table 2.3. Results demonstrate that 0.20Fe-Ga-α-Al_2O_3 and 0.20Ba-Ga-α-Al_2O_3 show a higher ethylene formation rate and higher ethylene selectivity than Ga-α-Al_2O_3, respectively. Each product selectivity over Ga-α-Al_2O_3, 0.20Fe-Ga-α-Al_2O_3, and 0.20Ba-Ga-α-Al_2O_3 is presented in Figure 2.3. Also, 0.20Fe-Ga-α-Al_2O_3 showed higher CO and CO_2 selectivity than Ga-α-Al_2O_3. This phenomenon indicates that 0.20Fe-Ga-α-Al_2O_3 promoted steam reforming of ethane. Consequently 0.20Fe-Ga-α-Al_2O_3 was unsuitable for dehydrogenation of ethane in the presence of steam. However, 0.20Ba-Ga-α-Al_2O_3 showed lower CO and CO_2 selectivity than Ga-α-Al_2O_3. Therefore, we concluded that Ba was the best additive for Ga-α-Al_2O_3 catalyst.

To ascertain the optimum amount of Ba, we prepared *x*Ba-Ga-α-Al_2O_3 catalysts with various Ba/Ga molar ratios (*x* = 0, 0.070, 0.10, 0.20, 0.33 and 1.0) and 5wt% Ba-α-Al_2O_3 catalyst and evaluated their catalytic activities. Structural and textural characterizations were conducted using XRD, BET, and ICP as presented in Figure 2.4 and Table 2.4. From XRD results, no peak for Ga

species was observed, indicating that Ga was highly dispersed on α-Al_2O_3. However, peaks for $BaAl_2O_4$ and $BaCO_3$ were observed with the increase in the loading amount of Ba. As shown in Table 2.4, the BET surface area of the catalysts was almost identical (about 6.0 m^2 g^{-1}). The Ba/Ga molar ratio of the prepared catalysts was almost equal to the desired value.

The activity test results are presented in Figure 2.5. Specific values of the catalytic performance are presented in Table 2.5. Although ethylene selectivity increased by Ba addition, the ethylene formation rate decreased concomitantly with increasing Ba loading amount. The result suggests that the excess Ba covered Ga active sites in the catalysts with a high Ba/Ga molar ratio. In addition, 5wt%Ba-α-Al_2O_3 showed comparable activity to that of α-Al_2O_3, indicating that the supported Ba is inactive. However, 0.10Ba-Ga-α-Al_2O_3 showed a high ethylene formation rate and ethylene selectivity. Therefore, we found 0.10Ba-Ga-α-Al_2O_3 as the optimal catalyst for dehydrogenation of ethane in the presence of steam. After the reaction, little changes in XRD pattern and BET surface area of the spent 0.10Ba-Ga-α-Al_2O_3 were verified (Figure 2.6 and Table 2.6), indicating 0.10Ba-Ga-α-Al_2O_3 is stable under hydrothermal conditions.

2.3.3. Catalytic stability and coke formation

The catalyst stability was evaluated using long-term reaction tests. The time courses of the ethylene formation rate and ethylene selectivity are portrayed in Figure 2.7. For this study, α-Al_2O_3 was used as a model of the AFTALLOY inner surface (*i.e.* cracking coil). Thermal cracking of ethane, which is the non-catalytic and radical reaction in gas phase, occurred at temperatures higher than 883 K.[29] In the case of α-Al_2O_3, ethylene formation was attributed to the gas phase reaction because α-Al_2O_3 shows no catalytic activity for the dehydrogenation of ethane. As portrayed in Figure 2.7(a), ethylene formation rate on Ga-α-Al_2O_3 is higher than on bare α-Al_2O_3. Further improvement in ethylene formation rate was achieved by Ba addition. In addition, 0.10Ba-Ga-α-Al_2O_3 catalyst showed higher ethylene selectivity than Ga-α-Al_2O_3 (Figure 2.7(b)) by virtue of the decrease in CO and CO_2 selectivity (Figure 2.8). These results demonstrate that Ba addition to Ga-α-Al_2O_3 suppressed CO and CO_2 formation, improving not only stability but also ethylene selectivity.

In the present reaction system, possible CO and CO_2 formation pathways are ethane steam reforming (2.4), gasification of carbonaceous deposit (2.5), and water gas shift reaction (2.6), as shown in the following reaction formula.

$$C_2H_6 + 2H_2O \rightarrow 2CO + 5H_2 \quad (2.4)$$

$$C + H_2O \rightarrow CO + H_2 \quad (2.5)$$

$$CO + H_2O \rightarrow CO_2 + H_2 \quad (2.6)$$

No report of the relevant literature describes that Ga or Ba catalyst shows catalytic activity for steam reforming of ethane. Therefore, CO and CO_2 formation were attributed to gasification of carbonaceous deposits (2.5) and a subsequent water gas shift reaction (2.6). Considering these pathways, Ba addition can be expected to contribute to the suppression of carbon deposition. Also

coke formation is attributable to ethylene decomposition. Thus, 0.10Ba-Ga-α-Al_2O_3 exhibited higher ethylene formation rate than Ga-α-Al_2O_3.

The amounts of carbon deposition on spent α-Al_2O_3, Ga-α-Al_2O_3, and 0.10Ba-Ga-α-Al_2O_3 catalysts were quantified using temperature programmed oxidation (TPO). To evaluate their coke resistance, dehydrogenation of ethane was conducted under severe conditions (at 1073 K for 24 h) because the amount of carbon deposition was too small to quantify at 973 K. The amounts of carbon deposition on the spent catalysts are shown in Table 2.7. In the case of α-Al_2O_3, no carbon deposition was observed. The amount of carbon deposition on Ga-α-Al_2O_3 was 20.6 mg g_{cat}^{-1}, demonstrating that carbon deposition occurred mainly on Ga sites. No carbon deposition on 0.10Ba-Ga-α-Al_2O_3 was observed. These results indicate that carbon deposition at Ga sites was suppressed by Ba addition. Therefore, we concluded that the suppression of carbon deposition on 0.10Ba-Ga-α-Al_2O_3 contributed to the inhibition of CO and CO_2 formation and stable catalytic activity.

To assess the effects of Ba addition on ethylene decomposition experimentally, the amounts of carbon deposition *via* ethylene decomposition on Ga-α-Al_2O_3 and 0.10Ba-Ga-α-Al_2O_3 were compared. Instead of ethane, ethylene was fed to the reactor at 1073 K for 7 h; the spent Ga-α-Al_2O_3 and 0.10Ba-Ga-α-Al_2O_3 were obtained. The amounts of carbon deposition on the spent catalysts are shown in Table 2.7. Although the amount of carbon deposition on Ga-α-Al_2O_3 was 196.3 mg g_{cat}^{-1}, no carbon deposition was observed over the spent 0.10Ba-Ga-α-Al_2O_3. These results revealed that ethylene decomposition on Ga sites was suppressed by Ba addition.

2.3.4. Electronic state and structure of Ga

To elucidate the effects of Ba addition on the electronic state of the supported Ga species, Ga-α-Al_2O_3 and 0.10Ba-Ga-α-Al_2O_3 were characterized by XPS. XP spectra of Ga-α-Al_2O_3 and 0.10Ba-Ga-α-Al_2O_3 are shown in Figure 2.9. In the spectrum of Ba, two peaks for $Ba3d_{5/2}$ and $Ba3d_{3/2}$ were observed at 780 and 795 eV, respectively, corresponded to Ba^{2+}.[30,31] From the results of XRD (Figure 2.6), we observed $BaCO_3$ and $BaAl_2O_4$ in *x*Ba-Ga-α-Al_2O_3 (*x* = 0.20–1.0). Generally, $Ba3d_{5/2}$ peaks for $BaCO_3$ and $BaAl_2O_4$ are observed at similar binding energy around 780 eV.[30,31] Therefore, these peaks would be attributable to $BaCO_3$ or $BaAl_2O_4$. In the Ga2p spectra, peaks for $Ga2p_{3/2}$ and $Ga2p_{1/2}$ were observed at 1118 and 1145 eV, respectively, corresponded to Ga^{3+}.[32,33] Biding energy for both peaks was not affected by Ba addition, indicating that the electronic state of Ga was not varied whether Ba was added to the catalyst or not.

Ga *K*-edge XANES spectra and their enlarged spectra around the white lines are presented in Figure 2.10. β-Ga_2O_3 was used as a reference sample of Ga^{3+} species. The $\boldsymbol{E}_0$ values were calculated as zero-crossing of 2nd derivative, and these of β-Ga_2O_3 (10371.2 eV), Ga-α-Al_2O_3 (10371.6 eV) and 0.10Ba-Ga-α-Al_2O_3 (10371.6 eV) were almost the same, indicating the presence of Ga^{3+} in Ga-α-Al_2O_3 and 0.10Ba-Ga-α-Al_2O_3. Reportedly, the two peaks for β-Ga_2O_3 at 10375 eV and 10379 eV are attributed to tetrahedrally coordinated Ga species denoted as Ga(T) and

octahedrally coordinated Ga species denoted as Ga(O), respectively.[34] Although the peak intensity around white line was slightly different, Ga *K*-edge XANES spectra of Ga-α-Al_2O_3 and 0.10Ba-Ga-α-Al_2O_3 showed two peaks at the same position as that of β-Ga_2O_3. This indicated that Ga species in Ga-α-Al_2O_3 and 0.10Ba-Ga-α-Al_2O_3 had β-Ga_2O_3 structure. The Ga(T)/Ga(O) ratio could be calculated from each peak intensity.[34] Compared with the spectrum of β-Ga_2O_3, the high peak intensity of Ga(T) was observed in the spectra of Ga-α-Al_2O_3 and 0.10Ba-Ga-α-Al_2O_3. To the contrary, the peak intensity of Ga(O) in the spectra of supported Ga catalysts was lower than that in the spectrum of β-Ga_2O_3. These indicate the high Ga(T)/Ga(O) ratios of Ga-α-Al_2O_3 and 0.10Ba-Ga-α-Al_2O_3 in comparison with β-Ga_2O_3. Moreover, since XANES spectrum of 0.10Ba-Ga-α-Al_2O_3 were almost the same as that of Ga/α-Al_2O_3, coordination environment of Ga in the bulk was hardly affected by Ba addition.

TEM images and EDX mappings of 0.10Ba-Ga-α-Al_2O_3 were also measured to observe Ga oxide. Concentration of each component (O, Al, Ga and Ba) quantified by EDX were summarized in Table 2.8. As shown in Figures 2.11(a) and (b), Ga oxide nanoparticles were observed on the α-Al_2O_3 support. The interplanar *d*-spacing shown in Figure 2.11(b) is 0.255 nm, corresponded to β-Ga_2O_3(111) facet.[35] The existence of β-Ga_2O_3 was verified using TEM in addition to XAFS. EDX mapping for Ba revealed that Ba was highly dispersed on β-Ga_2O_3 and α-Al_2O_3. This would indicate that coverage of β-Ga_2O_3 with Ba affect the catalytic performance because Ba addition had little influence on the electronic state and crystalline structure of Ga.

2.3.5. Coordination environment of surface Ga

To investigate the coordination environment of surface Ga, observations of hydrogen adsorption by FT-IR were conducted. Collins *et al*. reported that the surface Ga(T)/Ga(O) ratio can be estimated using FT-IR after adsorption of hydrogen on Ga_2O_3.[22] The subtracted FT-IR spectra of hydrogen adsorption at 873 K are presented in Figure 2.12. A broad absorption band attributed to Ga-H was observed around 2000 cm^{-1}. To estimate the surface Ga(T)/Ga(O) ratio, peak deconvolution was conducted. In our case, the absorption band was deconvoluted with Gaussian. The results of peak deconvolution of the IR spectra are presented in Table 2.9.

According to reports of the literature,[22,36] band 2 (Ga-α-Al_2O_3: 1974 cm^{-1}, 0.070Ba-Ga-α-Al_2O_3: 1975 cm^{-1}, 0.10Ba-Ga-α-Al_2O_3: 1964 cm^{-1}, 0.20Ba-Ga-α-Al_2O_3: 1951 cm^{-1}) was assigned to Ga(O)-H, and band 3 (Ga-α-Al_2O_3: 2003 cm^{-1}, 0.070Ba-Ga-α-Al_2O_3: 1999 cm^{-1}, 0.10Ba-Ga-α-Al_2O_3: 2001 cm^{-1}, 0.20Ba-Ga-α-Al_2O_3: 1992 cm^{-1}) was assigned to Ga(T)-H. Then, the peak area ratio of band 3 over band 2 (Area3/Area2 in Table 2.9) shows the exposed Ga(T)/Ga(O) ratio at the catalyst surface. The Area3/Area2 ratios decreased with the increase in the Ba/Ga molar ratios (3.30→1.06→0.98→0.89), indicating that the amount of surface Ga(T) sites decreased by coverage with Ba. Therefore, we deduce from the results of TPO and FT-IR that the surface Ga(T) sites cause carbon deposition. The surface Ga(T) sites would be covered with Ba, leading to the suppression of coke formation. Considering that 0.10Ba-Ga-α-Al_2O_3 exhibited the highest

ethylene formation rate, the coverage of the Ga(T) sites with Ba would be insufficient in case of 0.070Ba-Ga-α-Al_2O_3. Although the Area3/Area2 ratio of 0.20Ba-Ga-α-Al_2O_3 was smaller than that of 0.10Ba-Ga-α-Al_2O_3, the catalytic activity decreased with the increase in the Ba/Ga ratios (0.10→0.20). As shown in Figure 2.6, addition of the excess amount of Ba induce the formation of $BaCO_3$ and $BaAl_2O_3$. These impurities would be deposited on the active sites, resulting in the decrease in the intrinsic activity.

2.3.6. Ethane and ethylene adsorption energy

To evaluate the properties of Ga(T) and Ga(O), the respective adsorption energies of ethane and ethylene were calculated using first principles calculation. For this study, β-Ga_2O_3 was used as a structural model of the Ga catalysts because we experimentally verified that β-Ga_2O_3 exists in Ga-α-Al_2O_3 and Ga-0.10Ba-α-Al_2O_3. Based on the TEM image of 0.10Ba-Ga-α-Al_2O_3 (Figure 2.12) and XRD pattern of β-Ga_2O_3 (data not shown), we calculated ethane and ethylene adsorption on (111) and (002) facets of β-Ga_2O_3. As shown in Figure 2.1, two kinds of Ga(O) sites exist in these facets: coordinatively unsaturated Ga(O) sites with four oxygen in the (002) facet (distorted surface $GaO_4\square_2$ unit: Ga(O)-(002)) and those with five oxygen in the (111) facet (distorted surface $GaO_5\square_1$ unit: Ga(O)-(111)), respectively. In addition, coordinatively unsaturated Ga(T) sites with three oxygen (distorted surface $GaO_3\square_1$ unit: Ga(T)-(002) and Ga(T-(111)) also exist. The oxygen defects are described by the square symbol (□). Ethane and ethylene adsorption energy on these sites are calculated.

Although we preliminary examined molecular adsorption of ethane, all of the adsorption energy resulted in positive values (data not shown). Therefore, two models for dissociative adsorption of ethane (models (a) and (b)) and one model for molecular adsorption of ethylene (model (c)) were investigated. Results of the calculations are shown in Figure 2.13. The calculated adsorption energy is presented in Table 2.10. At the Ga(O)-(111) sites, all calculated values of adsorption energy were positive, indicating that Ga(O)-(111) sites are inert for activation of ethane and ethylene, probably because of the highest coordination number of Ga(O)-(111). Of the models (a) and (b), only model (a) at Ga(T)-(002), Ga(O)-(002), and Ga(T)-(111) sites were preferable to dissociative adsorption of ethane because their adsorption energy showed negative values. Adsorption energy of ethylene (model (c)) was negative at Ga(T)-(002), Ga(O)-(002) and Ga(T)-(111) sites, where activation of ethane (model (a)) also occurred. However, tendencies of adsorption energy on active sites were quite different if comparing the adsorption energy of model (a) and (c) at Ga(O)-(002) sites with those at Ga(T)-(002) and Ga(T)-(111). Specifically, the adsorption energy of model (a) was lower than that of model (c) at Ga(O)-(002) and *vice versa* at Ga(T)-(002) and Ga(T)-(111). Generally, strong ethylene adsorption causes carbon deposition *via* ethylene decomposition. Therefore, these results indicate that Ga(T)-(002) and Ga(T)-(111) sites are likely to cause carbon deposition rather than dehydrogenation of ethane, and *vice versa* for

Ga(O)-(002) sites. In other words, Ga(O)-(002) sites are suitable for selective ethylene formation without carbon deposition.

The theoretical and experimentally obtained results led us to infer that 0.10Ba-Ga-α-Al_2O_3 showed high selectivity and coke resistance by virtue of the coverage of Ga(T) sites with Ba. Based on these results, a schematic image of the effects of Ba addition on surface Ga sites is depicted in Figure 2.14.

2.4. Chapter Conclusion

Dehydrogenation of ethane over various M-Ga-α-Al_2O_3 catalysts was performed in the presence of steam. Results show that 0.10Ba-Ga-α-Al_2O_3 (Ba/Ga molar ratio = 0.10) exhibited high ethylene selectivity and stability by virtue of the suppression of carbon deposition. Subsequently, XRD, XAFS, and XPS measurements revealed highly dispersed β-Ga_2O_3 with numerous Ga(T) sites in Ga-α-Al_2O_3 and 0.10Ba-Ga-α-Al_2O_3. FT-IR measurements demonstrated that the surface Ga(T)/Ga(O) ratio decreased by Ba addition because surface Ga(T) sites were covered with Ba. First principles calculations revealed that surface Ga(T) sites were more likely to cause carbon deposition *via* ethylene decomposition than ethane dehydrogenation while surface Ga(O)-(002) sites preferentially promote ethane dehydrogenation. Results show that 0.10Ba-Ga-α-Al_2O_3 exhibits high ethylene selectivity and durability without carbon deposition by virtue of covering unfavorable Ga(T) sites with Ba.

References

1. C. A. Gärtner, A. C. van Veen, J. A. Lercher, Oxidative Dehydrogenation of Ethane: Common Principles and Mechanistic Aspects. *ChemCatChem* **2013**, *5*, 3196−3217.
2. J. J. Siirola, The Impact of Shale Gas in the Chemical Industry. *AIChE J.* **2014**, *60*, 810−819.
3. C. Zhao, C. Liu, Q. Xu, Cyclic Scheduling for Ethylene Cracking Furnace System with Consideration of Secondary Ethane Cracking. *Ind. Eng. Chem. Res.* **2010**, *49*, 5765−5774.
4. M. Takahashi, Y. Enjo, U. Shinichi, Cast Product Having Alumina Barrier Layer. US Patent US2011/0318593A1, **2011**.
5. M. M. Bhasin, J. H. McCain, B. V. Vora, T. Imai, P. R. Pujadó, Dehydrogenation and Oxydehydrogenation of Paraffins to Olefins. *Appl. Catal. A: Gen.* **2001**, *221*, 397−419.
6. B. M. Weckhuysen, R. A. Schoonheydt, Alkane Dehydrogenation over Supported Chromium Oxide Catalysts. *Catal. Today* **1999**, *51*, 223−232.
7. S. Lillehaug, K.J. Børve, M. Sierka, J. Sauer, Catalytic Dehydrogenation of Ethane over Mononuclear Cr(III) Surface Sites on Silica. Part I. C—H Activation by σ-Bond Metathesis. *J. Phys. Org. Chem.* **2004**, *17*, 990−1006.

8. U. Olsbye, A. Virnovskaia, O. Prytz, S. J. Tinnemans, B. M. Weckhuysen, Mechanistic Inshight in the Ethane Dehydrogenation Reaction over Cr/Al_2O_3 Catalysts. *Catal. Lett.* **2005**, *103*, 143−148.
9. T. V. M. Rao, E. M. Zahidi, A. Sayari, Ethane Dehydrogenation over Pore-Expanded Mesoporous Silica-Supported Chromium Oxide: 2. Catalytic Properties and Nature of Active Sites. *J. Mol. Catal. A: Chem.* **2009**, *301*, 159−165.
10. B. Zheng, W. Hua, Y. Yue, Z. Gao, Dehydrogenation of Propane to Propene over Different Polymorphs of Gallium Oxide. *J. Catal.* **2005**, *232*, 143−151.
11. K. Nakagawa, M. Okamura, N. Ikenaga, T. Suzuki, T. Kobayashi, Dehydrogenation of Ethane over Gallium Oxide in the Presence of Carbon Dioxide. *Chem. Commun.* **1998**, 1025−1026.
12. K. Nakagawa, C. Kajita, K. Okamura, N. Ikenaga, M. Nishitani-Gamo, T. Ando, T. Kobayashi, T. Suzuki, Role of Carbon Dioxide in the Dehydrogenation of Ethane over Gallium-Loaded Catalysts. *J. Catal.* **2001**, *203*, 87−93.
13. Z. Shen, J. Liu, H. Xu, Y. Yue, W. Hua, W. Shen, Dehydrogenation of Ethane to Ethylene over a Highly Efficient Ga_2O_3/HZSM-5 Catalyst in the Presence of CO_2. *Appl. Catal. A: Gen.* **2009**, *356*, 148−153.
14. S. de Miguel, A. Castro, O. Scelza, O. Scelza, J. L. G. Fierro, J. Soria, FTIR and XPS Study of Supported PtSn Catalysts Used for Light Paraffins Dehydrogenation. *Catal. Lett.* **1996**, *36*, 201−206.
15. A. Virnovskaia, S. Morandi, E. Rytter, G. Ghiotti, U. Olsbye, Characterization of Pt,Sn/Mg(Al)O Catalysts for Light Alkane Dehydrogenation by FT-IR Spectroscopy and Catalytic Measurements. *J. Phys. Chem. C* **2007**, *111*, 14732−14742.
16. V. Galvita, G. Siddiqi, P. Sun, A. T. Bell, Ethane Dehydrogenation on Pt/Mg(Al)O and PtSn/Mg(Al)O Catalysts. *J. Catal.* **2010**, *271*, 209−219.
17. P. Sun, G. Siddiqi, W. C. Vining, M. Chi, A. T. Bell, Novel Pt/Mg(In)(Al)O Catalysts for Ethane and Propane Dehydrogenation. *J. Catal.* **2011**, *282*, 165−174.
18. J. Wu, S. M. Sharada, C. Ho, A. W. Hauser, M. Head-Gordon, A. T. Bell, Ethane and Propane Dehydrogenation over PtIr/Mg(Al)O. *Appl. Catal. A: Gen.* **2015**, *506*, 25−32.
19. Z. Yu, J. A. Sawada, W. An, S. M. Kuznicki, PtZn-ETS-2: Novel Catalyst for Ethane Dehydrogenation. *AIChE J.* **2015**, *61*, 4367−4376.
20. D. Shee, A. Sayari, Light Alkane Dehydrogenation over Mesoporous Cr_2O_3/Al_2O_3 Catalysts. *Appl. Catal. A: Gen.* **2010**, *389*, 155–164.
21. H. H. Shin, S. McIntosh, Proton-Conducting Perovskites as Supports for Cr Catalysts in Short Contact Time Ethane Dehydrogenation. *ACS Catal.* **2015**, *5*, 95–103.
22. S. E. Collins, M. A. Baltanas, A. L. Bonivardi, Hydrogen Chemisorption on Gallium Oxide Polymorphs. *Langmuir* **2005**, *21*, 962−970.
23. G. Kresse, J. Hafner, *Ab initio* Molecular Dynamics for Liquid Metals. *Phys. Rev. B* **1993**, *47*, 558.

24. G. Kresse, J. Hafner, *Ab initio* Molecular-Dynamics Simulation of the Liquid-Metal-Amorphous-Semiconductor Transition in Germanium. *Phys. Rev. B* **1994**, *49*, 14251.
25. G. Kresse, J. Furthmüller, Efficiency of ab-initio Total Energy Calculations for Metals and Semiconductors Using a Plane-Wave Basis Set. *Comput. Mater. Sci.* **1996**, *6(1)*, 15–50.
26. G. Kresse, J. Furthmüller, Efficient Iterative Schemes for *ab initio* Total-Energy Calculations Using a Plane-Wave Basis Set. *Phys. Rev. B* **1996**, *54*, 11169.
27. G. Kresse, D. Joubert, From Ultrasoft Pseudopotentials to the Projector augmented-Wave Method. *Phys. Rev. B: Condens. Mater.* **1999**, *59*, 1758.
28. K. Momma, F. Izumi, *VESTA 3* for Three-Dimensional Visualization of Crystal, Volumetric and Morphology Data. *J. Appl. Crystallogr.* **2011**, *44*, 1272–1276.
29. E. Heracleous, A.A. Lemonidou, Homogeneous and Heterogeneous Pathways of Ethane Oxidation and Non-Oxidative Dehydrogenation Studied by Temperature-Programmed Reaction. *Appl. Catal. A: Gen.* **2004**, *269*, 123–135.
30. R. P. Vasquez, X-ray Photoelectron Spectroscopy Study of Sr and Ba Compounds. *J. Electron Spectrosc. Relat. Phenom.* **1991**, *56*, 217–240.
31. Z. Zhu, X. Li, H. Li, Y. Li, C. Sun, Y. Cao, Synthesis and Characterization of $BaAl_2O_4$ Nanorods by a Facile Solvothermal Method. *Mater. Lett.* **2012**, *86*, 1–4.
32. G. Schön, Auger and Direct Electron Spectra in X-ray Photoelectron Studies of Zinc, Zinc Oxide, Gallium and Gallium Oxide. *J. Electron Spectrosc. Relat. Phenom.* **1973**, *2*, 75–86.
33. T. Mathew, Y. Yamada, A. Ueda, H. Shioyama, T. Kobayashi, C. S. Gopinath, Effect of Support on the Activity of Ga_2O_3 Species for Steam Reforming of Dimethyl Ether. *Appl. Catal. A: Gen. 2006*, **300**, 58–66.
34. K. Nishi, K. Shimizu, M. Takamatsu, H. Yoshida, A. Satsuma, T. Tanaka, S. Yoshida, T. Hattori, Deconvolution Analysis of Ga K-Edge XANES for Quantification of Gallium Coordinations in Oxide Environments. *J. Phys. Chem. B* **1998**, *102*, 10190–10195.
35. L. M. Foster, G. V. Chandrashekhar, J. E. Scardefield, R. B. Bradford, Phase Diagram of the System $Na_2O\cdot Ga_2O_3$-Ga_2O_3 and Its Relation to the System $Na_2O\cdot Al_2O_3$-Al_2O_3. *J. Am. Ceram. Soc.* **1980**, *63*, 509–512.
36. W. Jochum, S. Penner, K. Fottinge, R. Kramer, G. Rupprechter, B. Klotzer, Hydrogen on Polycrystalline β-Ga_2O_3: Surface Chemisorption, Defect Formation, and Reactivity. *J. Catal.* **2008**, *256*, 268–277.

Figures and Tables

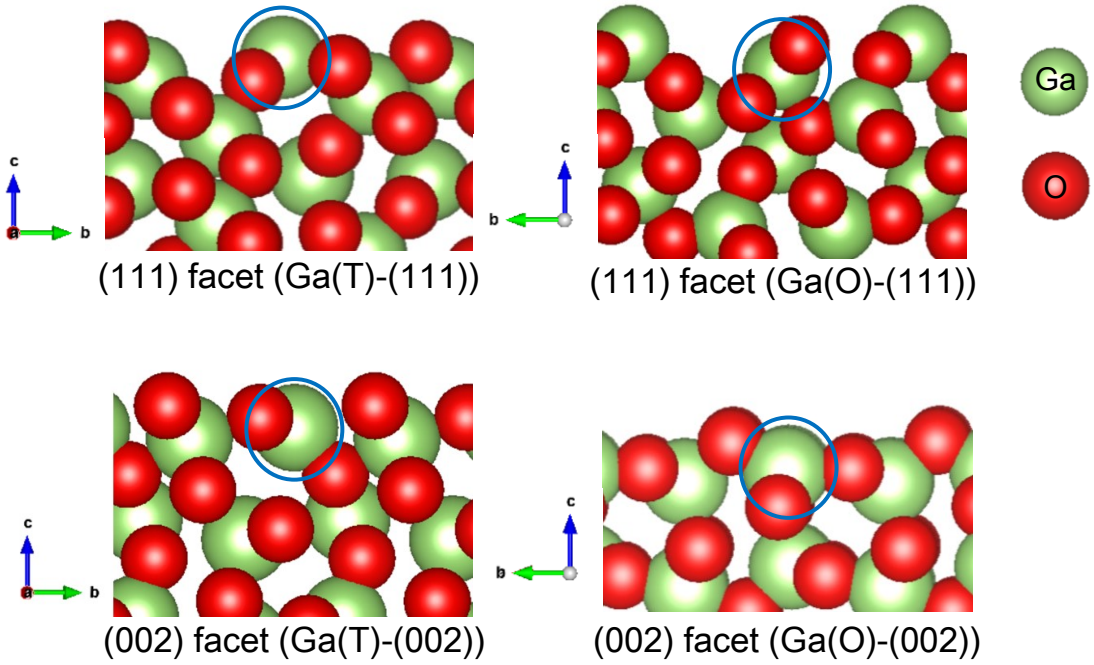

Figure 2.1. DFT calculation models for ethane or ethylene adsorption energy over β-Ga_2O_3. Adsorption sites are enclosed in the blue circles. Reprinted from H. Seki *et al.*, *Appl. Catal. A: Gen.* **2019**, *581*, 23–30. Copyright 2019 Elsevier B. V.

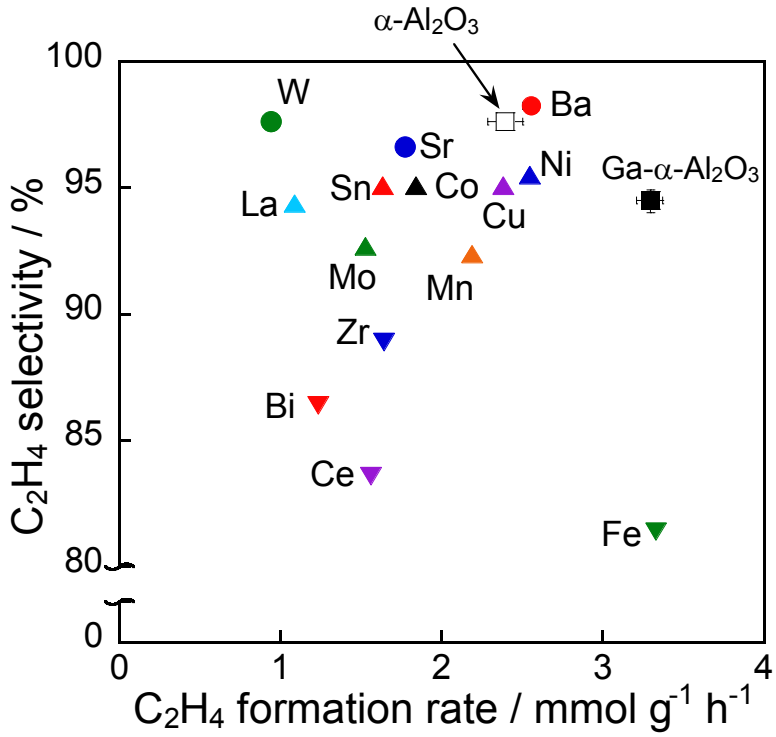

Figure 2.2. Ethylene formation rate vs. ethylene selectivity over 0.20M-Ga-α-Al_2O_3 (M = Ba, Bi, Ce, Co, Cu, Fe, La, Mn, Mo, Ni, Sn, Sr, W and Zr) at 973 K. M/Ga molar ratio was fixed to be 0.20. Reprinted from H. Seki *et al.*, *Appl. Catal. A: Gen.* **2019**, *581*, 23–30. Copyright 2019 Elsevier B. V.

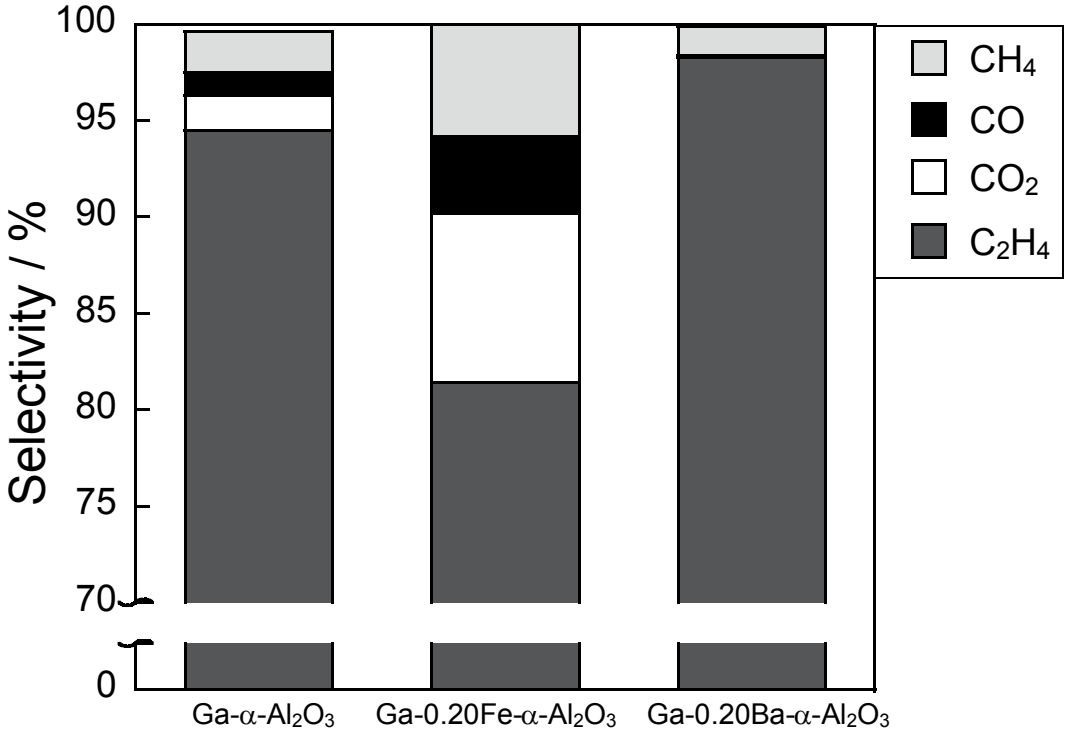

Figure 2.3. Selectivity to each product over Ga-α-Al_2O_3, 0.20Fe-Ga-α-Al_2O_3 and 0.20Ba-Ga-α-Al_2O_3 at 973 K. Reprinted from H. Seki *et al.*, *Appl. Catal. A: Gen.* **2019**, *581*, 23–30. Copyright 2019 Elsevier B. V.

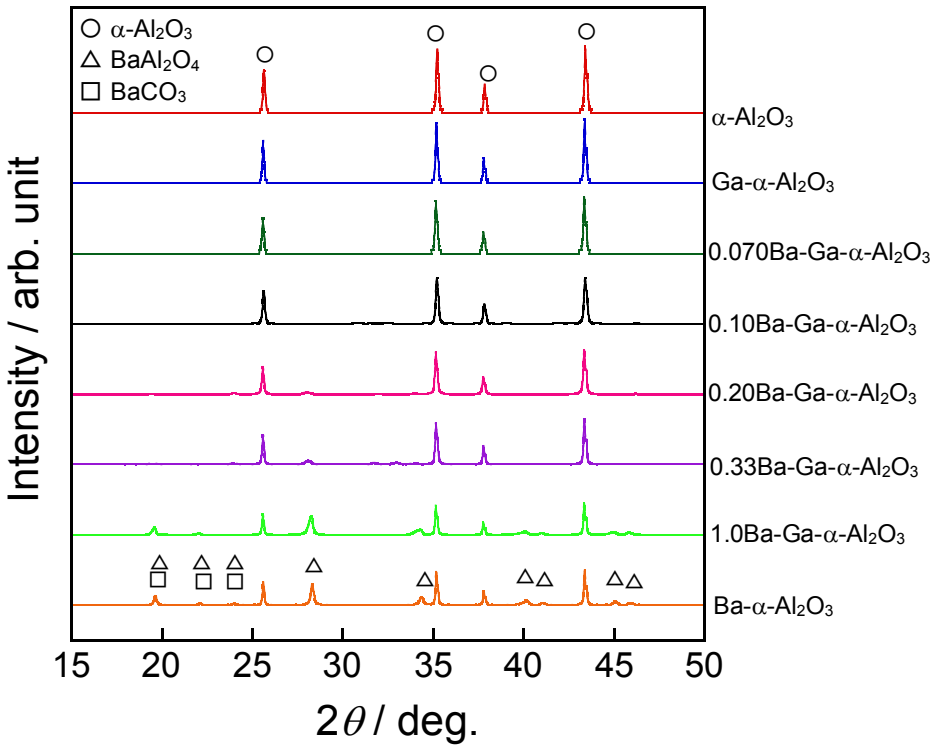

Figure 2.4. XRD patterns of various α-Al_2O_3 supported catalysts. Reprinted from H. Seki *et al.*, *Appl. Catal. A: Gen.* **2019**, *581*, 23–30. Copyright 2019 Elsevier B. V.

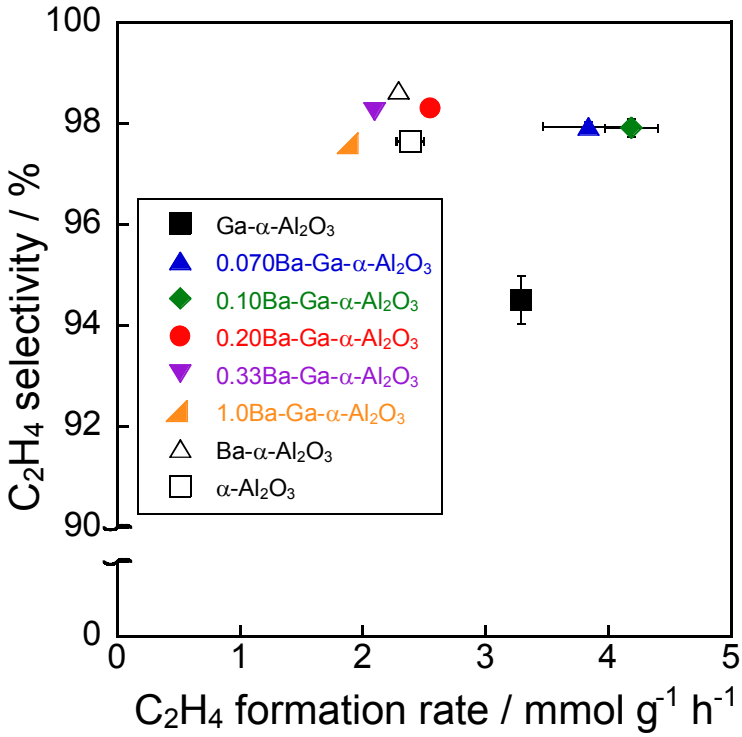

Figure 2.5. Ethylene formation rate vs. ethylene selectivity over *x*Ba-Ga-α-Al_2O_3 (*x* = 0, 0.070, 0.10, 0.20, 0.33 and 1.0), 5wt% Ba-α-Al_2O_3 and α-Al_2O_3 at 973 K. Ba/Ga molar ratio was represented by the letter "*x*". Reprinted from H. Seki *et al.*, *Appl. Catal. A: Gen.* **2019**, *581*, 23–30. Copyright 2019 Elsevier B. V.

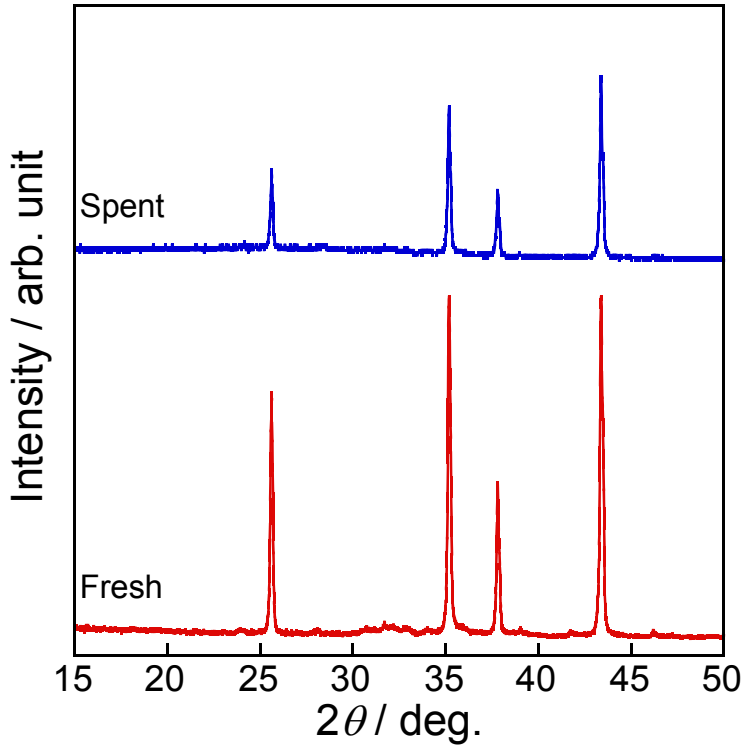

Figure 2.6. XRD patterns of fresh and spent 0.10Ba-Ga-α-Al_2O_3. The spent catalyst was obtained after the activity tests at 973 K for 3 h. Reprinted from H. Seki *et al.*, *Appl. Catal. A: Gen.* **2019**, *581*, 23–30. Copyright 2019 Elsevier B. V.

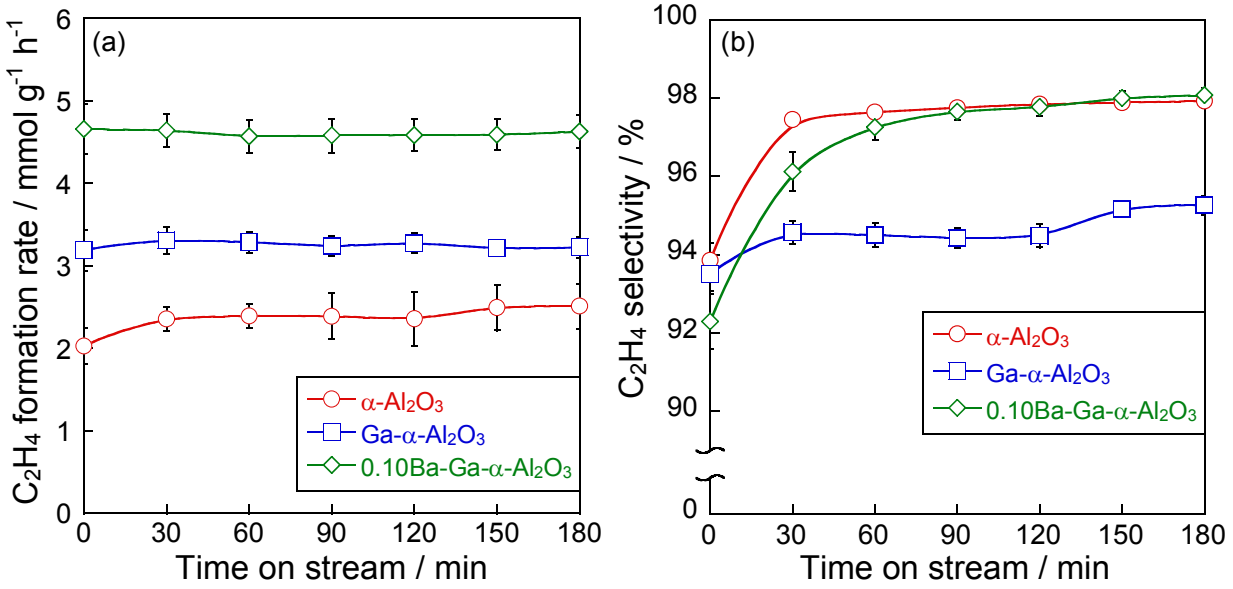

Figure 2.7. (a) Ethylene formation rate and (b) ethylene selectivity over α-Al_2O_3, Ga-α-Al_2O_3 and 0.10Ba-Ga-α-Al_2O_3 catalysts at 973 K. Reprinted from H. Seki *et al.*, *Appl. Catal. A: Gen.* **2019**, *581*, 23–30. Copyright 2019 Elsevier B. V.

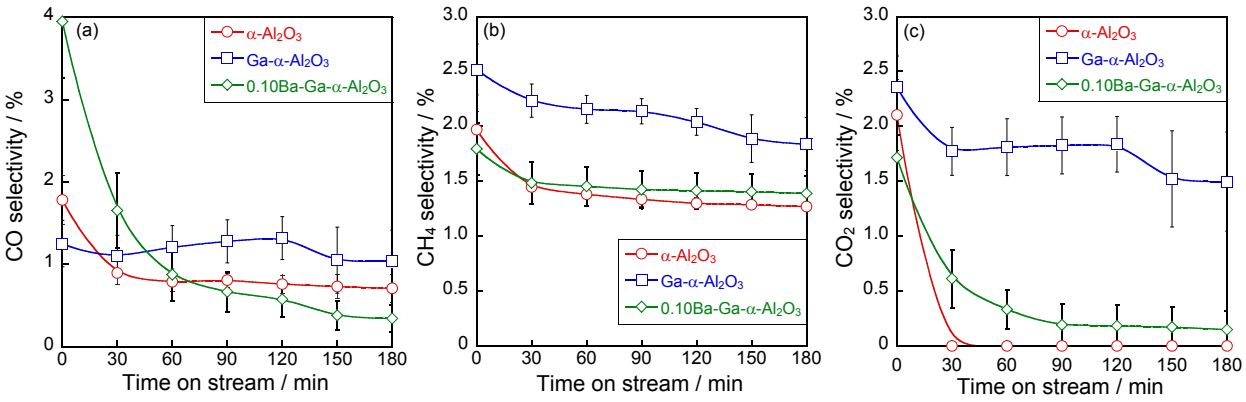

Figure 2.8. (a) CO, (b) CH_4 and (c) CO_2 selectivity over α-Al_2O_3, Ga-α-Al_2O_3 and 0.10Ba-Ga-α-Al_2O_3 catalysts at 973 K. Reprinted from H. Seki *et al.*, *Appl. Catal. A: Gen.* **2019**, *581*, 23–30. Copyright 2019 Elsevier B. V.

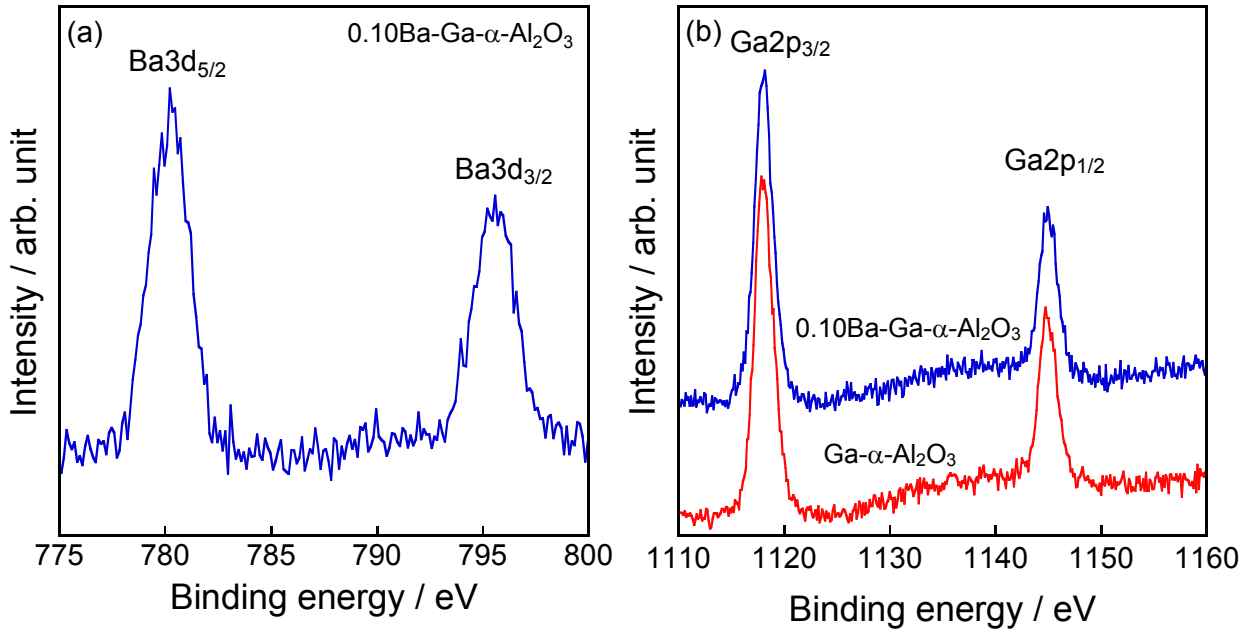

Figure 2.9. (a) Ba3d and (b) Ga2p spectra of Ga-α-Al_2O_3 and 0.10Ba-Ga-α-Al_2O_3. Reprinted from H. Seki *et al.*, *Appl. Catal. A: Gen.* **2019**, *581*, 23–30. Copyright 2019 Elsevier B. V.

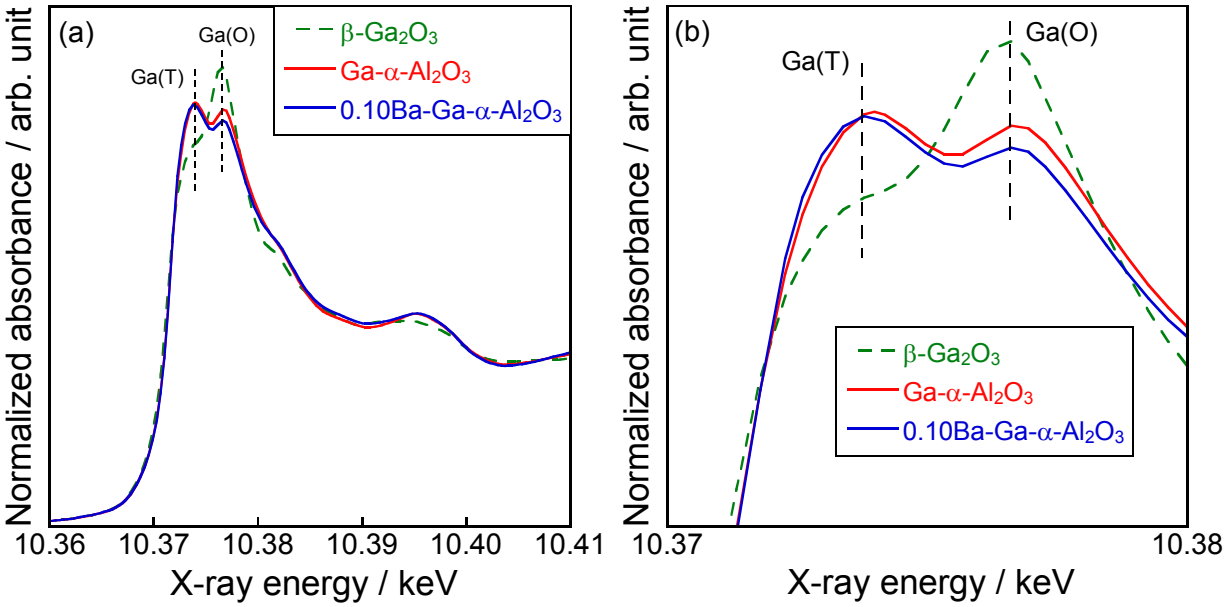

Figure 2.10. (a) Ga *K*-edge XANES spectra and (b) enlarged spectra of β-Ga_2O_3, Ga-α-Al_2O_3 and 0.10Ba-Ga-α-Al_2O_3. Ga(T) and Ga(O) represent tetrahedrally coordinated Ga and octahedrally coordinated Ga, respectively. Reprinted from H. Seki *et al.*, *Appl. Catal. A: Gen.* **2019**, *581*, 23–30. Copyright 2019 Elsevier B. V.

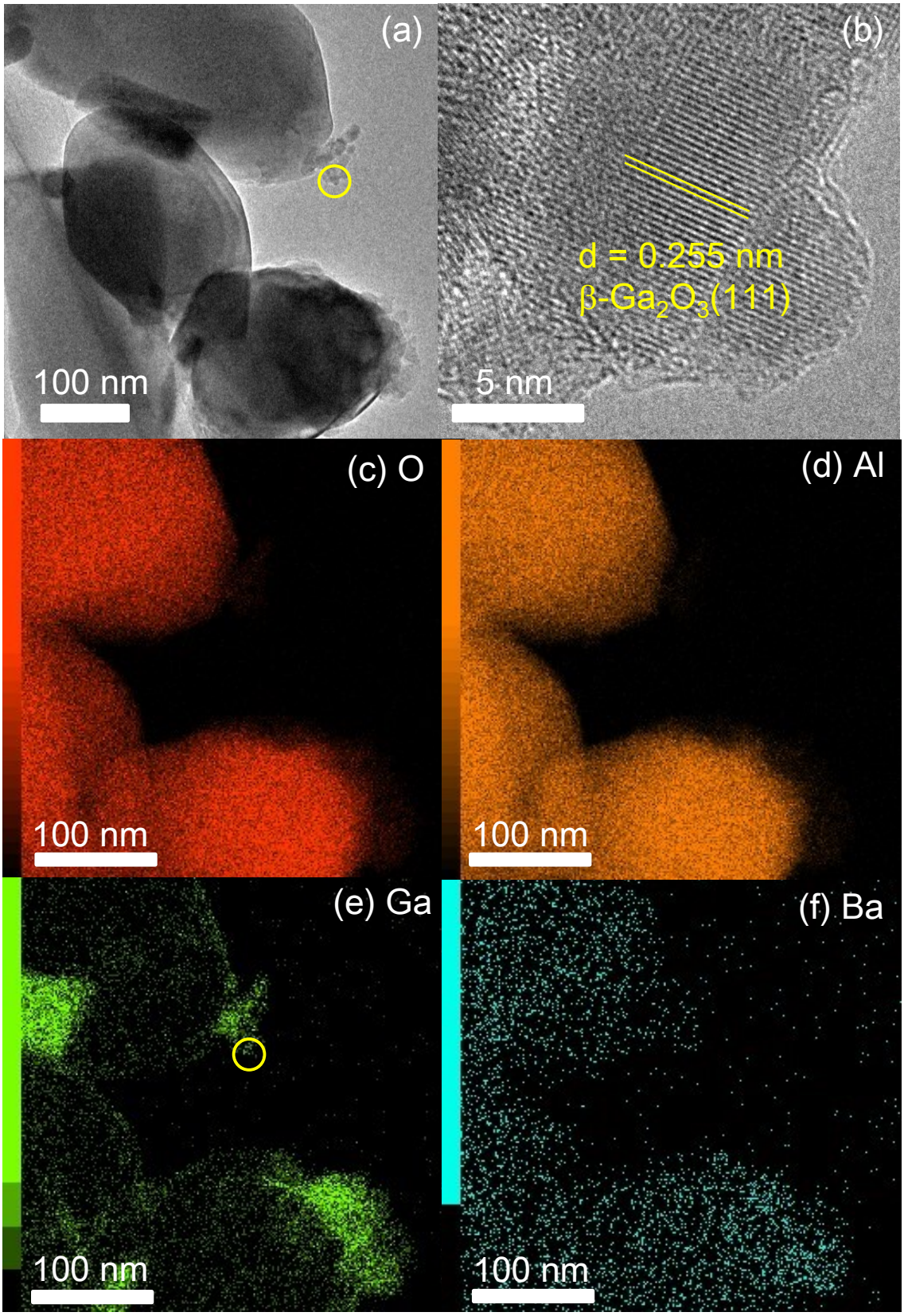

Figure 2.11. (a), (b) TEM images of 0.10Ga-Ba-α-Al_2O_3 and EDX mappings for (c) oxygen, (d) aluminum, (e) gallium and (f) barium. The enlarged spot corresponded to the image (b) is enclosed in the yellow circles. Reprinted from H. Seki *et al.*, *Appl. Catal. A: Gen.* **2019**, *581*, 23–30. Copyright 2019 Elsevier B. V.

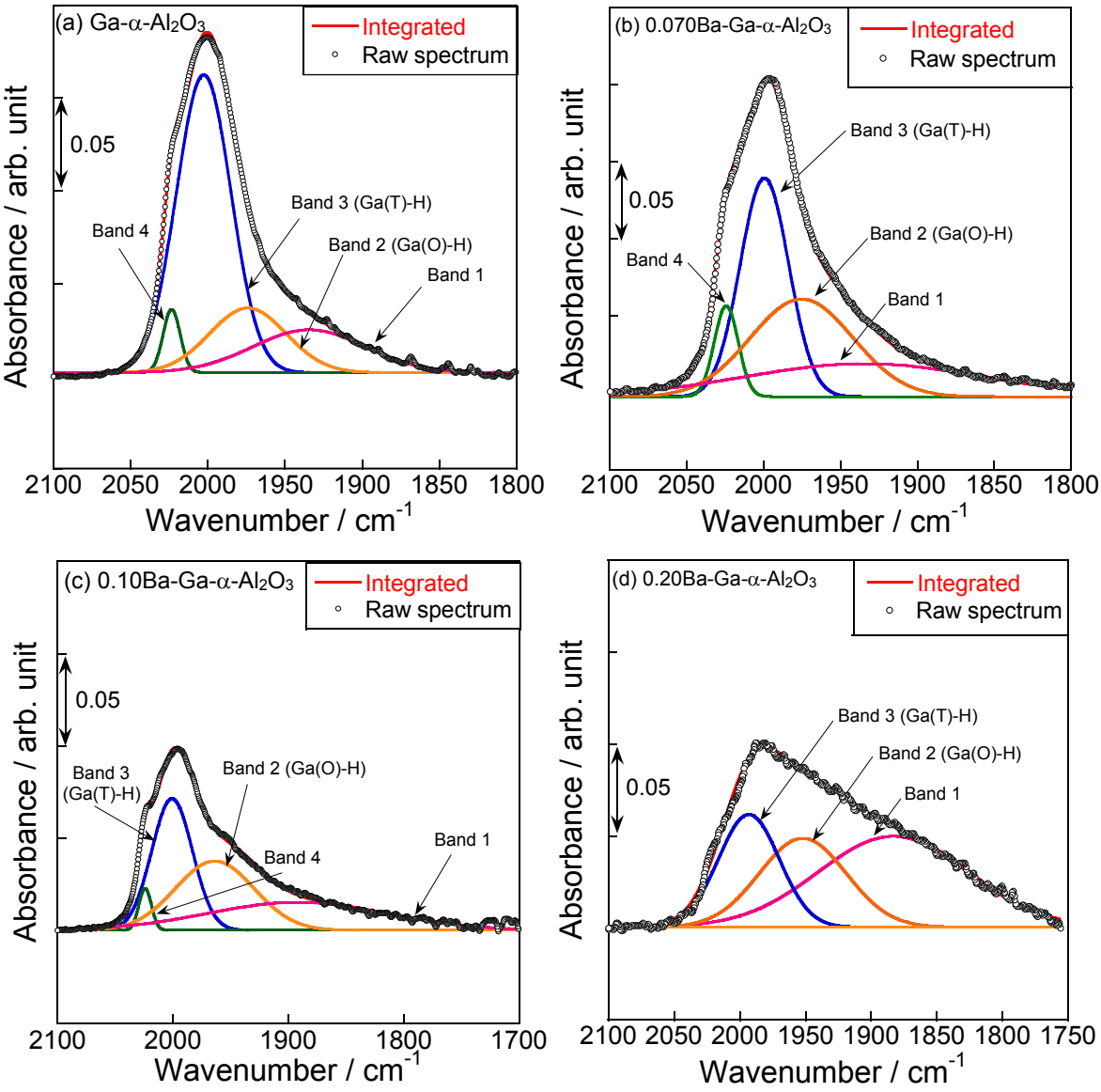

Figure 2.12. Subtracted FT-IR spectra of hydrogen dissociative adsorption over (a) Ga-α-Al_2O_3, (b) 0.070Ba-Ga-α-Al_2O_3, (c) 0.10Ba-Ga-α-Al_2O_3 and (d) 0.20Ba-Ga-α-Al_2O_3. Reprinted from H. Seki *et al.*, *Appl. Catal. A: Gen.* **2019**, *581*, 23–30. Copyright 2019 Elsevier B. V.

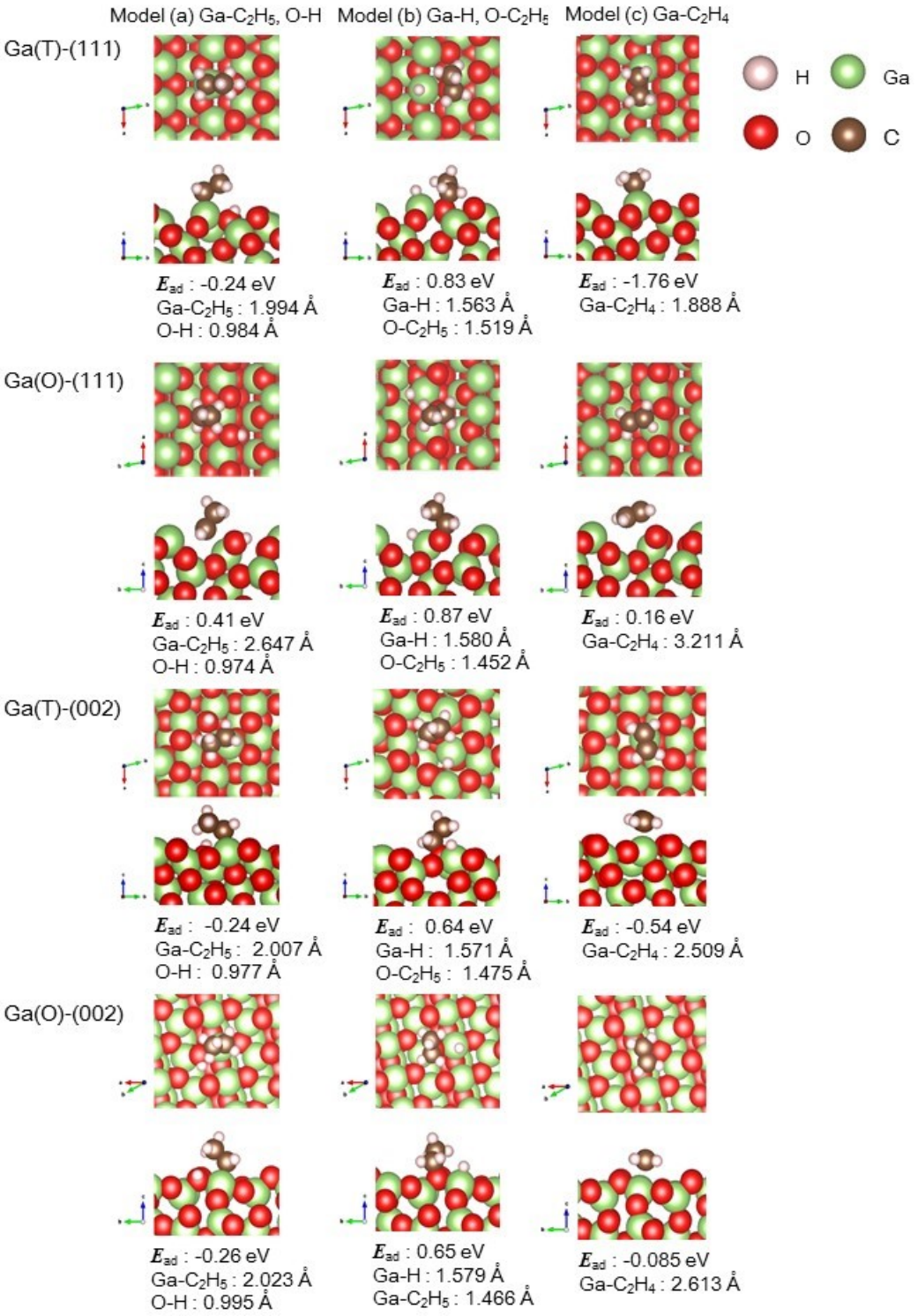

Figure 2.13. Ethane and ethylene adsorption models over Ga(T)-(111), Ga(O)-(111), Ga(T)-(002) and Ga(O)-(002) after structure optimization ((a) Ga-C_2H_5, O-H, (b) Ga-H, O-C_2H_5 and (c) Ga-C_2H_4). Reprinted from H. Seki *et al.*, *Appl. Catal. A: Gen.* **2019**, *581*, 23–30. Copyright 2019 Elsevier B. V.

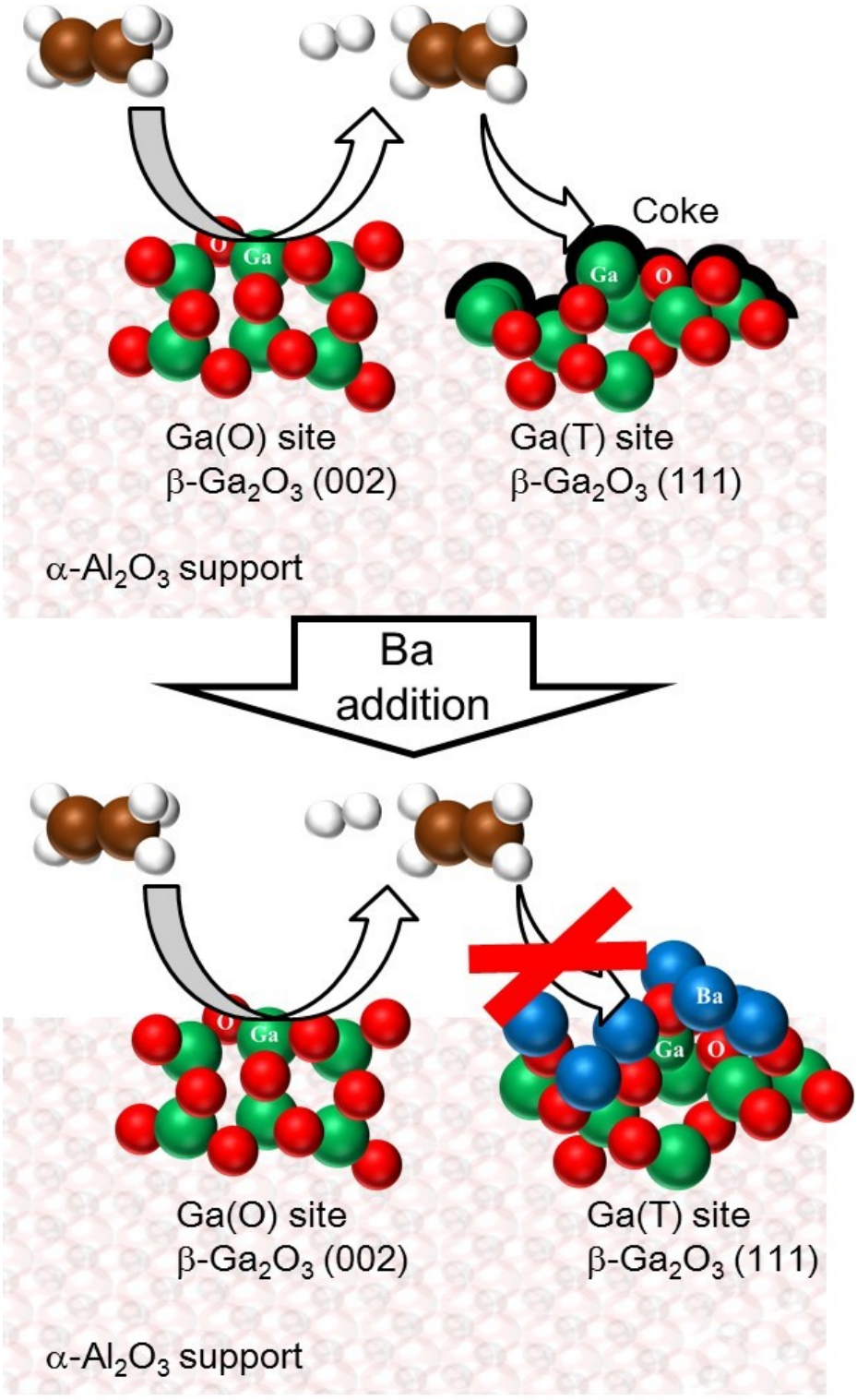

Figure 2.14. Schematic image of effect of Ba addition on surface Ga sites for dehydrogenation of ethane. Reprinted from H. Seki *et al.*, *Appl. Catal. A: Gen.* **2019**, *581*, 23–30. Copyright 2019 Elsevier B. V.

Table 2.1. Metal precursors of second metals. Reproduced from H. Seki *et al.*, *Appl. Catal. A: Gen.* **2019**, *581*, 23–30. Copyright 2019 Elsevier B. V.

Metal	Precursor
Mn	$Mn(NO_3)_2 \cdot 6H_2O$
Fe	$Fe(NO_3)_3 \cdot 9H_2O$
Co	$Co(NO_3)_2 \cdot 6H_2O$
Ni	$Ni(NO_3)_2 \cdot 6H_2O$
Cu	$Cu(NO_3)_2 \cdot 3H_2O$
Sr	$Sr(NO_3)_2$
Zr	$ZrO(NO_3)_2 \cdot 2H_2O$
Mo	$(NH_4)_6Mo_7O_{24} \cdot 4H_2O$
Sn	$C_4H_6O_4Sn$
Ba	$Ba(NO_3)_2$
La	$La(NO_3)_3 \cdot 6H_2O$
Ce	$Ce(NO_3)_3 \cdot 6H_2O$
W	$(NH_4)_6H_2W_{12}O_{40} \cdot x\,H_2O$
Bi	$Bi(NO_3)_3 \cdot 5H_2O$

Table 2.2. Catalytic activities and C_2H_4 selectivity over M-α-Al_2O_3 catalysts (M = Ga, In, Ge and Sn). Reproduced from H. Seki *et al.*, *Appl. Catal. A: Gen.* **2019**, *581*, 23–30. Copyright 2019 Elsevier B. V.

Catalyst	C_2H_4 formation rate / mmol g^{-1} h^{-1}	C_2H_4 selectivity / %
α-Al_2O_3	4.0	97.4
Ga-α-Al_2O_3	9.9	98.3
In-α-Al_2O_3	9.0	86.2
Ge-α-Al_2O_3	5.5	97.8
Sn-α-Al_2O_3	4.4	98.0

Table 2.3. Catalytic activities and products selectivity at 973 K over α-Al_2O_3, Ga-α-Al_2O_3 and 0.20M-Ga-α-Al_2O_3. Reproduced from H. Seki *et al.*, *Appl. Catal. A: Gen.* **2019**, *581*, 23–30. Copyright 2019 Elsevier B. V.

Catalyst	Conversion / %	Selectivity / %				C_2H_4 formation rate / mmol g^{-1} h^{-1}
		CO	CH_4	CO_2	C_2H_4	
α-Al_2O_3[a]	0.55 ± 0.03	0.79 ± 0.07	1.38 ± 0.00	0.00 ± 0.00	97.64 ± 0.03	2.39 ± 0.11
Ga-α-Al_2O_3[a]	0.76 ± 0.02	1.21 ± 0.36	2.16 ± 0.08	1.81 ± 0.35	94.50 ± 0.47	3.29 ± 0.08
Mn-Ga-α-Al_2O_3	0.51	1.12	2.69	3.52	92.41	2.19
Fe-Ga-α-Al_2O_3	0.84	3.41	5.82	8.63	81.40	3.33
Co-Ga-α-Al_2O_3	0.43	0.80	2.02	1.86	95.12	1.84
Ni-Ga-α-Al_2O_3	0.59	0.45	2.15	1.63	95.52	2.55
Cu-Ga-α-Al_2O_3	0.55	0.47	1.04	3.28	95.09	2.38
Sr-Ga-α-Al_2O_3	0.41	0.20	2.03	1.02	96.59	1.78
Zr-Ga-α-Al_2O_3	0.39	0.96	4.48	5.32	88.88	1.64
Mo-Ga-α-Al_2O_3	0.36	3.15	2.33	1.43	92.70	1.52
Sn-Ga-α-Al_2O_3	0.38	0.88	1.89	1.94	95.09	1.63
Ba-Ga-α-Al_2O_3[a]	0.58 ± 0.01	0.09 ± 0.00	1.51 ± 0.07	0.00 ± 0.00	98.30 ± 0.07	2.55 ± 0.05
La-Ga-α-Al_2O_3	0.25	0.25	2.84	2.28	94.41	1.08
Ce-Ga-α-Al_2O_3	0.39	4.31	1.91	9.78	83.61	1.56
W-Ga-α-Al_2O_3	0.22	0.18	2.09	0.00	97.56	0.94
Bi-Ga-α-Al_2O_3	0.30	3.27	4.37	5.42	86.44	1.23

[a] Average values of three times of activity tests

Table 2.4. Catalyst properties of α-Al_2O_3, *x*Ba-Ga-α-Al_2O_3 (*x* = 0, 0.070, 0.10, 0.20, 0.33 and 1.0) and Ba-α-Al_2O_3. Reproduced from H. Seki *et al.*, *Appl. Catal. A: Gen.* **2019**, *581*, 23–30. Copyright 2019 Elsevier B. V.

Catalyst	BET surface area / m^2 g^{-1}	Loading amount / wt%		Ba/Ga molar ratio / —
		Ga	Ba	
α-Al_2O_3	6.0	—	—	—
Ga-α-Al_2O_3	4.1	4.54	—	—
0.070Ba-Ga-α-Al_2O_3	6.8	4.56	0.783	0.0872
0.10Ba-Ga-α-Al_2O_3	5.8	4.69	0.974	0.106
0.20Ba-Ga-α-Al_2O_3	6.9	4.45	1.85	0.212
0.33Ba-Ga-α-Al_2O_3	7.0	4.34	2.62	0.307
1.0Ba-Ga-α-Al_2O_3	5.6	4.31	9.35	1.10
Ba-α-Al_2O_3	6.9	—	3.78	—

Table 2.5. Catalytic activities and products selectivity over α-Al_2O_3, Ga-α-Al_2O_3, *x*Ba-Ga-α-Al_2O_3 (*x* = 0.070, 0.10, 0.20, 0.33 and 1.0) and Ba-α-Al_2O_3. Reproduced from H. Seki *et al.*, *Appl. Catal. A: Gen.* **2019**, *581*, 23–30. Copyright 2019 Elsevier B. V.

Catalyst	Conversion / %	Selectivity / %				C_2H_4 formation rate / mmol g^{-1} h^{-1}
		CO	CH_4	CO_2	C_2H_4	
α-Al_2O_3[a]	0.55 ± 0.03	0.79 ± 0.07	1.38 ± 0.00	0.00 ± 0.00	97.64 ± 0.03	2.39 ± 0.11
Ga-α-Al_2O_3[a]	0.76 ± 0.02	1.21 ± 0.36	2.16 ± 0.08	1.81 ± 0.35	94.50 ± 0.47	3.29 ± 0.08
0.070Ba-Ga-α-Al_2O_3[a]	0.87 ± 0.09	0.11 ± 0.04	1.78 ± 0.01	0.19 ± 0.10	97.93 ± 0.09	3.84 ± 0.37
0.10Ba-Ga-α-Al_2O_3[a]	0.97 ± 0.04	0.42 ± 0.08	1.45 ± 0.16	0.16 ± 0.16	97.91 ± 0.18	4.19 ± 0.22
0.20Ba-Ga-α-Al_2O_3[a]	0.58 ± 0.01	0.09 ± 0.00	1.51 ± 0.07	0.00 ± 0.00	98.30 ± 0.07	2.55 ± 0.05
0.33Ba-Ga-α-Al_2O_3	0.48	0.14	1.28	0.00	98.44	2.10
1.0Ba-Ga-α-Al_2O_3	0.44	0.20	1.45	0.62	97.60	1.91
Ba-α-Al_2O_3	0.52	0.10	1.18	0.00	98.65	2.29

[a] Average values of three times of activity tests

Table 2.6. BET surface area of fresh and spent 0.10Ba-Ga-α-Al_2O_3. Reproduced from H. Seki *et al.*, *Appl. Catal. A: Gen.* **2019**, *581*, 23–30. Copyright 2019 Elsevier B. V.

Catalyst	BET surface area / m^2 g^{-1}
Fresh 0.10Ba-Ga-α-Al_2O_3	5.8
Spent 0.10Ba-Ga-α-Al_2O_3[a]	6.6

[a] The spent catalyst was obtained after the activity tests at 973 K for 3 h.

Table 2.7. The amount of carbon deposition on α-Al_2O_3, Ga-α-Al_2O_3 and 0.10Ba-Ga-α-Al_2O_3 after ethane dehydrogenation at 1073 K for 24 h or ethylene decomposition at 1073 K for 7 h. Reproduced from H. Seki *et al.*, *Appl. Catal. A: Gen.* **2019**, *581*, 23–30. Copyright 2019 Elsevier B. V.

Catalyst	The amount of carbon deposition / mg g_{cat}^{-1}	
	Ethane	Ethylene
α-Al_2O_3	n.d.	—
Ga-α-Al_2O_3	20.6	196.3
0.10Ba-Ga-α-Al_2O_3	n.d.	n.d.

Table 2.8. Concentration of O, Al, Ga and Ba in 0.10Ba-Ga-α-Al_2O_3 quantified by EDX. Reproduced from H. Seki *et al.*, *Appl. Catal. A: Gen.* **2019**, *581*, 23–30. Copyright 2019 Elsevier B. V.

Element	Edge	Energy / keV	Content	
			/ wt%	/ atom%
O	*K*	0.525	54.22	67.69
Al	*K*	1.486	42.35	31.35
Ga	*K*	9.241	3.23	0.92
Ba	*L*	4.465	0.21	0.03

Table 2.9. Deconvolution of absorption band for H_2 adsorption in the IR spectra (Figure 2.12). Reproduced from H. Seki *et al.*, *Appl. Catal. A: Gen.* **2019**, *581*, 23–30. Copyright 2019 Elsevier B. V.

Catalyst	Number of band	Wavenumber / cm^{-1}	Area / —	Area3/Area2 / —
Ga-α-Al_2O_3	1	1934	2.11	3.30
	2	1974	2.16	
	3	2003	7.13	
	4	2024	0.47	
0.070Ba-Ga-α-Al_2O_3	1	1934	4.19	1.06
	2	1975	5.30	
	3	1999	5.63	
	4	2024	1.15	
0.10Ba-Ga-α-Al_2O_3	1	1892	2.92	0.98
	2	1964	3.19	
	3	2001	3.14	
	4	2024	0.31	
0.20Ba-Ga-α-Al_2O_3	1	1883	7.09	0.89
	2	1951	4.00	
	3	1992	3.56	
	4	—	—	

Table 2.10. Adsorption energy of ethane or ethylene on Ga(T)-(111), Ga(O)-(111), Ga(T)-(002) and Ga(O)-(002) sites. Reproduced from H. Seki *et al.*, *Appl. Catal. A: Gen.* **2019**, *581*, 23–30. Copyright 2019 Elsevier B. V.

Site	Adsorption energy / eV		
	Ga-C_2H_5, O-H	Ga-H, O-C_2H_5	Ga-C_2H_4
Ga(T)-(111)	-0.24	0.83	-1.76
Ga(O)-(111)	0.41	0.87	0.16
Ga(T)-(002)	-0.24	0.64	-0.54
Ga(O)-(002)	-0.26	0.65	-0.085

Appendix of Chapter 2: Structure and activity of Ga catalysts supported on transition alumina

A2.1. Experimental

A2.1.1. Catalyst preparation

The γ-Al_2O_3 powder (JRC-ALO-6; Catalyst Society of Japan) was used as the catalyst support. Ga loading was conducted by the impregnation method described in section 2.2.1. After the impregnation, the obtained powder was calcined at 1323 or 1573 K for 3 h in a static air. Catalysts are denoted as Ga-Al_2O_3(1573pc + *x* c). We describe the calcination conditions in the parenthesis. The pre-calcination (pc) temperature before the impregnation is shown in case of α-Al_2O_3 as a support, because α-Al_2O_3 was obtained by the calcination of γ-Al_2O_3 at 1573 K. Then, the calcination temperature after the impregnation is denoted as *x* in the parenthesis. No expression for the pre-calcination condition is shown when γ-Al_2O_3 was used for impregnation.

A2.1.2. Catalytic activity tests

Catalytic activity was evaluated basically under the same conditions described in section 2.2.2. Briefly, a catalyst (100 mg) was sieved to 355–500 μm particles and was charged into the reactor with SiC (392 mg). After the furnace was heated to 973 K in a N_2 flow, the reaction gas composed of C_2H_6 : H_2O : N_2 = 1.0 : 1.4 : 5.5 at a total flow rate of 281.6 mL min^{-1} (SATP). Ethane conversion and selectivity to each product were calculated on the basis of equations (2.1) and (2.2).

A2.1.3. Characterizations

XRD, nitrogen adsorption, TEM and *ex-situ* Ga *K*-edge XAFS measurements were conducted under the same conditions described in section 2.2.3.

A2.1.4. Computational method

Plane wave basis pseudopotential calculations were implemented in the CASTEP code[1] to simulate Ga *K*-edge XANES spectra. The exchange correlation function was Perdew-Burke-Ernzerhof (PBE) out of the generalized gradient approximation (GGA). Ultrasoft pseudopotentials were used. The plane wave cutoff energy ($\boldsymbol{E}_{cut}$) was taken as 630 eV. The *k*-point separation in the Monkhorst–Pack reciprocal space was set as approximately 0.07 $Å^{-1}$. For comparison with the experimental spectra, the theoretical spectra were broadened using Gaussian and Lorentzian parameters set respectively as 0.2 eV and 0.4 eV. Details of spectrum calculation are given in the literature.[2] In the pseudopotential method, the transition energy cannot be obtained in cases where only valence

electrons are considered in all energy. It is also necessary to evaluate the core electron contribution. Details of transition energy calculations were described in an earlier report.[3]

A2.2. Results and discussion

A2.2.1. Effects of calcination temperature

To improve the catalytic performance of Ga-α-Al_2O_3 as presented in Table 2.1, catalysts were prepared using γ-Al_2O_3 as a support, which has much higher specific surface area than α-Al_2O_3. To ascertain whether Al–Ga solid solution is suitable or not for the purpose, the Ga catalysts supported on α-Al_2O_3 or γ-Al_2O_3 were calcined at 1573 K to form the solid solution. Results are presented in Figure A2.1. The ethylene formation rate tended to decrease irrespective of calcination temperature when α-Al_2O_3 was used as a support. Ga-Al_2O_3(1573pc+1323c), which corresponded to Ga-α-Al_2O_3 exhibited higher ethylene formation rate than the catalyst calcined at 1573 K. On the other hand, a high catalytic activity and stability were observed over Ga-Al_2O_3(1323c). In the case of Ga-Al_2O_3(1573c), the ethylene formation rate was low, but no decrease in catalytic activity was observed with time on stream. Although it is effective to use γ-Al_2O_3 as a support, no improvement could be observed over bare Al_2O_3(1323c). The catalytic activity of Al_2O_3(1323c) was the same level to that of Al_2O_3(1573c). Therefore, it should be considered that Ga species is important for the active sites and the high specific surface area of the support is only important for the dispersion of Ga.

For Ga-Al_2O_3(1573pc+1323c), the ethylene formation rate rapidly decreased with time on stream. In this reaction system, carbon deposition, sintering of Ga, and poisoning by the strong adsorption of hydrocarbons are regarded as factors to lower the catalytic activity. Carbon deposition is negligible in this study as mentioned above. Here, to assess the possibility of poisoning by the strong adsorption of hydrocarbons, N_2 purging was conducted after the reaction, then, the ethylene formation rate was measured. Results are presented in Table A2.1. The catalytic activities of Ga-Al_2O_3(1573pc+1323c) and Ga-Al_2O_3(1573pc+1573c) were regenerated by N_2 purging. Therefore, deactivation over these catalysts would be derived from the surface adsorption of hydrocarbons.

A2.2.2. Evaluation of apparent activation energy

Ga-Al_2O_3(1323c) showed better performance than the other catalysts in this work. To elucidate the causes of its high performance, catalytic activity tests were conducted at various temperatures (953–1033 K) for Ga-Al_2O_3(1323c) catalyst and α-Al_2O_3 (i.e. Al_2O_3 (1573c)) as a model of AFFTALLOY to measure the apparent activation energy ($\boldsymbol{E}_a$). Arrhenius plots for both catalysts are shown in Figure A2.2. Based on the results, $\boldsymbol{E}_a$ of the gas phase reaction (*i.e.* over bare alumina without Ga) was 283.7 kJ mol^{-1} and $\boldsymbol{E}_a$ of the surface reaction with Ga was 211.4 kJ mol^{-1}. These results show that coating Ga on the AFTALLOY can lower the reaction temperature drastically.

A2.2.3. Structural characterizations

To evaluate the crystalline structure of the supported-Ga catalysts, XRD was conducted for Ga-Al_2O_3(1573pc+1323c), Ga-Al_2O_3(1573pc+1573c), Ga-Al_2O_3(1323c) and Ga-Al_2O_3(1573c). Results are portrayed in Figure A2.3. From the results, only Ga-Al_2O_3(1323c) showed θ-Al_2O_3 structure. The others showed α-Al_2O_3 phase. Peaks for Ga species were not detected, indicating that Ga species exist on the catalyst with highly dispersed.

To evaluate the effects of the specific surface area of the support on the catalytic activity, we measured BET surface area of the catalyst as presented in Table A2.2. BET surface area of Ga-Al_2O_3(1323c) was 49.3 m^2 g^{-1}, which is 10 times higher than that of the other catalysts, by virtue of θ-Al_2O_3.

As presented in Figure A2.1, Ga-Al_2O_3(1323c) showed the high ethylene formation rate and stability, but the catalytic activity of Ga-Al_2O_3(1573pc+1323c), Ga-Al_2O_3(1573pc+1573c) decreased with time on stream. To identify the factors for this difference in stability, HAADF images and EDX mappings were observed by FE-TEM. Figure A2.4(a) presents HAADF images and EDX mappings of Ga-Al_2O_3(1323c), Ga-Al_2O_3(1573pc+1323c), Ga-Al_2O_3(1573c) and Ga-Al_2O_3(1573pc+1573c). Ga was agglomerated on Ga-Al_2O_3(1573pc+1323c), whereas Ga was highly dispersed on Ga-Al_2O_3(1323c). No significant difference was observed in the dispersion of Ga even when the catalyst were calcined at 1573 K. Sintering was not observed by high temperature calcination. Figure A2.4(b) presents the results of HAADF and EDX of Ga-Al_2O_3(1323c) and Ga-Al_2O_3(1573pc+1323c) after the reaction. In comparison with Figure A2.4(a), the dispersion of Ga did not change after the reaction in both cases.

A2.2.4. Coordination environment of Ga species

To investigate the coordination environment and the electronic state of Ga species on Ga-Al_2O_3 (*x* c) catalysts, Ga *K*-edge XANES spectra were measured. Figure A2.5(a) depicts experimental Ga *K*-edge XANES spectra for Ga-Al_2O_3(1323c), Ga-Al_2O_3(1573c) and reference samples of β-Ga_2O_3 and α-Ga_2O_3. Figure A2.5(b) portrays the calculated spectra for α-Ga_2O_3, β-Ga_2O_3, α-Ga_2O_3(Al-rep), and β-Ga_2O_3(Al-rep) with *ab initio* calculations. The description "Al-rep" means the replacement of one of the nearest Ga cations with an Al cation. Comparing the experimental spectra with the calculated ones, the peak position of Ga-Al_2O_3(1323c) was similar to that of the calculated spectrum of β-Ga_2O_3. However, the peak intensity of the low transition energy (10373 eV) is higher than that of the high transition energy (10378 eV).[4] It is known that β-Ga_2O_3 is the only stable phase[5] and it contains two kinds of Ga, tetrahedral Ga and octahedral Ga, in its structure.[6] Thus, we calculated XANES spectra of tetrahedral Ga and octahedral Ga as shown in Figure A2.5(b) because we suppose that the difference between the experimental and theoretical spectra is derived from the coordination environment of Ga. As shown Figure A2.5(b), tetrahedral Ga in β-Ga_2O_3 showed relatively low peak position (10413 eV). Therefore, it is considered that

the amount of tetrahedral Ga is larger than that of octahedral Ga in the Ga-Al_2O_3(1323c) catalyst. The spectrum of Ga-Al_2O_3(1573c) resembles the calculated spectrum of α-Ga_2O_3. The experimental spectrum of α-Ga_2O_3 did not fit the calculated spectrum of α-Ga_2O_3 because it might contain an amorphous phase as a result of the low calcination temperature in preparation of α-Ga_2O_3. As shown in Figure A2.5(c), the transition energy of Ga-Al_2O_3(1573c) is higher than that of the α-Ga_2O_3. The transition energy of Ga-Al_2O_3(1323c) is higher than the that of the β-Ga_2O_3. As shown in Figure A2.5(d), the Al-substituted samples such as α-Ga_2O_3(Al-rep) and β-Ga_2O_3(Al-rep) have higher transition energy than those of α-Ga_2O_3 and β-Ga_2O_3 respectively. Therefore, the shift of the transition energy indicates the existence of Al near Ga because the coordination environment of Ga in Ga-Al_2O_3(1573c) and Ga-Al_2O_3(1323c) includes the Al–Ga solid solution.

The XANES spectra revealed that the crystalline structure of Ga was influenced by the calcination temperature. The structure of Ga, which is close to β-Ga_2O_3 in the Ga-Al_2O_3(1323c) catalyst and is near α-Ga_2O_3 when the catalyst calcined at 1573 K, affect the catalytic activity strongly. Some reports described that tetrahedral Ga shows high catalytic activity for dehydrogenation of propane.[7–9] As shown in Figure A2.6, the shape of the XANES spectra suggests that the proportion of tetrahedral Ga increased by forming Al-Ga solid solution. Therefore, this increase can be regarded as one reason for obtaining the high catalytic performance. On the other hand, the structure of Ga on the catalyst calcined at 1573 K is close to α-Ga_2O_3, similar to the α-Al_2O_3 structure (the corundum structure). Accordingly, Ga in Ga-Al_2O_3(1573c) is regarded as having 6 coordination and it leads to the low catalytic activity. On the Ga-Al_2O_3(1323c) catalyst, it shows high activity because Ga is mainly existed in tetrahedral coordination state and it is highly dispersed, *i.e.* the high specific surface area of the active sites.

References

1. S. J. Clark, M. D. Segall, C. J. Pickard, P. J. Hasnip, M. J. Probert, K. Refson, M. C. Payne, First Principles Methods Using CASTEP. *Z. Kristallogr*., **2005**, *220*, 567–570. (2005).
2. S.-P. Gao, C. J. Pickard, M. C. Payne, J. Zhu, J. Yuan, Theory of Core-Hole Effects in **1*s*** Core-Level Spectroscopy of the First-Row Elements. *Phys. Rev. B*, **2008**, *77*, 115122.
3. T. Mizoguchi, I. Tanaka, S.-P. Gao, C. J. Pickard, First-Principles Calculation of Special Features, Chemical Shift and Absolute Threshold of ELNES and XANES Using a Plane Wave Pseudopotential Method. *J. Phys. Condens. Matter*, 2009, **21**, 104204.
4. K. Nishi, K. Shimizu, M. Takamatsu, H. Yoshida, A. Satsuma, T. Tanaka, S. Yoshida, T. Hattori, Deconvolution Analysis of Ga K-Edge XANES for Quantification of Gallium Coordinations in Oxide Environments. *J. Phys. Chem. B* **1998**, *102*, 10190–10195.
5. R. Roy, V. G. Hill, E. F. Osborn, Polymorphism of Ga_2O_3 and the System Ga_2O_3–H_2O. *J. Am. Chem. Soc.* **1952**, *74*, 719–722.
6. S. Geller, Crystal Structure of β-Ga_2O_3. *J. Chem. Phys.* **1960**, *33*, 676.

7. B. Zheng, W. Hua, Y. Yue, Z. Gao, Dehydrogenation of Propane to Propene over Different Polymorphs of Gallium Oxide. *J. Catal.* **2005**, *232*, 143−151.
8. M. Chen, J. Xu, F.-Z. Su, Y.-M. Liu, Y. Cao, H.-Y. He, K.-N. Fan, Dehydrogenation of Propane over Spinel-Type Gallia-Alumina Solid Solution Catalysts. *J. Catal.* **2008**, *256(10)*, 293–300.
9. M. Chen, J. Xu, Y.-M. Liu, Y. Cao, H.-Y. He, J.-H. Zhuang, K.-N. Fan, Enhanced Activity of Spinel-Type Ga_2O_3–Al_2O_3 Mixed Oxide for the Dehydrogenation of Propane in the Presence of CO_2. *Catal. Lett.* **2008**, *124*, 369–375.

Figures and Tables

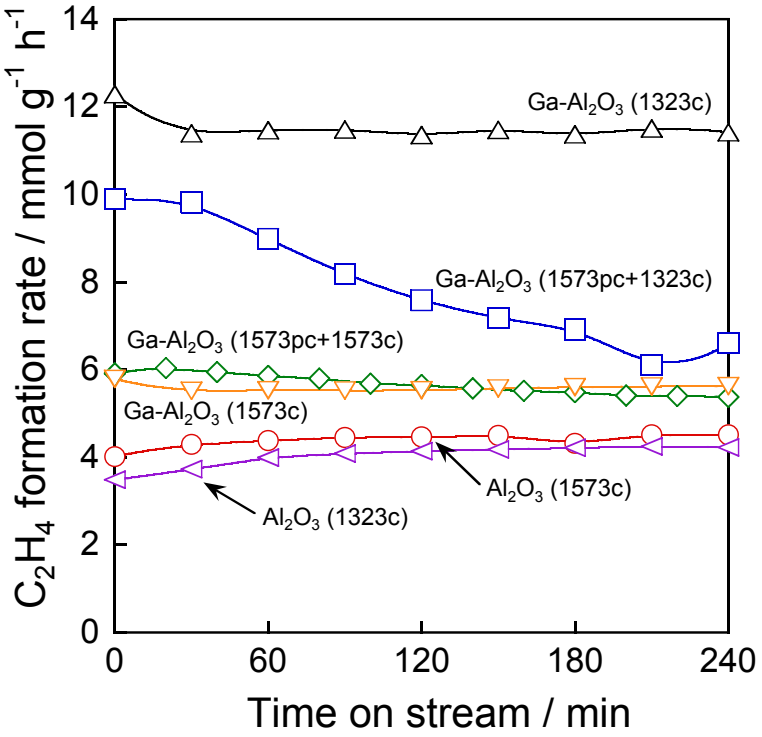

Figure A2.1. Ethylene formation rate at 973 K over various Ga catalysts. Reprinted with permission from H. Saito *et al.*, *J. Jpn. Petrol. Inst.* **2017**, *60*, 203–210. Copyright 2017 The Japan Petroleum Institute.

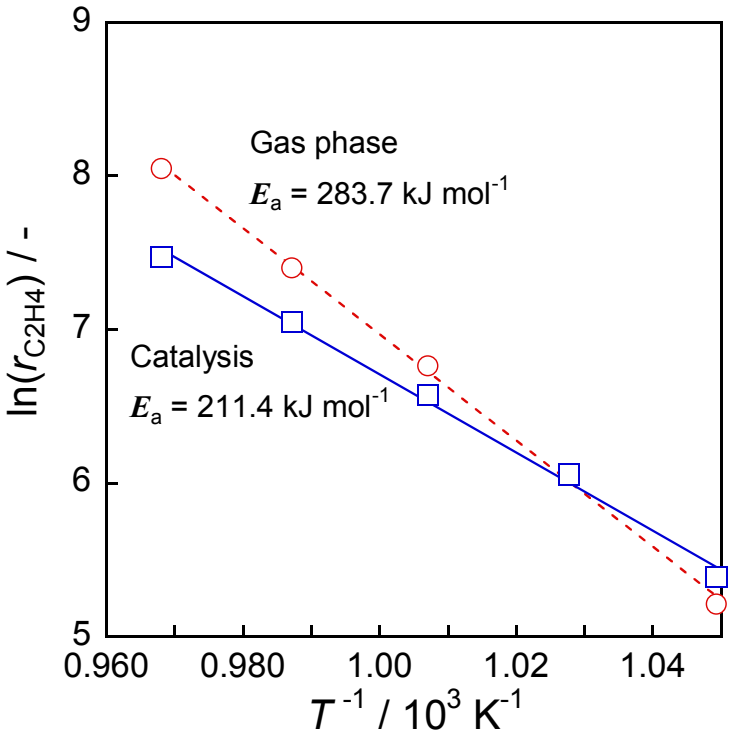

Figure A2.2. Arrhenius plots for dehydrogenation of ethane in the presence of steam over Ga-Al_2O_3(1323c) and Al_2O_3(1573c). Reprinted with permission from H. Saito *et al.*, *J. Jpn. Petrol. Inst.* **2017**, *60*, 203–210. Copyright 2017 The Japan Petroleum Institute.

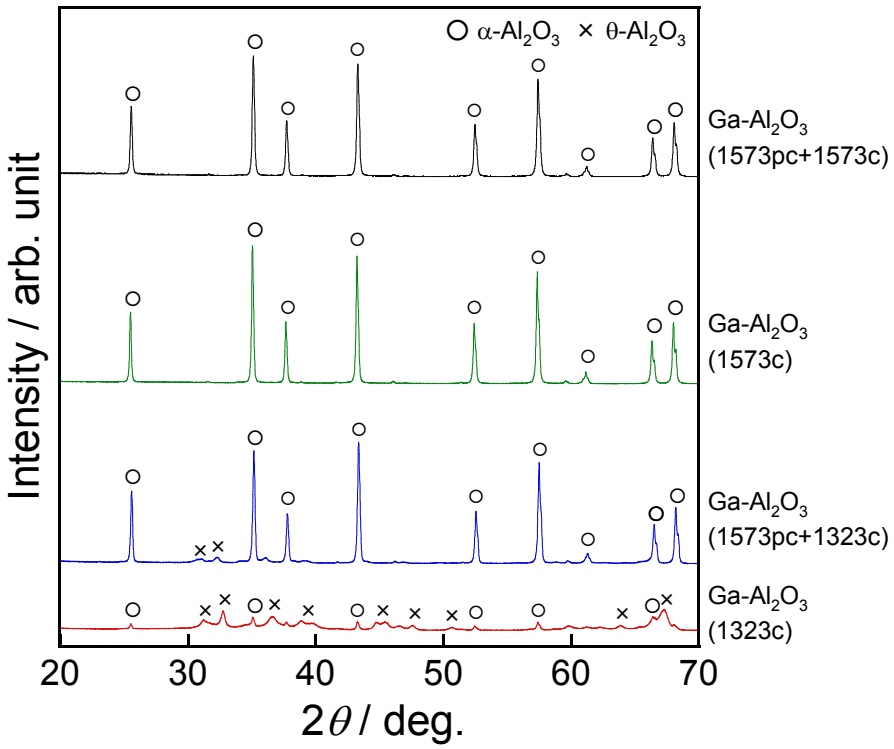

Figure A2.3. XRD patterns of Ga-Al_2O_3(1323c), Ga-Al_2O_3(1573pc+1323c), Ga-Al_2O_3(1573c) and Ga-Al_2O_3(1573pc+1573c). Reprinted with permission from H. Saito *et al.*, *J. Jpn. Petrol. Inst.* **2017**, *60*, 203–210. Copyright 2017 The Japan Petroleum Institute.

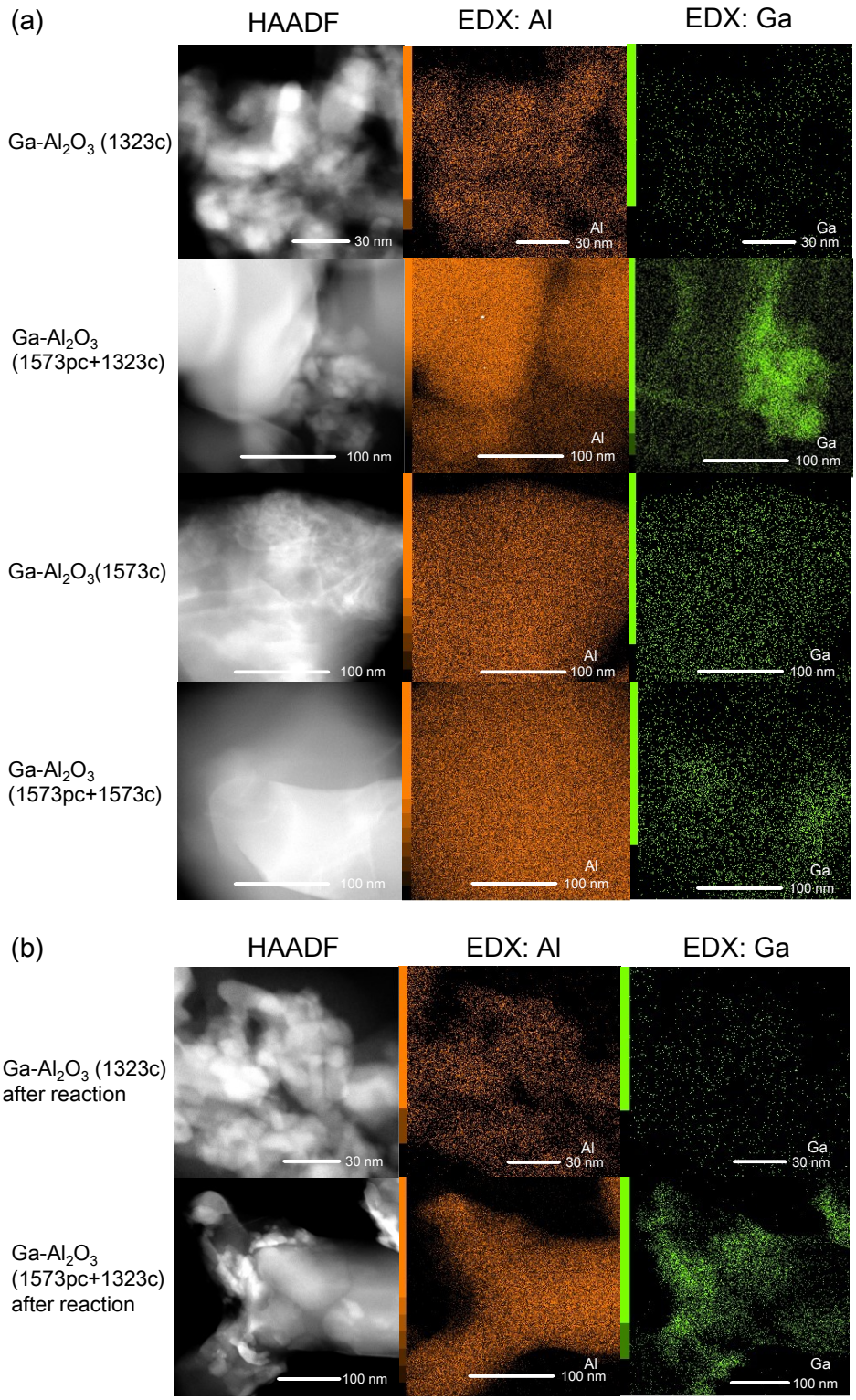

Figure A2.4. HAADF images and EDX mappings for (a) Ga-Al_2O_3 catalysts calcined at various temperatures and (b) Ga-Al_2O_3(1323c), Ga-Al_2O_3(1573pc+1323c) after the reaction. Reprinted with permission from H. Saito *et al.*, *J. Jpn. Petrol. Inst.* **2017**, *60*, 203–210. Copyright 2017 The Japan Petroleum Institute.

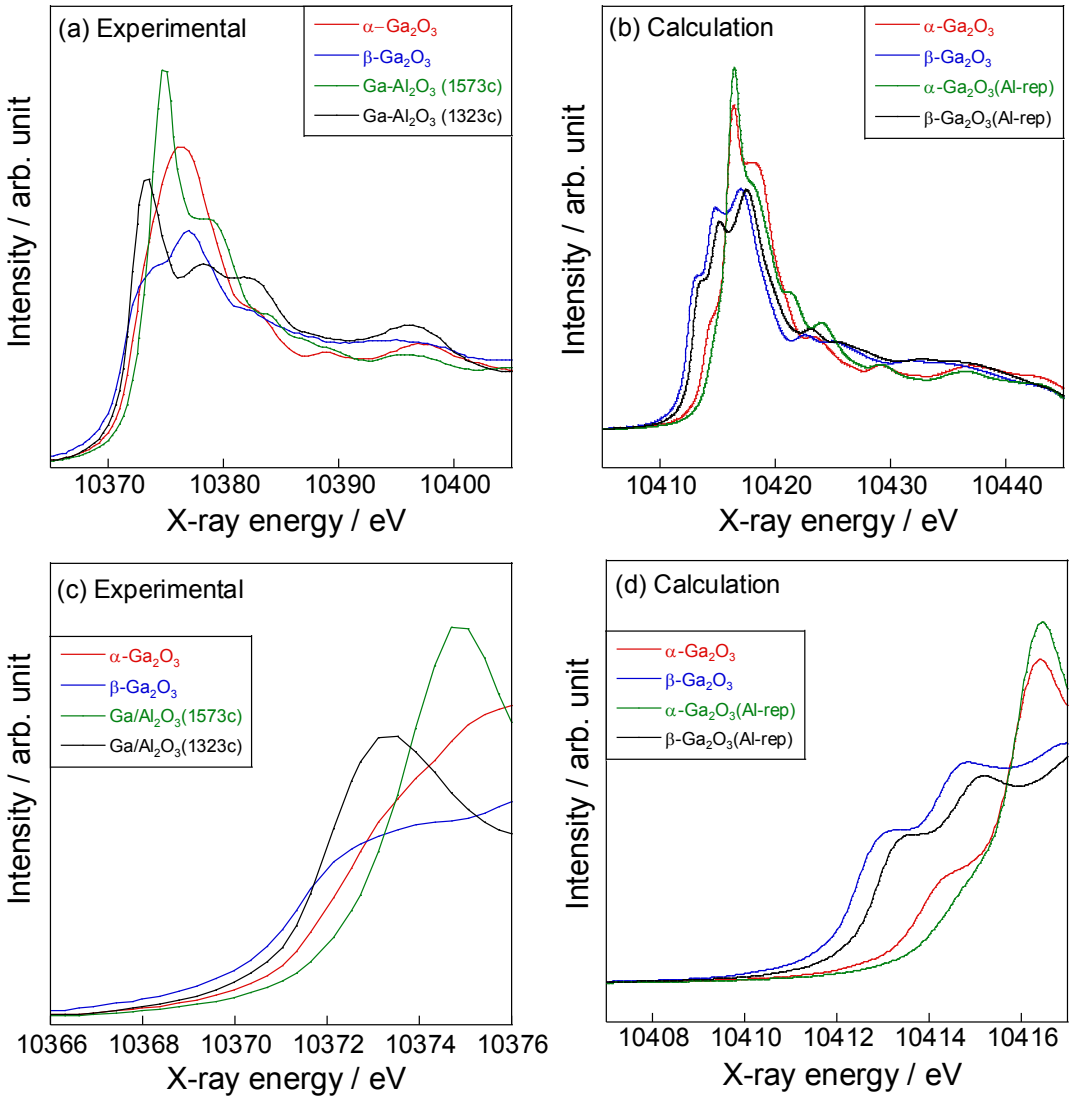

Figure A2.5. (a) Ga *K*-edge XANES spectra of Ga-Al_2O_3(1573c) and Ga-Al_2O_3(1323c). (b) calculated spectra of α-Ga_2O_3 and β-Ga_2O_3. (c), (d) enlarged spectra corresponded to (a) and (b), respectively. Reprinted with permission from H. Saito *et al.*, *J. Jpn. Petrol. Inst.* **2017**, *60*, 203–210. Copyright 2017 The Japan Petroleum Institute.

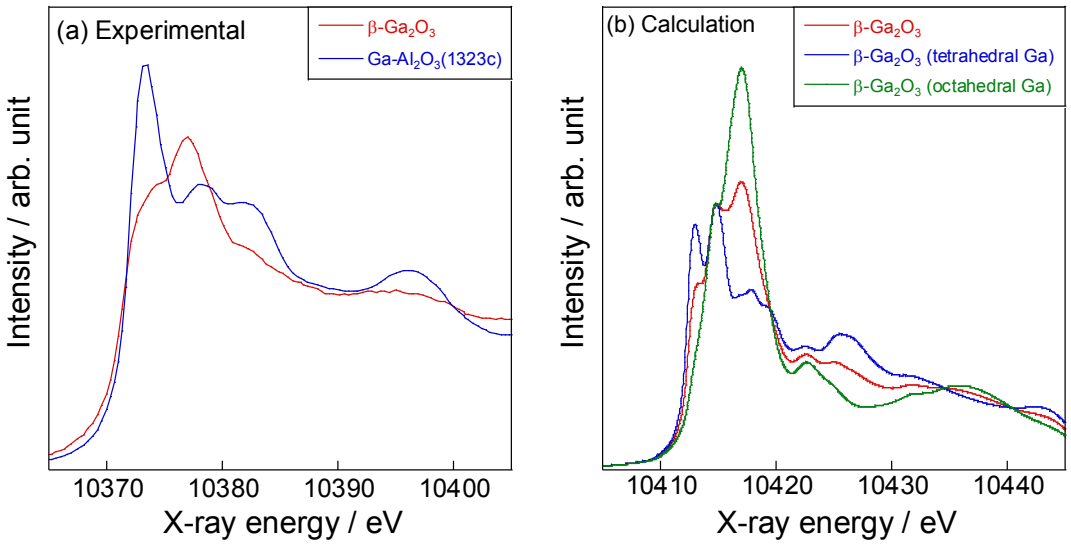

Figure A2.6. (a) Ga *K*-edge XANES spectra of β-Ga_2O_3 and Ga-Al_2O_3(1323c) and (b) comparison of experimental β-Ga_2O_3 spectra with calculated ones. Reprinted with permission from H. Saito *et al.*, *J. Jpn. Petrol. Inst.* **2017**, *60*, 203–210. Copyright 2017 The Japan Petroleum Institute.

Table A2.1. Catalyst regeneration by N_2 purge. Reproduced with permission from H. Saito *et al.*, *J. Jpn. Petrol. Inst.* **2017**, *60*, 203–210. Copyright 2017 The Japan Petroleum Institute.

Catalyst	Initial activity / mmol g^{-1} h^{-1}	Activity at 180 min / mmol g^{-1} h^{-1}	Initial activity after N_2 purge / mmol g^{-1} h^{-1}
Ga-Al_2O_3(1573pc+1573c)	6.0	5.6	5.9
Ga-Al_2O_3(1573pc+1323c)	9.8	6.9	8.1

Table A2.2. BET surface area of various Ga catalysts. Reproduced with permission from H. Saito *et al.*, *J. Jpn. Petrol. Inst.* **2017**, *60*, 203–210. Copyright 2017 The Japan Petroleum Institute.

Catalyst	BET surface area / m^2 g^{-1}
Ga-Al_2O_3(1323c)	49.3
Ga-Al_2O_3(1573pc+1323c)	5.5
Ga-Al_2O_3(1573c)	4.3
Ga-Al_2O_3(1573pc+1573c)	4.4

Chapter 3 Dehydrogenation of ethane over perovskite oxides in the presence of steam

3.1. Introduction

As described in the chapter 2, ethylene is an indispensable chemical in the modern world because it is a raw material for petrochemical products such as plastics, synthetic fibers, synthetic rubbers, and fertilizers.[1-3] Oxidative dehydrogenation of ethane is studied widely to produce ethylene at low reaction temperatures. Using O_2 as an oxidant, the reaction is exothermic and thermodynamically favorable to low reaction temperatures (673–873 K).[3,4] Various catalysts have been reported, including V-based oxides,[5,6] Ni-based oxides,[7,8] Mo-V-mixed oxides,[9,10] and alkali chlorides.[11] To obtain high ethylene yield, inhibition of the subsequent oxidation of ethylene to CO/CO_2 is necessary for the catalyst. Furthermore, removal of an adequate amount of heat prevents the process from being implemented on a large scale. To suppress the sequential conversion of ethylene, CO_2 is an alternative candidate for use as a mild oxidant. In the presence of CO_2, the reaction proceeds at around 923 K by virtue of the removal of H_2 from the reaction system through reverse water gas shift.[12] Studies of Cr-based and Ga-based oxides have been reported.[13–16] However, development of a suitable catalyst remains as a challenge impeding the activation of inert CO_2. As a consequence, oxidative dehydrogenation of ethane using O_2 or CO_2 has not been conducted on a practical scale.

From a practical perspective, the introduction of a catalyst for dehydrogenation of ethane to the steam cracking process has great feasibility compared with the oxidative dehydrogenation process. Some researchers investigated the dehydrogenation of ethane over Ga-based catalysts, [17–21] H_2 recombination and desorption are unfavorable because oxygen atoms next to Ga^{3+} cations have strong Lewis basicity. Hensen *et al.* demonstrated that coexistence of H_2O in the reaction system improved the catalytic activity of Ga/H-ZSM-5 for dehydrogenation of propane.[22] Results of their investigation suggest that desorption of H_2O proceeds rather than that of H_2 in dehydrogenation of ethane. Consequently, catalysts with redox properties are expected to be effective for dehydrogenation of ethane in the presence of H_2O. Hydrothermal resistance also requires the use of a catalyst in the steam cracking process. The previously described β-Ga_2O_3 and Ga/H-ZSM-5 catalysts are unsuitable for practical use because of their respective insufficient redox properties

and hydrothermal resistance. Perovskite oxide (ABO_3) is a promising material because of its high redox ability and hydrothermal stability.[23] Lattice oxygens in various perovskite oxides, especially La-based perovskite oxides, are known to contribute to the oxidation of hydrocarbons, including ethane, concomitantly with the formation of oxygen-defected sites in the perovskite oxides.[24–26] Reactive lattice oxygens in La-based perovskite oxides can be regenerated using H_2O as an oxidizing agent.[27–29] Dehydrogenation of ethane in the presence of H_2O through the Mars–van Krevelen (MvK) mechanism can be described as shown below.

$$C_2H_6 + O_{lat}^{2-} \rightarrow C_2H_4 + H_2O + V_O^{\cdot\cdot} + 2e^- \quad (3.1)$$

$$H_2O + V_O^{\cdot\cdot} + 2e^- \rightarrow H_2 + O_{lat}^{2-} \quad (3.2)$$

Herein, O_{lat}^{2-} and $V_O^{\cdot\cdot}$ are denoted respectively as the lattice oxygen and oxygen vacancy. Overall reaction is regarded as non-oxidative dehydrogenation of ethane using H_2O for regeneration of the lattice oxygens. Therefore, the reaction is completely different from oxidative dehydrogenation of ethane using O_2 although oxidative dehydrogenation over a V-based or Ni-based oxide catalyst proceeds *via* the MvK mechanism.[30–32]

To develop catalysts with a high activity for dehydrogenation of ethane in the presence of H_2O, we evaluated catalytic activities of $LaMO_3$ (M = Cr, Mn, Fe, Co and Ni) perovskite catalysts. In addition, a part of La sites in $LaMnO_3$, $LaFeO_3$, and $LaCoO_3$ was replaced with various alkaline earth metals (Ca, Sr and Ba) to enhance their redox ability. To elucidate the reaction mechanism, isotopic transient tests were conducted. The electronic state of Mn was investigated using X-ray analyses. Reducibility of Mn in the catalysts were evaluated by temperature programmed reduction using H_2 (H_2-TPR). These experiments have demonstrated that Ba-doped $LaMnO_3$ perovskite oxide showed higher activity on ethane dehydrogenation by the MvK mechanism.

3.2. Experimental

3.2.1. Catalyst preparation

La-based perovskite oxides were synthesized by a complex polymerization method. First, metal nitrates (Kanto Chemical Co., Inc.) were dissolved in distilled water. Then, citric acid and ethylene glycol (Kanto Chemical Co., Inc.) were added to the solution. The molar ratio of metal: citric acid: ethylene glycol was 1 : 3 : 3. The solution was stirred in a water bath at *ca.* 343 K for 16 h to promote polymerization. Subsequently, the solution was dried with a hot stirrer. The obtained powder was pre-calcined at 673 K for 2 h in static air, and then calcined at 1123 K for 10 h.

3.2.2. Catalytic activity tests

Dehydrogenation of ethane was conducted in a fixed bed flow reactor at atmospheric pressure. The catalyst was shaped and sieved to obtain fractions with a particle size of 425–825 μm. The sieved catalyst (100 mg) was mixed with SiC (*ca.* 392 mg) and charged into a quartz tube (i.d.: 4 mm, o.d.: 6 mm). The reaction gas composition was $C_2H_6 : H_2O : N_2 = 1.0 : 1.4 : 5.5$ at a total flow

rate of 143 mL min^{-1}. The catalyst was heated to 973 K with a ramp rate of 10 K min^{-1} under N_2 atmosphere before the reaction gas was fed to the reactor. Products including CH_4, CO, CO_2 and C_2H_4 were quantified by an online GC-FID (GC-8A; Shimadzu) equipped with a Porapak Q packed column and a methanizer (Ru/Al_2O_3 catalyst). Ethane conversion and selectivity to each product were calculated as follows.

$$\text{Ethane conversion [\%]} = \frac{r_{CO} + r_{CH_4} + r_{CO_2} + 2r_{C_2H_4}}{r_{CO} + r_{CH_4} + r_{CO_2} + 2r_{C_2H_4} + 2r_{C_2H_6}} \cdot 100 \quad (3.3)$$

$$\text{Selectivity [\%]} = \frac{n_p \cdot r_p}{r_{CO} + r_{CH_4} + r_{CO_2} + 2r_{C_2H_4}} \cdot 100 \quad (3.4)$$

Here, n and r denote the number or carbon atom and formation rate in outlet gas, respectively. Products were described in the subscripts. The subscript "p" in equation (3.4) means one of the products (CH_4, CO, CO_2 or C_2H_4).

Periodic dry-wet operation tests were performed to clarify release and regeneration of lattice oxygens. First, C_2H_6 and N_2 were fed to the reactor without H_2O (dry atmosphere). After the catalyst was purged in N_2, dehydrogenation was conducted in the presence of H_2O (wet atmosphere). These operations were repeated two times. During the reaction, conditions including temperature, contact time and partial pressure of ethane were the same as the standard activity test. Products were quantified using the on-line GC-FID. When D_2O was used instead of H_2O, H_2 (m/z = 2), HD (m/z = 3) and D_2 (m/z = 4) were detected with a quadruple mass spectrometer (HPR-20; Hiden Analytical Ltd.).

3.2.3. Characterizations

Powder X-ray diffraction (XRD) measurement was conducted with an X-ray diffractometer (Smart Lab-III; Rigaku) using Cu $K\alpha$ radiation at 40 kV and 40 mA.

The specific surface areas were calculated from nitrogen adsorption isotherm at 77 K by Brunauer-Emmett-Teller (BET) method (Gemini VII 2390a; Micromeritics Instrument). Prior to the measurements, samples were heated to 473 K for 2 h under N_2 atmosphere to remove adsorbates on the catalyst surface.

Temperature programmed reduction under H_2 atmosphere (H_2-TPR) was conducted to investigate reducibility of the fresh catalysts. H_2-TPR profiles were obtained using an automated catalyst analyzer (BELCAT II; MicrotracBEL) with a TCD. Prior to the measurement, a sample (*ca.* 100 mg) was oxidized at 873 K for 30 min in a 10vol% O_2/Ar flow at a flow rate of 50 mL min^{-1}. After the cooling to 323 K under the same atmosphere, Ar was fed to the sample for 10 min to remove physisorbed oxygen. Then, the sample was heated to 1173 K at a ramping rate of 10 K min^{-1} in a 5vol% H_2/Ar flow (50 mL min^{-1}).

Temperature programmed oxidation (TPO) was performed to quantify the amount of carbon deposition on the spent catalysts. TPO was conducted with thermogravimetry (TGA-50; Shimadzu). Prior to the measurement, a sample (*ca.* 30 mg) was heated to 873 K under Ar to

remove adsorbed species. After cooling to 323 K, the sample was heated to 1173 K at a ramping rate of 10 K min^{-1} under 5vol% O_2/Ar. The amount of carbon deposition was calculated on the basis of the weight loss.

The amount of reactive lattice oxygens was estimated by replacing a part of lattice $^{16}O^{2-}$ with $^{18}O^{2-}$ using $H_2{}^{18}O$. First, dehydrogenation of ethane was conducted for 1 h under the same conditions as the normal activity test except for the reaction gas composition. Ethane, $H_2{}^{16}O$ mixed with $H_2{}^{18}O$ ($H_2{}^{16}O$: $H_2{}^{18}O$ = 3 : 2), Ar, and balanced N_2 were fed to the reactor at a total flow rate of 143 mL min^{-1} (C_2H_6 : H_2O : Ar : N_2 = 1.0 : 1.4 : 1.1 : 4.4). After purging the catalyst with N_2 and decay of the $H_2{}^{18}O$ signal, the normal activity test was subsequently conducted for 1 h. $H_2{}^{18}O$ (*m/z* = 19) and Ar (*m/z* = 40) were detected with the quadruple mass spectrometer.

The electronic state of Mn in $LaMnO_3$ and $La_{1-x}Ba_xMnO_{3-\delta}$ (x = 0.1–0.4) was evaluated by *ex-situ* and *in-situ* Mn *K*-edge X-ray absorption fine structure (XAFS) at the BL14B2 beam line of SPring-8 in Japan. XAFS spectra were measured in transmission mode using Si(111) crystal monochromator. Prior to the measurements, each catalyst was mixed with BN, and then 7 mmϕ pellets for *ex-situ* measurements and 10 mmϕ pellets for *in-situ* measurements were formed. For the *ex-situ* measurements, XAFS spectra of samples including reference materials (MnO, MnO_2, Mn_2O_3, and Mn_3O_4) were measured at room temperature. *In-situ* XAFS measurements were performed at 973 K under reductive (C_2H_6/He) and oxidative (H_2O/He) conditions. The specific procedure for the *in-situ* XAFS measurements is shown in Figure 3.1. At the beginning, the pellet was heated to 973 K in helium at a ramp rate of 10 K min^{-1}, and a reference spectrum was measured. Then, 30% C_2H_6 and balanced He were fed to the sample (1st C_2H_6) and a XAFS spectrum was measured. Successively, 20vol% H_2O and balanced He were introduced (1st H_2O) and a XAFS spectrum was recorded. This cycle was continuously repeated again (2nd C_2H_6 and H_2O). X-ray absorption near-edge structure (XANES) spectra were analyzed with software (Demeter ver. 0.9.025; Bruce Ravel).

The electronic state of Mn in the catalysts was evaluated by X-ray photoelectron spectroscopy (XPS) with an XPS instrument (VersaProbeII; ULVAC-PHI). XPS measurements were conducted using Al *K*α X-ray source. The binding energy was calibrated with the C1s peak at 284.8 eV.

3.3. Results and discussion

3.3.1. Screening the effective catalyst for dehydrogenation of ethane

To develop a highly active catalyst for dehydrogenation of ethane using H_2O, prescreening tests were conducted for various La-based perovskite oxide catalysts. The A-site metal of the perovskite oxide (ABO_3) was fixed to La; then various transition metals belonging to the fourth period were tested for use as the B-site metal. The ethylene formation rate and ethylene selectivity over $LaMO_3$ (M = Cr, Mn, Fe, Co and Ni) perovskites are shown in Figure 3.2(a). Catalytic performance at 120 min with time on stream was compared to evaluate the catalytic performance under the steady state. All the catalytic performance including ethane conversion and selectivity to the other

products are summarized in Table 3.1. $LaFeO_3$ showed the highest ethane conversion (4.1%) among them, although its ethylene selectivity was low (69.2%). In addition to ethylene, formation of CO, CH_4, and CO_2 was verified, resulting in the comparable ethylene yield to $LaMnO_3$ and $LaCoO_3$. Then, 20% of La sites in $LaFeO_3$, $LaMnO_3$, and $LaCoO_3$ were replaced with alkaline earth metals (Ca, Sr, and Ba) to improve their redox properties because the partial substitution of alkaline earth metals for La is an effective means of enhancing redox properties.[26–28] Catalytic activities and ethylene selectivity over $La_{0.8}A_{0.2}MO_{3-\delta}$ (A = Ca, Sr and Ba; M = Mn, Fe and Co) are presented in Figure 3.2(b). Ethane conversion and selectivity to the by-products are presented in Table 3.2. The catalytic performance of $La_{0.8}Ba_{0.2}MnO_{3-\delta}$ was greatly improved in comparison with that of bare perovskite oxides and exhibited the highest ethylene yield among the tested catalysts. Its ethylene formation rate was stable for at least 4 h as shown in Figure 3.3 thanks to the negligibly small amount of carbon deposition on spent $La_{0.8}Ba_{0.2}MnO_{3-\delta}$ (Table 3.3): the amount of carbon deposition was at most 0.2% of converted ethane during the reaction for 4 h. Thus, it was regarded as suitable for additional investigation.

3.3.2. Reducibility of the alkaline earth metals-doped $LaMnO_3$

Partial replacement of La in $LaMnO_3$ with alkaline earth metals enhanced catalytic performance in case of $La_{0.8}B_{0.2}MnO_{3-\delta}$. Hereafter $LaMnO_3$ and $La_{0.8}B_{0.2}MnO_{3-\delta}$ are denoted as LMO and LBMO, respectively. Differences in the doping effects on the catalytic performance would be attributed to the charge compensation mechanism and redox properties of the catalysts.

In general, the partial substitution of divalent alkaline earth metal cations (Ca^{2+}, Sr^{2+} or Ba^{2+}) with trivalent La^{3+} cations induce a charge imbalance in its structure. One possibility to compensate for a negative charge is the change in the oxidation state of the B-site metal, for example, from Mn^{3+} to Mn^{4+}. Alternatively, oxygen vacancies could be generated instead of the change in the oxidation state. According to literature, [33–38] oxygen vacancies are mainly generated to compensate for the negative charge in alkaline earth metals-doped $LaFeO_3$ and $LaCoO_3$. In contrast, the charge imbalance in alkaline earth metals-doped LMO is compensated by the oxidation of Mn^{3+} to Mn^{4+}.[37–39] This indicates that redox properties of the B-site metals can be improved in case of LMO. As described in reactions (3.1) and (3.2), lattice oxygens would be released and regenerated concomitantly with the redox of Mn during the reaction. Thus, the improvement in the redox properties of Mn by the partial replacement of La^{3+} cations would enhance the catalytic activity.

Thus, H_2-TPR was conducted to elucidate the effect of different dopants (Ca, Sr and Ba) on reducibility of LMO. H_2-TPR profiles of fresh LMO and alkaline earth metals-doped LMO are shown in Figure 3.4. In the profiles (Figure 3.4(a)), two reduction peaks were observed: a low temperature peak at 500–800 K and a high temperature peak over 1000 K. The low temperature peak includes three components such as the reduction of adsorbed oxygen species (O_{ad}), Mn^{4+} to Mn^{3+}, and a part of Mn^{3+} to Mn^{2+}.[24,40] The high temperature peak is attributable to the reduction

of Mn^{3+} to Mn^{2+} in bulk, resulting in the decomposition of the perovskite structure. Although Mn cations in LMO should be trivalent, it is generally reported that Mn^{4+} cations exist in LMO.[39,40] The electronic state of Mn in LMO was evaluated by *ex-situ* Mn *K*-edge (XAFS spectroscopy. MnO(*Fm-3m*), Mn_2O_3(*Ia-3a*), and MnO_2(*P4₂/mnm*) were used as reference materials. X-ray absorption near edge structure (XANES) spectrum of fresh LMO is shown in Figure 3.5. The electronic state of Mn in LMO was close to that of Mn in Mn_2O_3 and MnO_2, indicating that Mn^{3+} and Mn^{4+} exist in $LaMnO_3$. However, linear combination fitting was not applicable because of no isosbestic point. XPS was also performed to evaluate the electronic state of Mn although determination of the Mn valence is difficult because of the slight difference in binding energy for Mn^{3+} and Mn^{4+}.[41,42] However, the broad peak in the $Mn2p_{3/2}$ spectrum demonstrated that Mn^{3+} and Mn^{4+} coexisted in LMO (Figure 3.6). These indicate that LMO had excess amount of oxygen such as $LaMnO_{3+\delta}$ to maintain its charge neutrality. During the first reduction step, removal of the excess oxygen and the subsequent formation of oxygen vacancies would proceed with the reduction of Mn cations as follows.

$$LaMn^{3+}{}_{1-x}Mn^{4+}{}_xO_{3+x/2} + xH_2 \rightarrow LaMn^{3+}O_3 + xH_2O \quad (3.5)$$

$$LaMn^{3+}O_3 + yH_2 \rightarrow LaMn^{2+}{}_yMn^{3+}{}_{1-y}O_{3-y/2} + yH_2O \quad (3.6)$$

Assuming that dehydrogenation of ethane proceeds *via* the MvK mechanism, the redox properties of Mn would be a key factor for the catalytic performance because the redox of Mn would occur simultaneously with the release and regeneration of lattice oxygens. Since the perovskite structure of LBMO was stable after the activity test (Figure 3.7), the redox of Mn species at 500–800 K would contribute to dehydrogenation of ethane.

Therefore, peak deconvolution of the first reduction peak in the TPR profiles was conducted to further investigate the reducibility of Mn cations. Deconvoluted profiles and calculated H_2 consumption are presented in Figure 3.4(b)–(e) and Table 3.4, respectively. In the H_2-TPR profile of Ca or Sr-doped LMO, a lower temperature peak below 600 K, corresponded to the reduction of O_{ad}, was clearly observed. In addition, the reduction temperature of Mn^{4+} to Mn^{3+} increased by Ca and Sr doping. This would indicate the stabilization of Mn^{4+}, resulting in the low redox properties of Mn in $La_{0.8}Ca_{0.2}MnO_{3-\delta}$ and $La_{0.8}Sr_{0.2}MnO_{3-\delta}$. Although the amount of Mn^{4+} slightly increased by the partial substitution of Ca^{2+} or Sr^{2+} cations for La^{3+}, the reduction of Mn^{3+} to Mn^{2+} was inhibited. As a result, Ca or Sr-doped LMO would have lower redox ability of Mn species than that of LMO, exhibiting the low catalytic activities.

In contrast, H_2-TPR profile of LBMO (Figure 3.4(e)) was similar to that of LMO except for the reduction peak for a part of Mn^{3+}. Compared with the profile of LMO, evolution of the peak at 710 K was observed, indicating the improvement in the redox properties of Mn in LBMO. Consequently, the large amount of Mn^{3+} can be reduced to Mn^{2+} thanks to the partial substitution of Ba^{2+} for La^{3+}. Among the dopants, Ba^{2+} has the largest ionic radius (1.61 Å) in comparison with the others (Ca^{2+}: 1.34 Å, Sr^{2+}: 1.44 Å).[43] Herein, the coordination number of A-site cations in $La_{0.8}A_{0.2}MnO_{3-\delta}$ (A = Ca, Sr, or Ba) is assumed to be 12 although these perovskites had a rhombohedral symmetry on the basis of our XRD measurements. The large ionic radius of Ba^{2+}

would be useful to stabilize the perovskite structure even though the large amount of oxygen vacancies was generated during the reduction step (reaction (3.6)).

3.3.3. Elucidation of reaction mechanism

To verify whether H_2O contributes to dehydrogenation of ethane, or not, periodic dry–wet operation tests were conducted at 973 K over LMO and LBMO. Results are presented in Figure 3.8. Under the dry atmosphere, the ethylene formation rate decreased rapidly, indicating that ethane reacted with the lattice oxygen of the perovskites. Furthermore, the lattice oxygen amount decreased because no oxidizing agent was present for regenerating the perovskite lattice oxygen. TPO was also performed to verify whether coke formation induce the deactivation or not. As presented in Table 3.3, the amount of carbon deposition on LBMO after the dry test (1.9 mg g_{cat}^{-1}) was smaller than that after the normal activity test for 4 h (2.5 mg g_{cat}^{-1}). The catalytic activity of LBMO in the presence of steam was stable for at least 4 h as shown in Figure 3.3. On the other hand, its activity quickly decreased within 40 min. Thus, coke formation during the dry test did not inhibit ethylene formation. We also verified that the perovskite structure of LBMO was maintained even after the dry test (Figure 3.7). These results demonstrate that consumption of the lattice oxygen induced the deactivation and the coexistence of H_2O plays a crucial role in ethylene formation. The ethylene formation rate over deactivated LMO and LBMO was comparable to that of α-Al_2O_3, which is known to have no catalytic activity for the dehydrogenation of ethane under similar reaction conditions.[17,18] After the reactive lattice oxygens in the catalysts were consumed monotonically, thermal cracking of ethane to ethylene in gas phase mainly proceeded. When steam was co-fed (in a wet atmosphere), the activities soon recovered and reached a steady state. This phenomenon elucidated that the consumed reactive surface lattice oxygen of perovskite for ethylene formation can be regenerated by steam under the wet condition. Although this behavior was observed in both cases (LMO and LBMO), LBMO showed the higher activity than LMO under the wet atmosphere because LBMO has high redox ability by virtue of Ba doping as mentioned in the H_2-TPR part. These results indicate that dehydrogenation of ethane over LMO and LBMO proceeds *via* the MvK mechanism as described in the reactions (3.1) and (3.2).

Furthermore, periodic dry–wet tests were conducted using D_2O instead of H_2O under the wet atmosphere. If dehydrogenation of ethane in the presence of steam proceeds through the MvK mechanism, then D_2 formation must be observed when the reactive lattice oxygens were regenerated (reaction (3.2)). The time course of the formation rate of ethylene and D_2 over LBMO is presented in Figure 3.9. Under the dry atmosphere, ethane would be dehydrogenated concomitantly with the formation of lattice oxygen vacancies (reaction (3.1)). Subsequent coexistence of D_2O (1st wet atmosphere) induced D_2 formation, clearly indicating regeneration of the lattice oxygen (reaction (3.2)). Particularly, D_2 formation rate was high at the initial stage to compensate the oxygen vacancies formed during the dry condition. Moreover, D_2 formation was observed in the second cycle (2nd wet atmosphere). This result demonstrates clearly that oxygen

release and regeneration are reversible during the reaction. These results show that, in the present catalytic system, ethane is oxidatively dehydrogenated to ethylene on the surface lattice oxygens of the perovskite with the formation of H_2O and oxygen vacancies. The consumed lattice oxygens are reproduced with the formation of H_2 (the MvK mechanism). In addition, ethylene formation rate was higher than D_2 formation rate, indicating that not all of the lattice oxygen were regenerated by D_2O. Formation of H_2 and HD was also observed under the wet atmosphere (Figure 3.10). H_2 must be originated from H atoms in ethane molecules. Because H_2O can be formed through dehydrogenation of ethane (reaction (3.1)), re-adsorption of H_2O and regeneration of the lattice oxygen resulted in the formation of H_2 (reaction (3.2)). In addition, H_2O can be formed through the oxidation of ethane and ethylene. Formation of CO and CO_2 was actually observed during the reaction as shown in Table 3.2. As a result, H_2O formed during the reaction regenerates the lattice oxygen in competition with D_2O.

Oxygen release behavior was verified using $H_2{}^{16}O$ and $H_2{}^{18}O$ mixture ($H_2{}^{16}O$: $H_2{}^{18}O$ = 3 : 2). First, dehydrogenation of ethane was conducted at 973 K in the presence of $H_2{}^{18}O$ to replace a part of lattice $^{16}O^{2-}$ with $^{18}O^{2-}$. Then, the normal activity test was subsequently performed using $H_2{}^{16}O$. Results are shown in Figure 3.11. Evolution of $H_2{}^{18}O$ was verified in case of both $LaMnO_3$ and $La_{0.8}Ba_{0.2}MnO_{3-\delta}$ during the normal activity test. This clearly indicates that the reactive lattice oxygens are released and regenerated through H_2O as an oxygen medium. In addition, the total amount of released $H_2{}^{18}O$ increased thanks to Ba doping, demonstrating the enhancement of the redox properties of $LaMnO_3$ by Ba doping.

3.3.4. Redox behavior of Mn

To evaluate the electronic state of Mn in LMO and LBMO during the reaction, *in-situ* Mn *K*-edge XAFS measurements of LMO and LBMO were taken, respectively, in a C_2H_6 flow and a H_2O flow. The reaction atmosphere was varied continuously at 973 K as shown in Figure 3.1. XAFS spectra in the 1st cycle are shown in Figure 3.12, which also shows that the absorption edge was shifted to lower energy region in C_2H_6. Subsequent H_2O feeding shifted the absorption edge to a higher energy region. In addition, similar behaviors were observed in the second cycle (Figure 3.13). These results indicate that Mn cations in LMO and LBMO were reduced in C_2H_6 and oxidized in H_2O during the catalytic reaction. In other words, the redox reaction of Mn would be accompanied by the release and regeneration of the lattice oxygens during dehydrogenation of ethane in the presence of H_2O. Comparing the spectra of LBMO with those of LMO, the shift width of the white line position of LBMO was larger than that of LMO. These results revealed that Mn in LBMO has higher redox ability than that in LMO by virtue of the replacement of a part of La sites with Ba. Taking the results of isotopic transient tests with D_2O and $H_2{}^{18}O$, the reactive surface lattice oxygen of the perovskite is reduced through dehydrogenation of ethane and desorbed as H_2O with the reduction of Mn and formation of oxygen vacancies. These vacant sites are regenerated by oxidation using H_2O with the oxidation of Mn.

3.3.5. Effects of Ba doping

We clarified that the partial substitution of Ba for La improved the redox ability of Mn, resulting in the high activity for dehydrogenation of ethane in the presence of H_2O. The Ba doping amount effect on the catalytic performance was investigated. The ethylene formation rate and ethylene selectivity over $La_{1-x}Ba_xMnO_{3-\delta}$ (x = 0–0.4) are presented in Figure 3.14. Catalytic performance including ethane conversion and selectivity to by-products are presented in Table 3.5. The ethylene formation rate increased as the Ba doping amount increased to 0.3. Subsequently, it decreased with the further increase in the Ba doping amount. Ethylene selectivity also increased with the increment of the Ba doping amount. Among these catalysts, $La_{0.7}Ba_{0.3}MnO_{3-\delta}$ showed the highest ethane conversion (4.8%) and ethylene selectivity (88%).

XRD measurements of $La_{1-x}Ba_xMnO_{3-\delta}$ were taken to investigate the effects of the amounts of Ba doping on the perovskite structure. XRD patterns of $La_{1-x}Ba_xMnO_{3-\delta}$ are presented in Figure 3.15. Figure 3.15(a) shows that all Ba-doped LMO consisted of the perovskite structure. However, small peaks for $BaMnO_3$ were observed in the XRD patterns of $La_{0.7}Ba_{0.3}MnO_{3-\delta}$ and $La_{0.6}Ba_{0.4}MnO_{3-\delta}$. We specifically examined the enlarged XRD patterns (Figure 3.15(b)), the diffraction peak derived from (024) facet for $LaMnO_3$ was shifted to the lower degree region and was broadened by Ba doping. This result demonstrated that the Ba dopant was located in the perovskite structure, thereby instilling the high redox ability to the structure.

Moreover, Mn *K*-edge XANES spectra of $La_{1-x}Ba_xMnO_{3-\delta}$ were measured to elucidate the fine structure of Mn in $La_{1-x}Ba_xMnO_{3-\delta}$. The results are presented in Figure 3.16. The white line position shifted to the high energy region as the Ba doping amount increased. These results revealed that MnO_6 octahedra in LBMO were distorted by Ba doping.[44] This distortion is probably attributable to the partial contraction of Mn cations through the oxidation of Mn cations such as $Mn^{3+} \rightarrow Mn^{4+}$ to compensate the lack of a positive charge derived from substitution of the bivalent Ba^{2+} cations for trivalent La^{3+} cations.

Finally, H_2-TPR was conducted to evaluate the reducibility of Mn in fresh $La_{1-x}Ba_xMnO_{3-\delta}$. H_2-TPR profiles are shown in Figure 3.17(a). The high temperature peak (> 1000 K) is attributable to the reduction of Mn^{3+} to Mn^{2+} in bulk, resulting in the decomposition of the perovskite structure. The low temperature peak is composed of three reduction peaks corresponded to the reduction of O_{ad}, Mn^{4+}, and Mn^{3+}. The low temperature peak was deconvoluted to elucidate the effect of Ba doping amount on the redox properties of Mn. Results of the peak deconvolution and calculated H_2 consumption are presented in Figure 3.17(b)–(e) and Table 3.6, respectively. H_2 consumption for O_{ad} and Mn^{4+} in $La_{0.9}Ba_{0.1}MnO_{3-\delta}$ decreased in comparison with that in LMO. Among Ba-doped LMO, the reducible Mn^{4+} increased with the increase in the amount of Ba. In contrast, reducible Mn^{3+} monotonously increased by Ba doping including LMO. The trend of ethylene formation rate (Figure 3.14) was in accordance with that of the reducible Mn^{3+}. This indicates that the redox of Mn between Mn^{3+} and Mn^{2+} would rather contribute to dehydrogenation of ethane than that between Mn^{4+} and Mn^{3+} probably because of the difficulty in the oxidation of Mn^{3+} to

Mn^{4+} by H_2O. The results of *in-situ* Mn *K*-edge XAFS (Figures 3.12 and 3.13) also support the assumption. The absorption edge under the C_2H_6 atmosphere incompletely returned to the same position of the fresh LMO and LBMO under the H_2O atmosphere, demonstrating that the electronic state of Mn under the H_2O atmosphere was more reduced than that of Mn in the fresh samples.

Based on H_2-TPR, clear relationship between ethylene formation rate and sum of H_2 consumption for O_{ad} and Mn^{3+} was developed as shown in Figure 3.18. Clear correlation between ethylene formation rate and BET surface area was not obtained (Table 3.7). Thus, the catalytic activity for dehydrogenation of ethane would be related to not only O_{ad} but also the amount of reducible Mn^{3+}. Considering the catalytic activities and the amount of reducible Mn in LMO and $La_{0.9}Ba_{0.1}MnO_{3-\delta}$, the redox of Mn between Mn^{3+} and Mn^{2+} would be a more important factor for the catalytic activity than that of O_{ad}. It is probably because the consumption rate of surface lattice oxygens is faster than the regeneration of oxygen vacancies through oxygen diffusion in bulk. Oxygen diffusion from bulk to surface requires reduction of Mn^{3+} in bulk. Therefore, improvement in the redox properties of Mn^{3+} would enhance bulk oxygen mobility, leading to fast regeneration of the lattice oxygen.

3.4. Chapter Conclusion

Dehydrogenation of ethane in the presence of H_2O at 973 K over La-based perovskite oxide catalysts was investigated. $La_{0.7}Ba_{0.3}MnO_{3-\delta}$ perovskite showed the highest activity among the tested catalysts. The results of periodic dry-wet operation tests showed that the stable catalytic activities of $LaMnO_3$ (LMO) and $La_{0.8}Ba_{0.2}MnO_{3-\delta}$ (LBMO) were supported by redox with H_2O, indicating that dehydrogenation of ethane proceeded *via* the MvK mechanism. Also, D_2 formation was observed using D_2O instead of H_2O as an oxidizing agent. On the catalyst surface, ethane was dehydrogenated oxidatively to ethylene with the reactive surface lattice oxygen. The consumed lattice oxygen can be oxidized by H_2O, leading to the completion of the catalytic redox cycle. The isotopic transient tests with $H_2{}^{18}O$ also revealed that the reactive lattice oxygens are released and regenerated by H_2O. The reversible redox behaviors of Mn in LMO and LBMO under the reaction atmosphere were verified using *in-situ* Mn *K*-edge XAFS spectroscopy. Comparison of the energy shift of LMO with that of LBMO in the spectra revealed that LBMO showed higher redox ability than that of LMO. Results of XRD and XAFS demonstrated that the perovskite structure of LMO was distorted by Ba doping, because of the partial oxidation of Mn cations for charge compensation. H_2-TPR revealed that the amount of reducible Mn^{3+} can be expected to play an important role in the reaction. Consequently, LBMO showed the high activity for dehydrogenation of ethane in the presence of H_2O by virtue of its high redox properties of Mn derived from the partial substitution of bivalent Ba^{2+} cations for trivalent La^{3+} cations. Schematic image of dehydrogenation of ethane over LBMO is portrayed in Figure 3.19.

References

1. J. J. Siirola, The Impact of Shale Gas in the Chemical Industry. *AIChE J*. **2014**, *60*, 810−819.
2. J. J. H. B. Sattler, J. Ruiz-Martinez, E. Santillan-Jimenez, B. M. Weckhuysen, Catalytic Dehydrogenation of Light Alkanes on Metals and Metal Oxides. *Chem*. *Rev*. **2014**, *114*, 10613–10653.
3. C. A. Gärtner, A. C. van Veen, J. A. Lercher, Oxidative Dehydrogenation of Ethane: Common Principles and Mechanistic Aspects. *ChemCatChem* **2013**, *5*, 3196–3217.
4. R. Grabowski, Kinetics of Oxidative Dehydrogenation of C_2-C_3 Alkanes on Oxide Catalysts. *Catal. Rev. –Sci. Eng.* **2006**, *48*, 199–268.
5. T. Blasco, J. M. L. Nieto, Oxidative Dehydrogenation of Short Chain Alkanes on Supported Vanadium Oxide Catalysts. *Appl. Catal. A: Gen.* **1997**, *157*, 117–142.
6. M. D. Argyle, K. Chen, A. T. Bell, E. Iglesia, Effect of Catalyst Structure on Oxidative Dehydrogenation of Ethane and Propane on Alumina-Supported Vanadia. *J. Catal*. **2002**, *208*, 139–149.
7. E. Heracleous, A. F. Lee, K. Wilson, A. A. Lemonidou, Investigation of Ni-Based Alumina-Supported Catalysts for the Oxidative Dehydrogenation of Ethane to Ethylene: Structural Characterization and Reactivity Studies. *J. Catal*. **2005**, *231*, 159–171.
8. H. Zhu, D. C. Rosenfeld, M. Harb, D. H. Anjum, M. N. Hedhili, S. Ould-Chikh, J. Basset, Ni−M−O (M = Sn, Ti, W) Catalysts Prepared by a Dry Mixing Method for Oxidative Dehydrogenation of Ethane. *ACS Catal.* **2016**, *6*, 2852–2866.
9. W. Ueda, K. Oshihara, Selective Oxidation of Light Alkanes over Hydrothermally Synthesized Mo-V-M-O (M=Al, Ga, Bi, Sb, and Te) Oxide Catalysts. *Appl. Catal. A: Gen.* **2000**, *200*, 135–143.
10. P. Botella, E. García-González, A. Dejoz, J. M. L. Nieto, M. I. Vázquez, J. González-Calbet, Selective Oxidative Dehydrogenation of Ethane on MoVTeNbO Mixed Metal Oxide Catalysts. *J. Catal.* **2004**, *225*, 428–438.
11. C. A. Gärtner, A. C. van Veen, J. A. Lercher, Oxidative Dehydrogenation of Ethane on Dynamically Rearranging Supported Chloride Catalysts. *J. Am. Chem. Soc.* **2014**, *136*, 12691–12701.
12. D. Mukherjee, S. Park, B. M. Reddy, CO_2 as a Soft Oxidant for Oxidative Dehydrogenation Reaction: An Eco Benign Process for Industry. *J. CO_2 Util.* **2016**, *16*, 301−312.
13. S. Wang, K. Murata, T. Hayakawa, S. Hamakawa, K. Suzuki, Dehydrogenation of Ethane with Carbon Dioxide over Supported Chromium Oxide Catalysts. *Appl*. *Catal*. *A*: *Gen*. **2000**, *196*, 1−8.
14. N. Mimura, M. Okamoto, H. Yamashita, S. T. Oyama, K. Murata, Oxidative Dehydrogenation of Ethane over Cr/ZSM-5 Catalysts Using CO_2 as an Oxidant. *J. Phys. Chem. B* **2006**, *110*, 21764−21770.

15. K. Nakagawa, C. Kajita, K. Okumura, N. Ikenega, M. Nishitani-Gamo, T. Ando, T. Kobayashi, T. Suzuki, Role of Carbon Dioxide in the Dehydrogenation of Ethane over Gallium-Loaded Catalysts. *J. Catal*. **2001**, *203*, 87−93.
16. R. Koirala, R. Buechel, F. Krumeich, S. E. Pratsinis, A. Baiker, Oxidative Dehydrogenation of Ethane with CO_2 over Flame-Made Ga-Loaded TiO_2. *ACS Catal.* **2015**, *5*, 690−702.
17. H. Saito, S. Maeda, H. Seki, M. Manabe, Y. Miyamoto, S. Ogo, K. Hashimoto, Y. Sekine, Supported Ga-Oxide Catalyst for Dehydrogenation of Ethane. *J. Jpn. Petrol. Inst.* **2017**, *60*, 203−210.
18. H. Seki, H. Saito, K. Toko, Y. Hosono, T. Higo, J. G. Seo, S. Maeda, K. Hashimoto, S. Ogo, Y. Sekine, Effect of Ba Addition to Ga-α-Al_2O_3 Catalyst on Structure and Catalytic Selectivity for Dehydrogenation of Ethane. *Appl. Catal. A: Gen.* **2019**, *581*, 23–30.
19. E. A. Pidko, E. J. M. Hensen, R. A. van Santen, Dehydrogenation of Light Alkanes over Isolated Gallyl Ions in Ga/ZSM-5 Zeolites. *J. Phys. Chem. C* **2007**, *111*, 13068−13075.
20. E. A. Pidko, R. A. van Santen, E. J. M. Hensen, Multinuclear Gallium-Oxide Cations in High-Silica Zeolites. *Phys. Chem. Chem. Phys.* **2009**, *11*, 2893−2902.
21. E. A. Pidko, R. A. van Santen, Structure-Reactivity Relationship for Catalytic Activity of Gallium Oxide and Sulfide Clusters in Zeolite. *J. Phys. Chem. C* **2009**, *113*, 4246−4249.
22. E. J. M. Hensen, E. A. Pidko, N. Rane, R. A. van Santen, Water-Promoted Hydrocarbon Activation Catalyzed by Binuclear Gallium Sites in ZSM-5 Zeolite. *Angew. Chem. Int. Ed.* **2007**, *46*, 7273−7276.
23. J. Zhu, H. Li, L. Zhong, P. Xiao, X. Xu, X. Yang, Z. Zhao, J. Li, Perovskite Oxides: Preparation, Characterizations, and Applications in Heterogeneous Catalysis. *ACS Catal.* **2014**, *4*, 2917−2940.
24. Y. N. Lee, R. M. Lago, J. L. G. Fierro, V. Cortés, F. Sapiña, E. Martínez, Surface Properties and Catalytic Performance for Ethane Combustion of $La_{1-x}K_xMnO_{3+\delta}$ Perovskites. *Appl. Catal. A: Gen.* **2001**, *207*, 17–24.
25. K. S. Song, D. Klvana, J. Kirchnerova, Kinetics of Propane Combustion over $La_{0.66}Sr_{0.34}Ni_{0.3}Co_{0.7}O_3$ Perovskite. *Appl. Catal. A: Gen.* **2001**, *213*, 113–121.
26. S. Royer, H. Alamdari, D. Duprez, S. Kaliaguine, Oxygen Storage Capacity of $La_{1-x}A'_xBO_3$ Perovskites (with A'= Sr, Ce; B = Co, Mn) – Relation with Catalytic Activity in the CH_4 Oxidation Reaction. *Appl. Catal. B: Environ.* **2005**, *58*, 273–288.
27. R. Watanabe, Y. Sekine, J. Kojima, M. Matsukata, E. Kikuchi, Dehydrogenation of Ethylbenzene over Highly Active and Stable Perovskite Oxide Catalyst – Effect of Lattice Oxygen on/in Perovskite Oxide and Role of A/B site in Perovskite Oxide. *Appl. Catal. A: Gen.* **2011**, *398*, 66–72.
28. R. Watanabe, Y. Hondo, K. Mukawa, C. Fukuhara, E. Kikuchi, Y. Sekine, Stable and Selective Perovskite Catalyst for Dehydrogenation of Propane Working with Redox Mechanism. *J. Mol. Catal. A: Chem*. **2013**, *377*, 74–84.

29. D. Mukai, S. Tochiya, Y. Murai, M. Imori, T. Hashimoto, Y. Sugiura, Y. Sekine, Role of Support Lattice Oxygen on Steam Reforming of Toluene for Hydrogen Production over $Ni/La_{0.7}Sr_{0.3}AlO_{3-\delta}$ Catalyst. *Appl. Catal. A: Gen.* **2013**, *453*, 60–70.
30. M. D. Argyle, K. Chen, A. T. Bell, E. Iglesia, Ethane Oxidative Dehydrogenation Pathways on Vanadium Oxide Catalysts. *J. Phys. Chem. B* **2002**, *106*, 5421–5427.
31. F. Klose, M. Joshi, C. Hamel, A. Seidel-Morgenstern, Selective Oxidation of Ethane over a VO_x/γ-Al_2O_3 Catalyst – Investigation of the Reaction Network. *Appl. Catal. A: Gen.* **2004**, *260*, 101–110.
32. E. Heracleous, A. A. Lemonidou, Ni–Nb–O Mixed Oxides as Highly Active and Selective Catalysts for Ethene Production via Ethane Oxidative Dehydrogenation. Part II: Mechanistic Aspects and Kinetic Modeling. *J. Catal.* **2002**, *237*, 175–189.
33. P. Ciambelli, S. Cimino, L. Lisi, M. Faticanti, G. Minelli, I. Pettiti, P. Porta, La, Ca and Fe Oxide Perovskites: Preparation, Characterization and Catalytic Properties for Methane Combustion. *Appl. Catal. B: Environ.* **2001**, *33*, 193–203.
34. N. A. Merino, B. P. Barbero, P. Grange, L. E. Cadús, $La_{1-x}Ca_xCoO_3$ Perovskite-type Oxides: Preparation, Characterization, Stability, and Catalytic Potentially for the Total Oxidation of Propane. *J. Catal.* **2005**, *231*, 232–244.
35. B. P. Barbero, J. A. Gamboa, L. E. Cadús, Synthesis and Characterization of $La_{1-x}Ca_xFeO_3$ Perovskite-type Oxide Catalysts for Total Oxidation of Volatile Organic Compounds. *Appl. Catal. B: Environ.* **2006**, *65*, 21–30.
36. G. Pecchi, M. G. Jiliberto, A. Buljan, E. J. Delgado, Relation between Defects and Catalytic Activity of Calcium Doped $LaFeO_3$ Perovskite. *Solid State Ionics* **2011**, *187*, 27–32.
37. W. Y. Hernández, M. N. Tsampas, C. Zhao, A. Boreave, F. Bosselet, P. Vernoux, La/Sr-based Perovskites as Soot Oxidation Catalysts for Gasoline Particulate Filters. *Catal. Today* **2015**, *258*, 525–534.
38. J. A. Onrubia, B. Pereda-Ayo, U. De-La-Torre, J. R. González-Velasco, Key Factors in Sr-doped $LaBO_3$ (B = Co or Mn) Perovskites for NO Oxidation in Efficient Diesel Exhaust Purification. *Appl. Catal. B: Environ.* **2017**, *213*, 198–210.
39. S. Ponce, M. A. Penã, J. L. G. Fierro, Surface Properties and Catalytic Performance in Methane Combustion of Sr-Substituted Lanthanum Manganites, *Appl. Catal. B: Environ.* **2000**, *24*, 193–205.
40. H. Najjar, J.-F. Lamonier, O. Mentré, J.-M. Giraudon, H. Batis, Optimization of the Combustion Synthesis towards Efficient $LaMnO_{3+y}$ Catalysts in Methane Oxidation. *Appl. Catal. B: Environ*. **2011**, *106*, 149–159.
41. V. D. Castro, G. Polzonetti, XPS Study of MnO Oxidation. *J. Electron Spectrosc. Relat. Phenom.* **1989**, *48*, 117–123.
42. A. J. Nelson, J. G. Reynolds, J. W. Roos, Core-level Satellites and Outer Core-Level Multiplet Splitting in Mn Model Compounds. *J. Vac. Sci. Technol. A* **2000**, *18*, 1072–1076.

43. R. D. Shannon, Revised Effective Ionic Radii and Systematic Studies of Interatomic Distances in Halides and Chaleogenides. *Acta Cryst*. **1976**, *A32*, 751–767.
44. J. Chaboy, Relationship between the Structural Distortion and the Mn Electronic State in $La_{1-x}Ca_xMnO_3$: A Mn *K*-Edge XANES Study. *J. Synchrotron Rad*. **2009**, *16*, 533–544.

Figures and Tables

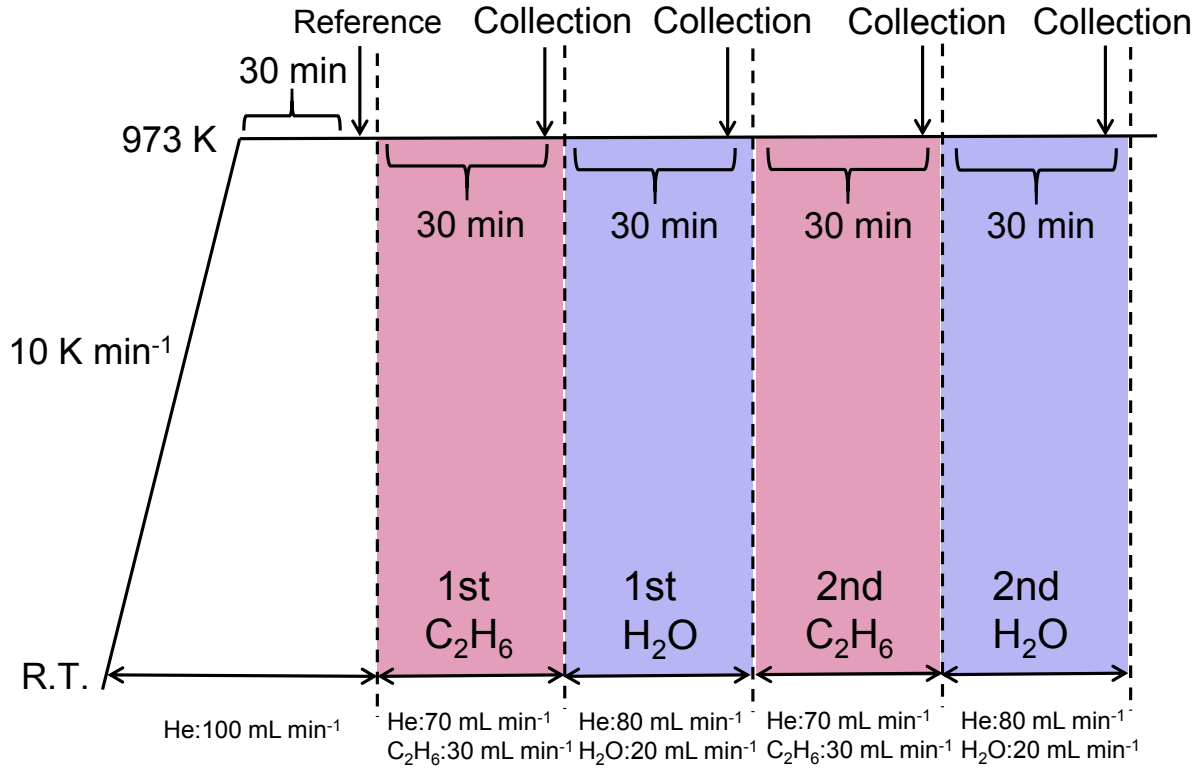

Figure 3.1. The specific procedure for *in-situ* XAFS measurements. Reprinted with permission from H. Saito *et al.*, *J. Phys. Chem. C* **2019**, *123*, 26272–26281. Copyright 2019 American Chemical Society.

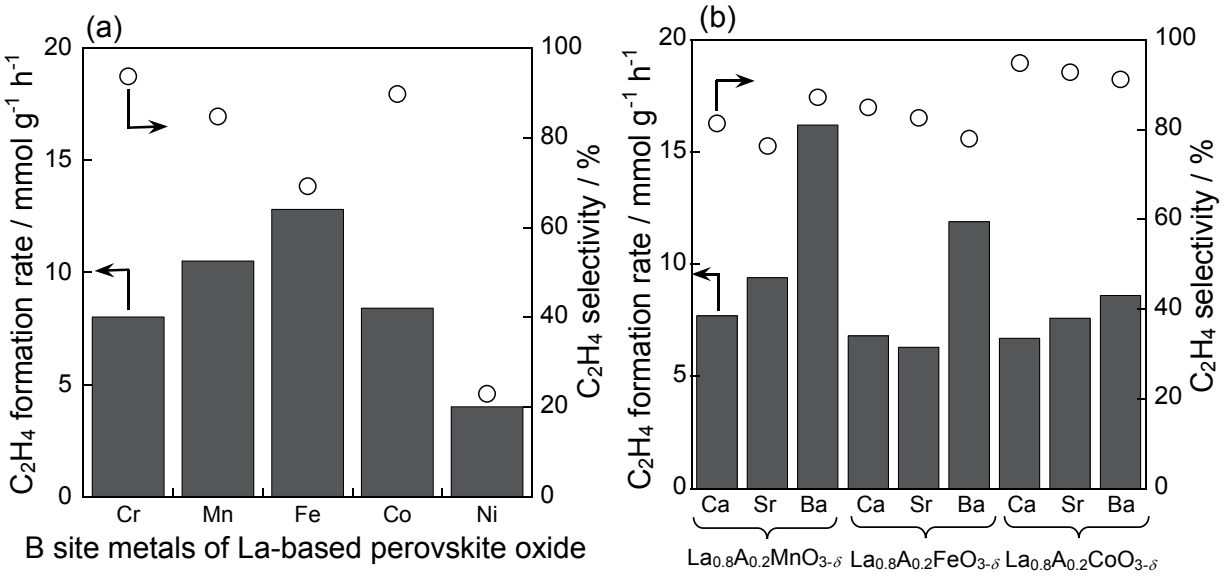

Figure 3.2. C_2H_4 formation rate and C_2H_4 selectivity over (a) $LaMO_3$ (M = Cr, Mn, Fe, Co and Ni) and (b) $La_{0.8}A_{0.2}MO_{3-\delta}$ (A = Ca, Sr and Ba; M = Mn, Fe and Co). Reprinted with permission from H. Saito *et al.*, *J. Phys. Chem. C* **2019**, *123*, 26272–26281. Copyright 2019 American Chemical Society.

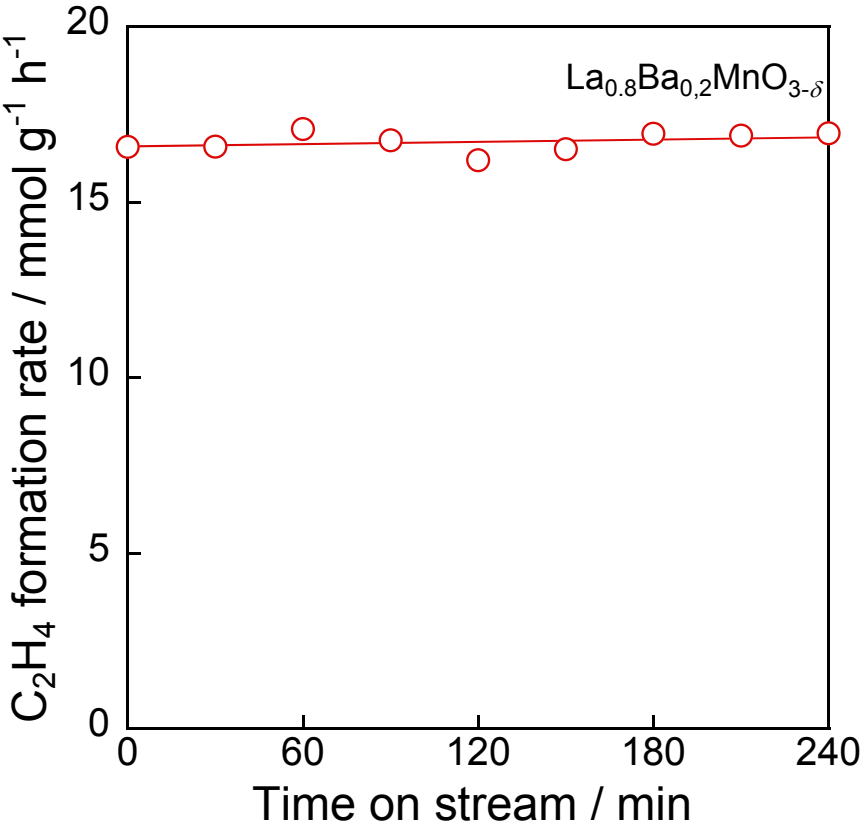

Figure 3.3. Time course of C_2H_4 formation rate at 973 K over $La_{0.8}Ba_{0.2}MnO_{3-\delta}$. Reprinted with permission from H. Saito *et al.*, *J. Phys. Chem. C* **2019**, *123*, 26272–26281. Copyright 2019 American Chemical Society.

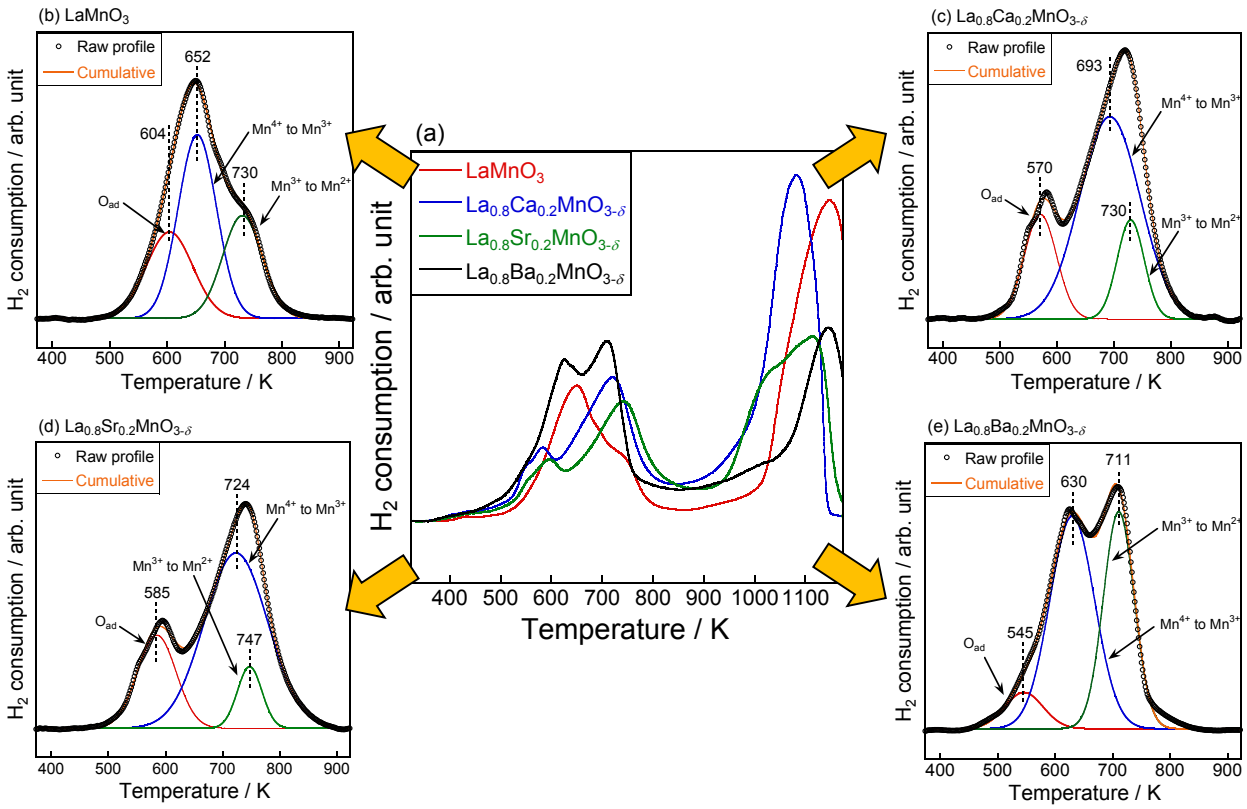

Figure 3.4. H_2-TPR profiles of (a) $LaMnO_3$ and $La_{0.8}A_{0.2}MnO_{3-\delta}$ (A = Ca, Sr, and Ba). Enlarged profiles of (b) $LaMnO_3$, (c) $La_{0.8}Ca_{0.2}MnO_{3-\delta}$, (d) $La_{0.8}Sr_{0.2}MnO_{3-\delta}$ and (e) $La_{0.8}Ba_{0.2}MnO_{3-\delta}$ in the temperature range of 373–923 K. Reprinted with permission from H. Saito *et al.*, *J. Phys. Chem. C* **2019**, *123*, 26272–26281. Copyright 2019 American Chemical Society.

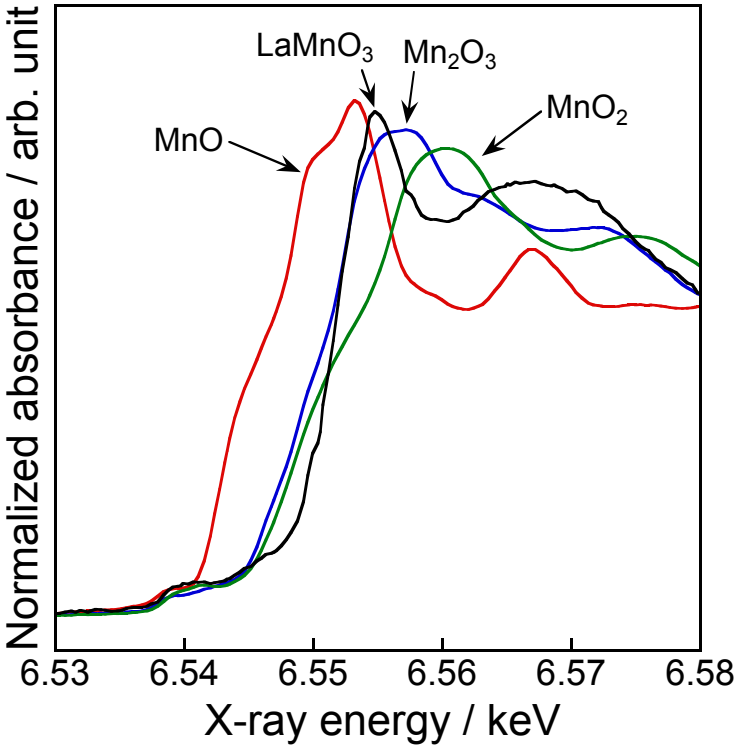

Figure 3.5. Mn *K*-edge XANES spectra of fresh $LaMnO_3$. MnO, Mn_2O_3, and MnO_2 were used for reference materials. Reprinted with permission from H. Saito *et al.*, *J. Phys. Chem. C* **2019**, *123*, 26272–26281. Copyright 2019 American Chemical Society.

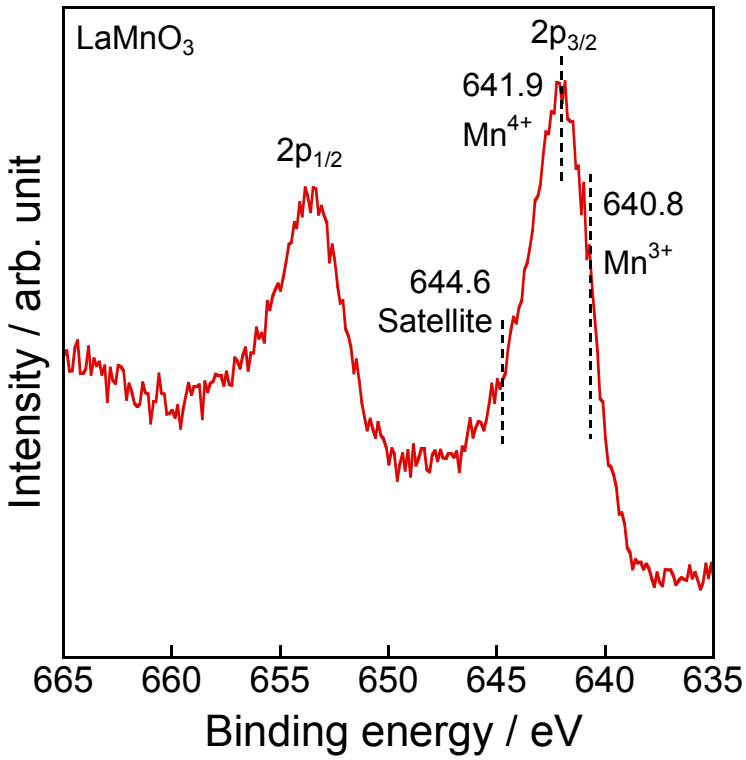

Figure 3.6. Mn2p X-ray photoelectron spectrum of $LaMnO_3$. Reprinted with permission from H. Saito *et al.*, *J. Phys. Chem. C* **2019**, *123*, 26272–26281. Copyright 2019 American Chemical Society.

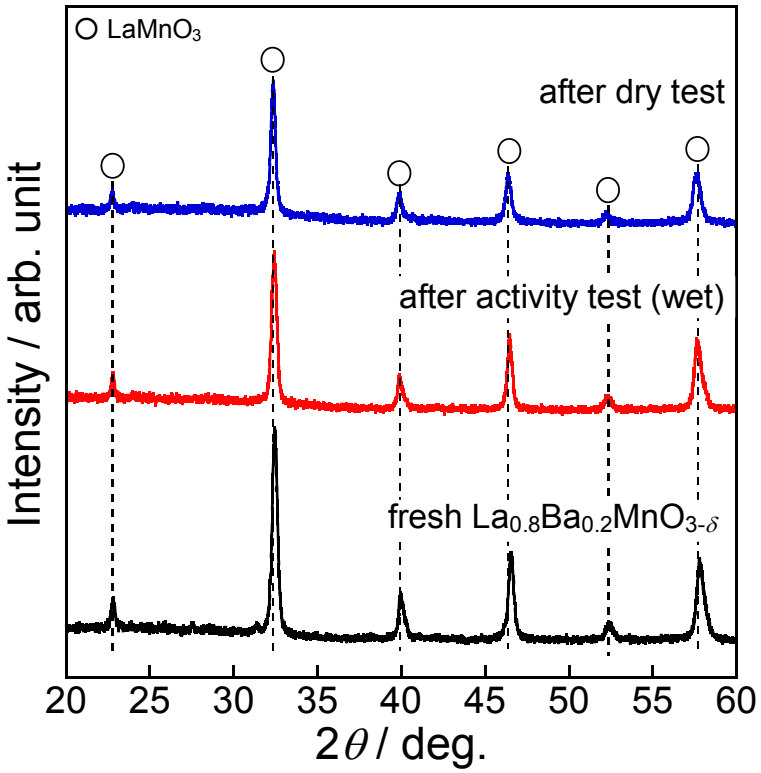

Figure 3.7. XRD patterns of fresh and spent $La_{0.8}Ba_{0.2}MnO_{3-\delta}$. Reprinted with permission from H. Saito *et al.*, *J. Phys. Chem. C* **2019**, *123*, 26272–26281. Copyright 2019 American Chemical Society.

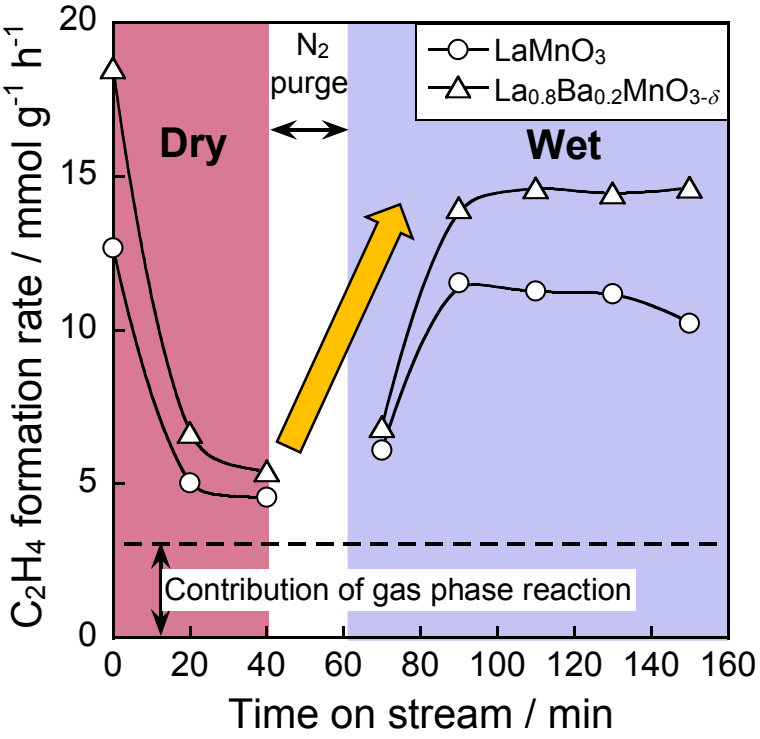

Figure 3.8. Time course of C_2H_4 formation rate over $LaMnO_3$ and $La_{0.8}Ba_{0.2}MnO_{3-\delta}$ under dry and wet atmosphere. Reprinted with permission from H. Saito *et al.*, *J. Phys. Chem. C* **2019**, *123*, 26272–26281. Copyright 2019 American Chemical Society.

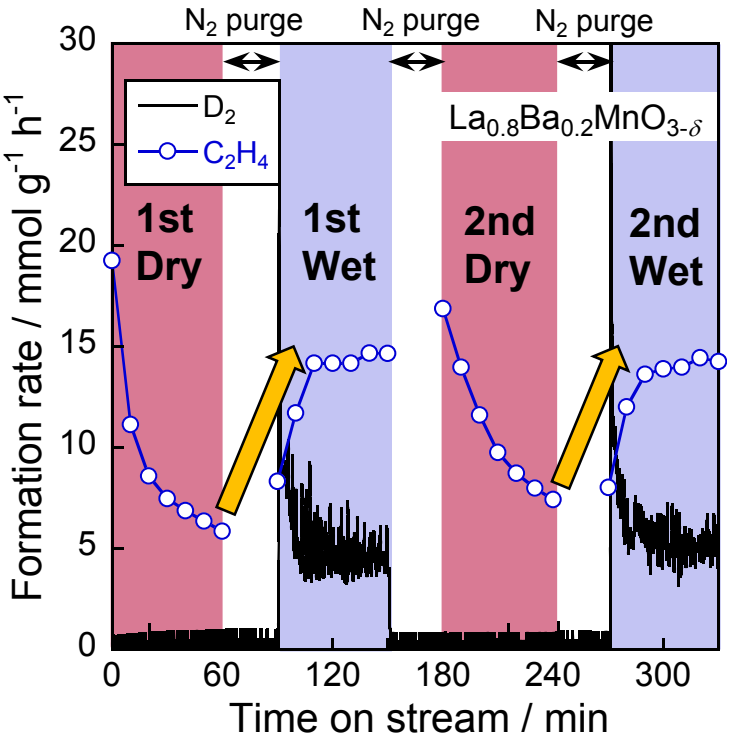

Figure 3.9. Time course of the formation rate of C_2H_4 and D_2 at 973 K over $La_{0.8}Ba_{0.2}MnO_{3-\delta}$ under the dry and wet atmospheres. Reprinted with permission from H. Saito *et al.*, *J. Phys. Chem. C* **2019**, *123*, 26272–26281. Copyright 2019 American Chemical Society.

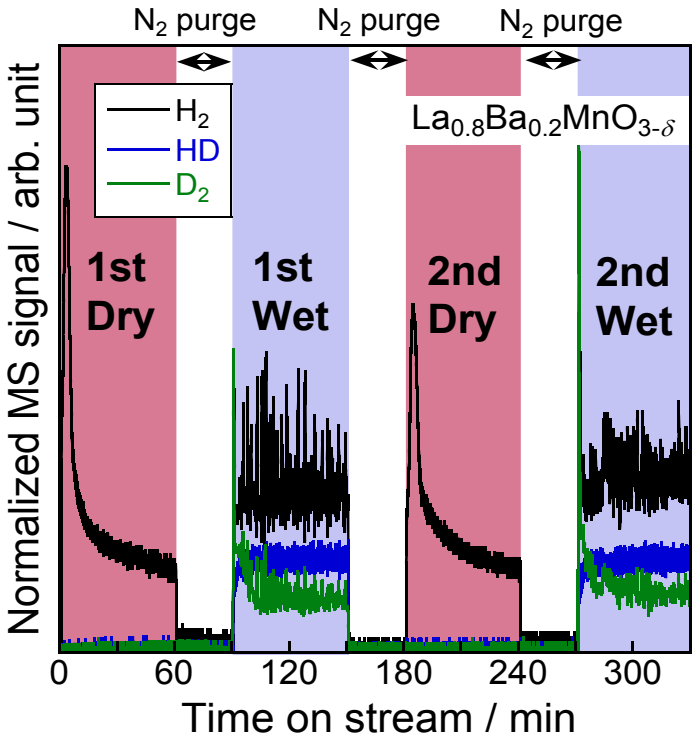

Figure 3.10. Time course of H_2, HD and D_2 evolution at 973 K over $La_{0.8}Ba_{0.2}MnO_{3-\delta}$ under the dry and wet atmospheres. Reprinted with permission from H. Saito *et al.*, *J. Phys. Chem. C* **2019**, *123*, 26272–26281. Copyright 2019 American Chemical Society.

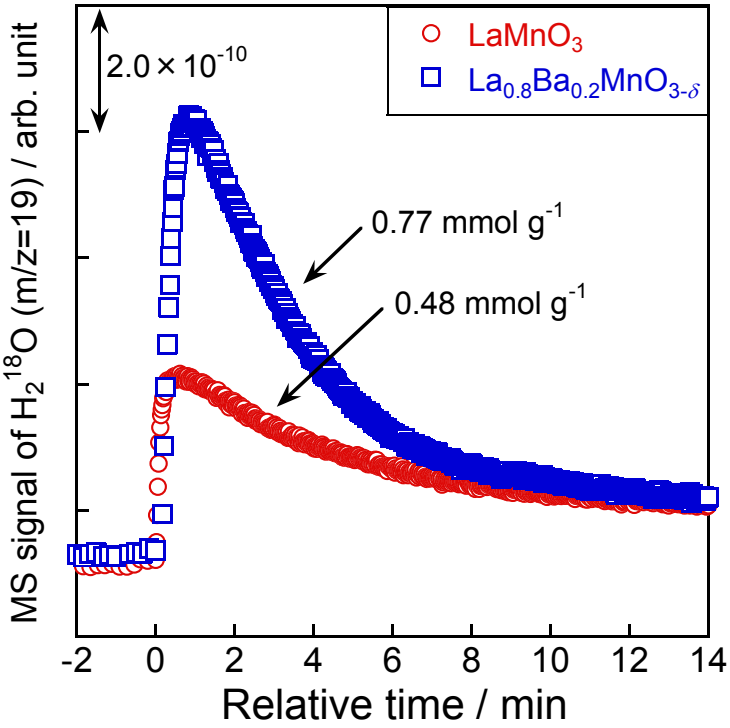

Figure 3.11. Time course of $H_2{}^{18}O$ formation at 973 K over $LaMnO_3$ and $La_{0.8}Ba_{0.2}MnO_{3-\delta}$. Reprinted with permission from H. Saito *et al.*, *J. Phys. Chem. C* **2019**, *123*, 26272–26281. Copyright 2019 American Chemical Society.

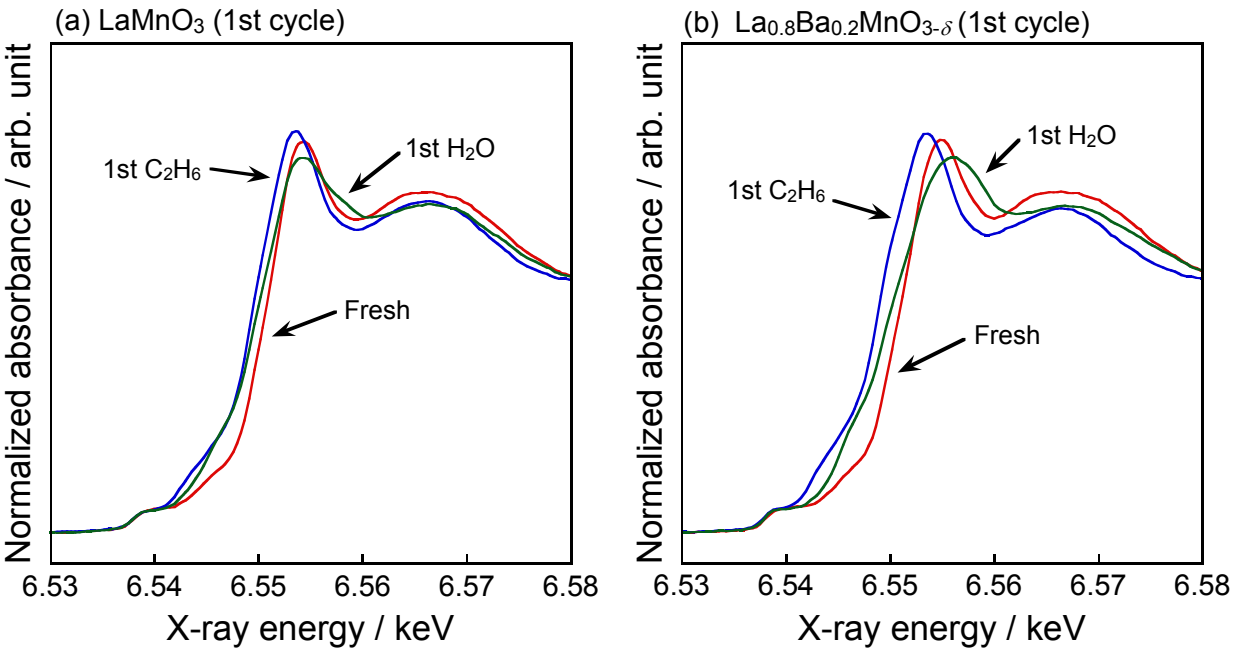

Figure 3.12. *In-situ* Mn *K*-edge XANES spectra of (a) $LaMnO_3$ and (b) $La_{0.8}Ba_{0.2}MnO_{3-\delta}$ under He (red), dry (blue) and wet (green) atmospheres (1st cycle). Reprinted with permission from H. Saito *et al.*, *J. Phys. Chem. C* **2019**, *123*, 26272–26281. Copyright 2019 American Chemical Society.

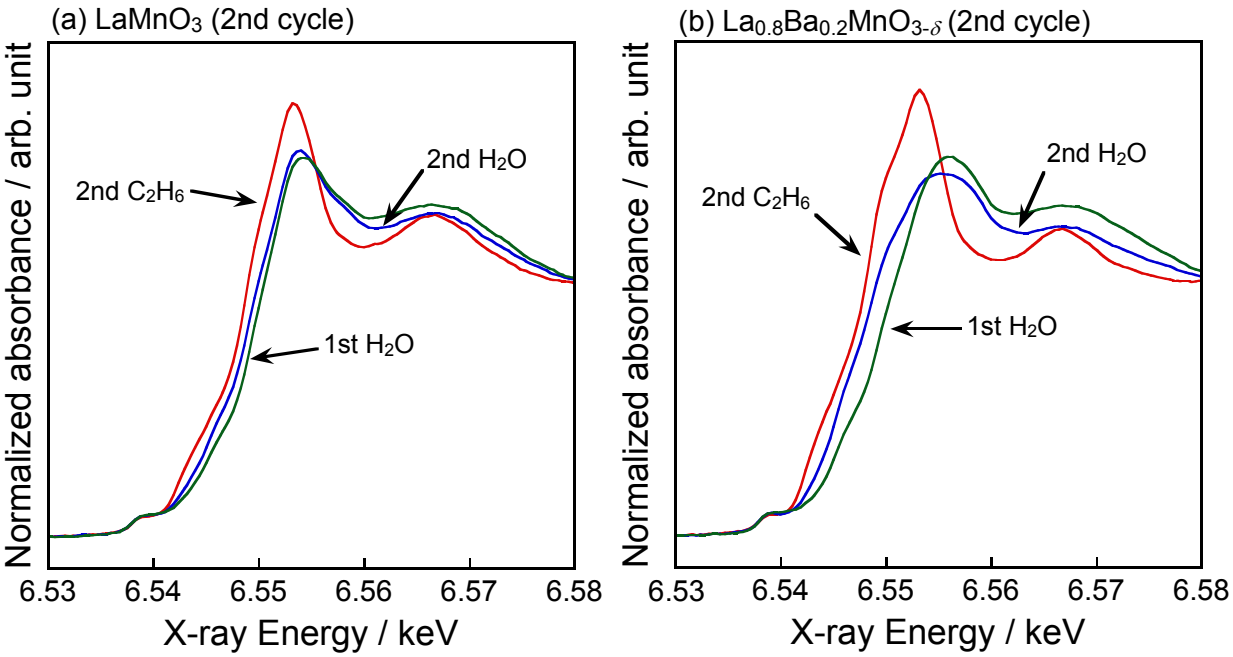

Figure 3.13. *In-situ* Mn *K*-edge XANES spectra of (a) $LaMnO_3$ and (b) $La_{0.8}Ba_{0.2}MnO_{3-\delta}$ under the dry (red) and wet (blue) atmospheres (2nd cycle). Reprinted with permission from H. Saito *et al.*, *J. Phys. Chem. C* **2019**, *123*, 26272–26281. Copyright 2019 American Chemical Society.

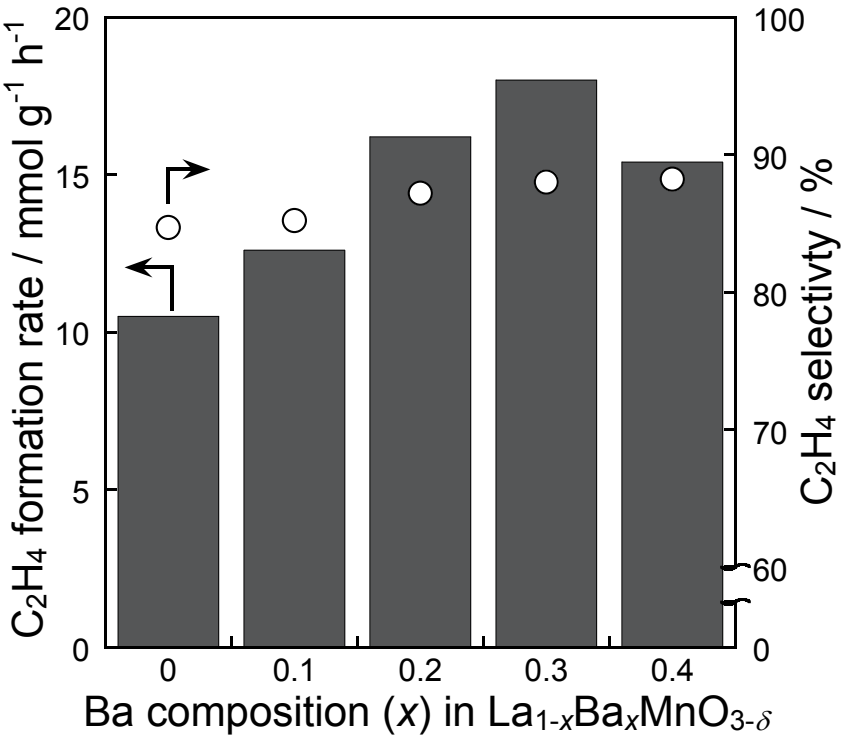

Figure 3.14. C_2H_4 formation rate and C_2H_4 selectivity at 973 K over $La_{1-x}Ba_xMnO_{3-\delta}$ (x = 0–0.4). Reprinted with permission from H. Saito *et al.*, *J. Phys. Chem. C* **2019**, *123*, 26272–26281. Copyright 2019 American Chemical Society.

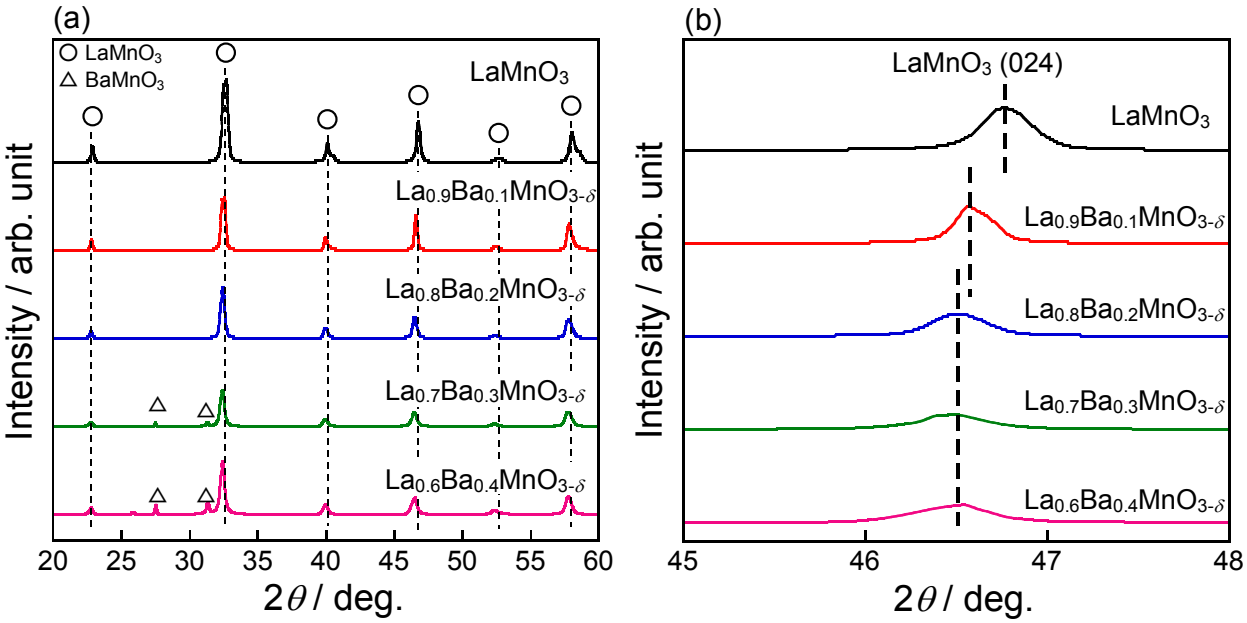

Figure 3.15. XRD patterns of (a) $La_{1-x}Ba_xMnO_{3-\delta}$ (x = 0–0.4) and (b) enlarged one. Reprinted with permission from H. Saito *et al.*, *J. Phys. Chem. C* **2019**, *123*, 26272–26281. Copyright 2019 American Chemical Society.

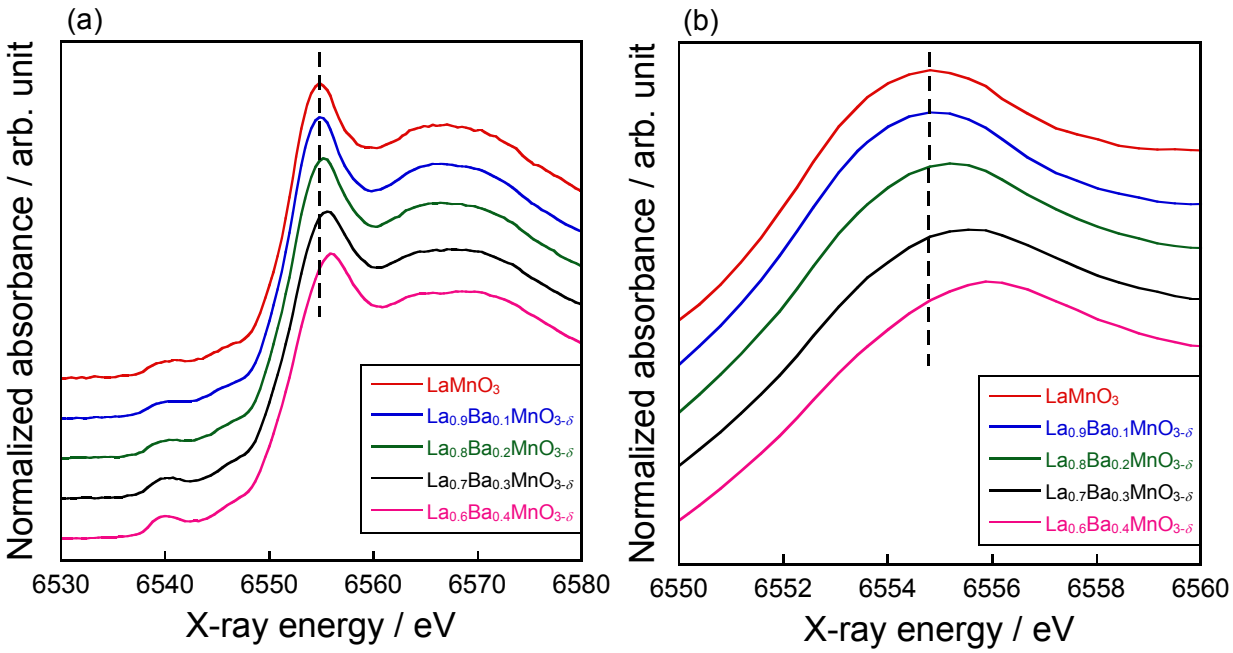

Figure 3.16. Mn *K*-edge XANES spectra of (a) $La_{1-x}Ba_xMnO_{3-\delta}$ (x = 0–0.4) and (b) enlarged spectra. Reprinted with permission from H. Saito *et al.*, *J. Phys. Chem. C* **2019**, *123*, 26272–26281. Copyright 2019 American Chemical Society.

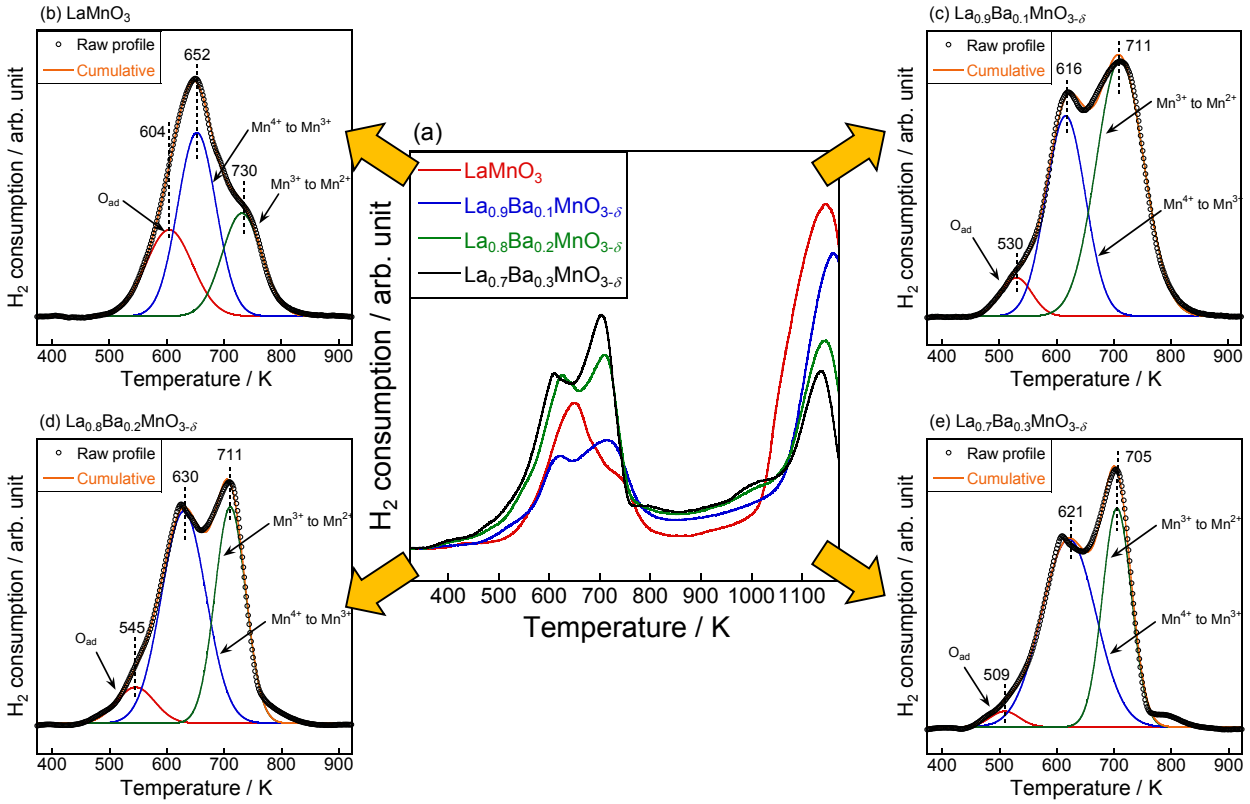

Figure 3.17. H_2-TPR profiles of (a) $La_{1-x}Ba_xMnO_{3-\delta}$ (x = 0–0.3). Enlarged profiles of (b) $LaMnO_3$, (c) $La_{0.9}Ba_{0.1}MnO_{3-\delta}$, (d) $La_{0.8}Ba_{0.2}MnO_{3-\delta}$ and (e) $La_{0.7}Ba_{0.3}MnO_{3-\delta}$ in the temperature range of 373–923 K. Reprinted with permission from H. Saito *et al.*, *J. Phys. Chem. C* **2019**, *123*, 26272–26281. Copyright 2019 American Chemical Society.

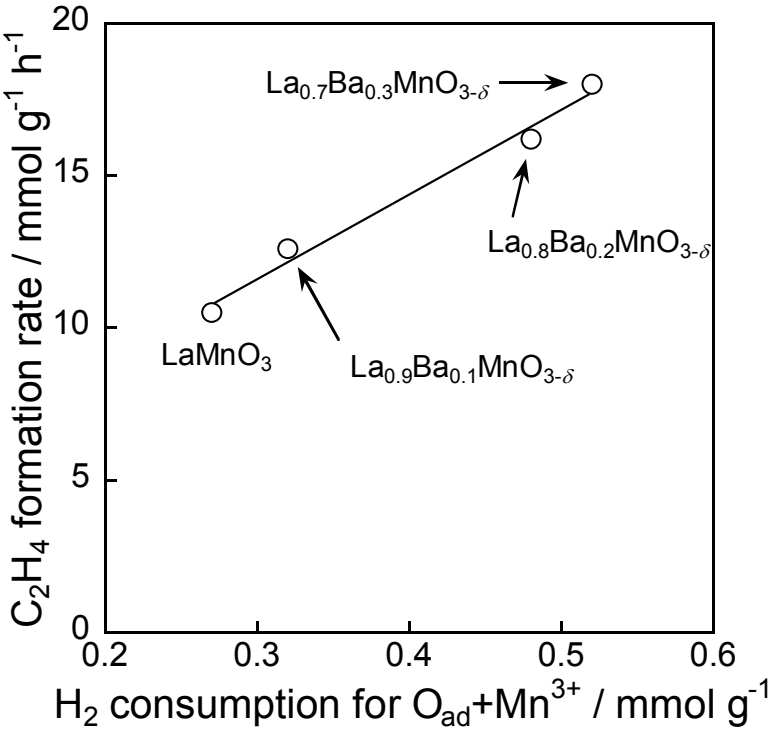

Figure 3.18. Activity and reducibility relationship for dehydrogenation of ethane in the presence of steam over $La_{1-x}Ba_xMnO_{3-\delta}$ (x = 0–0.3). Adsorbed oxygen denoted as O_{ad} and reducible Mn^{3+} were quantified by H_2-TPR. Reprinted with permission from H. Saito *et al.*, *J. Phys. Chem. C* **2019**, *123*, 26272–26281. Copyright 2019 American Chemical Society.

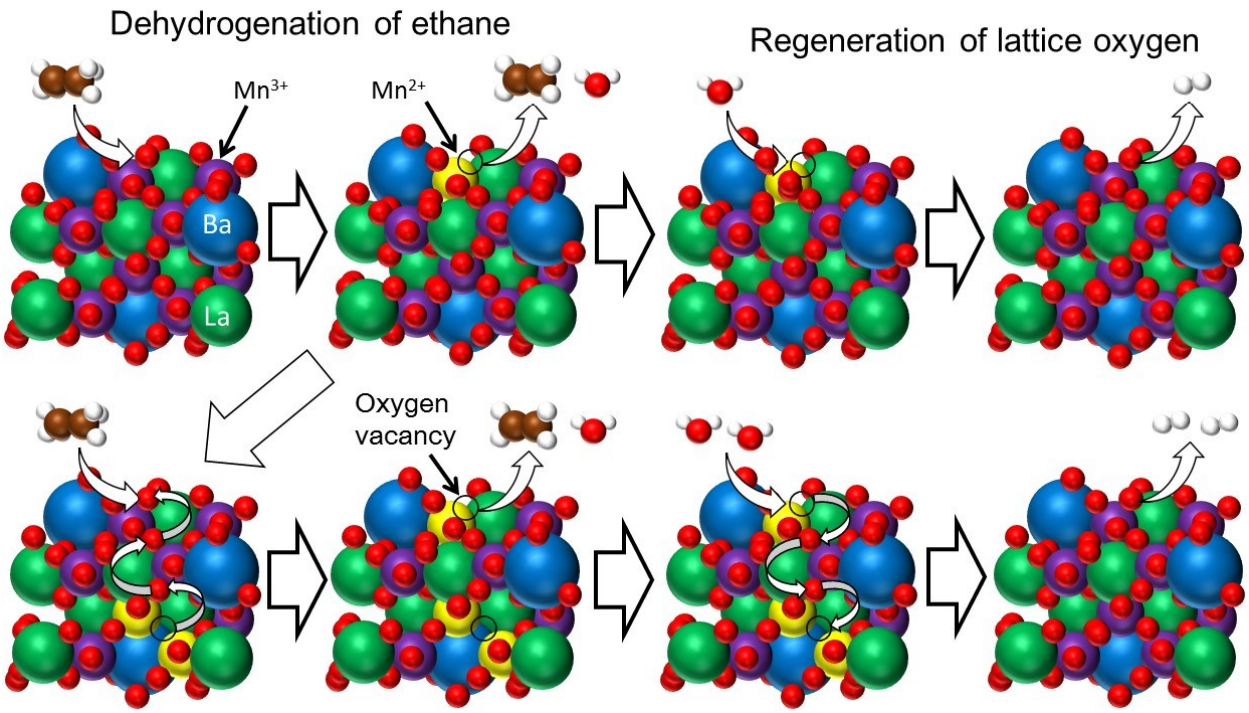

Figure 3.19. Schematic image of dehydrogenation of ethane over Ba-doped $LaMnO_3$ in the presence of steam. Reprinted with permission from H. Saito *et al.*, *J. Phys. Chem. C* **2019**, *123*, 26272–26281. Copyright 2019 American Chemical Society.

Table 3.1. Catalytic performance of $LaBO_3$ perovskites (B = Cr, Mn, Fe, Co and Ni) at 973 K after 120 min with time on stream. Reproduced with permission from H. Saito *et al.*, *J. Phys. Chem. C* **2019**, *123*, 26272–26281. Copyright 2019 American Chemical Society.

Catalyst	Conversion / %	Selectivity / %				C_2H_4 formation rate / mmol g^{-1} h^{-1}
		CO	CH_4	CO_2	C_2H_4	
$LaCrO_3$	1.9	1.4	1.1	3.8	93.7	8.0
$LaMnO_3$	2.9	0.7	0.7	13.9	84.7	10.5
$LaFeO_3$	4.1	2.0	1.2	27.6	69.2	12.8
$LaCoO_3$	2.1	0.2	1.0	9.1	89.7	8.4
$LaNiO_3$	4.0	22.3	0.3	54.5	22.9	4.0

Table 3.2. Catalytic performance of $La_{0.8}A_{0.2}BO_{3-\delta}$ perovskites (A = Ca, Sr and Ba; B = Mn, Fe and Co) at 973 K after 120 min with time on stream. Reproduced with permission from H. Saito *et al.*, *J. Phys. Chem. C* **2019**, *123*, 26272–26281. Copyright 2019 American Chemical Society.

Catalyst	Conversion / %	Selectivity / %				C_2H_4 formation rate / mmol g^{-1} h^{-1}
		CO	CH_4	CO_2	C_2H_4	
$La_{0.8}Ca_{0.2}MnO_{3-\delta}$	2.2	0.3	2.8	15.5	81.4	7.7
$La_{0.8}Sr_{0.2}MnO_{3-\delta}$	2.9	0.4	7.3	16.0	76.3	9.4
$La_{0.8}Ba_{0.2}MnO_{3-\delta}$	4.1	0.2	5.1	7.5	87.2	16.2
$La_{0.8}Ca_{0.2}FeO_{3-\delta}$	1.9	0.3	1.1	13.7	84.9	6.8
$La_{0.8}Sr_{0.2}FeO_{3-\delta}$	1.8	0.4	0.5	16.5	82.6	6.3
$La_{0.8}Ba_{0.2}FeO_{3-\delta}$	3.5	0.6	3.1	18.2	78.0	11.9
$La_{0.8}Ca_{0.2}CoO_{3-\delta}$	1.7	0.1	0.6	4.5	94.8	6.7
$La_{0.8}Sr_{0.2}CoO_{3-\delta}$	1.9	0.1	1.4	5.8	92.8	7.6
$La_{0.8}Ba_{0.2}CoO_{3-\delta}$	2.3	0.1	1.7	7.0	91.2	8.6

Table 3.3. The amount of carbon deposition on spent $La_{0.8}Ba_{0.2}MnO_{3-\delta}$. Reproduced with permission from H. Saito *et al.*, *J. Phys. Chem. C* **2019**, *123*, 26272–26281. Copyright 2019 American Chemical Society.

Catalyst	The amount of carbon deposition / mg g_{cat}^{-1}
$La_{0.8}Ba_{0.2}MnO_{3-\delta}$ [a]	2.5
$La_{0.8}Ba_{0.2}MnO_{3-\delta}$ after dry [b]	1.9

[a] The spent catalyst after the reaction for 4 h was used for the measurement.

[b] The catalyst after the dry test for 40 min was used for the measurement.

Table 3.4. H_2 consumption of $LaMnO_3$ and $La_{0.8}A_{0.2}MnO_{3-\delta}$ (A = Ca, Sr and Ba) calculated from H_2-TPR profiles. Reproduced with permission from H. Saito *et al.*, *J. Phys. Chem. C* **2019**, *123*, 26272–26281. Copyright 2019 American Chemical Society.

Catalyst	H_2 consumption / mmol g^{-1}		
	O_{ad} [a]	Mn^{4+} to Mn^{3+}	Mn^{3+} to Mn^{2+}
$LaMnO_3$	0.10	0.31	0.16
$La_{0.8}Ca_{0.2}MnO_{3-\delta}$	0.094	0.37	0.081
$La_{0.8}Sr_{0.2}MnO_{3-\delta}$	0.10	0.34	0.049
$La_{0.8}Ba_{0.2}MnO_{3-\delta}$	0.14	0.36	0.34

[a] O_{ad}: adsorbed oxygen

Table 3.5. Catalytic performance of $La_{1-x}Ba_xMnO_{3-\delta}$ perovskites (x = 0–0.4) at 120 min with time on stream. Reproduced with permission from H. Saito *et al.*, *J. Phys. Chem. C* **2019**, *123*, 26272–26281. Copyright 2019 American Chemical Society.

Catalyst	Conversion / %	Selectivity / %				C_2H_4 formation
		CO	CH_4	CO_2	C_2H_4	rate / mmol g^{-1} h^{-1}
$LaMnO_3$	2.9	0.7	0.7	13.9	84.7	10.5
$La_{0.9}Ba_{0.1}MnO_{3-\delta}$	3.5	0.2	5.3	9.2	85.2	12.6
$La_{0.8}Ba_{0.2}MnO_{3-\delta}$	4.1	0.2	5.1	7.5	87.2	16.2
$La_{0.7}Ba_{0.3}MnO_{3-\delta}$	4.8	0.2	5.2	6.5	88.0	18.0
$La_{0.6}Ba_{0.4}MnO_{3-\delta}$	4.0	0.1	5.2	6.5	88.2	15.4

Table 3.6. H_2 consumption of $La_{1-x}Ba_xMnO_{3-\delta}$ (x = 0–0.3) calculated from H_2-TPR profiles. Reproduced with permission from H. Saito *et al.*, *J. Phys. Chem. C* **2019**, *123*, 26272–26281. Copyright 2019 American Chemical Society.

Catalyst	H_2 consumption / mmol g^{-1}		
	O_{ad} [a]	Mn^{4+} to Mn^{3+}	Mn^{3+} to Mn^{2+}
$LaMnO_3$	0.10	0.31	0.16
$La_{0.9}Ba_{0.1}MnO_{3-\delta}$	0.025	0.18	0.29
$La_{0.8}Ba_{0.2}MnO_{3-\delta}$	0.14	0.36	0.34
$La_{0.7}Ba_{0.3}MnO_{3-\delta}$	0.13	0.40	0.39

[a] O_{ad}: adsorbed oxygen

Table 3.7. BET surface area of $La_{1-x}Ba_xMnO_{3-\delta}$ (x = 0–0.4). Reproduced with permission from H. Saito *et al.*, *J. Phys. Chem. C* **2019**, *123*, 26272–26281. Copyright 2019 American Chemical Society.

Catalyst	BET surface area / $m^2\ g^{-1}$
$LaMnO_3$	9.7
$La_{0.9}Ba_{0.1}MnO_{3-\delta}$	7.2
$La_{0.8}Ba_{0.2}MnO_{3-\delta}$	12.8
$La_{0.7}Ba_{0.3}MnO_{3-\delta}$	17.8
$La_{0.6}Ba_{0.4}MnO_{3-\delta}$	11.8

Chapter 4 Dehydroaromatization of ethane over Co/H-ZSM-5 catalyst

The text in this chapter is reproduced in part from H. Saito, R. Terunuma, K. Kojima, T. Yabe, S. Ogo, H. Hirayama, Y. Tanaka, Y. Sekine, Non-Oxidative Ethane Dehydroaromatization on Co/H-ZSM-5 Catalyst. *Chem. Lett.* **2017**, *46*, 1646–1649. Copyright 2017 The Chemical Society of Japan.

4.1. Introduction

Producing aromatic hydrocarbons such as benzene, toluene, and xylene (BTX) from natural gas is attracting attention because of the vast abundance, low-cost, and wide distribution of natural gas resources. Methane, the main component of natural gas, can be converted to BTX at temperatures higher than 973 K because of thermodynamic limitations, resulting in an energy-intensive process.[1] Ethane, a gas accompanying natural gas, is now converted to ethylene using an ethane cracker. Conversion of ethane to BTX, a process designated as ethane dehydroaromatization (EDA), presents benefits for the effective utilization of ethane. It can occur at temperatures lower than 873 K.[2] Therefore, valuable BTX can be produced efficiently from a cheap ethane feedstock.

In the EDA reaction, **MFI**-type zeolite (ZSM-5) in H-form is often used as a catalyst support because ZSM-5 has micropores that are nearly equal to the kinetic diameter of BTX (*ca.* 0.5 nm).[3] Actually, ZSM-5 exhibits shape selectivity to form BTX. Active metals are loaded to promote dehydrogenation of ethane to ethylene, regarded as an intermediate for EDA.[4] Ethylene was converted sequentially to BTX through oligomerization, cyclization, and dehydrogenation on Brønsted acid sites and active metal sites.[5, 6] Reportedly, active metals such as Ga, Zn, Mo, Re, and Pt are effective for the reactions.[6–10] These active metals, however, present several difficulties. Actually, Zn exhibits high catalytic activity, but its oxides are readily reduced and vaporized under reductive conditions,[11] which can decrease the number of active sites. The industrial use of Pt is difficult because of its high cost. Mo and Re are unsuitable for their regeneration under oxidative conditions because sublimation of MoO_3 and Re_2O_7 occurs.[12, 13] The Ga catalyst (Ga/H-ZSM-5) shows a lower activity than Zn/H-ZSM-5.[7] Therefore, a novel metal catalyst must be used to overcome these difficulties. In other words, an active metal with the high catalytic performance is expected to be cost-effective and stable under the reaction and the oxidative atmosphere.

In this chapter, we investigated active metals belonging to the fourth period in the periodic table: V, Mn, Fe, Co, Ni, Cu, and Ga. Cr and Zn were excluded because CrO_3 has toxicity and because ZnO is easily reduced and vaporized under the reaction atmosphere. Among them, we found that the Co/H-ZSM-5 catalyst exhibited superior performance. Therefore, the effects of catalyst

preparation on Co/H-ZSM-5 were investigated. Finally, various characterizations were conducted to elucidate the nature of Co species on the H-ZSM-5 zeolite.

4.2. Experimental

4.2.1. Catalyst preparation

Catalyst support of H-ZSM-5 was achieved by calcining NH_4-ZSM-5 (CBV 5524G; Zeolyst) at 823 K for 5 h. Metal-supported H-ZSM-5 catalysts containing 5wt% active metal were prepared respectively using an impregnation (IM) method. First H-ZSM-5 was soaked in distilled water and was stirred for 2 h *in vacuo* with a rotary evaporator at room temperature. Next, aqueous solution of a metal precursor was added to the suspension and was stirred at atmospheric pressure for 2 h. The vanadium precursor was its ammonium salt. Others were their nitrate. Subsequently, the suspension was evaporated to dryness, dried in air with an oven at 393 K for 24 h, and calcined at 773 K for 5 h. Co/H-ZSM-5 was also prepared using an ion-exchange (IE) method. First, H-ZSM-5 was soaked and stirred in the 0.02 mol L^{-1} aqueous solution of $Co(NO_3)_2 \cdot 6H_2O$ at 353 K for 24 h. The suspension contained 1 g of H-ZSM-5 in 100 mL of the aqueous solution. Then, the powder was separated by suction filtration, washed with distilled water and dried in air with an oven at 393 K for 24 h. The dried powder was calcined at 773 K for 5 h. The Co/H-ZSM-5 catalysts prepared using the IM and IE method are denoted, respectively, as Co/H-ZSM-5 IM and Co/H-ZSM-5 IE.

4.2.2. Catalytic activity tests

Catalytic activity tests were conducted in a fixed bed reactor at atmospheric pressure for 4 h. Catalyst of 0.2 g was charged into a quartz tube (i.d. 6 mm). The temperature was raised to 873 K under Ar atmosphere. Then, 80vol% C_2H_6 and balanced N_2 were supplied at a total flow rate of 25 mL min^{-1} (SATP). All reactions were conducted under *pseudo*-kinetic conditions, i.e. the conversion rate is not high. Products were analyzed using a gas chromatograph (GC-8A; Shimadzu Corp.) equipped with a thermal conductivity detector (TCD) using a Shincarbon ST packed column (3 mm × 4 m; Shinwa Chemical Industries Ltd.) to separate H_2, N_2, CH_4, C_2H_4, and C_2H_6, and an on-line gas chromatograph (GC-8A; Shimadzu Corp.) equipped with a flame ionization detector (FID) using a HP-PLOT/Q capillary column (0.53 mm × 30 m; Agilent Technologies Inc.) to separate CH_4, C_2H_4, C_2H_6, C_3 hydrocarbons, C_4 hydrocarbons, benzene, toluene, ethylbenzene, and xylene. Ethane conversion and product selectivity were calculated as shown below.

$$\text{Ethane conversion [\%]} = \frac{\sum_{n=1}^{8} n \cdot f^{\text{out}}_{C_n}}{2 f^{\text{in}}_{C_2H_6}} \cdot 100 \tag{4.1}$$

$$\text{Selectivity [\%]} = \frac{n \cdot f^{\text{out}}_{C_n}}{\sum_{n=1}^{8} n \cdot f^{\text{out}}_{C_n}} \cdot 100 \quad (4.2)$$

Here, letters f and n in equations (4.1) and (4.2) respectively denote the formation rates of hydrocarbons shown as the subscript and the number of carbon atoms in the hydrocarbon. C_n in equations (4.1) and (4.2) denote hydrocarbon products. The superscripts of "in" and "out" also respectively stand for the inlet and outlet gas. The effective carbon number was used to calculate the formation rates of C_4 hydrocarbons, benzene, toluene, ethylbenzene, and xylene.

4.2.3. Characterizations

BET specific surface area was calculated from the nitrogen adsorption isotherm obtained using N_2 physisorption at 77 K (Gemini VII 2390a; Micromeritics Instrument Corp.). The Al and Co contents in catalysts were measured using an induced coupled plasma (ICP) emission spectrometer (iCAP-6500; Thermo Scientific).

X-ray diffraction (XRD) patterns were measured for crystal structure analyses using an X-ray diffractometer (SmartLab 3; Rigaku Corp.) with Cu $K\alpha$ radiation at 40 kV and 40 mA.

Temperature-programmed oxidation (TPO) was used to ascertain the amounts of carbon deposition on the spent catalysts with thermogravimetry (TGA-50; Shimadzu Corp.). The amount of carbon deposition was calculated from the weight loss of samples as follows.

$$\text{The amount of carbon deposition [mg } g^{-1}_{\text{cat}}] = \frac{W_i - W_f}{W_f} \quad (4.3)$$

Variables W_i and W_f in equation (4.3) respectively denote the initial and final weight of the samples.

Temperature-programmed reduction (TPR) was also used to investigate the reducibility of Co species under H_2 atmosphere. The TPR profiles were obtained using a catalyst analyzer (BELCAT II; MicrotracBEL Corp.) equipped with a TCD.

X-ray absorption fine structure (XAFS) spectroscopy was applied to elucidate the electronic state of Co species on fresh and spent catalysts. XAFS spectra were obtained for Co K-edge at the BL14B2 station of SPring-8 in Japan. The catalysts were physically mixed with BN using a planetary mill (Pulverisette 6; Fritsch GmbH) to shape pellets (7 mmϕ). Spent catalysts were prepared by exposing the pellets under the reaction conditions. Subsequently, the spent catalysts were packed and sealed under Ar atmosphere without exposure in O_2 atmosphere. XAFS spectroscopy was conducted at room temperature in transmission mode using the Si(111) crystal monochromator. Analyses by X-ray absorption near-edge structure (XANES) were done using software (Demeter ver. 0.9.025; Bruce Ravel).

4.3. Results and discussion

4.3.1. Screening an appropriate active metal

Figure 4.1 presents ethane conversion and aromatics selectivity with time on stream over H-ZSM-5 and 5wt% M/H-ZSM-5 (M = V, Mn, Fe, Co, Cu or Ga). Selectivity to other products at 67 min with time on stream is presented in Table 4.1. The result of Ni is not presented in Figure 4.1 and Table 4.1 because the catalyst bed was plugged by coke deposition. Fe and Co catalysts exhibited high catalytic activity and aromatics selectivity. Although high aromatics selectivity (*ca.* 20%) was obtained over Ga/H-ZSM-5, ethane conversion of Ga/H-ZSM-5 was lower than that of Fe or Co/H-ZSM-5. As a result, the aromatics yield decreases in the order Fe ≈ Co > Ga. The other M/H-ZSM-5 catalysts showed low ethane conversion and aromatics selectivity. The aromatics selectivity of Fe/H-ZSM-5 increased at the initial stage, corresponding to the formation of the active sites under the reaction atmosphere. Tan reported that Fe on H-ZSM-5 was carburized in non-oxidative methane dehydroaromatization.[14] The carburized Fe species played an important role in the formation of aromatic hydrocarbons. However, the formation of Fe carbides is unsuitable for its regeneration under oxidative conditions because Fe carbides can be oxides such as Fe_2O_3, which results in the disappearance of active sites for the formation of aromatic hydrocarbons. Therefore, Co/H-ZSM-5 is the optimal catalyst for the EDA reaction.

4.3.2. Effects of preparation method

To investigate the influences of catalyst preparation method on catalytic properties, Co/H-ZSM-5 was also prepared using IE method. Table 4.2 presents physicochemical and textural properties of these catalysts. BET specific surface area of Co/H-ZSM-5 IM decreased in comparison with Co/H-ZSM-5 IE. Elemental analyses revealed that the Co content of Co/H-ZSM-5 IE was much lower than that of Co/H-ZSM-5 IM. The Co/Al molar ratio of Co/H-ZSM-5 IM exceeded the ion-exchange capacity (Co/Al = 0.5). These results would indicate that Co oxides are located on the external surface of Co/H-ZSM-5 IM. The decrease in the BET specific surface area would be caused by the plugging of micropores, which is caused by the Co oxide formation. Figure 4.2 shows XRD patterns of fresh Co/H-ZSM-5 catalysts and Co_3O_4 as a control. The **MFI** structure was maintained after Co loading. A peak derived from Co_3O_4(311) was observed in the pattern of Co/H-ZSM-5 IM, but no peak derived from Co species was observed in that of Co/H-ZSM-5 IE. Therefore, Co_3O_4 existed on the external surface of Co/H-ZSM-5 IM. Also, Co species in micropores (*ca.* 0.5 nm) would be highly dispersed. Peaks of these Co species cannot be observed using XRD measurements.

Figure 4.3 presents ethane conversion and aromatics selectivity with time on stream over Co/H-ZSM-5 catalysts prepared by the IM and IE methods. Co/H-ZSM-5 IE exhibited higher catalytic activity and aromatics selectivity than Co/H-ZSM-5 IM did. In addition, Co/H-ZSM-5 IE showed no rapid decrease in aromatics selectivity at the initial stage. As shown in Table 4.2, the amount of carbon deposition on Co/H-ZSM-5 IE was much less than that on Co/H-ZSM-5 IM. In the EDA reaction, the catalytic performance is known to be deactivated by coke formation.[2] Therefore, the high catalytic performance of Co/H-ZSM-5 IE is attributable to the suppression of coke formation.

Improvement in the catalytic performance of Co/H-ZSM-5 is derived from the difference in catalyst preparation that affects the nature of active sites, especially Co species. Therefore, we first performed TPR measurement under H_2 atmosphere to investigate the reducibility of Co species on the catalysts. Figure 4.4 shows TPR profiles of Co/H-ZSM-5 catalysts and Co_3O_4 as a control. No definite peak was observed in the profile of Co/H-ZSM-5 IE, which indicates that Co species existing at ion-exchange sites were not reduced easily. However, three peaks (641, 718, and 935 K) appeared in the profile of Co/H-ZSM-5 IM. In comparison with the profile of Co_3O_4, the first two peaks respectively corresponded to the reduction of bulk Co_3O_4 to CoO and CoO to Co^0. The shift of the reduction peaks to lower temperature was also reported in the literature.[15] The peak at 935 K might be attributed to the reduction of CoO_x ($1 \leq x \leq 1.5$) clusters existing in micropores of H-ZSM-5.[16] Considering the reaction temperature and XRD pattern of Co/H-ZSM-5 IM, the bulk Co_3O_4 existing on the external surface of H-ZSM-5 is reduced to Co^0.

In addition, Co *K*-edge XANES analyses were used to elucidate the electronic state of Co species on Co/H-ZSM-5 IM and IE. Figure 4.5 portrays XANES spectra of fresh and spent Co/H-ZSM-5 IM and IE. Co foil, CoO, and Co_3O_4 were also measured as standard samples to assess the electronic state of Co. The XANES spectrum of the fresh Co/H-ZSM-5 IM was similar to that of Co_3O_4. This result is in accordance with the XRD pattern of Co/H-ZSM-5 IM. The electronic state of Co species on the spent Co/H-ZSM-5 IM shows good agreement with that of Co^0. Moreover, features in X-ray energy range around 7.72 keV indicate that the spent Co/H-ZSM-5 IM contains Co^{2+}, which probably corresponds to CoO_x clusters not reduced at the reaction temperature. As presented in Table 4.3, the results of the linear combination fitting of XANES spectra also indicate that the spent Co/H-ZSM-5 IM contains Co^{2+} species. In contrast, little difference was observed between fresh and spent Co/H-ZSM-5 IE. In both spectra, the pre-edge feature resembles CoO. Therefore, we presumed that only Co^{2+} cations exist in Co/H-ZSM-5 IE and that ion-exchanged Co^{2+} cations are extremely stable during the reaction.

We anticipate that the differences in the nature of Co species affect catalytic activity, stability, and aromatics selectivity. The schematic image of perspective Co/H-ZSM-5 during the reaction is shown in Figure 4.6. Co_3O_4 on the external surface of Co/H-ZSM-5 IM was reduced to Co^0 during the reaction. The large amount of carbon deposition on Co/H-ZSM-5 IM indicates that Co^0 promotes the decomposition of ethane to form coke,[17] which results in deactivation of the catalyst. However, most of the Co species in Co/H-ZSM-5 IE are highly dispersed Co^{2+} cations. They are not reduced easily under the reaction atmosphere. The high catalytic activity and small amount of carbon deposition on Co/H-ZSM-5 IE demonstrate that Co^{2+} cations efficiently promoted dehydrogenation of ethane to ethylene, which is an intermediate in the EDA reaction, without coke formation.

4.4. Chapter Conclusion

We investigated various metal-supported H-ZSM-5 catalysts for use in non-oxidative ethane dehydroaromatization. Co/H-ZSM-5 exhibited high aromatics yield without the induction period in the formation of aromatic hydrocarbons. Prepared by the IE method, improvement in the catalytic performance of Co/H-ZSM-5 was achieved. TPO measurement revealed that the amount of carbon deposition decreased, which would explain the high catalytic performance. XRD, TPR, and XANES measurements also revealed highly dispersed and non-reducible Co^{2+} cations existing in Co/H-ZSM-5 IE. These Co^{2+} cations play a crucially important role in promoting the activation of ethane without coke formation.

References

1. J. J. Spivey, G. Hutchings, Catalytic Aromatization of Methane. *Chem. Soc. Rev.* **2014**, *43*, 792–803.
2. A. Hagen, F. Roessner, Ethane to Aromatic Hydrocarbons: Past, Present, Future. *Catal. Rev. –Sci. Eng.* **2000**, *42(4)*, 403–437.
3. C. Baerlocher, L. B. McCusker, D. H. Olson, *Atlas of Zeolite Framework Types 6th Ed*., Elsevier, Amsterdam, **2007**, 212–213; See also: http://www.iza-structure.org/databases/.
4. O. P. Keipert, D. Wolf, P. Schulz, M. Baerns, Kinetics of Ethane Aromatization over a Gallium-Doped H-ZSM-5 Catalyst. *Appl. Catal. A: Gen.* **1995**, *131*, 347–365.
5. Y. Ono, Transformation of Lower Alkanes into Aromatic Hydrocarbons over ZSM-5 Zeolites. *Catal. Rev. –Sci. Eng.* **1992**, *34(3)*, 179–226.
6. P. Schulz, M. Baerns, Aromatization of Ethane over Gallium-Promoted H-ZSM-5 Catalysts. *Appl. Catal.* **1991**, *78*, 15–29.
7. V. I. Yakerson, T. V. Vasina, L. I. Lafer, V. P. Sytnyk, G. L. Dykh, A. V. Mokhov, O. V. Bragin, Kh. M. Minachev, The Properties of Zinc and Gallium Containing Pentasils — The Catalysts for the Aromatization of Lower Alkanes. *Catal. Lett.* **1989**, *3*, 339–346.
8. F. Solymosi, A. Szőke, Conversion of Ethane into Mo_2C/ZSM-5 Catalyst. *Appl. Catal. A: Gen.* **1998**, *166*, 225–235.
9. F. Solymosi, P. Tolmacsov, Conversion of Ethane into Benzene on Re/ZSM-5. *Catal. Lett.* **2004**, *93(1-2)*, 7–11.
10. K.-H. Steinberg, U. Mroczek, F. Roessner, Aromatization of Ethane on Platinum Containing ZSM-5 Zeolites. *Appl. Catal.* **1990**, *66*, 37–44.
11. D. J. C. Yates, The Stability of Metallic Cations in Zeolites. *J. Phys. Chem.* **1965**, *69*, 1676–1683.
12. R. W. Borry III, Y. H. Kim, A. Huffsmith, J. A. Reimer, E. Iglesia, Structure and Density of Mo and Acid Sites in Mo-Exchanged H-ZSM5 Catalysts for Nonoxidative Methane Conversion. *J. Phys. Chem. B* **1999**, *103*, 5787–5796.
13. C. Bolivar, H. Charcosset, R. Frety, M. Primet, L. Tournayan, Platinum-Rhenium/Alumina Catalysts: I. Investigation of Reduction by Hydrogen. *J. Catal.* **1975**, *39*, 249–259.

14. P. Tan, Active Phase, Catalytic Activity, and Induction Period of Fe/zeolite Material in Nonoxidative Aromatization of Methane. *J. Catal.* **2016**, *338*, 21–29.
15. A. Rokicińska, M. Drozdek, B. Dudek, B. Gil, P. Michorczyk, D. Brouri, S. Dzwigaj, P. Kuśtrowski, Cobalt-Containing BEA Zeolite for Catalytic Combustion of Toluene. *Appl. Catal. B: Environ.* **2017**, *212*, 59–67.
16. W. Li, S. Y. Yu, G. D. Meitzner, E. Iglesia, Structure and Properties of Cobalt-Exchanged H-ZSM-5 Catalysts for Dehydrogenation and Dehydrocyclization of Alkanes. *J. Phys. Chem. B* **2001**, *105*, 1176–1184.
17. U. Narkiewicz, M. Podsiadły, R. Jędrzejewski, I. Pełech, Catalytic Decomposition of Hydrocarbons on Cobalt, Nickel and Iron Catalysts to Obtain Carbon Nanomaterials. *Appl. Catal. A: Gen.* **2010**, *384*, 27–35.

Figures and Tables

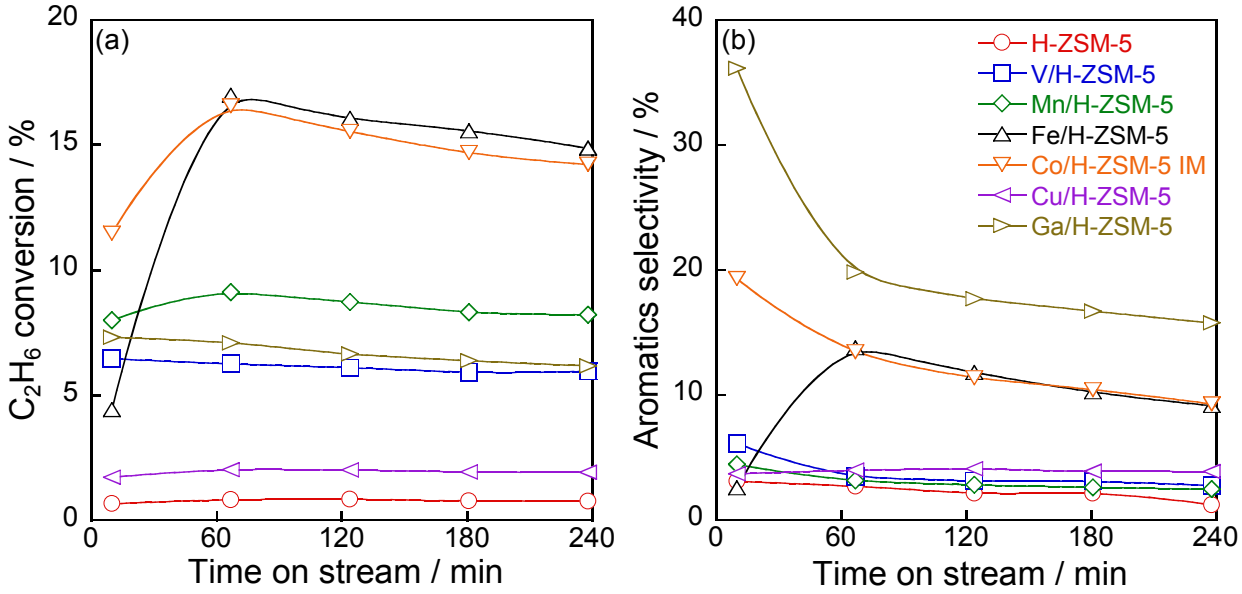

Figure 4.1. (a) C_2H_6 conversion and (b) aromatics selectivity at 873 K with time on stream over various H-ZSM-5 catalysts. Reprinted from H. Saito *et al.*, *Chem. Lett.* **2017**, *46*, 1646–1649. Copyright 2017 The Chemical Society of Japan.

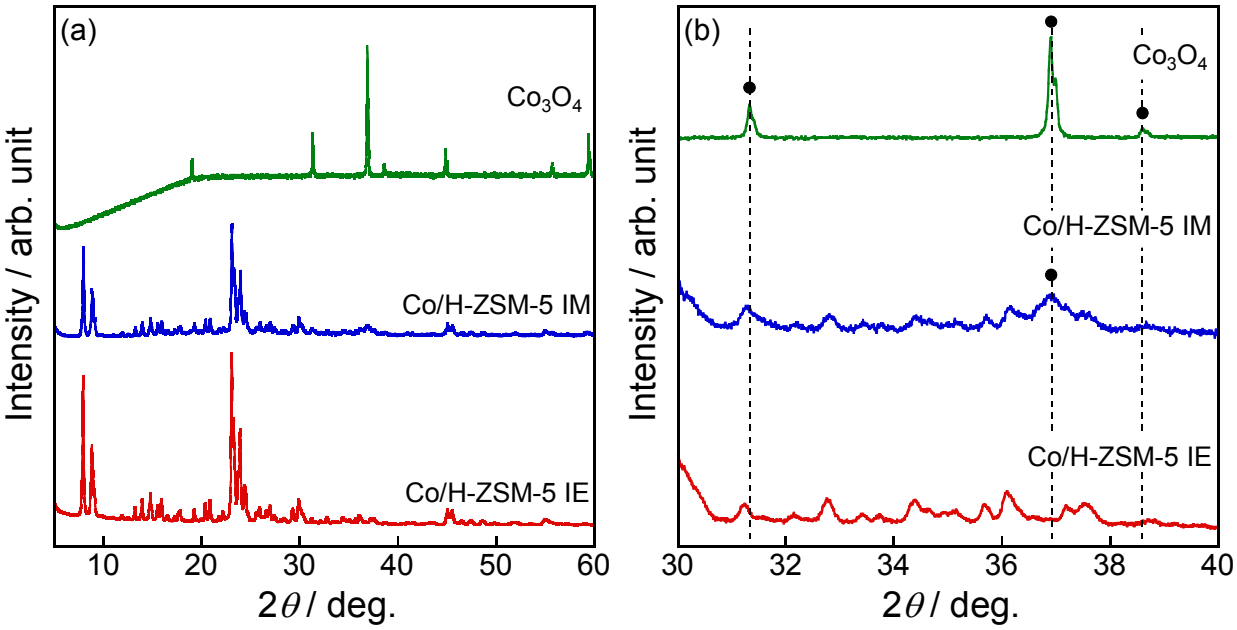

Figure 4.2. (a) XRD patterns of Co/H-ZSM-5 IE, Co/H-ZSM-5 IM and Co_3O_4 as a control and (b) the enlarged patterns in the 2θ range from 30 to 40 degree. Reprinted from H. Saito *et al.*, *Chem. Lett.* **2017**, *46*, 1646–1649. Copyright 2017 The Chemical Society of Japan.

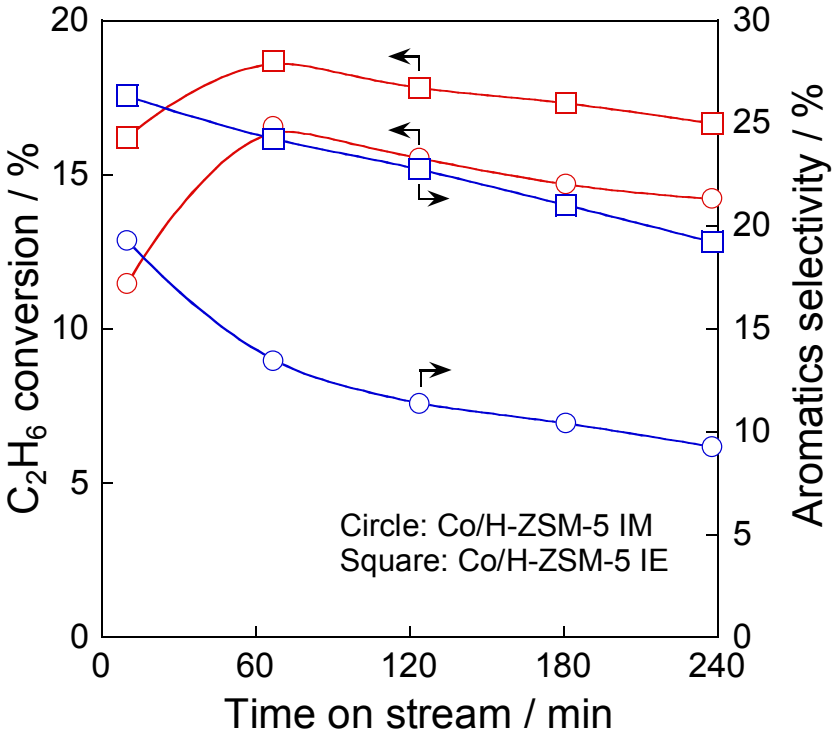

Figure 4.3. C_2H_6 conversion (blue) and aromatics selectivity (red) with time on stream over Co/H-ZSM-5 IM (circle) and Co/H-ZSM-5 IE (square). Reprinted from H. Saito *et al.*, *Chem. Lett.* **2017**, *46*, 1646–1649. Copyright 2017 The Chemical Society of Japan.

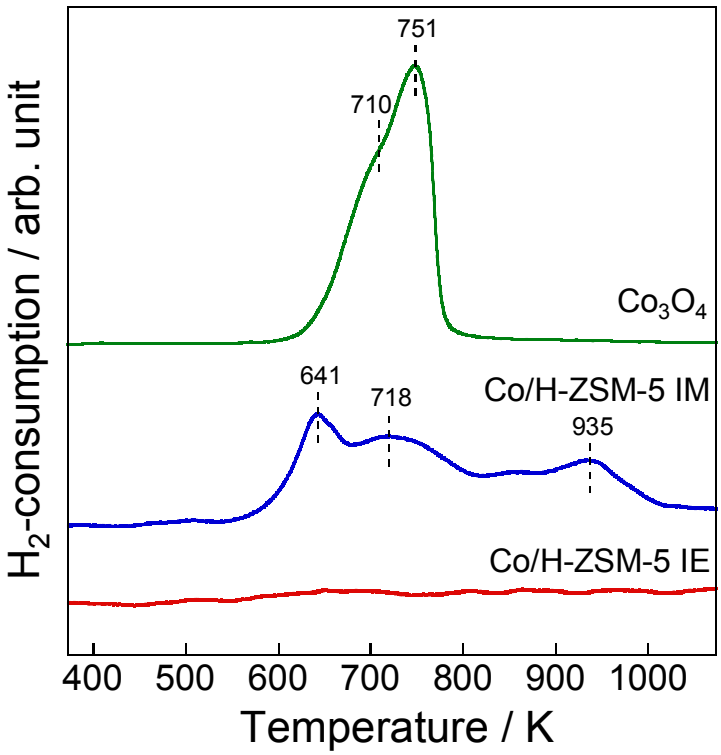

Figure 4.4. TPR profiles of Co/H-ZSM-5 IE, Co/H-ZSM-5 IM and Co_3O_4. Reprinted from H. Saito *et al.*, *Chem. Lett.* **2017**, *46*, 1646–1649. Copyright 2017 The Chemical Society of Japan.

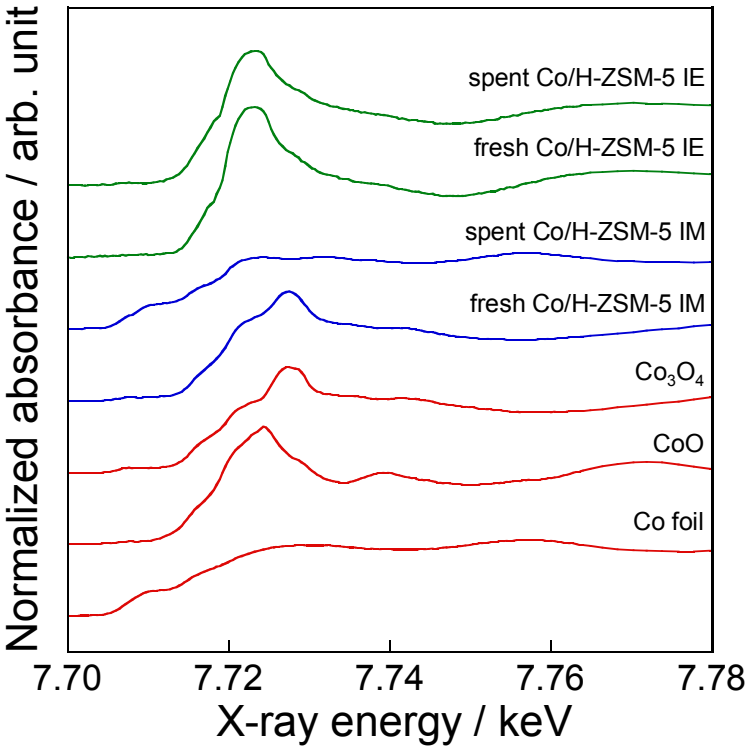

Figure 4.5. Co *K*-edge XANES spectra of fresh and spent Co/H-ZSM-5 catalysts and standards (Co foil, CoO and Co_3O_4). Reprinted from H. Saito *et al.*, *Chem. Lett.* **2017**, *46*, 1646–1649. Copyright 2017 The Chemical Society of Japan.

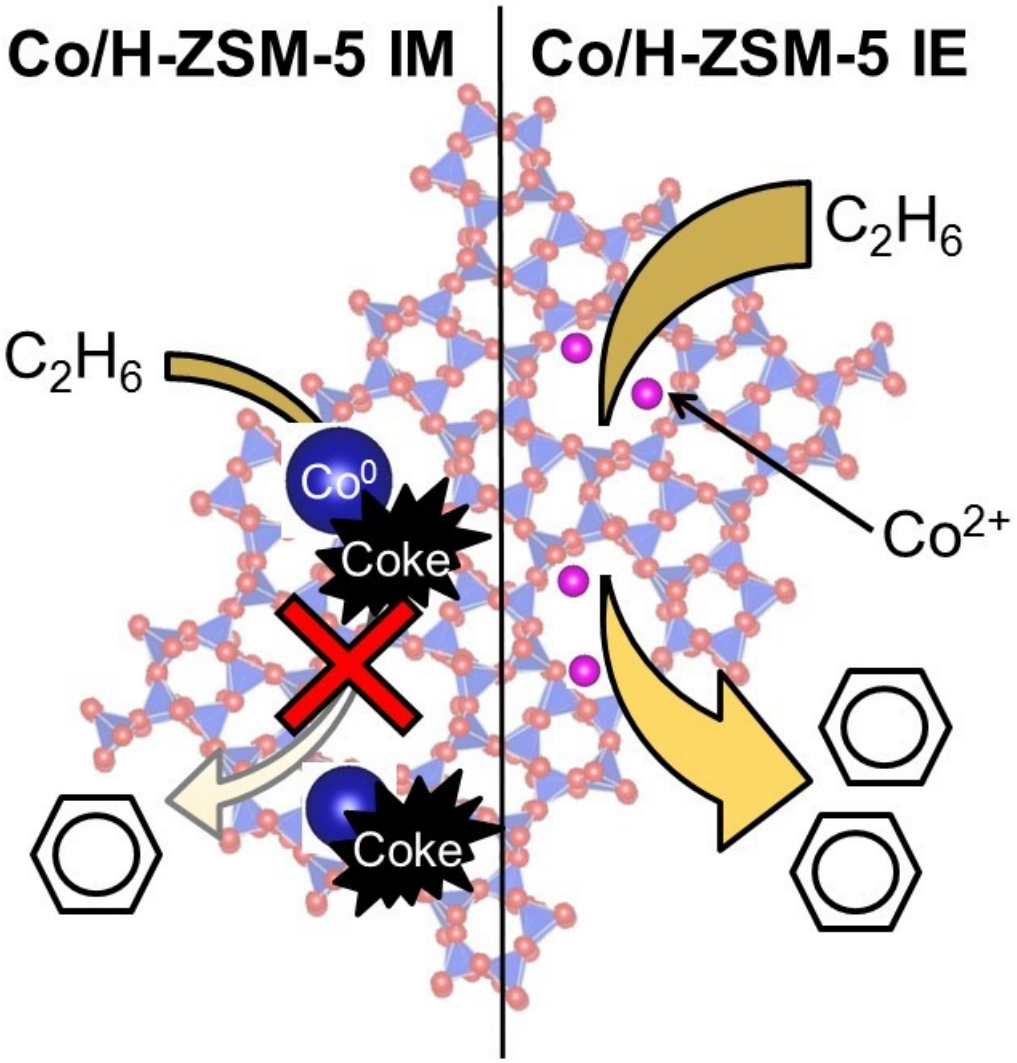

Figure 4.6. Schematic image of ethane dehydroaromatization over Co/H-ZSM-5 prepared by different method. Reprinted from H. Saito *et al.*, *Chem. Lett.* **2017**, *46*, 1646–1649. Copyright 2017 The Chemical Society of Japan.

Table 4.1. Catalytic activity and products selectivity over various catalysts at 67 min with time on stream. Reproduced from H. Saito *et al.*, *Chem. Lett.* **2017**, *46*, 1646–1649. Copyright 2017 The Chemical Society of Japan.

Catalyst[a]	Conversion / %	Selectivity / %				
		CH_4	C_2H_4	C_3	C_4	Aromatics
H-ZSM-5	1.1	24.2	62.7	10.1	0.0	2.9
V/H-ZSM-5	6.3	2.6	88.7	4.1	1.1	3.5
Mn/H-ZSM-5	9.1	1.2	92.6	1.9	1.2	3.1
Fe/H-ZSM-5	17.0	7.9	70.0	6.3	1.6	13.8
Co/H-ZSM-5 IM	16.6	1.6	76.4	6.5	1.8	13.4
Cu/H-ZSM-5	2.0	15.5	63.6	17.0	0.0	3.9
Ga/H-ZSM-5	7.1	1.0	73.1	4.4	1.5	19.8

[a] Respective catalysts contained 5wt% active metals.

Table 4.2. Physicochemical and textual properties of catalysts. Reproduced from H. Saito *et al.*, *Chem. Lett.* **2017**, *46*, 1646–1649. Copyright 2017 The Chemical Society of Japan.

Catalyst	BET surface area / $m^2\ g^{-1}$	Content / mmol g^{-1}		Co/Al molar ratio / −	The amount of carbon deposition / mg g_{cat}^{-1}
		Al	Co		
H-ZSM-5	368.1	0.38	−	−	−
Co/H-ZSM-5 IM	312.5	0.39	0.82	2.13	232.3
Co/H-ZSM-5 IE	363.9	0.40	0.06	0.16	11.8

Table 4.3. The proportion of Co species on Co/H-ZSM-5 IM calculated by linear combination fitting. Reproduced from H. Saito *et al.*, *Chem. Lett.* **2017**, *46*, 1646–1649. Copyright 2017 The Chemical Society of Japan.

Catalyst	Fraction / %		
	Co^0	CoO	Co_3O_4
Fresh Co/H-ZSM-5 IM	−	19.8	80.2
Spent Co/H-ZSM-5 IM	96.7	3.3	−

Chapter 5 Dehydroaromatization of ethane over Zn/H-ZSM-5 catalyst

The text in this chapter is reproduced in part from H. Saito, S. Inagaki, K. Kojima, Q. Han, T. Yabe, S. Ogo, Y. Kubota, Y. Sekine, Preferential Dealumination of Zn/H-ZSM-5 and Its High and Stable Activity for Ethane Dehydroaromatization. *Appl. Catal. A: Gen.* **2018**, *549*, 76–81.

5.1. Introduction

As shown in chapter 4, benzene, toluene, and xylene, called BTX, are extremely important as fundamental raw chemicals used in the petrochemical industry. Many studies have reported dehydroaromatization of methane which is abundant and cheap feedstock, conducted at temperatures higher than 973 K because of thermodynamic limitations.[1-3] To form BTX selectively, **MFI** type zeolite (ZSM-5) in H-form supported metal cations or oxides including Zn, Ga, Re[4–6] is effective because ZSM-5 has a three-dimensional 10-ring channel system with micropores of about 0.55 nm,[7,8] which is close to the kinetic diameter of BTX. The active metals play a role in promoting the dehydrogenation of ethane to ethylene. Brønsted acid sites within the zeolite are involved in the oligomerization of ethylene to form aromatic hydrocarbons.[3,5] The formed alkenes were also converted to aromatic hydrocarbons on active metal sites.[9] Especially, Zn is cost-effective. It exhibits high catalytic performance in all the reactions described above. However, the Zn/H-ZSM-5 catalyst is rapidly deactivated over time on stream because of coke deposition, which prevents reactants from approaching the active sites because of blocking of the micropores of the support. The carbon deposition on the external and internal surfaces of zeolites also decreases the catalytic activity and benzene selectivity in cases of the conversion of methane to benzene, as described in the literature.[10,11] Weckhuysen *et al.* reported that carbon species of three types were formed on the Mo/H-ZSM-5 surface.[12] In addition to the carbon derived from Mo carbide, graphite-like carbon on the internal surface and sp-hybridized carbon on the external surface were observed by X-ray photoelectron spectroscopy. Ma *et al*. inferred that the coke formed on Mo/MCM-22 zeolite, which has **MWW** topology, was associated with Brønsted acid sites,[13] based on the results of temperature-programmed techniques.

Based on the previous research, use of H-ZSM-5 with higher Si/Al molar ratios in this type of reaction is expected to suppress the coke formation because of the small amount of Brønsted acid sites. However, low catalytic activity in initial dehydrogenation would occur because of the lower cation-exchange capacity for loading the active metal species. Therefore, dealumination of the framework Al by post-synthetic treatment[14–20] after loading of active metal species on H-ZSM-5

with low Si/Al ratios is expected to be an effective means of realizing tuning of the Brønsted acidity of the zeolite with high content active metal species.

In this chapter, we found that Zn/H-ZSM-5 showed high initial activity for the conversion of ethane to BTX, therefore we investigated the effects of steam treatment on the catalytic performance of the Zn/H-ZSM-5 catalysts for non-oxidative ethane dehydroaromatization. It is known that tetrahedrally coordinated Al atoms located in the zeolite framework was hydrolytically removed by water molecules.[21–23] Various characterizations were conducted for elucidating the influence of steam treatment on the catalysts.

5.2. Experimental

5.2.1. Catalyst preparation

Zeolite H-ZSM-5 was obtained by calcination of NH_4-ZSM-5 (HSZ-820NHA; Tosoh) at 773 K for 5 h. The loading of Zn on the zeolite support was carried out by an ion-exchange method. First, H-ZSM-5 was soaked and stirred in the 0.02 mol L^{-1} aqueous solution of $Zn(NO_3)_2 \cdot 6H_2O$ (Kanto Chemical Co., Inc.) at 353 K for 24 h. The suspension contained 1 g of the zeolite in 100 mL of the aqueous solution. Next, the powder was separated by suction filtration, washed with distilled water and dried in air with an oven at 393 K for 24 h. Finally, the dried powder was calcined at 823 K for 5 h.

Steam treatment of H-ZSM-5 and Zn/H-ZSM-5 was conducted in a fixed bed reactor. The catalyst (*ca.* 0.9 g) was charged into a quartz tube and then temperature was raised to 823 K under Ar atmosphere. After that, steam treatment was conducted at 823 K for 1 h in a H_2O diluted with Ar flow at a constant partial pressure of water (38 kPa). The water vapor was introduced to the reactor by an Ar flow through a bubbler heated at 348 K. The partial pressure of water was controlled by the bubbler temperature calculated from the Antoine equation. The catalyst was subsequently purged at 823 K for 30 min under Ar flow. The steam-treated samples are denoted as H-ZSM-5 ST and Zn/H-ZSM-5 ST.

5.2.2. Catalytic activity tests

Catalytic activity tests were carried out in a fixed bed reactor at atmospheric pressure for 4 h. The catalyst (0.2 g) was charged into a quartz tube (i.d. 6 mm) and then temperature was raised to 873 K under Ar atmosphere. The feed gas of 80vol% C_2H_6 and balanced N_2 was supplied at a flow rate of 25 mL min^{-1} (SATP). Products were analyzed by a gas chromatography (GC-8A; Shimadzu) equipped with a thermal conductivity detector (TCD) using a Shincarbon ST packed column (3 mm × 4 m, Shinwa Chemical Industries Ltd.) to detect H_2, N_2, CH_4, C_2H_4 and C_2H_6, and an on-line gas chromatography (GC-8A; Shimadzu) equipped with a flame ionization detector (FID) using a HP-PLOT/Q capillary column (0.53 mm × 30 m, Agilent) to detect CH_4, C_2H_4, C_2H_6, C_3

hydrocarbons, C_4 hydrocarbons, benzene, toluene, ethylbenzene and xylene. Ethane conversion and products selectivity were calculated as follows.

$$\text{Ethane conversion [\%]} = \frac{\sum_{n=1}^{8} n \cdot f^{out}_{C_n} - 2f^{out}_{C_2H_6}}{2f^{in}_{C_2H_6}} \cdot 100 \quad (5.1)$$

$$\text{Selectivity [\%]} = \frac{n \cdot f^{out}_{C_n}}{\sum_{n=1}^{8} n \cdot f^{out}_{C_n} - 2f^{out}_{C_2H_6}} \cdot 100 \quad (5.2)$$

Here, the description of f, n means the formation rate of a detected hydrocarbon shown as the subscript and the number of carbon atoms of the hydrocarbon respectively. The superscripts of "in" and "out" also express the inlet and outlet gas.

Catalyst regeneration was performed continuously at 873 K for 1 h in a 20vol% O_2/Ar flow at a rate of 25 mL min^{-1} (SATP) after the catalytic activity test, and the reactant was supplied again to evaluate the catalytic performance.

5.2.3. Characterizations

BET specific surface area was calculated from nitrogen adsorption−desorption isotherm obtained by nitrogen physisorption at 77 K, measured by a surface area gas sorption analyzer (Autosorb iQ; Quantachrome Instruments). The external surface area and micropore volume were estimated by the *t*-plot method. Prior to the measurement, the samples (*ca.* 80 mg) were heated *in vacuo* to 673 K for 12 h to remove adsorbed water.

XRD patterns were measured using an X-ray diffractometer (SmartLab III; Rigaku) using Cu $K\alpha$ radiation at 40 kV and 40 mA in the 2θ range from 5 to 60 degree at a scan rate of 5 degree min^{-1}.

Temperature programmed oxidation (TPO) was performed to determine the amount of carbon deposition on the spent catalysts using a thermogravimetry (TGA-50; Shimadzu). The samples (*ca.* 15 mg) were firstly heated to 873 K for 30 min under Ar atmosphere to remove adsorbed water and volatile hydrocarbons. After cooling to 323 K, the temperature was raised at a ramping rate of 10 K min^{-1} in a 20vol% O_2/Ar flow. The weight loss of the sample was regarded as the weight of coke formed on the catalysts. The amount of carbon deposition was calculated as follows.

$$\text{The amount of carbon deposition [mg } g_{cat}^{-1}\text{]} = \frac{W_i - W_f}{W_f} \quad (5.3)$$

The description of W_i and W_f means initial and final weight of the sample respectively.

Temperature programmed desorption of ammonia (NH_3-TPD) was also carried out to estimate the amount of adsorbed ammonia corresponded to acid sites. The desorbed ammonia was detected by a catalyst analyzer (BELCAT II; MicrotracBEL) equipped with a TCD. Prior to measurements, the samples (*ca.* 50 mg) were heated to 773 K for 1 h in a He flow and cooled to 373 K. After that, 5vol% NH_3/He was introduced to the sample for 30 min and purged under He flow for 15 min.

After the pre-treatment, NH_3-TPD profile was obtained at a ramping rate of 10 K min^{-1} in the temperature range from 373 to 873 K.

Al and Zn contents in the catalysts were measured by elemental analyses using an ICP emission spectrometer (iCAP-6500; Thermo Scientific). The samples (*ca.* 10 mg) were dissolved in HF to prepare the aqueous solution of the sample for the measurement.

UV-Vis diffuse reflectance spectra were obtained using a UV-Vis spectrometer (Lambda 650; PerkinElmer) equipped with an integrating sphere coated by $BaSO_4$. $BaSO_4$ was used as a reference material and then relative reflectance of the catalysts was measured. The range of wave length was from 190–800 nm at a scan rate of 96 nm min^{-1}. The obtained reflectance was converted by Kubelka–Munk (KM) function given in the following equation.

$$F(R_\infty) = \frac{(1 - R_\infty)^2}{2R_\infty} \tag{5.4}$$

Here, R_∞ is relative reflectance and $F(R_\infty)$ is KM function that is proportional to the absorption coefficient.

The solid-state MAS NMR measurements were performed on an ADVANCEIII-600 (600 MHz (^{1}H); Bruker Biospin) with a 4 mm diameter ZrO_2 rotor. The loading amount of sample powder was *ca.* 60−80 mg. The ^{27}Al direct-excitation (DE) MAS NMR spectra (156.4 MHz) were recorded at 0.5 s of the contact time for 1024 times at a spinning rate of 13.0 kHz. The ^{27}Al chemical shifts were determined using aqueous $Al(NO_3)_3$ solution, the resonance peak of which was adjusted to 0 ppm. The ^{29}Si dipolar decoupling (DD) MAS NMR spectra (119.2 MHz) were recorded at 30 s of the contact time for 1024 times at a spinning rate of 10.0 kHz. The ^{29}Si cross polarization (CP)/MAS NMR spectra were also recorded at 4 s of the contact time for 4096 times at a spinning rate of 10 kHz. The reference of ^{29}Si chemical shifts was determined with reference to the ^{29}Si signal of hexamethylcyclotrisiloxane (HMCS) at −9.66 ppm.

Pyridine-IR measurements were conducted to examine the acidity of the catalysts. Self-supporting zeolite wafers (*ca*. 60 mg) were suspended between NaCl windows in a cylindrical cell. The sample was then heated to 773 K under vacuum (< 10^{-3} Pa), held for 1 h, and cooled to 373 K. During the cooling, the blank spectrum was recorded at 473 K prior to the adsorption experiments. While maintaining the temperature at 373 K, pyridine (*ca.* 4.0 kPa) was injected into the cell. The cell was left in vacuum to allow physically adsorbed pyridine to desorb. After that, the sample was heated to 473 K. The spectrum was then recorded and averaged over 64 scans between 400 and 4000 cm^{-1} with 4 cm^{-1} resolution at 473 K. From this spectrum, the blank spectrum was subtracted to obtain the spectrum of adsorbed pyridine.

5.3. Results and discussion

5.3.1. Textural and physicochemical properties of various catalysts

Before examining the catalytic activity, we evaluated the textural and chemical properties of catalysts. Textural properties including the BET surface area, the external surface area and

micropore volume and the results of elemental analyses are presented in Table 5.1. Nitrogen adsorption-desorption isotherms of the catalysts are shown in Figure 5.1. According to IUPAC classification,[24] all isotherms were typical type-I isotherms with hysteresis loops, indicating the existence of mesopores. The steep increase in the volume of adsorbed nitrogen at high relative pressure (> 0.9) indicates the existence of macropores derived from intercrystalline spaces. As presented in Table 5.1, steam treatment or Zn loading on parent H-ZSM-5 did not greatly affected the textural properties. On the other hand, degradation of microporosity was observed for catalysts modified by both steam treatment and Zn loading. The decrease in Al content of Zn/H-ZSM-5 could be attributed to the increase in the weight of the catalysts caused by the exchange of H^+ with Zn^{2+} or leaching out Al species, especially existed on the extra framework, during ion-exchange. X-ray diffraction (XRD) patterns of the catalysts indicate that ion-exchange and steam treatment had little influence on the **MFI** structure as shown in Figure 5.2. The absence of peaks arising from ZnO and/or Zn crystalline phases suggests that Zn species are highly dispersed on the external and internal surface of the supports.

5.3.2. Catalytic performance for dehydroaromatization of ethane

Ethane conversion and selectivity to aromatic compounds over various catalysts with time on stream are investigated. Results are presented in Figure 5.3. Selectivity to the other products (methane, ethylene, C_3, and C_4) is also presented in Figure 5.4. Higher ethane conversion and aromatics selectivity at the initial stage were observed by the introduction of Zn without steam treatment. They decreased rapidly with time on stream because of carbon deposition at the pore mouth or in the micropores. Catalyst regeneration under oxidative conditions at 873 K also indicates the deactivation caused by coke formation as shown in Figure 5.5. The stability of catalytic performance of Zn/H-ZSM-5 was improved by Zn loading followed by steaming. As shown in Table 5.2, the amount of carbon deposition of Zn/H-ZSM-5 ST was one-tenth less than that of Zn/H-ZSM-5. The suppression of coke formation by steam treatment contributes to the improvement in the catalytic stability, while maintaining sufficient catalytic activity to form BTX. Steam-treated Zn/H-ZSM-5 before ion-exchange with Zn^{2+} (Zn/H-ZSM-5 ST bef. IE), however, exhibited low catalytic performance because the catalyst contained a small amount of Zn, which indicates that the amount of the H^+ (Brønsted acid) exchanged with Zn^{2+} during ion-exchange[4,25] would decrease by dealumination *via* steaming, thereby causing the limitation of Zn loading.

Ethylene selectivity gradually increased concomitantly with decreasing aromatic selectivity (Figure 5.4(b)). This is because ethylene can be formed on the external surface, on the other hand sequential conversion of ethylene to aromatic hydrocarbons in micropores was inhibited by coke formation. To clarify coke formation in micropores, nitrogen adsorption-desorption isotherms of spent catalysts were measured as shown in Figure 5.6. Textural properties of these catalysts also presented in Table 5.3. For Zn/H-ZSM-5, the volume of adsorbed nitrogen at very low relative pressure drastically decrease in comparison with Figure 5.1(c) although the behavior at higher

relative pressure was almost the same. As presented Table 5.3, micropore surface area and micropore volume of spent Zn/H-ZSM-5 become lower than those of fresh one (see also Table 5.1). These results indicate that coke mainly formed in the micropore. It is note that the volume of coke formed during the reaction cannot fill with the micropore volume of Zn/H-ZSM-5 (0.148 cm^3) even if the density of the formed coke is equal to benzene. Therefore, the plugging the pore mouth would occur, and nitrogen molecules could not enter into a part of the micropore. In case of Zn/H-ZSM-5 ST, the volume of adsorbed nitrogen at very low relative pressure slightly decreased corresponded to the small amount of carbon deposition. Micropore surface area and micropore volume little decreased after the reaction. The decrease in BET surface area is mainly due to the decrease in the external surface area. Therefore, coke would formed on the external surface of Zn/H-ZSM-5 ST, indicating that plugging the pore mouth would partly occur and thereby aromatics selectivity gradually decreased with time on stream.

5.3.3. Effects of steam treatment on the catalysts

UV-Vis diffuse reflectance spectroscopy (DRS) was used to elucidate the influence of steam treatment on coordination environment of Zn species in the catalyst. The spectra of fresh and steam-treated H-ZSM-5 and Zn/H-ZSM-5 are shown in Figure 5.7. The bulk ZnO did not exist on the supports in accordance with XRD patterns because a large absorption band around 380 nm derived from band gap[26] was not observed. In the spectra of steam-treated samples, the increase in the absorbance around 250 nm would be associated with the interaction between Al species formed by dealumination and oxygen in the framework. The coordination environment of Zn species was unaffected by steam treatment. Therefore, improvement in the stability of the catalytic performance by steam treatment can be attributed to dealumination of the zeolite support.

MAS NMR spectroscopy was applied to obtain information related to the local structure of the zeolites. The ^{27}Al MAS NMR spectra of fresh and steam-treated samples are presented in Figure 5.8(a). Peaks of the parent H-ZSM-5 correspond to tetrahedrally coordinated Al species (Al_F) in the **MFI** framework around 55 ppm and octahedrally coordinated extra-framework Al species (Al_{EF}) at 0 ppm. In the spectrum of H-ZSM-5 ST, the peak intensity of Al_F decreased in comparison with the parent H-ZSM-5. A new broad peak around 35 ppm assigned to penta-coordinated Al_{EF}[27] appeared. However, the peak intensity of Al_F decreased slightly by steam treatment in the case of Zn/H-ZSM-5 ST. The dealumination of Al_F occur through hydrolysis.[21–23] These results demonstrate that the Zn/H-ZSM-5 catalyst only slightly dealuminates because Zn cations would cover Al sites. Therefore, H_2O molecules cannot approach such Al sites.

The ^{29}Si MAS NMR spectra of the catalysts are presented in Figure 5.8(b). We attributed a peak at −112 ppm and a shoulder peak at −115 ppm to Q^4(0Al), which means $\underline{Si}(OSi)_4$. The difference in chemical shift reflects the non-equivalent Q^4(0Al) sites.[28] A peak at −106 ppm corresponded to Q^4(1Al), which means $(AlO)\underline{Si}(OSi)_3$, because no distinct peak around −100 ppm derived from Q^3(0Al)[29,30] was observed in ^{29}Si cross-polarization (CP)/MAS NMR spectra as shown in Figure

5.9. In the spectra of steam-treated catalysts, the decrease in the peak intensity of $Q^4(1Al)$ was observed because of dealumination during steam treatment. The Si/Al molar ratios in the zeolite framework calculated from the equation given in the literature[31] are presented in Table 5.2. The values clearly show the degree of dealumination. Increases in the Si/Al ratios of steam-treated samples corresponded to the change of the ^{27}Al MAS NMR spectra, which indicates that bared Al_F (without correspondence of Zn species) were preferentially dealuminated because of hydrolysis with H_2O molecules. The selective dealumination would correspond to the decrease in the amount of Brønsted acid sites.

Pyridine-IR measurements were performed to investigate the acidic properties of the catalysts. The spectra of H-ZSM-5, Zn/H-ZSM-5 and steam treated ones are shown in Figure 5.10. Bands for pyridine adsorbed on Lewis and Brønsted acid sites were observed at 1452 and 1542 cm^{-1}, respectively.[32] The absorbance of each samples is different because of the difference in the molar extinction coefficients. It is also known that the molar extinction coefficient determined by other groups cannot be applied to our measurement system.[33] Therefore, we cannot distinguish the decrease in the band at 1542 cm^{-1} from the increase in the band at 1452 cm^{-1}. Instead of pyridine-IR measurements, NH_3-TPD measurement mentioned below clearly show the decrease in the acid sites by steam treatment.

NH_3-TPD profiles of fresh and steam-treated samples are shown in Figure 5.11. In the profile of parent H-ZSM-5, two desorption peaks corresponded to the low temperature peak around 500 K (*l*-peak) and the high temperature peak around 720 K (*h*-peak) were observed. The *l*-peak is derived from physical adsorption of NH_3 or NH_3 weakly adsorbed on NH^{4+}; the *h*-peak is attributed to NH_3 adsorbed on acid sites.[34] In comparison with parent H-ZSM-5, the intensity of *h*-peak decreased in the profile of H-ZSM-5 ST. This indicates that the number of acid sites corresponded to Brønsted acid sites probably decreased by steam treatment. The intensity of *h*-peak also decreased by Zn loading because of the exchange of H^+ with Zn^{2+}. Steam treatment of Zn/H-ZSM-5 caused the further decrease in the intensity of *h*-peak because bared Al_F were preferentially dealuminated. As a result, a reasonable amount of Brønsted acid sites in Zn/H-ZSM-5 ST can avoid coke formation. Thereby Zn/H-ZSM-5 ST exhibited high catalytic performance.

5.3.4. Discussion

We presume that the high catalytic performance of Zn/H-ZSM-5 ST is attributable to the suppression of coke formation by steam treatment. The ^{27}Al and ^{29}Si MAS NMR spectra revealed that dealumination of bared Al_F occurred. In the NH_3-TPD profiles of fresh and steam-treated Zn/H-ZSM-5, the decrease in the intensity of *h*-peak corresponded to the desorption of NH_3 adsorbed on acid sites was observed. The slight change in the Zn content and its coordination environment by steam treatment also supports the preferential dealumination. Improved catalytic performance was achieved by steam treatment after Zn loading because of the removal of the extra Brønsted acid sites, which also promotes coke formation.

From a microscopic perspective, preferential dealumination is expected to affect the proximity between a Zn^{2+} cation and a proton. Coke formation in ethane dehydroaromatization was similar to that in methane dehydroaromatization. This phenomenon might derive from consecutive conversion of olefins and aromatic hydrocarbons by Brønsted acid. As presented in Table 2, dealumination of Al_F decreased the number of Al per unit cell calculated from the chemical formula of the **MFI** structure.[35] A certain amount of Al_F decreased by steam treatment, irrespective of the existence of Zn. However, Zn species were quantitatively and qualitatively stable during steam treatment. Therefore, Zn^{2+} cation in Zn/H-ZSM-5 ST is expected to be located far from Brønsted acid site by the selective dealumination as portrayed in Figure 5.12. The decrease in the adjacent protons can suppress the consecutive conversion of products (i.e. benzene and ethylene) to coke precursors. The optimal amount of Brønsted acid sites is indispensable to achieve high catalytic performance.

5.4. Chapter Conclusion

In conclusion, high catalytic performance of the Zn/H-ZSM-5 catalyst for non-oxidative dehydroaromatization was achieved by steam treatment after Zn loading. Our TPO measurements revealed that steam treatment suppressed coke formation. The results of elemental analyses, UV-Vis DRS, and XRD demonstrated that Zn species on the support were highly stable during steam treatment. The ^{27}Al and ^{29}Si MAS NMR spectra of Zn/H-ZSM-5 indicate that dealumination occurs preferentially on bared Al_F sites. NH_3-TPD measurement also indicate steam treatment decrease in the amount of acid sites. These suggest that steam treatment after Zn ion-exchange efficiently removes the extra Brønsted acid sites which promote coke formation. Results show that preferential dealumination of Zn/H-ZSM-5 enables high performance for ethane dehydroaromatization thanks to the optimal amount of Brønsted acid sites.

References

1. Z. R. Ismagilov, E. V. Matus, L. T. Tsikoza, Direct Conversion of Methane on Mo/ZSM-5 Catalysts to Produce Benzene and Hydrogen: Achievements and Perspectives. *Energy Environ. Sci.* **2008**, *1*, 526–541.
2. J. J. Spivey, G. Hutchings, Catalytic Aromatization of Methane. *Chem. Soc. Rev.* **2014**, *43*, 792–803.
3. A. Hagen, F. Roessner, Ethane to Aromatic Hydrocarbons: Past, Present, Future. *Catal. Rev. –Sci. Eng.* **2000**, *42(4)*, 403–437.
4. V. I. Yakerson, T. V. Vasina, L. I. Lafer, V. P. Sytnyk, G. L. Dykh, A. V. Mokhov, O. V. Bragin, Kh. M. Minachev, The Properties of Zinc and Gallium Containing Pentasils — The Catalysts for the Aromatization of Lower Alkanes. *Catal. Lett.* **1989**, *3*, 339–346.

5. P. Schulz, M. Baerns, Aromatization of Ethane over Gallium-Promoted H-ZSM-5 Catalysts. *Appl. Catal.* **1991**, *78*, 15–29.
6. A. Krogh, A. Hagen, T. W. Hansen, C. H. Christensen, I. Schmidt, Re/H-ZSM-5: A New Catalyst for Ethane Aromatization with Improved Stability. *Catal. Commun.* **2003**, *4*, 627–630.
7. D. H. Olson, G. T. Kokotailo, S. L. Lawton, W. M. Meier, Crystal Structure and Structure-Related Properties of ZSM-5. *J. Phys. Chem.* **1981**, *85*, 2238–2243.
8. C. Baerlocher, L. B. McCusker, D. H. Olson, *Atlas of Zeolite Framework Types 6th Ed.*, Elsevier, Amsterdam, **2007**; See also: http://www.iza-structure.org/databases/.
9. Y. Ono, Transformation of Lower Alkanes into Aromatic Hydrocarbons over ZSM-5 Zeolites. *Catal. Rev. –Sci. Eng.* **1992**, *34(3)*, 179–226.
10. C. H. L. Tempelman, E. J. M. Hensen, On the Deactivation of Mo/HZSM-5 in the Methane Dehydroaromatization Reaction. *Appl. Catal. B: Environ.* **2015**, *176–177*, 731–739.
11. Y. Song, Y. Xu, Y. Suzuki, H. Nakagome, Z.-G. Zhang, A Clue to Exploration of the Pathway of Coke Formation on Mo/H-ZSM-5 Catalyst in the Non-Oxidative Methane Dehydroaromatization at 1073 K. *Appl. Catal. A: Gen.* **2014**, *482*, 387–396.
12. B. M. Weckhuysen, M. P. Rosynek, J. H. Lunsford, Characterization of Surface Carbon Formed during the Conversion of Methane to Benzene over Mo/H-ZSM-5 Catalysts. *Catal. Lett.* **1998**, *52*, 31–36.
13. D. Ma, D. Wang, L. Su, Y. Shu, Y. Xu, X. Bao, Carbonaceous Deposition on Mo/HMCM-22 Catalysts for Methane Aromatization: A TP Technique Investigation. *J. Catal.* **2002**, *208*, 260–269.
14. M. Müller, G. Harvey, R. Prins, Comparison of the Dealumination of Zeolites Beta, Mordenite, ZSM-5 and Ferrierite by Thermal Treatment, Leaching with Oxalic Acid and Treatment with $SiCl_4$ by ^{1}H, ^{29}Si and ^{27}Al MAS NMR. *Micropor. Mesopor. Mater*. **2000**, *34*, 135–147.
15. C. S. Triantafillidis, A. G. Vlessidis, L. Nolbandian, N. P. Evmiridis, Effect of the Degree and Type of the Dealumination Method on the Structural, Compositional and Acidic Characteristics of H-ZSM-5 Zeolites. *Micropor. Mesopor. Mater.* **2001**, *47*, 369–388.
16. C. D. Chang, De-Aluminization of Aluminosilicates. *US Patent*, **1981**, 4273753.
17. S. Namba, A. Inaka, T. Yashima, Effect of Selective Removal of Aluminium from External Surfaces of HZSM-5 Zeolite on Shape Selectivity. *Zeolites* **1986**, *6*, 107–110.
18. Y. Lu, D. Ma, Z. Xu, Z. Tian, X. Bao, L. Lin, A High Coking-Resistance Catalyst for Methane Aromatization. *Chem. Commun.* **2001**, 2048–2049.
19. S. M. T. Almutairi, B. Mezari, E. A. Pidko, P. C. M. M. Magusin, E. J. M. Hensen, Influence of Steaming of the Acidity and the Methanol Conversion Reaction of HZSM-5 Zeolite. *J. Catal.* **2013**, *307*, 194–203.
20. N. Viswanadham, J. K. Gupta, G. Murali Dhar, M. O. Garg, Effect of Synthesis Methods and Modification Treatments of ZSM-5 on Light Alkane Aromatization. *Energy Fuels* **2006**, *20*, 1806–1814.

21. T. Sano, H. Ikeya, T. Kasuno, Z. B. Wang, Y. Kawakami, K. Soga, Influence of Crystallinity of HZSM-5 on Its Dealumination Rate. *Zeolites* **1997**, *19*, 80–86.
22. T. Masuda, Y. Fujikata, S. R. Mukai, K. Hashimoto, Changes in Catalytic Activity of MFI-type Zeolites Caused by Dealumination in a Steam Atmosphere. *Appl. Catal. A: Gen.* **1998**, *172*, 73–83.
23. L. H. Ong, M. Dömök, R. Olindo, A. C. van Veen, J. A. Lercher, Dealumination of HZSM-5 via Steam-Treatment. *Micropor. Mesopor. Mater.* **2012**, *164*, 9–20.
24. M. Thommes, K. Kaneko, A. V. Neimark, J. P. Olivier, F. R.-Reinoso, J. Rouquerol, K. S. W. Sing, Physisorption of Gases, with Special Reference to the Evaluation of Surface Area and Pore Size Distribution. *Pure Appl. Chem.* **2015**, *87(9–10)*, 1051–1069.
25. H. Berndt, G. Lietz, J. Völter, Zinc Promoted H-ZSM-5 Catalysts for Conversion of Propane to Aromatics II. Nature of the Active Sites and Their Activation. *Appl. Catal. A: Gen.* **1996**, *146*, 365–379.
26. S. Bordiga, C. Lamberti, G. Ricchiardi, L. Regli, F. Bonino, A. Damin, K.-P. Lillerud, M. Bjorgen, A. Zecchina, Electronic and Vibrational Properties of a MOF-5 Metal-Organic Framework: ZnO Quantum Dot Behaviour. *Chem. Commun.* **2004**, 2300–2301.
27. A. Samoson, E. Lippmaa, G. Engelhardt, U. Lohse, H.-G. Jerschkewitz, Quantitative High-Resolution ^{27}Al NMR: Tetrahedral Non-Framework Aluminium in Hydrothermally Treated Zeolites. *Chem. Phys. Lett*. **1987**, *134*, 589–592.
28. S. Ramdas, J. Klinowski, A Simple Correlation between Isotropic 29Si-NMR Chemical Shifts and T–O–T Angles in Zeolite Framework. *Nature* **1984**, *308*, 521–523.
29. S. L. Burkett, M. E. Davis, Mechanism of Structure Direction in the Synthesis of Si-ZSM-5: An Investigation by Intermolecular ^{1}H-^{29}Si CP MAS NMR. *J. Phys. Chem*. **1994**, *98*, 4647–4653.
30. J. Dedecek, V. Balgová, V. Pashkova, P. Klein, B. Wichterlová, Synthesis of ZSM-5 Zeolites with Defined Distribution of Al Atoms in the Framework and Multinuclear MAS NMR Analysis of the Control of Al Distribution. *Chem. Mater.* **2012**, *24*, 3231–3239.
31. C. A. Fyfe, G. C. Gobbi, G. J. Kennedy, J. D. Graham, R. S. Ozubko, W. J. Murphy, A. Bother-By, J. Dadok, A. S. Chesnick, Detailed Interpretation of the ^{29}Si and ^{27}Al High-Field *MAS* N.M.R. Spectra of Zeolites Offretite and Omega, *Zeolites* **1985**, *5*, 179–183.
32. E. P. Parry, An Infrared Study of Pyridine Adsorbed on Acidic Solids. Characterization of Surface Acidity, *J. Catal.* **1963**, *2*, 371–379.
33. J. A. Lercher, C. Gründling, G. Eder-Mirth, Infrared Studies of the Surface Acidity of Oxides and Zeolites Using Adsorbed Probe. *Catal. Today* **1996**, *27*, 353–376.
34. M. Sawa, M. Niwa, Y. Murakami, Relationship between Acid Amount and Framework Aluminum Content in Mordenite. *Zeolites* **1990**, *10*, 532–538.
35. G. T. Kokotailo, S. L. Lawton, D. H. Olson, W. M. Meier, Structure of Synthetic Zeolite ZSM-5. *Nature* **1978**, *272*, 437–438.

Figures and Tables

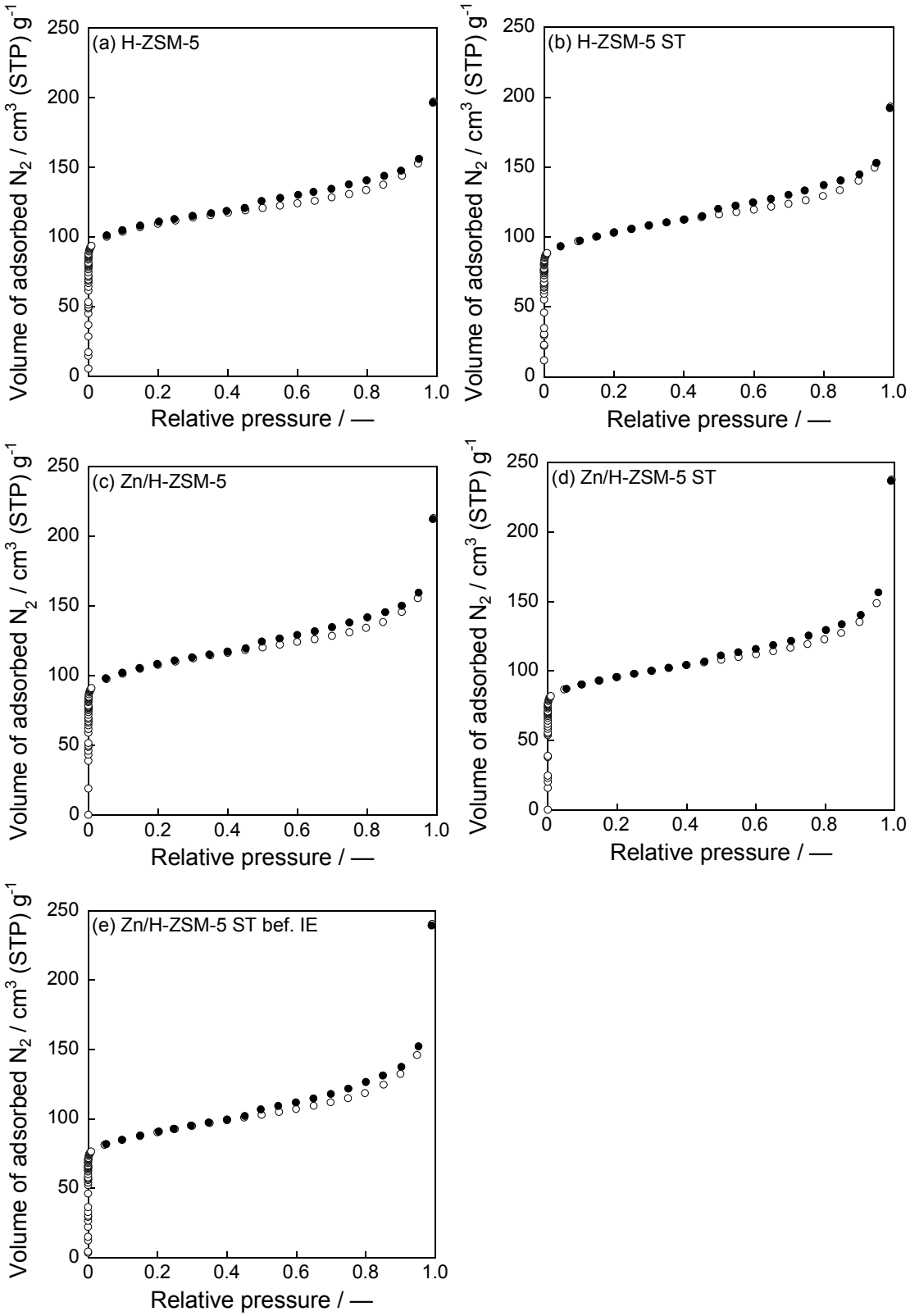

Figure 5.1. Nitrogen adsorption-desorption isotherms of (a) H-ZSM-5, (b) H-ZSM-5 ST, (c) Zn/H-ZSM-5, (d) Zn/H-ZSM-5 ST and (e) Zn/H-ZSM-5 ST bef. IE. Open and closed symbols indicate adsorption and desorption, respectively. Reprinted from H. Saito *et al.*, *Appl. Catal. A: Gen.* **2018**, *549*, 76–81. Copyright 2017 Elsevier B. V.

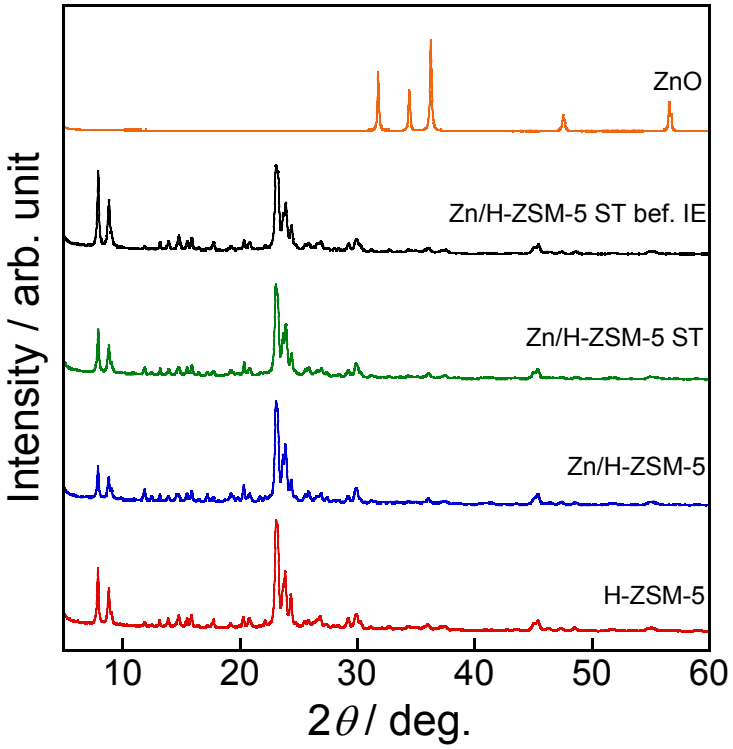

Figure 5.2. XRD patterns of H-ZSM-5, various Zn/H-ZSM-5 and ZnO as a control. The expressions of "ST", "bef." and "IE" mean steam treatment, before and ion-exchange respectively. Reprinted from H. Saito *et al.*, *Appl. Catal. A: Gen.* **2018**, *549*, 76–81. Copyright 2017 Elsevier B. V.

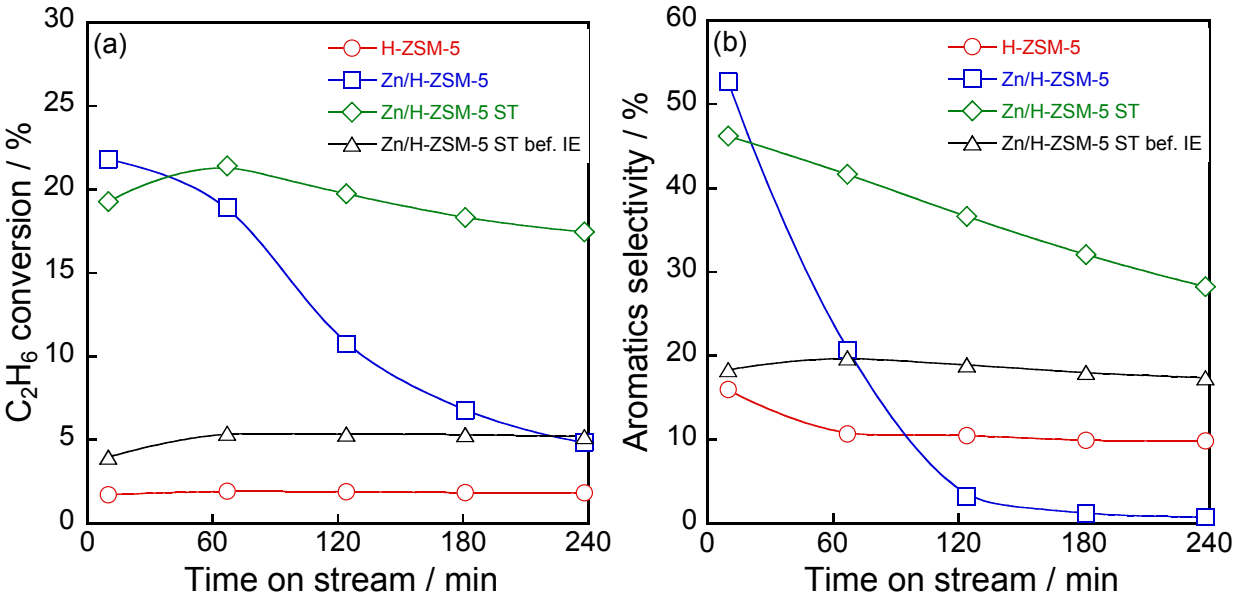

Figure 5.3. (a) C_2H_6 conversion and (b) aromatics selectivity with time on stream over H-ZSM-5 and various Zn/H-ZSM-5 catalysts. Reprinted from H. Saito *et al.*, *Appl. Catal. A: Gen.* **2018**, *549*, 76–81. Copyright 2017 Elsevier B. V.

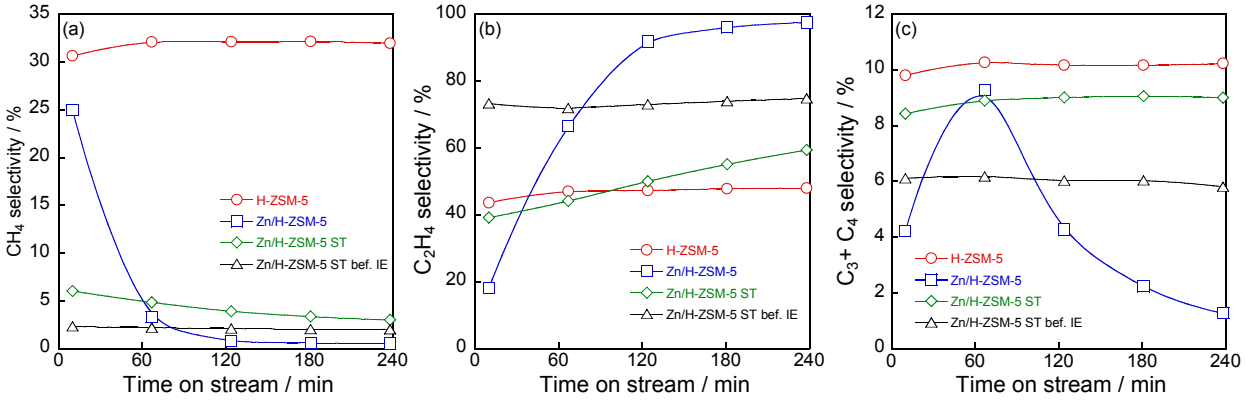

Figure 5.4. (a) Selectivity of CH_4, (b) C_2H_4 and (c) C_3+C_4 hydrocarbons with time on stream over H-ZSM-5 and various Zn/H-ZSM-5 catalysts. Reprinted from H. Saito *et al.*, *Appl. Catal. A: Gen.* **2018**, *549*, 76–81. Copyright 2017 Elsevier B. V.

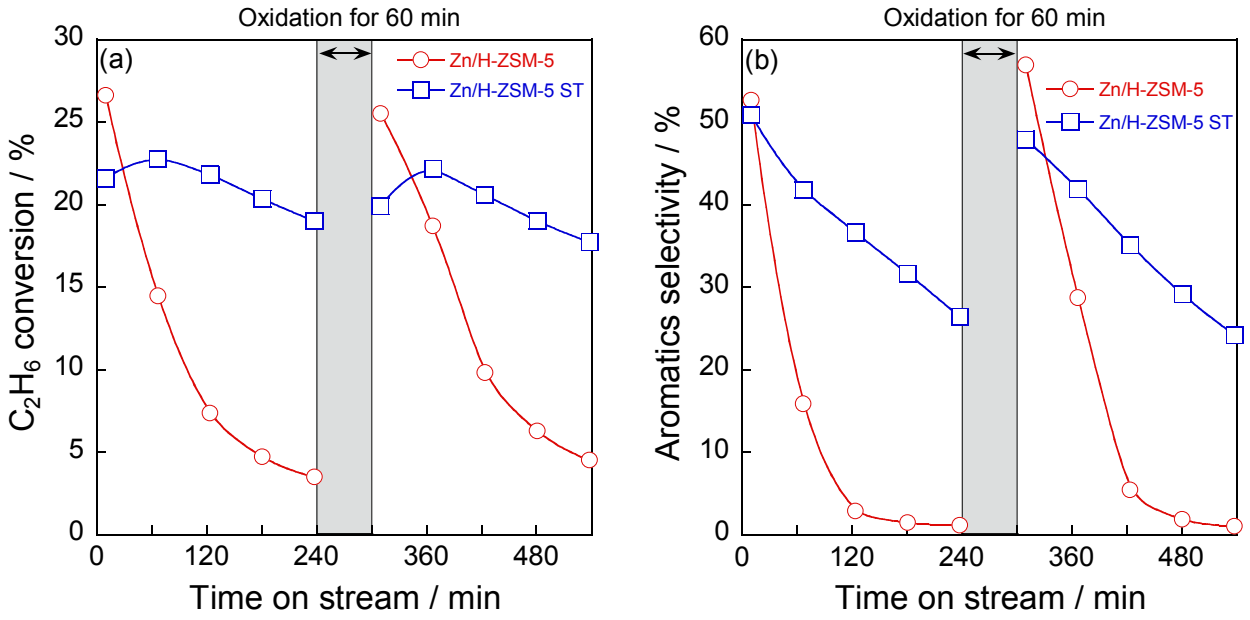

Figure 5.5. (a) C_2H_6 conversion and (b) aromatics selectivity with time on stream over Zn/H-ZSM-5 and Zn/H-ZSM-5 ST. Catalyst regeneration was conducted after 4 h of the first reaction in 20vol% O_2/Ar atmosphere at 873 K. Reprinted from H. Saito *et al.*, *Appl. Catal. A: Gen.* **2018**, *549*, 76–81. Copyright 2017 Elsevier B. V.

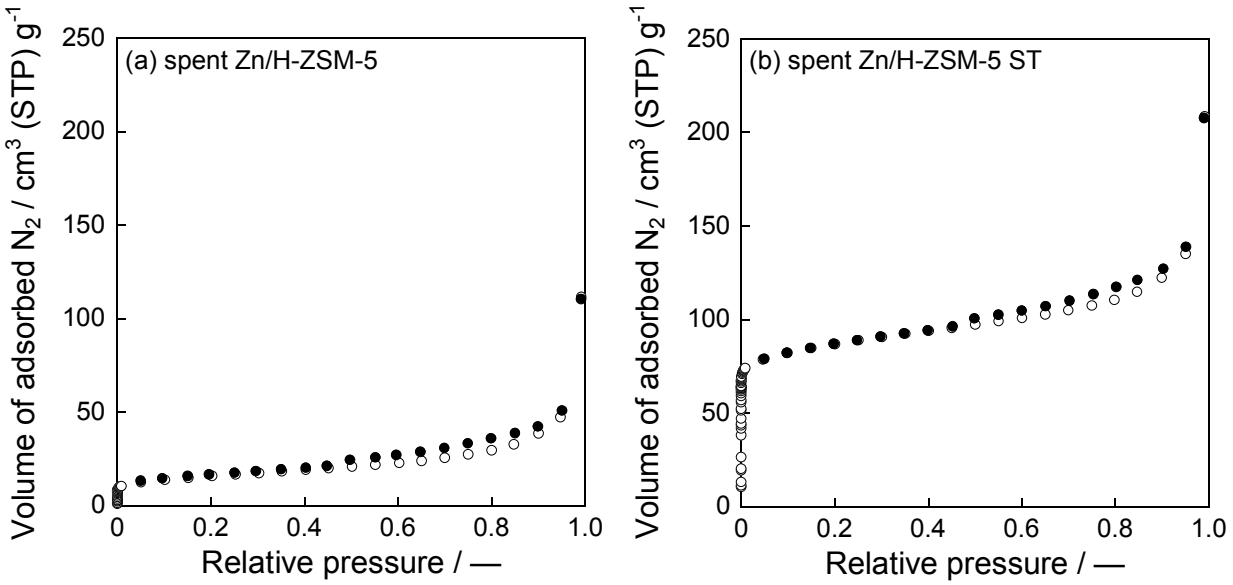

Figure 5.6. Nitrogen adsorption-desorption isotherms of spent (a) Zn/H-ZSM-5 and (b) Zn/H-ZSM-5 ST. Reprinted from H. Saito *et al.*, *Appl. Catal. A: Gen.* **2018**, *549*, 76–81. Copyright 2017 Elsevier B. V.

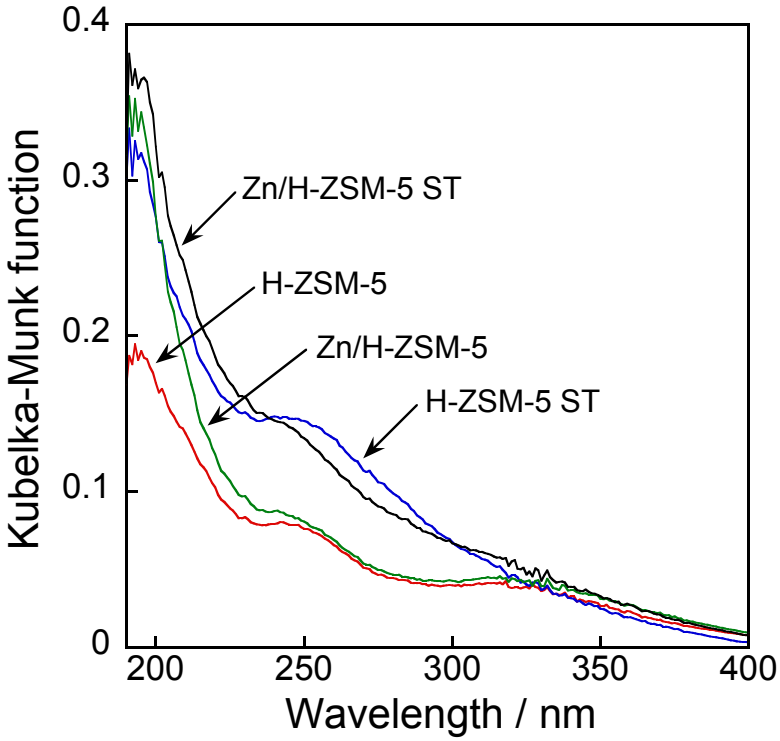

Figure 5.7. UV-vis diffuse reflectance spectra of H-ZSM-5 (red), H-ZSM-5 ST (blue), Zn/H-ZSM-5 (green) and Zn/H-ZSM-5 ST (black). Reprinted from H. Saito *et al.*, *Appl. Catal. A: Gen.* **2018**, *549*, 76–81. Copyright 2017 Elsevier B. V.

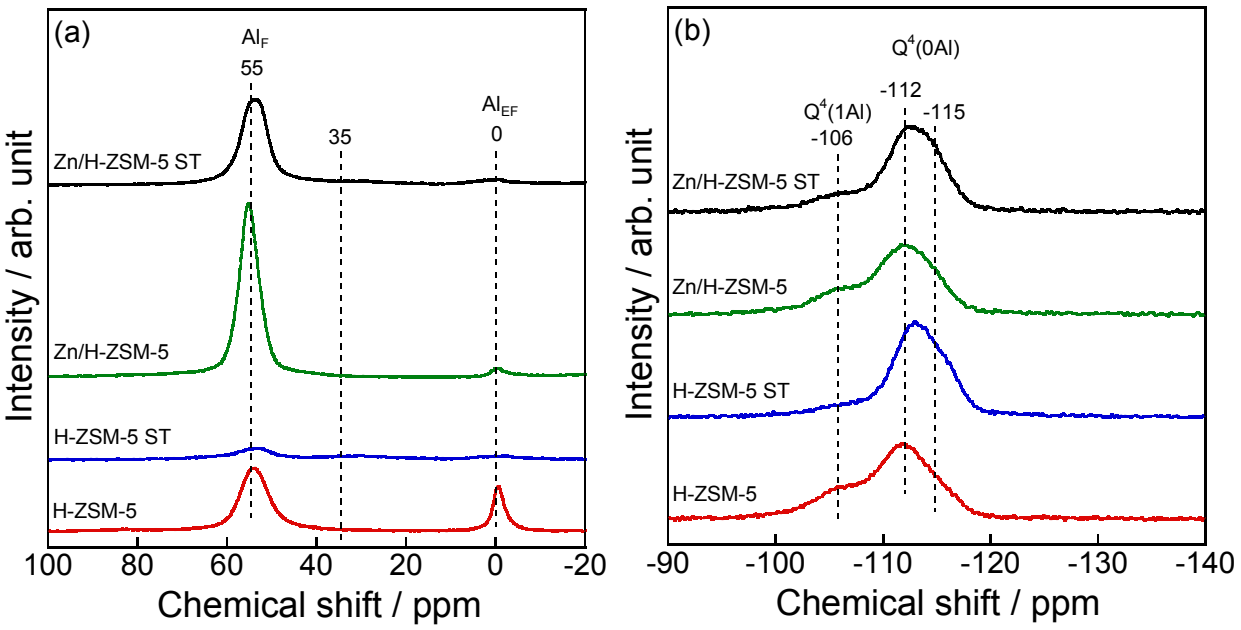

Figure 5.8. (a) ^{27}Al MAS NMR spectra and (b) ^{29}Si MAS NMR spectra of H-ZSM-5, Zn/H-ZSM-5 and steam-treated ones. Reprinted from H. Saito *et al.*, *Appl. Catal. A: Gen.* **2018**, *549*, 76–81. Copyright 2017 Elsevier B. V.

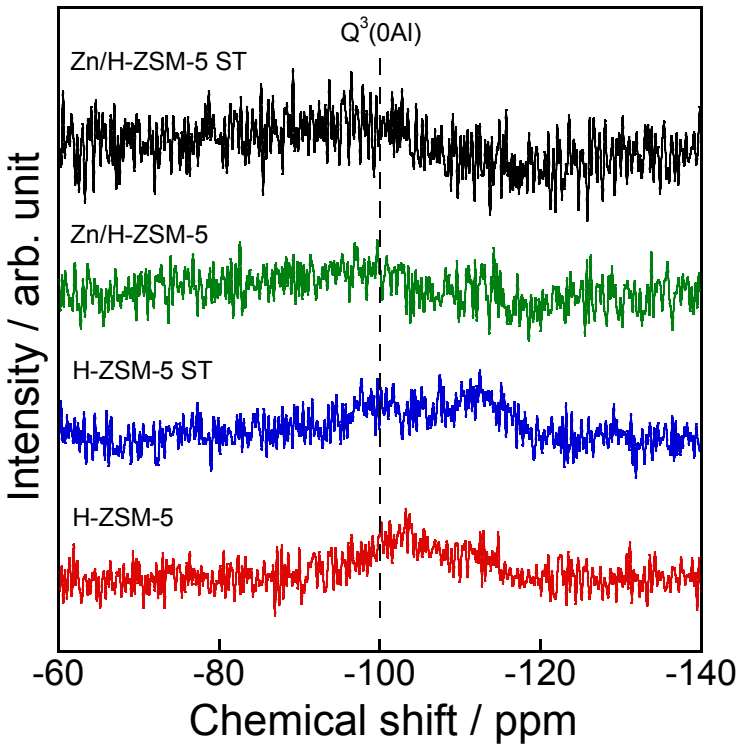

Figure 5.9. ^{29}Si CP-MAS NMR spectra of H-ZSM-5, Zn/H-ZSM-5 and steam-treated ones. Reprinted from H. Saito *et al.*, *Appl. Catal. A: Gen.* **2018**, *549*, 76–81. Copyright 2017 Elsevier B. V.

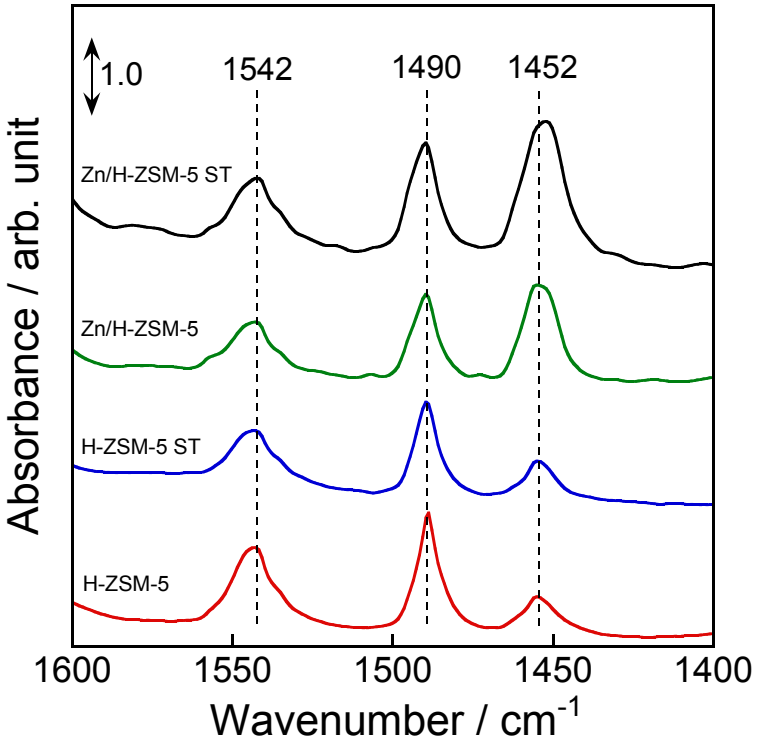

Figure 5.10. Subtracted IR spectra of various catalysts after pyridine adsorption at 373 K, followed by evacuation at 473 K. Spectra were measured at 473 K. Reprinted from H. Saito *et al.*, *Appl. Catal. A: Gen.* **2018**, *549*, 76–81. Copyright 2017 Elsevier B. V.

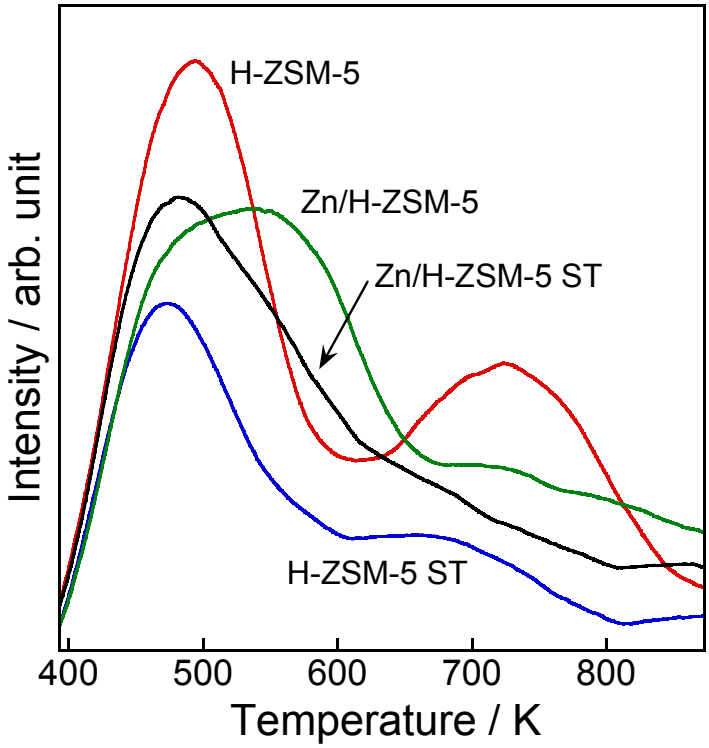

Figure 5.11. NH_3-TPD profiles of H-ZSM-5 (red), H-ZSM-5 ST (blue), Zn/H-ZSM-5 (green) and Zn/H-ZSM-5 ST (black). Reprinted from H. Saito *et al.*, *Appl. Catal. A: Gen.* **2018**, *549*, 76–81. Copyright 2017 Elsevier B. V.

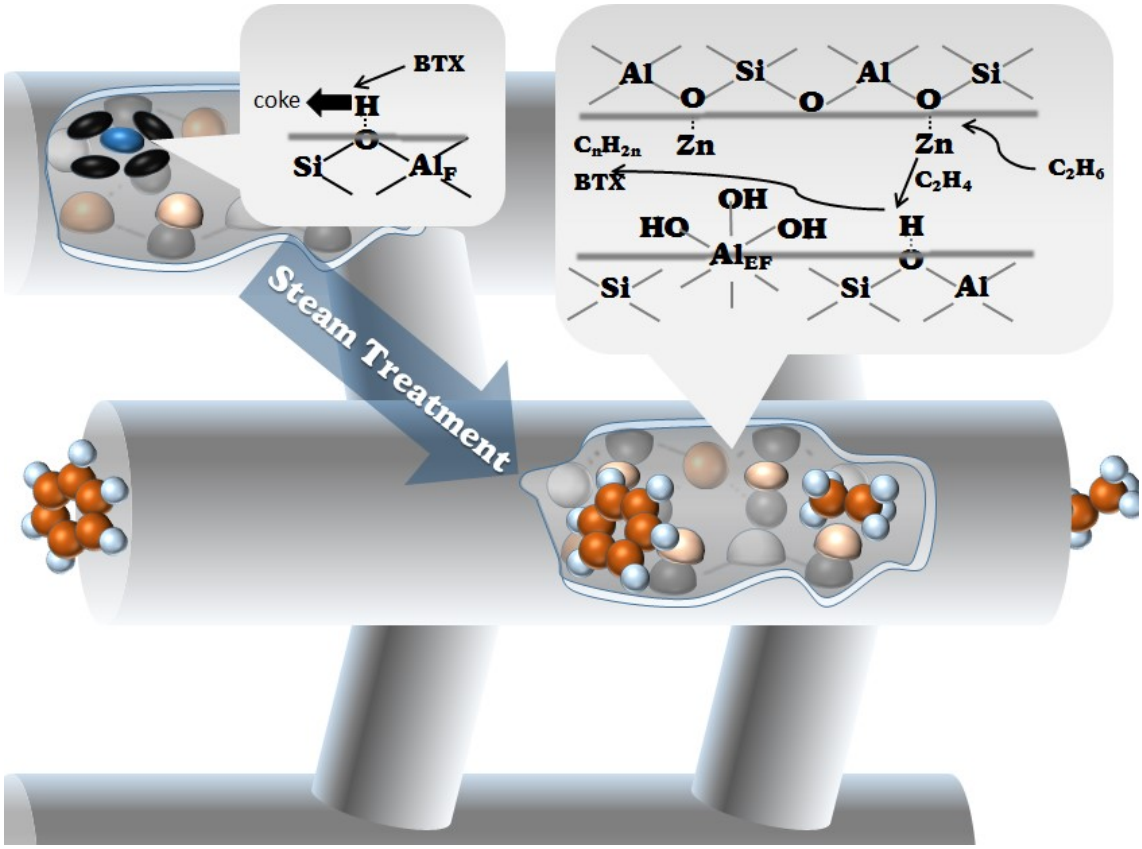

Figure 5.12. Schematic image of the preferential dealumination by steam treatment and active sites for dehydroaromatization of ethane. Reprinted from H. Saito *et al.*, *Appl. Catal. A: Gen.* **2018**, *549*, 76–81. Copyright 2017 Elsevier B. V.

Table 5.1. Textural and chemical properties of various H-ZSM-5 and Zn/H-ZSM-5 catalysts. Reproduced from H. Saito *et al.*, *Appl. Catal. A: Gen.* **2018**, *549*, 76–81. Copyright 2017 Elsevier B. V.

Catalyst	BET surface area / $m^2\ g^{-1}$	External surface area / $m^2\ g^{-1}$	Microporous surface area / $m^2\ g^{-1}$	Micropore volume / $cm^3\ g^{-1}$	Al content / mmol g^{-1}	Zn content / mmol g^{-1}	Zn/Al ratio
H-ZSM-5	409.0	55.0	354.0	0.151	1.18	—	—
H-ZSM-5 ST	387.8	55.9	331.9	0.143	1.21	—	—
Zn/H-ZSM-5	399.3	59.6	339.7	0.148	1.05	0.370	0.352
Zn/H-ZSM-5 ST	358.9	62.2	296.7	0.127	1.09	0.383	0.350
Zn/H-ZSM-5 ST bef. IE	335.0	64.9	270.1	0.117	1.06	0.063	0.059

Table 5.2. The amount of carbon deposition and Si/Al ratios of various H-ZSM-5 and Zn/H-ZSM-5 catalysts. Reproduced from H. Saito *et al.*, *Appl. Catal. A: Gen.* **2018**, *549*, 76–81. Copyright 2017 Elsevier B. V.

Catalyst	The amount of carbon deposition[a] / mg g_{cat}^{-1}	Si/Al ratio	The number of Al per unit cell
H-ZSM-5	n.d.	14.9	6.0
H-ZSM-5 ST	—	48.0	2.0
Zn/H-ZSM-5	118.8	15.4	5.9
Zn/H-ZSM-5 ST	11.1	26.4	3.5
Zn/H-ZSM-5 ST bef. IE	n.d.	—	—

[a]The expression of "n.d." indicates the amount of carbon deposition could not be detected.

Table 5.3. Textural properties of spent Zn/H-ZSM-5 and Zn/H-ZSM-5 ST. Reproduced from H. Saito *et al.*, *Appl. Catal. A: Gen.* **2018**, *549*, 76–81. Copyright 2017 Elsevier B. V.

Catalyst	BET surface area / $m^2\ g^{-1}$	External surface area / $m^2\ g^{-1}$	Microporous surface area / $m^2\ g^{-1}$	Micropore volume / cm^3
Spent Zn/H-ZSN-5	47.5	34.0	13.5	0.010
Spent Zn/H-ZSN-5 ST	323.6	55.0	268.6	0.115

Chapter 6 General conclusion

Catalytic conversion of ethane to ethylene and aromatic hydrocarbons over metal oxides and zeolite-supported metals catalysts are described throughout this thesis. In chapters 2 and 3, dehydrogenation of ethane over β-Ga_2O_3/α-Al_2O_3 and Ba-doped $LaMnO_3$ ($La_{1-x}Ba_xMnO_{3-\delta}$) perovskite catalysts was investigated in the presence of steam. The aim of these chapters is developing catalysts for dehydrogenation of ethane in the presence of steam, leading to the application of the catalysts to the steam cracking process. In chapters 4 and 5, dehydroaromatization of ethane over the **MFI**-type zeolite-supported Co and Zn catalysts were examined to develop an alternative process to the steam cracking of naphtha for the BTX production. Through the research, the performance of the catalysts was enhanced by the control of the quality and quantity of their active sites.

In chapter 2, the β-Ga_2O_3 active site contains two kinds of Ga species in its structure: tetrahedrally and octahedrally coordinated Ga denoted as Ga(T) and Ga(O), respectively. In general, Ga(T) promotes C–H bond activation of light alkanes. However, it is inferred from adsorption energy of ethane and ethylene calculated on the basis of DFT that ethylene decomposition to the coke is induced by Ga(T). In addition, dissociative adsorption of ethane proceeds on unsaturated Ga(O) such as Ga(O) at the (002) facet, which results in the formation of Ga–C_2H_5 and O–H species. From the experimental insight, it is demonstrated that the contribution of Ga(T) is inhibited by the modification of β-Ga_2O_3/α-Al_2O_3 with Ba, resulting in the high activity and ethylene selectivity. The similar effect was verified by the Sr modification. The Ga(T) would exhibit stronger Lewis acidity than Ga(O) because of the small coordination number. The basic metals (Sr and Ba) would interact with Ga(T), resulting in the poisoning of Ga(T) and the suppression of the coke formation.

In chapter 3, the active center for ethane activation is ascribed to the surface lattice oxygen of the $La_{1-x}Ba_xMnO_{3-\delta}$ perovskite. The reaction proceeds *via* the Mars-van Krevelen mechanism in the presence of steam, which is completely different from β-Ga_2O_3. Ethane is oxidatively activated at the surface lattice oxygen, resulting in the formation of ethylene and water concomitantly with the oxygen vacancy. Then, water under the reaction atmosphere regenerate the oxygen vacancy with hydrogen desorption (water splitting), leading to the completion of the catalytic cycle. The Ba doping increases the capacity of the reactive surface lattice oxygen probably because the larger ionic radius of Ba^{2+} than La^{3+} induce the lattice strain. In addition, the high redox ability of Mn, which can be various oxidation states in comparison with Co and Fe, is an important factor for the catalytic performance. The activity of $La_{1-x}Ba_xMnO_{3-\delta}$ was higher than β-Ga_2O_3/α-Al_2O_3. Therefore, use of reducible oxides would change the reaction mechanism of ethane dehydrogenation in the presence of steam. Activation of ethane would be easy to proceed on the reactive surface lattice oxygen in comparison with metal–oxygen couple such as Ga–O.

In chapter 4, dehydrogenation of ethane proceeds at the Co active sites. The formed ethylene is

subsequently converted to the aromatic hydrocarbons. Prepared by the impregnation method, Co metal particles existed on the H-ZSM-5 support. Ethane was activated on the Co particles, resulting in the coke formation. On the other hand, Co^{2+} cations existed at the ion-exchange sites of H-ZSM-5 in the case where Co/H-ZSM-5 was prepared by the ion-exchange method. At the Co^{2+} cation sites, ethane was dehydrogenated to ethylene with the little amount of carbon deposition. Therefore, the ion-exchanged Co^{2+} is better active sites for dehydrogenation of ethane, which is the first step of BTX formation, than Co metal.

In chapter 5, the steam treatment of Zn/H-ZSM-5, which exhibited the higher activity at the initial stage than Co/H-ZSM-5, was performed to control the amount of Brønsted acid sites. In analogous to Co/H-ZSM-5, the ion-exchange method was used for the preparation of Zn/H-ZSM-5, indicating the existence of Zn^{2+} cations at the ion-exchange sites. The pristine Zn/H-ZSM-5 rapidly deactivated by coke formation catalyzed by Brønsted acid sites. The steam treatment of Zn/H-ZSM-5 inhibited the coke formation, leading to the high and stable activity and selectivity to aromatic hydrocarbons. The steam treatment after the Zn loading realize the high Zn content with the appropriate amount of Brønsted acid sites. On the other hand, the steam treatment before the Zn loading induces the lack of the ion-exchange sites (Brønsted acid sites), resulting in the low Zn content. Therefore, the framework Al, which is the origin of Brønsted acid sites, is stabilized if the ion-exchange sites are occupied by metal cations. This indicates that the desirable amount of the active sites (metal cations and Brønsted acid sites) could be obtained by means of the steam treatment and ion-exchange method.

Throughout the thesis, the quality and quantity of the active sites for ethane conversion was controlled by the various techniques to develop optimal catalysts. For dehydrogenation of ethane, oxidative activation of ethane at the reactive surface lattice oxygens of reducible oxides is facile in comparison with that at the surface metal–oxygen couple of non-reducible oxides. This would be also the case in dehydrogenation of propane and butane. In addition, the conventional dehydrogenation processes require periodic regeneration of catalysts deactivated by the coke formation. The reducible metal oxide catalyst would exhibit stable activity for dehydrogenation of propane and butane in the presence of steam. For ethane dehydroaromatization, ethane is activated at the ion-exchanged metal cation sites. The steam treatment in combination with the ion-exchange method realize the appropriate amount of Brønsted acid sites with the large amount of the metal cations. Taking the results of ethane dehydrogenation into account, activation of ethane efficiently proceeds *via* the Mars-van Krevelen mechanism. This requires oxygenated metal cations at the ion-exchange sites in the zeolite in addition to use of any oxidizing agent. It is desirable that redox of the metal cations proceeds with carbon dioxide to suppress sequential oxidation of the products in addition to carbon dioxide utilization. Thus, these catalytic science and technology contribute to not only the efficient production of the valuable chemicals from ethane but future petrochemical industry as a bridging technology to the sustainable society.

Acknowledgement

I would like to express the deepest appreciation to Prof. Yasushi Sekine (Waseda University), who is the supervisor. He gave me various guidance through a lot of discussions, opportunities for collaborations. I would like to deeply thank Prof. Kenichi Oyaizu (Waseda University), Prof. Hideaki Tsuneki (Waseda University) and Prof. Emiel J. M. Hensen (Eindhoven University of Technology), who are the referees for my thesis defense, for evaluating my thesis defense and giving valuable suggestions. Prof. Tsuneki also gave me various suggestions for my research form the chemical engineering point of view. Prof. Hensen also accepted my temporary stay in Eindhoven, where I worked on our collaboration.

I would like to be grateful to Assistant Prof. Nikolay Kosinov (Eindhoven University of Technology) and Dr. Evgeny A. Uslamin (Eindhoven University of Technology), who are the collaborators in Eindhoven, for giving me instruction and frequent discussion. I would like to express my gratitude to Ms. Emma J. J. Eltink (Eindhoven University of Technology), who is a management assistant, for arranging the office procedures in Eindhoven. I want be grateful to the technicians and students at Eindhoven University of Technology.

I would like to express my deep gratitude to Associate Prof. Shuhei Ogo (Waseda University) for helpful discussions, suggestions and corrections of many documents. I'm deeply grateful to Dr. Takuma Higo (Waseda University) for a lot of suggestions, XPS and XAFS measurements in addition to a lot of guidance when I was a bachelor student. I would like to thank Assistant Prof. Tomohiro Yabe (University of Tokyo) and Prof. Jeong Gil Seo (Myongji University) for various suggestions on my research. I would like to show my appreciation to Ms. Masami Kawaharabata, who is a secretary of Sekine laboratory, for the arrangement of the office procedures.

I would like to be grateful to Prof. Yoshihiro Kubota (Yokohama National University), Associate Prof. Satoshi Inagaki (Yokohama National University), Mr. Qiao Han (Yokohama National University) and Prof. Norikazu Nishiyama (Osaka University) for giving me valuable suggestions, comments on my research and various kinds of zeolite samples for ethane dehydroaromatization. I would like to thank Mr. Kunihide Hashimoto (Kubota Corporation), Mr. Shun Maeda (Kubota Corporation), Mr. Yukio Tanaka (Mitsubishi Heavy Industries, Ltd.) and Mr. Haruaki Hirayama (Mitsubishi Heavy Industries, Ltd.) for providing research samples and the financial supports as research expense for the work on ethane dehydrogenation (Kubota Corporation) and dehydroaromatization (Mitsubishi Heavy Industries, Ltd.).

This work was supported by the Leading Graduate Program in Science and Engineering, Waseda University from MEXT, Japan. I would like to thank Prof. Toru Asahi (Waseda University), Prof. Yukio Furukawa (Waseda University) on behalf of the program and all the office staff for their kind support.

Finally, I want to thank all colleagues: Shota Manabe, Kiria Kojima, Hirofumi Seki, Yuji Miyamoto, Ryota Terunuma, Kenta Toko and Yukiko Hosono. Without their help, support and

effort, I could not make the significant achievements.

Tokyo, December 2019
Hikaru Saito

早稲田大学　博士（工学）　学位申請　研究業績書

(List of research achievements for application of doctorate (Dr. of Engineering), Waseda University)

氏 名　斎藤　晃 (Hikaru SAITO)

（As of January, 2020）

種 類 別 (By Type)	連名者（申請者含む）、題名、発表・発行掲載誌名、発表・発行年月 (name of authors inc. yourself, theme, journal name, date & year of publication)
○Academic papers	Hikaru Saito, Hirofumi Seki, Yukiko Hosono, Takuma Higo, Jeong Gil Seo, Shun Maeda, Kunihide Hashimoto, Shuhei Ogo, Yasushi Sekine, Dehydrogenation of ethane via Mars-van Krevelen mechanism over $La_{0.8}Ba_{0.2}MnO_{3-\delta}$ perovskite under anaerobic conditions, *J. Phys. Chem. C*, **2019**, *123*, 26272–26281, available online 7 October 2019.
○Academic papers	Hirofumi Seki, Hikaru Saito, Kenta Toko, Yukiko Hosono, Takuma Higo, Jeong Gil Seo, Shun Maeda, Kunihide Hashimoto, Shuhei Ogo, Yasushi Sekine, Effect of Ba addition to Ga-α-Al_2O_3 catalyst on structure and catalytic selectivity for dehydrogenation of ethane, *Appl. Catal. A: Gen*., **2019**, *581*, 23–30, available online 12 May 2019.
○Academic papers	Hikaru Saito, Satoshi Inagaki, Kiria Kojima, Qiao Han, Tomohiro Yabe, Shuhei Ogo, Yoshihiro Kubota, Yasushi Sekine, Preferential dealumination of Zn/H-ZSM-5 and its high and stable activity for ethane dehydroaromatization, *Appl. Catal. A: Gen*., **2018**, *549*, 76–81, available online 22 September 2017.
○Academic papers	Hikaru Saito, Ryota Terunuma, Kiria Kojima, Tomohiro Yabe, Shuhei Ogo, Haruaki Hirayama, Yukio Tanaka, Yasushi Sekine, Non-oxidative ethane dehydroaromatization on Co/H-ZSM-5 catalyst, *Chem. Lett.*, **2017**, *46*, 1646–1649, available online 9 September 2017.
○Academic papers	Hikaru Saito, Shun Maeda, Hirofumi Seki, Shota Manabe, Yuji Miyamoto, Shuhei Ogo, Kunihide Hashimoto, Yasushi Sekine, Supported Ga-oxide catalyst for dehydrogenation of ethane, *J. Jpn. Petrol. Inst.*, **2017**, *60(5)*, 203–210, available online 1 September 2017.
Academic papers	Evgeny A. Uslamin, Hikaru Saito, Nikolay Kosinov, Evgeny A. Pidko, Yasushi Sekine, Emiel J. M. Hensen, Aromatization of ethylene over zeolite-based catalysts, *Catal. Sci. Technol*., **2020**, in press, doi: 10.1039/C9CY02108F, available online 6 January 2020.
Academic papers	Takuma Higo, Hikaru Saito, Shuhei Ogo, Yukihiro Sugiura, Yasushi Sekine, Promotive effect of Ba addition on the catalytic performance of Ni/$LaAlO_3$ catalysts for steam reforming of toluene, *Appl. Catal. A: Gen*., **2017**, *530*, 125–131, available online 19 November 2016.
Lectures (Oral)	Hikaru Saito, Yukiko Hosono, Hirufumi Seki, Shun Maeda, Kunihide Hashimoto, Takuma Higo, Shuhei Ogo, Yasushi Sekine, Promotive effect of Ba doping on redox properties of Mn in Ba-doped $LaMnO_3$ for dehydrogenation of ethane, 49th Petroleum-Petrochemicals Symposium of The Japan Petroleum Institute, Yamagata, Japan, October 2019.
Lectures (Poster)	Hikaru Saito, Satoshi Inagaki, Qiao Han, Ryota Terunuma, Tomohiro Yabe, Shuhei Ogo, Yoshihiro Kubota, Yasushi Sekine, High and stable activity of dealuminated Zn/H-ZSM-5 for ethane dehydroaromatization, 12th Natural Gas Conversion Symposium, San Antonio, The United States of America, June 2019.

早稲田大学　博士（工学）　学位申請　研究業績書

(List of research achievements for application of doctorate (Dr. of Engineering), Waseda University)

種 類 別 (By Type)	連名者（申請者含む）、題名、　発表・発行掲載誌名、発表・発行年月 (name of authors inc. yourself, theme, journal name, date & year of publication)
Lectures (Poster)	Hikaru Saito, Satoshi Inagaki, Qiao Han, Ryota Terunuma, Tomohiro Yabe, Shuhei Ogo, Yoshihiro Kubota, Yasushi Sekine, Dealumination of Zn/H-ZSM-5 by steam treatment for the suppression of coke formation in ethane dehydroaromatization, The 8th Tokyo Conference on Advance Catalytic Science and Technology, Yokohama, Japan, August 2018.
Lectures (Oral)	斎藤　晃、稲垣　怜史、小嶋　希莉亜、窪田　好浩、小河　脩平、平山　晴章、田中　幸男、関根　泰、Zn/H-ZSM-5 によるエタン脱水素芳香族化反応、触媒学会第 120 回触媒討論会、愛媛、2017 年 9 月
Lectures (Oral)	斎藤　晃、小嶋　希莉亜、小河　脩平、平山　晴章、田中　幸男、関根　泰、エタンの脱水素芳香族化における触媒探索、触媒学会第 118 回触媒討論会、岩手、2016 年 9 月
Lectures (Oral)	斎藤　晃、比護　拓馬、杉浦　行寛、久保　浩一、小河　脩平、関根　泰、トルエン水蒸気改質における $Ni/LaAlO_3$ 触媒への Ba 添加効果、石油学会第 64 回研究発表会、東京、2015 年 5 月
Publications	矢部　智宏、斎藤　晃、小河　脩平、関根　泰、メタン転換・C1 化学におけるゼオライト、*ナノ空間材料*、エヌ・ティー・エス、**2016**, 第 3 章 8 節、288–295.